Diffusion and Perfusion MRI and Applications in Cerebral Ischaemia

Fernando Calamante

Radiology and Physics Unit
Institute of Child Health
University College London

Submitted for the Degree of Doctor of Philosophy
University of London

January 2000

ProQuest Number: 10608996

All rights reserved

INFORMATION TO ALL USERS
The quality of this reproduction is dependent upon the quality of the copy submitted.

In the unlikely event that the author did not send a complete manuscript
and there are missing pages, these will be noted. Also, if material had to be removed,
a note will indicate the deletion.

ProQuest 10608996

Published by ProQuest LLC (2017). Copyright of the Dissertation is held by the Author.

All rights reserved.
This work is protected against unauthorized copying under Title 17, United States Code
Microform Edition © ProQuest LLC.

ProQuest LLC.
789 East Eisenhower Parkway
P.O. Box 1346
Ann Arbor, MI 48106 – 1346

ABSTRACT

Two MRI techniques, namely diffusion and perfusion imaging, are becoming increasingly used for evaluation of the pathophysiology of stroke. This work describes the use of these techniques, together with more conventional MRI modalities (such as T_1 and T_2 imaging) in the investigation of cerebral ischaemia. The work was performed both in a paediatric population in a whole-body clinical MR system (1.5 T) and in an animal model of focal ischaemia at high magnetic field strength (8.5 T).

For the paediatric studies, a single shot echo planar imaging (EPI) sequence was developed to enable the on-line calculation of maps of the trace of the diffusion tensor. In the process of this development, it was necessary to address two different imaging artefacts in these maps: eddy current induced image shifts, and residual Nyquist ghost artefacts. Perfusion imaging was implemented using an EPI sequence to follow the passage through the brain of a bolus of a paramagnetic contrast agent. Computer simulations were performed to evaluate the limitations of this technique in the quantification of cerebral blood flow when delay in the arrival and dispersion of the bolus of contrast agent are not accounted for. These MRI techniques were applied to paediatric patients to identify acute ischaemic events, as well as to differentiate between multiple acute events, or between acute and chronic events. Furthermore, the diffusion and perfusion findings were shown to contribute significantly to the management of patients with high risk of stroke, and in the evaluation of treatment outcome.

In the animal experiments, permanent middle cerebral artery occlusion was performed in rats to investigate longitudinally the acute MRI changes (first 4-6 hours) following an ischaemic event. This longitudinal analysis contributed to the understanding of the evolution of the ischaemic lesion. Furthermore, the findings allowed the acute identification of tissue 'at risk' of infarction.

CONTENTS

LIST OF FIGURES

LIST OF TABLES

ACKNOWLEDGEMENTS

I cannot find enough words to thank the continuous support, encouragement and help from my two supervisors Alan Connelly and David Gadian. They were always ready to discuss the problems and results I faced during my research. Thanks David also for helping me (twice!) to come and work in your group.

There is a group of people to whom I am very grateful. They made a very significant contribution to the work performed in this thesis. It was great to have the chance to work together with Mark Lythgoe, Dave Thomas and Gaby Pell. They not only help me a lot, but also became very good friends. Special thanks to Mark, one of my oldest English friends. I hope we continue having those discussions about crazy ideas to try out new experiments!

I am also very grateful to David Porter, who made my change from SMIS to Siemens a very simple and easy task. Thanks David for your continuous help!

Many thanks also to Martin King, a very good friend from whom I always learn something new. I hope Martin that you continue with your "Fernando, can I ask you a question?", because invariably you always end explaining me something I do not know (I hope my "answers" to your questions were of some use also to you!).

However, the list of people to whom I am very grateful does not end here. I have been lucky enough to work with many good people from whom I learned many things and to whom I am very grateful for their help. During my work at ICH: Nick van Bruggen, Alistair Howseman, Steve Williams, Albert Busza, Bob Turner, Roger Ordidge, Sally Dowsett, Neil Harris, Jane Utting and Chris Sotak. During my work at MR2: Cheryl Johnson, Kling Chong, Mike Bynevelt, Fenella Kirkham, Tim Cox, Vicky Holloway, Mara Prengler, Clare Marshall, Chevaun Williams, Astrid Shirley, David Atkinson and Derek Hill. Thanks also to Leif Østergaard from Copenhagen for the use of his software and very useful discussions about perfusion, and to Edgar Mueller and Wilfried Loeffler of Siemens (Erlangen) for helpful discussion and support during the course of my PhD.

A very special thanks go to a large group of friends from Argentina (las "lacras") who through email, visits and calls kept alive our friendship, and made my life in London not as if I was living thousands of miles from them.

Finally, a very HUGE thanks to my family, who always supported every one of my plans to come to England (and not because they just wanted to get rid of me!). Their never-ending support during these years was fundamental to me, and they managed to make me feel very close to them, regardless of living so far away.

Publications in peer reviewed journals during PhD thesis:

1. F. Calamante, D.A. Porter, D.G. Gadian, A. Connelly. *"Correction for eddy current induced B_0 shifts in diffusion-weighted echo planar imaging". Magn. Reson. Medicine* **41**: 95-102 (1999).
2. F. Calamante, M.F. Lythgoe, G.S. Pell, D.L. Thomas, M.D. King, A.L. Busza, C.H. Sotak, S.R. Williams, R.J. Ordidge, D.G. Gadian. *"Early Changes in Water Diffusion, Perfusion, T_1 and T_2 During Focal Cerebral Ischaemia in the Rat Studied at 8.5 T". Magn. Reson. Medicine* **41**: 479-485 (1999).
3. F. Calamante, D.L. Thomas, G.S. Pell, R. Turner. *"Measuring Cerebral Blood Flow using Magnetic Resonance Imaging Techniques", J. Cereb. Blood Flow Metab.* **19**: 701-735 (1999).
4. F. Calamante, D.G. Gadian, A. Connelly. *"Delay and dispersion effects in dynamic susceptibility contrast MRI: simulations using singular value decomposition".* Accepted subject to revision (*Magn. Reson. Medicine*).
5. D.A. Porter, F. Calamante, D.G. Gadian, A. Connelly. *"The Effect of Residual Nyquist Ghost in Quantitative Echo-Planar Diffusion Imaging". Magn. Reson. Medicine* **42**: 385-392 (1999).
6. D.G. Gadian, F. Calamante, F.J. Kirkham, M. Bynevelt, C.L. Johnson, D.A. Porter, W.K. Chong, M. Prengler, A. Connelly. *"Diffusion and Perfusion Magnetic Resonance Imaging in Childhood Stroke". J. Child. Neurol.* (in press).
7. S.G. Coley, D.A. Porter, F. Calamante, W.K. Chong, A. Connelly. *"Quantitative MR diffusion mapping and cyclosporin-induced neurotoxicity". AJNR Am. J. Neuroradiol.* **20**: 1507-1510 (1999).
8. G.S. Pell, D.L. Thomas, M.F. Lythgoe, F. Calamante, A. Howseman, D.G. Gadian, R.J. Ordidge. *"The implementation of quantitative FAIR perfusion imaging with a short repetition time in time-course studies". Magn. Reson. Medicine* **41**: 829-840 (1999).
9. G.S. Pell, M.F. Lythgoe, D.L. Thomas, F. Calamante, M.D. King, D.G. Gadian, R.J. Ordidge. *"Reperfusion in a gerbil model of forebrain ischemia using serial magnetic resonance FAIR perfusion imaging". Stroke* **30**: 1263-1270 (1999).
10. D. Atkinson, D.A. Porter, D.L.G. Hill, F. Calamante, A. Connelly. *"Sampling and reconstruction effects due to motion in diffusion-weighted interleaved echo planar imaging".* Accepted subject to revision (*Magn. Reson. Medicine*).
11. D.L. Thomas, M.F. Lythgoe, G.S. Pell, F. Calamante, R.J. Ordidge. *"The measurement of diffusion and perfusion in biological systems using magnetic resonance imaging". Phys. Med. Biol.* (in press)

'The other night I had a terrible nightmare. I dreamt that I knew the answers to all the questions. Luckily, it was just a dream, and I woke up to be reunited with my limited knowledge. What would be the challenge of doing science then?'

Nano

1. Introduction

Stroke is the most common neurological disorder causing death or disability in industrialised nations. It is often a devastating condition and ranks third as a cause of death, surpassed only by heart disease and cancer. In any given year in Britain, about 250,000 people suffer from some form of stroke.

The term 'stroke' is used to refer to a *clinical syndrome* (collection of symptoms and signs) of *permanent* neurological deficit, and whose vascular origins are limited to:

- thrombotic or embolic occlusion of a cerebral artery resulting in ischaemic infarction (accounting for approximately 85% of all strokes), or
- spontaneous rupture of a vessel resulting in intracerebral or subarachnoid haemorrhage.

Stroke is distinguished from other types of brain ischaemia, which are reversible:

- Transient ischaemic attack (TIA): resolution of symptoms and signs within 24 hours
- Reversible ischaemic neurological deficit (RIND): resolution within 3 weeks.

Currently, therapeutic interventions in ischaemic stroke are directed towards the reperfusion or salvage of tissue which is ischaemic but not irreversibly compromised. However, the distinction between tissue irreversibly destined for infarction, tissue which is potentially recoverable, and tissue which is not compromised has not been clearly delineated in patients. Several imaging modalities, such as computerised tomography (CT), positron emission tomography (PET) and single photon emission computerised tomography (SPECT) can be used to attempt identify these different states. However, none of these techniques is an ideal option. For example, CT is insensitive to the detection of ischaemia in the acute stages (first 12 hours after the onset of symptoms); PET is expensive and not widely available; and SPECT has low spatial resolution and provides only limited information. Furthermore, all of them involve ionising radiation, and are therefore unsuited to longitudinal investigations, particularly in children.

Magnetic resonance (MR) represents a powerful tool for the diagnosis and study of cerebral ischaemia. One of its unique characteristics is that it can provide structural, metabolic and functional information. An image can be sensitised to a large number of different parameters, such as proton density, relaxation times (T_1, T_2, T_2^*, $T_{1\rho}$), magnetisation transfer between different water pools, diffusion, perfusion, etc. This multi-parametric characteristic sets a challenge in the design and optimisation of pulse sequences, the aim being to increase the sensitivity of detection of particular types of tissue abnormality. Several of these parameters can be combined to increase the contrast between normal and abnormal tissue. However, it has been recognised that the quantification of individual parameters is generally more appropriate for an understanding of the pathophysiological changes occurring in the tissue, which may help in the differentiation of tissue types. MR has the additional advantage of being non-invasive, allowing the possibility of performing an unrestricted number of scans, such as in longitudinal studies. Finally, MR can play an important role in the evaluation of the outcome of the therapeutic strategy adopted.

The work performed for this thesis focuses on the use of magnetic resonance imaging (MRI) techniques for the study of cerebral ischaemia, and has four main objectives:

1. Implementation of quantitative diffusion MRI on a whole body 1.5 T clinical scanner.
2. Evaluation of the limitations of the quantification of perfusion using dynamic susceptibility contrast MRI (DSC-MRI) in stroke.
3. Application of diffusion and perfusion MRI to the study of brain abnormalities in childhood.
4. Study of the acute changes in MR parameters following middle cerebral artery (MCA) occlusion in the rat at high field strength (8.5 T).

The first objective required addressing image artefacts resulting from two well known sources in echo-planar imaging (EPI): eddy currents effects and residual Nyquist ghost.

The former is the subject of Chapter 4, where a method is described to correct the frequency shifts resulting from eddy currents that otherwise result in the misregistration of diffusion-weighted images and preclude the calculation of quantitative data. The method uses a non-phase encoded multi-slice reference scan for the correction of slice-dependent image shifts. This correction is implemented on-line as part of the image reconstruction process to produce maps of the apparent diffusion coefficient (ADC) free of misregistration artefacts, which allows their immediate assessment without the need for off-line post-processing. The effect of residual Nyquist ghost in quantitative diffusion maps is the subject of Chapter 5, which describes how the residual Nyquist ghost can produce severe artefacts when maps of the ADC are calculated from echo-planar images. These artefacts, generated by the *b*-value dependency of the Nyquist ghost of the orbits, are shown to produce regions of apparently low ADC which simulate regions of true reduced diffusion, such as those found in acute stroke. Methods to avoid this artefact are described, and phantom studies are used to provide an explanation for the pattern of artefacts observed *in vivo*.

The second objective is the subject of Chapter 6. Computer simulations are performed to evaluate the effects of delay and dispersion in the quantification of DSC-MRI data using singular value decomposition (SVD). Delay and dispersion are very common in patients with cerebrovascular disease, and it is shown that they introduce significant underestimation of the cerebral blood flow (CBF), and overestimation of the mean transit time (MTT). The effects of different delays and dispersions are evaluated, and the possible implications of such effects are discussed.

The third objective is the subject of Chapter 7. This chapter describes a number of applications where diffusion and perfusion MRI add extra information to that obtained using conventional MRI. This includes improvement of diagnosis, identification of 'at risk' tissue, contributing to patient management, evaluation of treatment outcome, and contribution to the understanding of the mechanisms of neurological abnormalities.

The fourth objective is the subject of Chapter 8. This work is different from the rest of the thesis in that it is performed on a small bore, high field (8.5 T) animal system, but is similar in that it is also directed at the study of the MRI changes associated with cerebral ischaemia. A model of MCA occlusion is used to follow the acute MRI changes. The combined diffusion/perfusion data distinguish three regions: a normal area, a 'moderately affected' area (with reduced perfusion and normal diffusion), and a 'severely affected' area (where both perfusion and diffusion are significantly reduced). The 'moderately affected' region appears similar to the 'at risk' tissue observed in children (Chapter 7), in that both regions are in the mismatch area between the diffusion and perfusion abnormalities. Furthermore, two novel MRI observations are reported, namely, a decrease in T_2 and an increase in T_1, both within the first few minutes of ischaemia, and possible reasons for these acute changes are discussed.

2. Introduction to MR relaxation times, diffusion and perfusion MRI

The intensity of an MR image can be influenced by many factors, such as spin-lattice relaxation time, spin-spin relaxation time, diffusion, perfusion, proton density, magnetisation transfer, spin-lattice relaxation in the rotating frame of reference ($T_{1\rho}$), etc. The most relevant contrast mechanisms for the work performed in this thesis are the first four mentioned. These will be considered in the following sections.

2.1 MR RELAXATION TIMES - T_1 AND T_2

2.1.1 The concept of T_1 and T_2 relaxation

When the equilibrium magnetisation of the nuclear spins in a magnetic field (with a net magnetisation along the direction of main magnetic field, B_0) is perturbed, various processes take place whereby the nuclear magnetisation returns to its initial equilibrium value. These processes are characterised by two relaxation times:

- the *spin-lattice relaxation time, T_1*: the time constant for the recovery of magnetisation along the direction of B_0.
- the *spin-spin relaxation time, T_2*: the time constant for the decay of magnetisation in the plane perpendicular to B_0.

Attempts to use T_1 and T_2 relaxation time measurements as specific markers of tissue pathology have suggested that the determinants of relaxation times do not have a simple relationship to any single tissue parameter (Fullerton, 1992). Therefore, the initial goal of finding a specific relationship between MR tissue relaxation time differences and specific disease states proved to be difficult. The main problem is that tissues are complex molecular systems with complex MR properties.

2.1.2 The correlation time and the spectral density

For an excited spin to relax it must transfer its energy either to another spin or to the surrounding environment. These processes are mediated by fluctuations in the local magnetic field ($\Delta B(t)$) experienced by the spin. The fluctuations contain frequencies covering a range which is dependent on the motion of the molecules. When there is a strong component of the fluctuating field that oscillates at the resonant frequency (Larmor frequency) there can be an exchange of energy (similar to the MR excitation process with the oscillating B_1 field provided by the RF transmitter). An autocorrelation time can be

defined for the field fluctuations whose time constant is generally referred to as the 'correlation time' (τ_c). Since the fluctuations of the field are associated with the movement of the molecules, the correlation time is related to the rotational tumbling time of the molecule. Therefore, the τ_c for free water ($\sim 10^{-11}$ s) is much shorter than that for bound water ($\sim 10^{-8}$ s).

The effects of the different frequency components on T_1 and T_2 relaxation can be seen by considering the problem in the rotating frame of reference (x',y',z'), which rotates about the z axis (the direction of B_0) at the Larmor frequency (ω_0) (Farrar and Becker, 1971). After the application of an RF pulse to perturb the equilibrium magnetisation, the rate of change of the magnetisation of an individual spin (μ) is given by:

$$\frac{d\vec{\mu}}{dt} = \gamma\vec{\mu} \times \Delta\vec{B} = \gamma \begin{pmatrix} \Delta B_{z'}\mu_{y'} - \Delta B_{y'}\mu_{z'} \\ \Delta B_{x'}\mu_{z'} - \Delta B_{z'}\mu_{x'} \\ \Delta B_{y'}\mu_{x'} - \Delta B_{x'}\mu_{y'} \end{pmatrix} \qquad (2.1)$$

where γ is the gyromagnetic ratio. Therefore, the T_1 processes (associated with changes in $\mu_{z'}$) are affected by $\Delta B_{x'}$ and $\Delta B_{y'}$ only, while T_2 processes (associated with $\mu_{x'}$ and $\mu_{y'}$) are affected by the field in all three directions. It is this extra component $\Delta B_{z'}$ (the fluctuations along the direction of B_0) that results in one of the fundamental differences between T_1 and T_2 relaxation mechanisms. Fluctuations in this direction in the rotating frame will appear as zero or close-to-zero frequencies when viewed from the laboratory frame. Therefore, T_2 relaxation will be mediated by frequencies close to ω=0 (*'static contribution'*). On the other hand, T_1 relaxation will not be sensitive to this range of frequencies, and the field fluctuations in the x' and y' directions will appear in the laboratory frame as a fairly narrow band of frequencies centred on the Larmor frequency (*'dynamic contribution'*). T_1 and T_2 are both affected by the transverse components of the ΔB, and hence both will be sensitive to the ω_0 fluctuations. This component will be dependent on the main field strength, explaining the much greater frequency sensitivity of T_1 than of T_2, where the static contribution is very important.

Due to the different frequency contributions to T_1 and T_2 relaxation, it is useful to introduce the concept of spectral density, $J(\omega)$, of the fluctuations. This function defines the distribution of frequency components of the magnetic field fluctuations (Farrar and Becker, 1971) (Fig. 2.1). As can be seen in Fig. 2.1, the spectral density is very different for liquid, viscous and solid systems. For example, the much more restricted motion of protons in a solid generates a small range of slow frequency fluctuations. As a consequence, the T_1 processes are very inefficient (T_1 very long), while the T_2 processes are very efficient (due to the high contribution from low frequencies). As the protons become more mobile, the range of frequencies in the field fluctuations increases, the dynamic contribution is increased and the static contribution decreased. Therefore, T_1 processes become more efficient than in solids, while T_2 processes become less so.

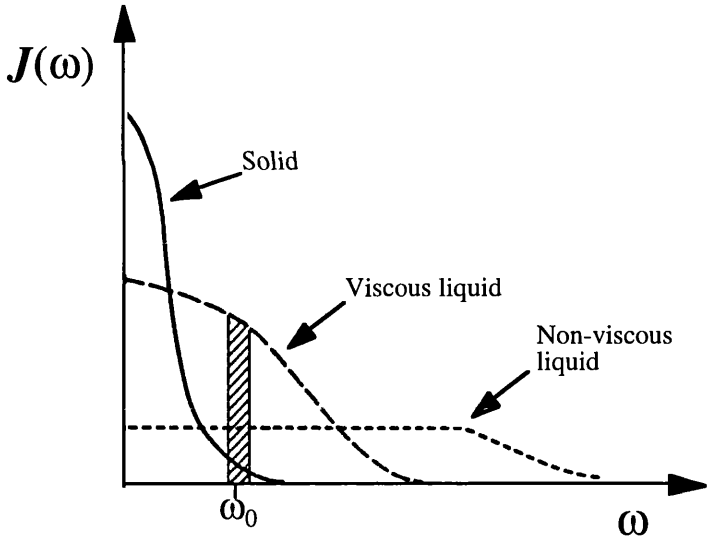

Figure 2.1.

Figure 2.1. Schematic plot of the spectral distribution $J(\omega)$ as a function of frequency for a solid (solid line), viscous liquid (dashed line), and non-viscous liquid (dotted line). In this example, the resonant frequency determined by the magnetic field $\omega_0=\gamma B_0$ is such that viscous liquid contains the highest fraction of total protons with correlation time that matches the resonant frequency ω_0 (within shaded area). Increasing the resonant frequency ω_0 by selecting a higher magnetic field would decrease the area under the curves of the viscous liquid and solid, making the T_1 longer. (Redrawn from Fullerton, 1992)

This behaviour can be described using the so-called 'BPP theory' of Bloembergen, Purcell, and Pound (Bloembergen et al., 1948). They applied this theory to express the T_1 and T_2 relaxation rates in terms of the τ_c and the resonant frequency ω_0 for the simple case of relaxation via the dipole-dipole interaction (see Section 2.1.3) between two like spins (e.g., the two protons of water):

$$\frac{1}{T_1} = K\left[\frac{\tau_c}{1+\omega_0^2\tau_c^2} + \frac{4\tau_c}{1+4\omega_0^2\tau_c^2}\right] \tag{2.2}$$

$$\frac{1}{T_2} = \frac{K}{2}\left[3\tau_c + \frac{5\tau_c}{1+\omega_0^2\tau_c^2} + \frac{2\tau_c}{1+4\omega_0^2\tau_c^2}\right] \tag{2.3}$$

where K is a constant. The extra term in Eq. (2.3), which is independent of ω_0, describes the static contribution, which affects T_2 but not T_1. A plot of the BPP relationships is shown in Fig. (2.2). For liquids ($\omega_0\tau_c<<1$), T_1 and T_2 relaxation times are predicted to be equal and independent of field strength: $1/T_1=1/T_2=5K\tau_c$. For solids ($\omega_0\tau_c>>1$), the dynamic contribution becomes very small, and therefore (from Eqs. (2.2) and (2.3)) T_1 is very long and frequency dependent, while T_2 is short due to the static contribution (see Fig. 2.2). For viscous systems ($\omega_0\tau_c\sim1$), the relaxation characteristics are intermediate between the extremes of liquids and solids, $T_1\sim T_2$ and both relaxation times show a frequency dependence.

2.1.3 Fundamental relaxation mechanisms

Most of the MRI studies are performed using the hydrogen nucleus, in which the main source of relaxation is that from magnetic dipole-dipole interaction. Each hydrogen nucleus in a water molecule possesses a magnetic moment, which generates a magnetic field. Therefore, each proton experiences a small additional contribution ΔB to the B_0 field. The rotational motion of the water molecule, therefore, exposes each proton to a

time dependent magnetic field. This fluctuating field constitutes an important source of relaxation for both T_1 and T_2.

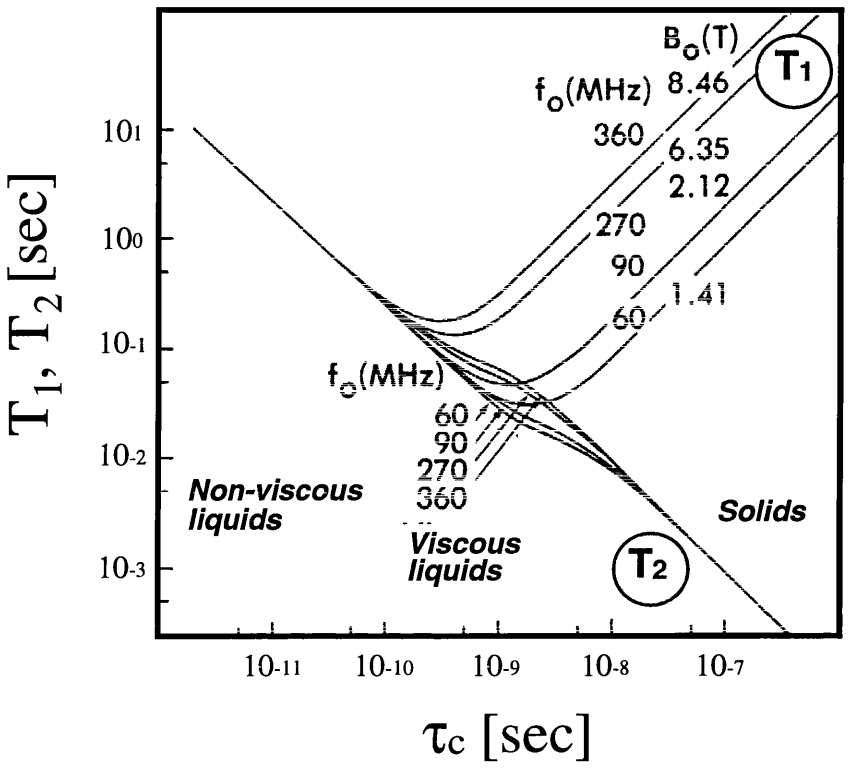

Figure 2.2.

Figure 2.2. A plot of the BPP relationships (Eqs. (2.2) and (2.3)) demonstrates the dependence of relaxation times on the rotational correlation time (τ_c). Non-viscous liquids such as water ($\tau_c \sim 10^{-12}$ sec) lie to the left where $T_1=T_2$. Solids such as ice ($\tau_c \sim 10^{-5}$ sec) lie to the right where $T_1 >> T_2$. Viscous liquids such as hydrophobic fats and oils lie in the central region where $\tau_c \sim 10^{-9}$ sec. Magnetic field strength is in Tesla (T); f_0 is the proton resonant frequency in MHz. (Redrawn from Fullerton, 1992).

However, in a more general situation, there are further sources of relaxation apart from the magnetic dipole-dipole interaction. After the equilibrium magnetisation is perturbed, any mechanism that causes a fluctuating magnetic field $\Delta B(t)$ at a nucleus constitutes, in principle, a possible relaxation source. In addition to the magnetic dipole-dipole interaction, the five further major interactions of nuclear magnetic dipoles with local magnetic and electric fields are (Farrar and Becker, 1971; Harris, 1983):

1. Electric quadrupole coupling.
2. Chemical shift anisotropy.
3. Scalar coupling.
4. Spin-rotation interaction.
5. Interactions with unpaired electron spins.

Of these five interactions, only the interaction with unpaired electron spins is likely to be significant for the relaxation of water protons. The presence of unpaired electrons (paramagnetic material) has an extremely strong effect on the relaxation time, because the electron magnetic moment is much larger than the nuclear magnetic moment.

It should be noted that for water in tissue, the situation is much more complicated than that described by the simple BPP theory. This theory is inadequate to describe multi-component solutions. The problem is that tissue is a heterogeneous system, which consists largely of water and macromolecules from compartments that interact (exchange) in different ways. This exchange is not described by the BPP theory. Therefore, for a complete understanding it would be necessary to consider all the possible mechanisms of relaxation for each of the different compartments in the tissue, as well as the influence of the exchange processes between them.

2.2 DIFFUSION MRI

2.2.1 The concept of diffusion

Molecular diffusion is the random, microscopic, translational motion of molecules, also known as 'Brownian motion'. This diffusion process (i.e., the random molecular walk) can be considered on a more macroscopic statistical scale. If we consider large molecular populations, this random walk process produces net displacements over time for a particular molecule, which are randomly distributed. For a simple liquid, the probability

that a molecule travels a distance r during a time interval τ is described by the Gaussian distribution:

$$P(r,t_d) = \frac{1}{\left(\frac{2}{3}\pi\langle r^2\rangle\right)^{3/2}} \exp\left(-\frac{r^2}{\frac{2}{3}\langle r^2\rangle}\right) \tag{2.4}$$

where the variance of the distance travelled is given by Einstein's equation: $<r^2>=6D\tau$. The proportionality constant D, the diffusion coefficient, characterises the mobility of molecules. Although the net mean displacement remains zero (the probability of moving in one direction is the same as that to move in the opposite direction), if one considers a large number of molecules, the diffusion volume increases with the square root of time (Fig. 2.3).

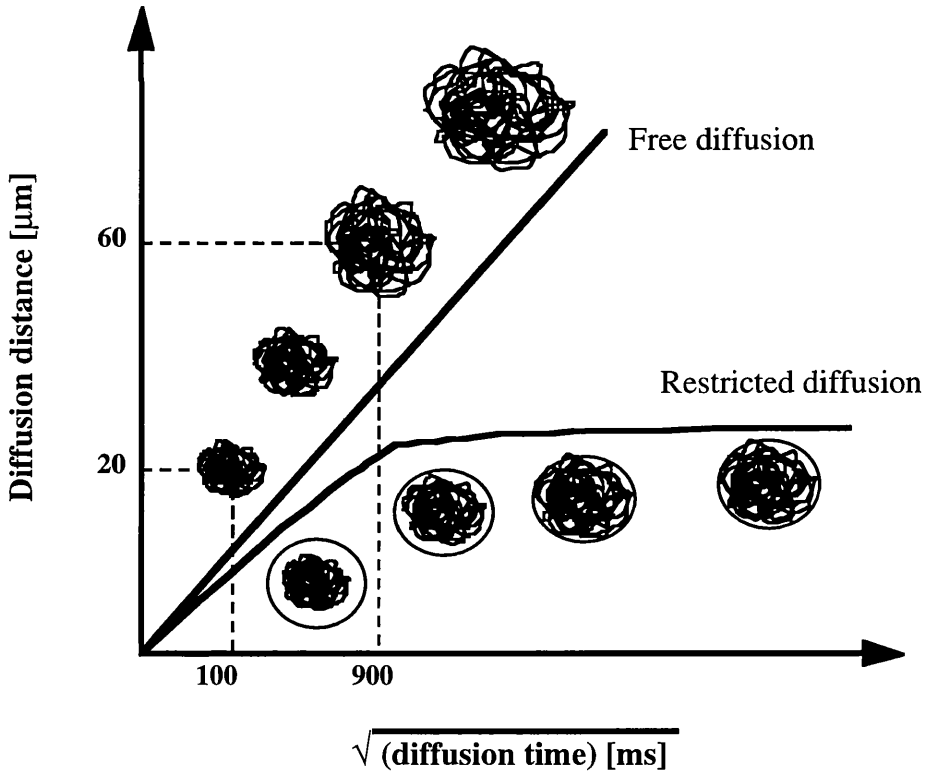

Figure 2.3.

Figure 2.3. Einstein's equation (free and restricted diffusion). With free diffusion, such as for water molecules in a bottle, the diffusion distance, $<r^2>^{1/2}$, increases linearly with

the square root of the diffusion time τ (straight line) according to Einstein's equation. The slope of this straight line defines the diffusion coefficient D. If diffusing molecules are restricted to a closed space, such as an impermeable cell, the apparent diffusion distance to which diffusion MRI is sensitive depends strongly on the diffusion time. For short diffusion times, most molecules do not have time to reach the boundaries of the medium. Therefore diffusion behaves as free diffusion; that is, the diffusion distance increases with the diffusion time. When the diffusion time increases, more molecules reach the boundaries and are reflected back into the medium, and the measured diffusion distance saturates (and the measured 'apparent' diffusion coefficient decreases progressively to zero). Between these two extreme situations the barriers are somewhat permeable to molecules. In this case the diffusion distance still increases with the square root of the diffusion time, but not linearly. (Redrawn from Le Bihan, 1995)

2.2.2 Free vs. restricted diffusion

If the molecules are confined by barriers to diffusion, the diffusion becomes restricted. When the molecules reach these barriers, they are reflected back into the medium. Therefore, the simple relationship between the diffusion distance (r) and the time interval (τ) is no longer valid for very long diffusion time; rather, this distance 'saturates' when all molecules have reached the boundaries (Fig. 2.3).

If one uses the same theory as for free diffusion (e.g., Eq. (2.4)) to interpret the results in the restricted case, the measured diffusion will not only depend on the diffusion properties of the molecules (i.e., its free diffusion coefficient, D_{free}) but also on the size and shape of the medium, permeability of the boundaries, and the diffusion time. Therefore, the measured coefficient is usually referred to as the 'apparent' diffusion coefficient (ADC). For example, in the case of completely impermeable membranes, the Einstein equation predicts that the ADC decreases progressively to zero as the diffusion time increases (Fig. 2.4).

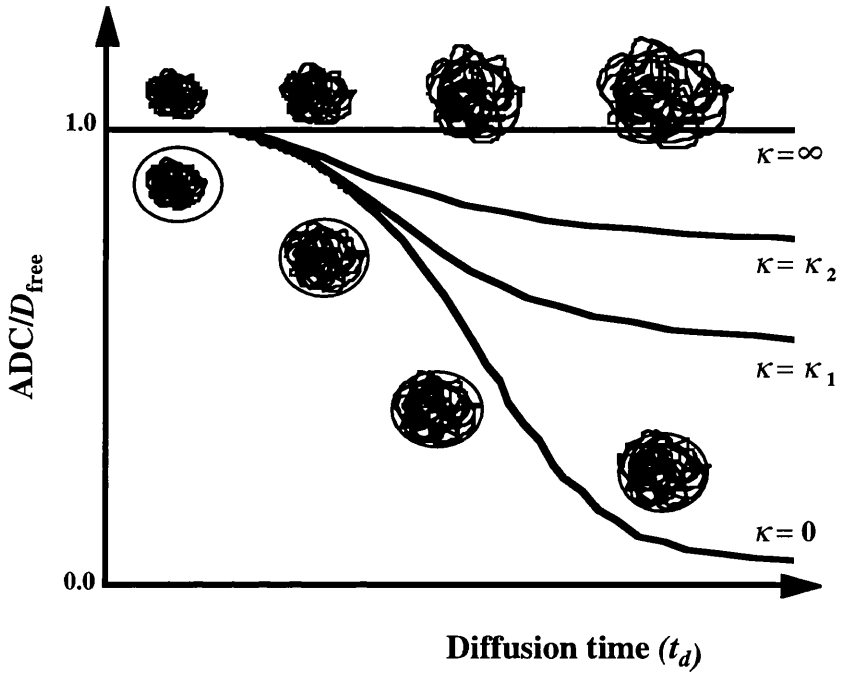

Figure 2.4.

Figure 2.4. Restriction by permeable barriers. When diffusion is restricted by permeable barriers, the dependence of the diffusion coefficient on the diffusion time is modulated by the permeability, κ, of the restrictive barriers. In particular, the measured diffusion coefficient ADC (or its ratio to the free diffusion coefficient) decreases with diffusion time t_d, but saturates at a level which depends on the permeability ($0< \kappa_1< \kappa_2<\infty$). In the absence of barriers ($\kappa =\infty$), ADC is expected to stay constant, while for total restriction ($\kappa =0$) the ADC would decrease toward zero. (Redrawn from Le Bihan, 1995)

2.2.3 Diffusion anisotropy and the diffusion tensor

Diffusion is a three-dimensional process. However, the molecular mobility may not be the same in all directions. In biological tissues, this anisotropy results from the asymmetrical disposition of obstacles that limit diffusion.

In order to study anisotropic diffusion, it is necessary to consider diffusion as a tensor, **D** (Stejskal and Tanner, 1965; Basser et al., 1994). The diagonal elements, D_{ii}, represent the molecular mobility in the three orthogonal directions of the reference system which

the tensor is calculated. The off-diagonal elements, D_{ij}, express how diffusion in one direction (i) is correlated with the molecular displacements in a perpendicular direction (j).

2.2.4 Measuring diffusion using MR

Under equilibrium conditions, it is not possible to measure the diffusion coefficient by monitoring macroscopic evolution and using Fick's first law:

$$J = -D \cdot \nabla C \tag{2.5}$$

where J is the macroscopic diffusive flux vector, and ∇C is the concentration gradient vector. In these situations, measurement of diffusion is usually performed by introducing a tracer in the medium. However, these techniques are highly invasive and may severely perturb the system under study.

In order to measure the diffusion coefficient using MR, it is necessary to tag or label specific molecules, so that their displacements can be measured over some time period. By applying magnetic field gradients, each water molecule in the system is labelled in terms of its position with respect to the applied gradient. The phase accumulated by the transverse magnetisation of spins at location r in the presence of a gradient G over a time interval τ is given by:

$$\phi = \int_0^\tau \omega dt = \gamma \int_0^\tau (B_0 + G \cdot r) dt = \phi_0 + \gamma \int_0^\tau (G \cdot r) dt \tag{2.6}$$

where ω is the Larmor frequency, B_0 is the main magnetic field, and ϕ_0 is the phase accumulated by spins at location r=0.

The most common MR pulse sequence used to measure diffusion was introduced by Stejskal and Tanner (1965), and it is usually referred to as a Stejskal-Tanner sequence or a pulsed-field gradient spin-echo sequence (Fig. 2.5). By applying a gradient pulse (G_{tag}) in the first half of the sequence (before the 180° RF pulse), each spin will accumulate a phase according to its position in the gradient (see Eq. (2.6)). Therefore, a degree of signal dephasing (signal loss) is introduced. After the 180° RF pulse, the dephasing is 'undone' by applying a second gradient pulse (G_{untag}). If G_{tag}=G_{untag}, one gradient pulse cancels the signal loss introduced by the other for the case of static spins. However, for moving spins (diffusing spins), there will be incomplete cancelling, resulting in signal loss. This signal loss is increased by each of the following:

a) increasing the amplitude of the diffusion gradients (G_{tag} and G_{untag}),

b) increasing the length of the diffusion gradient (δ),

c) increasing the time interval between the diffusion gradients (Δ), i.e., allowing more time for the molecules to diffuse, or

d) an increase in molecular diffusivity. With increased diffusion, fewer spins are brought back into phase by the second gradient pulse, and therefore, a smaller spin echo signal magnitude is obtained.

The signal attenuation can be used to measure the diffusion coefficient. In 1965, Stejskal and Tanner (1965) derived the now much-quoted result relating the signal attenuation to the diffusion coefficient:

$$\ln\left[\frac{S(G)}{S(0)}\right] = -\gamma^2 G^2 \delta^2 \left(\Delta - \frac{1}{3}\delta\right) D \qquad (2.7)$$

where Δ is the separation between the leading edges of the two pulsed gradients, and δ is their duration. For very short gradient pulses ($\delta \rightarrow 0$), the diffusion time will be given by the time interval between the pulses Δ. When the length of the gradient pulses cannot be neglected (as in most clinical scanners due to the limited maximum gradient strength availability), diffusion effects *during* the application of the gradient pulses become

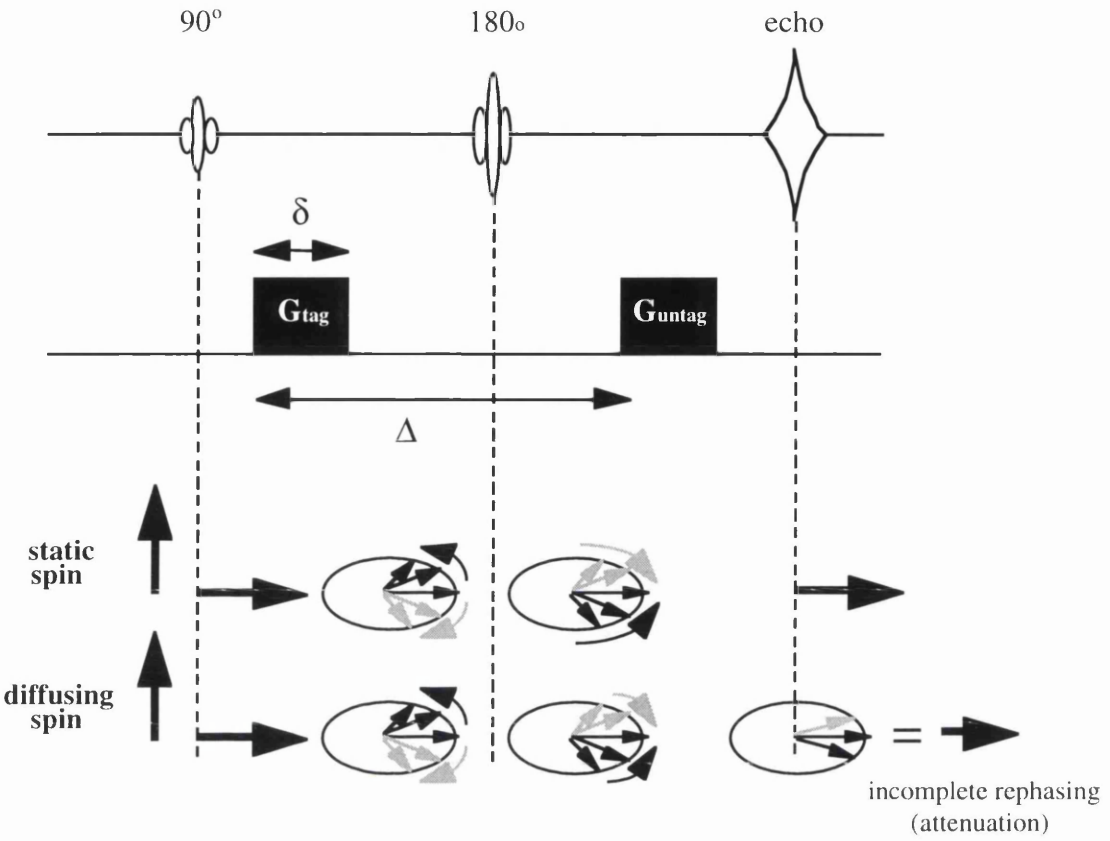

Figure 2.5.

Figure 2.5. Diffusion motion and magnetic field gradients. The effect of diffusion is usually not visible in an MR sequence, such as a spin echo sequence, unless the sequence is sensitised by magnetic field gradients. Because of the presence of the first 'tagging' gradient pulse (G_{tag}), molecules acquire a phase shift, which is a function of their position with respect to the gradient. For static spins, the dephasing is cancelled out by the second 'untagging' gradient pulse (G_{untag}). However, for diffusing spins, there is an incomplete rephasing, which results in echo attenuation.

significant. However, their contribution to the overall signal attenuation is not the same as for diffusion occurring between pulses. The diffusion time then becomes more difficult to define, although (Δ-δ/3) is often taken as the effective diffusion time (Stejskal and Tanner, 1965).

For a general imaging sequence, Eq. (2.7) can be written in the more general form:

$$\ln\left[\frac{S(G)}{S(0)}\right] = -bD \tag{2.8}$$

where the *b*-value is given by

$$b = \int_0^{TE} |k(t)|^2 dt \tag{2.9}$$

and

$$k(t) = \gamma \int_0^t G(t')dt' \tag{2.10}$$

The *b*-value represents the overall sensitivity of the sequence to motion. As can be seen, the *b*-value can be changed by altering the timing or the amplitude of the magnetic gradient pulses. In the general case of an anisotropic medium, the diffusion coefficient is replaced by a diffusion tensor, and the *b*-value by a *b*-matrix (Basser et al., 1994; Mattiello et al., 1994; 1997).

Diffusion sensitisation can be incorporated in a large variety of MRI pulse sequences (Le Bihan et al., 1995), such as spin-echoes (SE), gradient-echoes (GE), stimulated-echoes (STEAM), steady-state free precession (SSFP), echo-planar imaging (EPI), fast low-angle shot (FLASH), projection reconstruction, rapid-acquisition relaxation-enhancement (RARE) and gradient- and spin-echo (GRASE). However, due their motion sensitivity, multi-shot sequences are susceptible to ghosting artefacts.

2.2.4.1 Multi-shot vs. single-shot diffusion-weighted sequences

The particular sensitivity of diffusion imaging to patient motion and physiological effects, such as those related to the cardiac cycle, causes a high level of image artefact when conventional multi-shot imaging techniques are used (Fig. 2.6). These artefacts arise from motion-induced phase errors during the diffusion-sensitising part of the sequence that differ from one line of *k*-space to the next (see *The concept of k-space* (Section 3.1 from Chapter 3)).

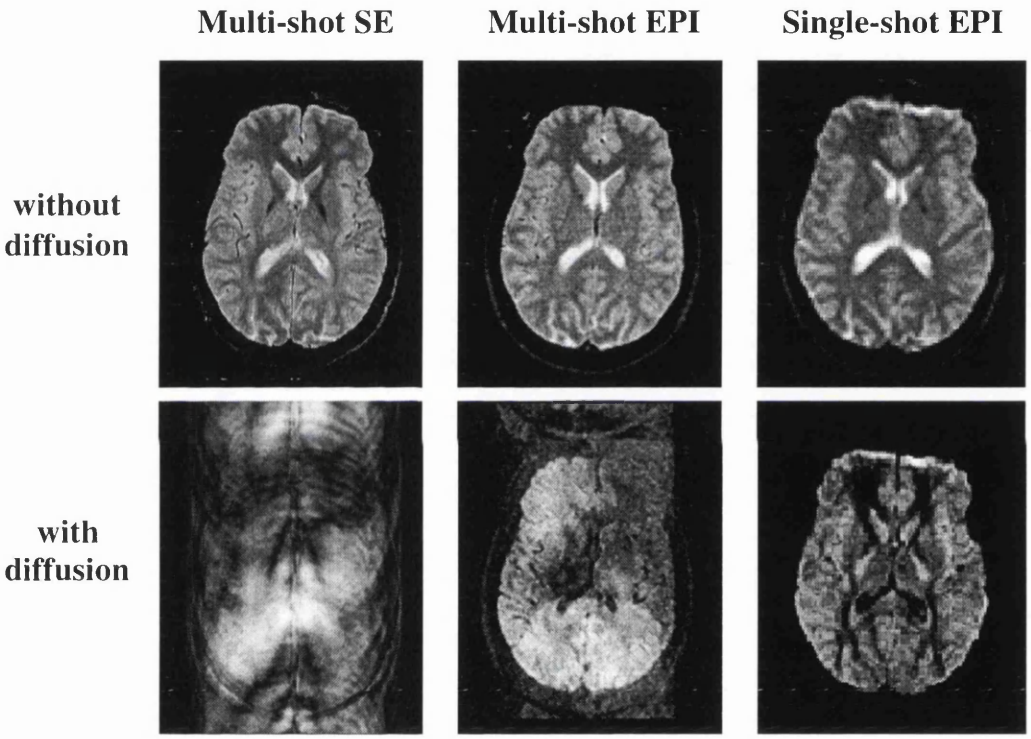

Figure 2.6.

Figure 2.6. Images acquired with three different diffusion-weighted sequences: conventional multi-shot 2D-FT spin-echo sequence (left column), multi-shot interleaved segmented EPI (16 segments) (middle column), and single-shot EPI (right column). The top row shows the images acquired with b-value = 0 s/mm^2 (unweighted images), while the bottom row shows the images with b-value ~ 600 s/mm^2. Motion induces phase errors in the multi-shot sequences, producing ghosting in the image.

One approach to removing these artefacts is to use navigator echoes that allow the phase errors in the raw data to be corrected before image reconstruction (Ordidge et al., 1994; Ehman and Felmlee, 1989; Anderson and Gore, 1994). Alternatively, the artefacts can be avoided by using single-shot imaging techniques which have the same motion-induced phase errors at all points in *k*-space. Single-shot diffusion imaging sequences based on either the RARE (Hennig et al., 1996) or GRASE (Oshio and Feinburg, 1991) techniques are also susceptible to image artefacts as a result of their sensitivity to the phase of the prepared magnetisation. These sequences rely on the amplitude stability of the Carr-Purcell-Meiboom-Gill (CPMG) sequence (Carr and Purcell, 1954), which depends on the Meiboom-Gill (MG) phase condition, so any changes in the phase of the transverse magnetisation caused by a diffusion preparation will result in a rapid attenuation and modulation of the echo amplitudes, and cause signal loss and blurring in the images. Although sequence modifications have been proposed to overcome this problem (Alsop, 1997; Schick, 1997; Liu et al., 1996), these sequences are not in widespread use. Instead, single-shot EPI can be used (see *Echo-planar imaging* (Section 3.2 from Chapter 3)). Although single-shot diffusion-weighted EPI (Turner and Le Bihan, 1990) is not suitable for all applications due to the relatively low spatial resolution and to the presence of susceptibility artefacts, it provides a robust method of avoiding motion artefacts. Furthermore, the short scan times make quantitative studies, requiring the acquisition of several images from each slice position, feasible in the examination of acutely ill patients. In recent years, single-shot EPI has become widely available on clinical systems, and the method is used at an increasing number of sites for performing diffusion-weighted imaging in clinical examinations.

2.2.4.2 Diffusion-weighted imaging vs. Quantitative diffusion mapping

As mentioned in the previous section, the presence of diffusion pulse gradients in the MRI sequence introduces a degree of signal attenuation in the image. This MRI modality is known as diffusion-weighted imaging (DWI), and results in relative signal

hyperintensity in regions of lower ADC (such as a region of acute stroke (see Section 2.2.5)) compared to regions with higher ADC (healthy tissue) (Fig. 2.7).

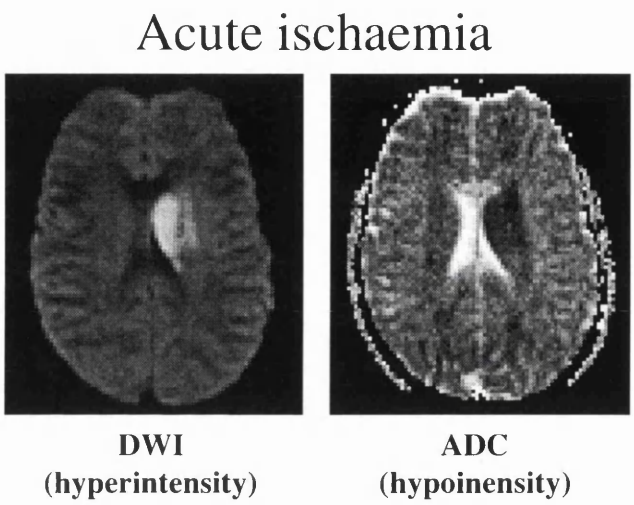

Figure 2.7.

Figure 2.7. In acute ischaemia, the reduced diffusion in the affected area is observed as a region of relative signal hyperintensity in the DW image (the lower the diffusion, the more rephasing introduced by G_{untag} (see Fig. 2.5)). On the other hand, the affected area is seen as a hypointensity region in the ADC map (decreased diffusion, decreased signal intensity).

However, the signal intensity in the diffusion-weighted (DW) image is not only weighted by the ADC, but also by T_2, T_1, and proton density (due to the S(0) factor in Eq. (2.8)). The relative contributions of these factors depends on the sequence parameters (TE, TR, Δ, δ, G). Therefore, in order to separate the effect of diffusion from the other contributions, it is necessary to calculate ADC maps. This can be done by acquiring two or more DW images and fitting the signal intensity dependency on the b-value to Eq. (2.8). In these ADC maps, the lower the diffusion, the darker the pixel intensity. Since lower diffusion is usually associated with higher signal in the DW image (depending on the contribution of the other factors), the image contrast on ADC maps is usually the opposite of that seen on the corresponding DW images (Fig. 2.7).

2.2.4.3 ADC, the diffusion tensor, and the trace

In an anisotropic medium, a single ADC measurement is not enough to characterise the diffusion properties since the value would depend on the particular direction chosen for the diffusion pulsed gradient. This is very relevant for *in-vivo* studies, since the measurement will depend on the orientation of the subject relative to the pulse gradient direction. Therefore, it may lead to erroneous interpretations, because different ADC values could either represent different diffusion properties of the tissue, or simply different orientation of the tissue structure. This has important consequences in stroke studies (see Section 2.2.5.5). A further complication with the use of single ADC measurements is when serial measurements (as in follow up studies) are performed. In these cases, it is very difficult to correlate the results because of the difficulty of reproducing exactly the orientation of the subject with respect of the gradient axes each time.

A full characterisation of diffusion requires the measurement of the diffusion tensor (Basser et al., 1994; 1996). A minimum of seven measurements is needed (as compared to two for the ADC) to sample the full diffusion tensor (Basser et al., 1994; 1998).

A simpler approach to avoid directional dependency in the ADC maps is to measure the trace of the diffusion tensor (Tr(**D**)). The trace of a matrix (the sum of its diagonal elements, i.e., $\mathrm{Tr}(\mathbf{D}) = D_{11}+D_{22}+D_{33}$) is one of the scalar invariants associated with a matrix. It is independent of the reference system (in which the components of the tensor are expressed) and the direction or orientation of the object (Basser et al., 1994). The physical meaning of the Tr(**D**) is the average diffusivity, averaged uniformly over all directions, and as such it is not biased towards any particular direction (unlike the ADC).

To measure the trace, it is not necessary to measure the full tensor. One approach is to design the diffusion pulse gradient pattern (applying multiple gradients with different directions within the same sequence) in order to cancel out all the contributions from the

off-diagonal elements of the diffusion tensor (D_{ij}) to the image contrast. In this way, an image that is weighted by the trace can be generated (Mori and van Zijl, 1995; Wong et al., 1995). Therefore, Tr(**D**) maps can be calculated with as few as two images. Another possibility is to acquire ADC maps in three orthogonal directions, and then calculate the average ADC (ADC_{AV}). When the contribution of the imaging gradients to the *b*-value can be neglected (compared to the diffusion gradient contribution), the ADC_{AV} will be a good approximation to the trace. However, only when there are no localisation gradients or when all cross-terms between imaging and diffusion gradients can be shown to vanish will the trace be equivalent to the ADC_{AV} (Basser, 1995).

It should be noted, however, that by measuring the trace, all the anisotropy information is discarded, since only the completely isotropic part of the diffusion tensor is measured (Basser and Pierpaoli, 1996):

$$\mathbf{D} = \mathbf{D}_{isotropic} + \mathbf{D}_{anisotropic} = \frac{Tr(\mathbf{D})}{3} \boldsymbol{I} + \left(\mathbf{D} - \frac{Tr(\mathbf{D})}{3} \boldsymbol{I} \right) \tag{2.11}$$

where $\boldsymbol{I}$ is the identity tensor, and the second term represent the anisotropic part (i.e., its trace is zero) or 'deviatoric' tensor, which measures the deviation of **D** from being isotropic.

2.2.5 Diffusion MRI and cerebral ischaemia

One of the reasons for the recent fast development of DWI techniques is their sensitivity to very early events in cerebral ischaemia. In 1990, Moseley et al. reported animal studies showing that DW images could be used to detect ischaemic regions of the brain before any changes could be detected with conventional MRI protocols (Moseley et al., 1990). This section describes diffusion MRI in the context of the mechanisms of change during ischaemia, CBF thresholds, metabolic correlations, time course in experimental and human stroke, and the influence of diffusion anisotropy.

2.2.5.1 Mechanisms of DWI decrease in stroke

Moseley et al. (1990) were the first to observe DWI changes in cerebral ischaemia and attributed this reduction of tissue water diffusion to an osmotically obliged shift of extracellular water to intracellular compartments as a result of a disruption of ion homeostasis and formation of cytotoxic oedema. Later work by Benveniste et al. (1992) supported this hypothesis with studies in which the ADC decreased during induction of cytotoxic oedema by administration of ouabain (a specific inhibitor of Na^+ and K^+-ATPase). It was suggested that the reduction of ADC is indeed caused by an influx of extracellular water, which has a high intrinsic diffusion, to intracellular compartments, where the water diffusion would be retarded due to various intracellular obstacles and the relatively high cytoplasmic viscosity. It is now accepted that an ischaemia-induced drop of the tissue water ADC is associated with the development of cytotoxic oedema.

However the exact biophysical mechanisms of water ADC reduction are still unclear. Several hypotheses have been advanced to account for the biophysical mechanisms underlying the ADC changes in ischaemia. Latour et al. have suggested, for example, that DWI changes are caused by a reduction in extracellular diffusion due to an increase in the tortuosity of the extracellular space that occurs after cell swelling (Latour et al., 1994). This view is supported by additional studies investigating the relationship between changes in MR diffusion to changes in cellular volume measured by electrical impedance (Verheul et al., 1994), and to changes in extracellular space and tortuosity measured by iontophoresis (van der Toorn et al., 1996). Alternatively, Helpern et al. suggested that a reduction in cell membrane permeability is the cause (Helpern et al., 1992), whereas DWI of intracellular metabolites indicate that a decrease in intracellular diffusivity might be involved (van der Toorn et al., 1994; Duong et al., 1998). Other possible factors include changes in brain temperature and cessation of brain pulsation.

2.2.5.2 Relation of diffusion changes to CBF

In 1992, using a gerbil model of forebrain ischaemia, Busza et al. (1992) found that DWI signal enhancement only occurred when the CBF fell below 20 ml/100g/min. Interestingly, this is similar to the flow threshold for the maintenance of tissue energy metabolism necessary for cellular ion homeostasis (Crockard et al., 1987). These results differ from those reported for the CBF threshold in a rat model of focal ischaemia, which was approximately 35 ml/100g/min (Kohno et al., 1995). This discrepancy may be due to the species difference, to the different properties of global and focal lesions, or to the different techniques used to measure CBF. However, both studies coincide in the idea of a flow threshold for changes in the diffusion properties of the tissue. Further work, using focal occlusion in rats, has shown a time-dependent increase in CBF threshold, indicating the growing sensitivity of the tissue to perfusion deficits (Kohno et al., 1995; Mancuso et al., 1995).

2.2.5.3 Relationship of diffusion changes to metabolic alterations

Mintorovitch et al. correlated DWI signal change with tissue water content, ATPase activity, and electrolyte content (Mintorovitch et al., 1994). Within 30 minutes of ischaemia, DWI changes had occurred with a concomitant decrease of 30-40% in ATPase activity, while tissue water content and electrolyte concentrations were normal. By 60 minutes, the ATPase activity had decreased further, the water and sodium content had increased, and the potassium concentration was lowered. These data indicate that DWI monitors very early disturbances of ion pumps, at times when such changes are thought to be potentially reversible. Autoradiographic techniques for measuring CBF, ATP, glucose, lactate and pH have been used to study the spatial relationship between DWI changes and metabolism following focal ischaemia in the rat (Kohno et al., 1995). It was found that during the early phase of cerebral ischaemia (30 minutes) the area of hyperintensity seen on DWI was significantly larger than the region of ATP depletion, although it matched the area exhibiting tissue acidosis. This difference became

progressively smaller with the evolution of the lesion, such that by 7 hours the area of tissue damage, as indicated by DWI, was identical to the region of ATP depletion and histological infarction. If in fact DWI changes result from an alteration in compartmentation of tissue water, then the latter observations indicate that water redistribution occurs prior to the impairment of energy metabolism. These observations do not necessarily contradict the former statements, since the anaerobic production of metabolites, including lactate, can also give rise to redistribution of water, which might be expected to result in DWI changes.

2.2.5.4 Time course of the ADC changes in animals and humans

As was mentioned before, the acute period following ischaemia is characterised by a decrease in the ADC. This decrease has been observed ~1-3 minutes after the onset in animal studies (Pierpaoli et al., 1996a; Davis et al., 1994), and as soon as the scan was performed in clinical examinations (~45 min, Sunshine et al., 1999). The ADC decreases to approximately 40-50% of control values (Baird and Warach, 1998; Hoehn-Berlage, 1995), and stays reduced for a few days. In the chronic stages of cerebral ischaemia, the ADC exhibits a very different pattern. The diffusion of water is characterised by an abnormally high value (Warach et al., 1992). This elevated ADC is associated with cellular lysis, with the loss of cellular barriers, combined with excessive accumulation of oedematous water (Pierpaoli et al., 1993). In progressing from the acute low ADC to the chronic high value, the diffusion must cross the normal value (Fig. 2.8). This stage is usually referred to as 'pseudonormalisation', because although the ADC returned to its original value, it does not reflect a return to normal tissue, but a progression towards infarction. The two tissue states (normal tissue and 'pseudonormalised' tissue) can be differentiated by their T_2 values (Welch et al., 1995), with the T_2 abnormally long in the latter case. Therefore, it has been suggested that a combined diffusion/T_2 analysis could be used to evaluate the evolution of the lesion (Welch et al., 1995). This is particularly relevant in human stroke, where there is no 'control' over the time (or degree) of occlusion, as in most animal studies.

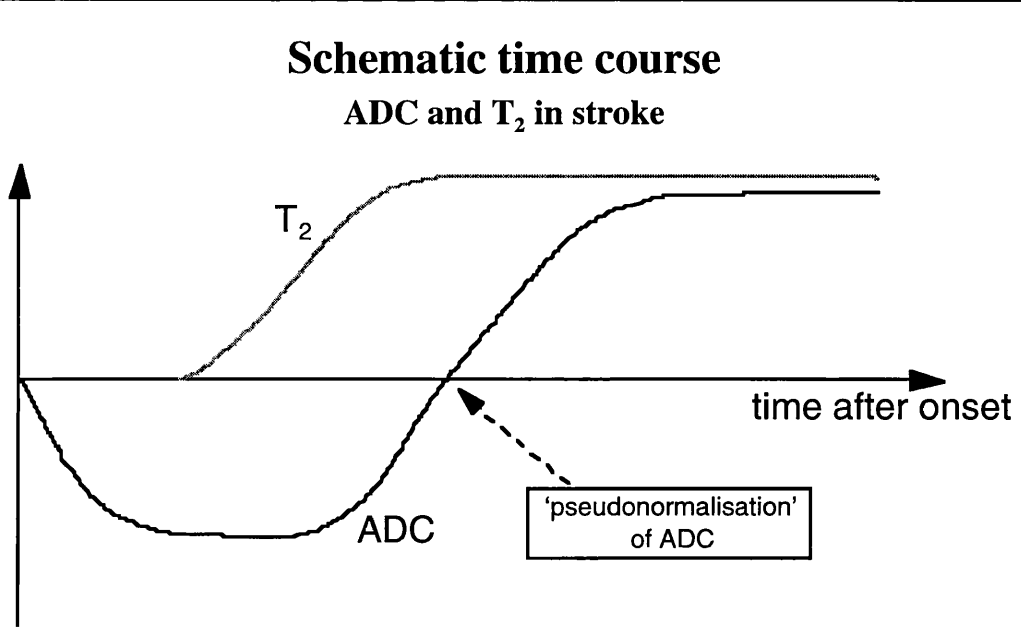

Figure 2.8.

Figure 2.8. Time evolution of the ADC and T_2 changes in stroke. Schematic representation of the time course of ADC (dark line) and T_2 (grey line) changes in stroke. Four 'stages' can be differentiated: decreased ADC and normal T_2; decreased ADC and increased T_2; normal ADC and increased T_2 ('pseudonormalisation); increased ADC and T_2.

Figure 2.8 shows a schematic representation of the time evolution of the ADC and T_2 after cerebral ischaemia. The evolution is qualitatively similar in animals and humans, although the time scale is different. For example, T_2 changes are usually observed approximately 2 hours after the onset in animal studies, while they are not detected until ~6-12 hours in human stroke. Similarly, the 'pseudonormalisation' occurs ~1-3 days in rats, and between ~3-10 days in humans (Knight et al., 1994; Schlaug et al., 1997). The larger variability in the time of 'pseudonormalisation' in humans probably reflects the more variable levels of occlusion observed in humans, the particular artery that is affected (most of the focal ischaemia animal experiments involve middle cerebral artery occlusion), as well as on the contribution from anisotropy in the ADC (Ulug et al., 1997), and to a lesser degree, the greater uncertainty in the determination of the onset time.

2.2.5.5 Stroke and the trace of the diffusion tensor

Due to the anisotropy of the tissue, an ADC measurement along a single direction can introduce systematic errors in the measurement of water diffusion, and even lead to erroneous interpretations in cerebral ischaemia studies. For example, the low ADC perpendicular to the axon in white matter tissue, or the high ADC parallel to the axon, may appear similar to an acute or chronic stroke respectively. This source of ambiguity can be avoided by using the rotationally invariant Tr(**D**). Furthermore, it has been suggested that the use of Tr(**D**) maps may improve definition of ischaemic lesion contrast by removing the confounding effects of diffusion anisotropy (van Gelderen et al., 1994) (see Fig. 2.9). This has been recently evaluated in a rat model of focal ischaemia, where a significant disagreement was found between the lesion delineated by a unidirectional ADC measurement and that delineated using the trace (Lythgoe et al., 1997). Therefore, the use of the trace is now generally accepted for the identification of the areas of reduced diffusion following ischaemia (Baird and Warach, 1998).

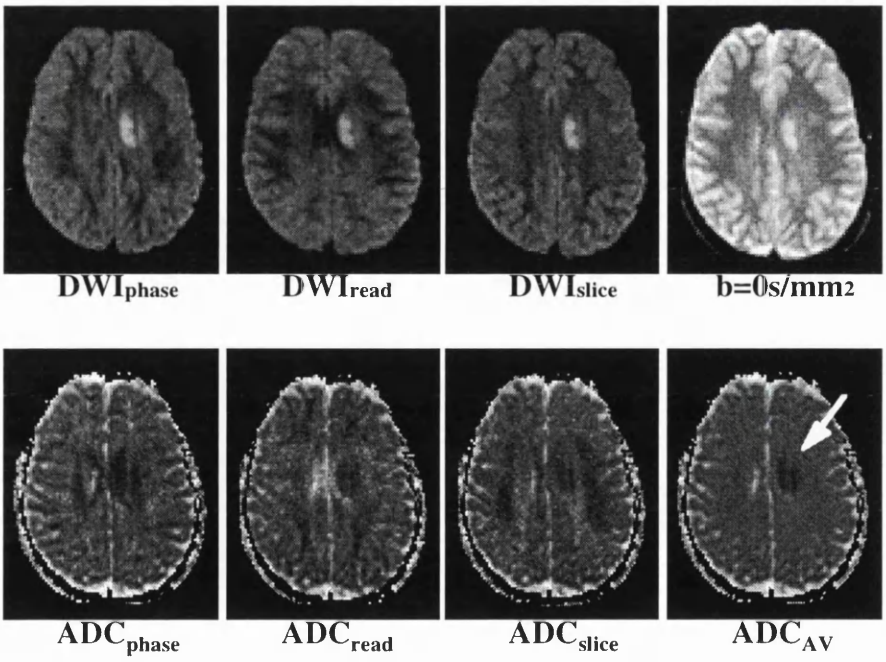

Figure 2.9.

Figure 2.9. Effect of diffusion anisotropy on lesion delineation in stroke. Diffusion weighted images (diffusion along phase, read, and slice directions), unweighted image

(b=0 s/mm^2), and ADC maps acquired approximately 24 h after the onset of stroke in a 10-year-old female. There is a region of hyperintensity in the left hemisphere (right side of the images) clearly seen in the DW images and the unweighted image (top row). The single directional ADC maps show this affected region as an area of reduced diffusion. However, there are also areas with similar diffusion restriction due to the anisotropy properties of the tissue. Therefore, it is not possible to distinguish these areas from the ischaemic region. The confounding effects of diffusion anisotropy on lesion delineation are eliminated in the average ADC map (bottom right). In this map, the small ischaemic area is clearly seen as a hypointense region (white arrow).

2.3 PERFUSION MRI

2.3.1 The concept of perfusion

Perfusion is often defined as the volume of blood delivered to the capillary beds of a block of tissue in a given period of time, and its units are therefore ml/100g/min. It is important to distinguish between perfusion and bulk flow: perfusion is flow at the capillary level, where exchange of nutrients between blood and tissue occurs, whereas bulk flow corresponds to flow through major vessels such as veins and arteries, where no exchange takes place. Perfusing blood delivers substances such as oxygen and glucose to the tissue, which are necessary for cellular metabolism, and carries away the waste products. The survival of the brain is dependent on a continuous and adequate supply of oxygen and nutrients, and failure of the cerebral circulation can result in cell death. For these reasons, the ability to measure perfusion accurately and with good spatial resolution would offer the chance to identify tissue that is at risk following stroke.

2.3.2 Measuring perfusion using NMR

Two distinct MRI techniques for measurements of perfusion have been developed in the last decade, each with well-supported claims to provide a quantitative assessment of

CBF. These methods differ in their respective use of an endogenous and exogenous MRI-visible tracer. The first of the techniques, arterial spin labelling, uses RF pulses to label moving spins in flowing blood, while the second, dynamic susceptibility contrast MRI, requires injection of a contrast agent.

2.3.2.1 Perfusion imaging using arterial spin labelling

An MR image can be sensitised to the effect of inflowing blood spins if those spins are in a different magnetic state from that of the static tissue. The family of techniques known as arterial spin labelling (ASL) uses this idea by magnetically labelling blood flowing into the slice of interest. Blood flowing into the imaging slice exchanges with tissue water, altering the tissue magnetisation. A perfusion-weighted image can be generated by the subtraction of an image in which inflowing spins have been labelled from an image in which spin labelling has not been performed. Quantitative perfusion maps can be calculated if other parameters (such as tissue T_1 and the efficiency of spin labelling; see below) are also measured. Since exogenous contrast agents are not required for these techniques, the perfusion measurement is completely non-invasive. Under the general heading of ASL, two distinct sub-groups exist: continuous ASL (Detre et al., 1992; Williams et al., 1992, Alsop and Detre, 1996) and pulsed ASL (Kwong et al., 1995; Kim, 1995; Edelman et al., 1994; Wong et al., 1998a).

2.3.2.1.1 Continuous arterial spin labelling (CASL)

2.3.2.1.1.1 Basic theory

The arterial spins can be magnetically labelled either by continuous inversion using adiabatic fast passage (Dixon et al., 1986; Williams et al., 1992; Zhang et al., 1992) or by repeated slice selective saturation pulses (Detre et al., 1992). The 'labelled' spins flow into the brain and, assuming water is a freely diffusible tracer, exchange completely with

brain tissue water, thus reducing the overall tissue magnetisation. A steady state develops where the regional magnetisation in the brain is directly related to cerebral blood flow. This steady state can be derived from the Bloch equation for longitudinal relaxation when it is modified to include flow and cross-relaxation with macromolecules (Zhang et al., 1992; 1995):

$$\frac{dM_b(t)}{dt} = \frac{M_b^0 - M_b(t)}{T_{1b}} + fM_a(t) - \frac{f}{\lambda} M_b(t) - k_f M_b(t) + k_r M_m(t) \qquad (2.12)$$

where $M_z(t)$ is the longitudinal magnetisation of the brain tissue per unit mass, M_b^0 is the magnetisation of fully relaxed tissue per unit mass, T_{1b} is the longitudinal relaxation time of brain tissue water, f is blood flow (perfusion), λ is the blood:brain partition coefficient for water (defined as (ml of water/g of brain)/(ml of water/ml of blood)), M_a is the magnetisation of water in the inflowing arterial blood per unit volume of blood, M_m is the magnetisation of macromolecules per unit weight of brain tissue, and k_f and k_r are the magnetisation transfer (MT) rate constants between tissue water and macromolecules.

When macromolecular spins are saturated ($M_m(t)=0$), Eq. (2.12) can be easily solved. This leads to the following equation for flow quantification (Zhang et al., 1995):

$$f = \frac{\lambda}{T_{1app}} \left(\frac{M_b^{cont} - M_b^{inv}}{2\alpha M_b^0} \right) \qquad (2.13)$$

where α is the degree of arterial spin water inversion (equal to 0.5 for saturation, 1 for perfect inversion), M_b^{inv} is the steady state magnetisation with arterial spin inversion (the perfusion-weighted image):

$$M_b^{inv} = M_b^0 \left(\frac{\frac{1}{T_{1b}} - \frac{f}{\lambda}(2\alpha - 1)}{\frac{1}{T_{1app}}} \right) \tag{2.14}$$

M_b^{cont} is the steady state magnetisation without arterial spin inversion (the control image):

$$M_b^{cont} = M_b^0 T_{1app} \left(\frac{1}{T_{1b}} + \frac{f}{\lambda} \right) \tag{2.15}$$

and T_{1app} is the constant that describes the exponential decay to the steady state magnetisation, and is defined by (Zhang et al., 1995) as:

$$\frac{1}{T_{1app}} = \frac{1}{T_{1b}} + \frac{f}{\lambda} + k_f \tag{2.16}$$

Equation (2.16) is the fundamental equation of ASL, describing how the apparent longitudinal relaxation time of brain tissue is affected by blood flow. By measuring T_{1app} and the ratio of magnetisation with and without arterial spin saturation, a value for flow can be calculated using Eq. (2.13).

2.3.2.1.1.2 CASL quantification issues

There are three main effects that influence the accuracy of the perfusion quantification using CASL:

a) Transit time

b) Magnetisation transfer

c) Intravascular signal

a) *Transit time effects*: since the time taken for spins to travel between the labelling plane and the imaging slice (henceforth referred to as the transit time, Δ) is non-zero, T_1 relaxation occurs during this period. Different regions of the brain have different transit times, depending on the distance from the labelling plane and the cerebrovascular anatomy. This effect reduces the labelling (α is overestimated by the assumed value), introducing an underestimation of perfusion (see Eq. (2.13)). For an accurate quantification, this effect must be taken into account. If the value of Δ is known (Zhang et al., 1993; Ye et al., 1997a; Wong et al., 1997; Barbier et al., 1999; Branch et al., 1998), the transit time effect can be incorporated into Eq. (2.13) by modifying the degree of inversion:

$$\alpha' = \alpha \exp(-\Delta / T_{1a}) \tag{2.17}$$

where T_{1a} is the longitudinal relaxation time of arterial blood water.

b) *Magnetisation transfer effects*: since CASL is a steady state technique, an off-resonance RF pulse of several seconds duration must be used for the labelling. Although the direct saturation effect on the water magnetisation can be neglected, the off-resonance RF introduces a significant saturation of the macromolecular magnetisation. This attenuates the free water signal through magnetisation transfer (Wolff and Balaban, 1989), which reduces the perfusion-dependent signal difference between the control and spin-labelled images. The relationship in Eq. (2.13) is valid only in the case of complete saturation of the macromolecules. For a more general case, McLaughlin et al. (1997) have developed a more comprehensive analysis based on a four-compartment model of free and bound solvent and macromolecular protons.

c) *Intravascular signal contribution*: another possible source of systematic error in CASL techniques is the presence of intravascular signal in the subtraction (control minus labelled) images. All the theoretical models describing the relationship between flow and signal difference (e.g. Eq. (2.12) to (2.17)) are based on the assumption that signal

comes exclusively from tissue. If a significant amount of signal emanates from the vasculature, perfusion will be overestimated. One way to minimise this effect is by including flow-crushing gradients in the imaging sequence, which are intended to completely eliminate signal from intravascular spins (Ye et al., 1997a).

To address some of these considerations, Alsop and Detre (1996) introduced a modification to the conventional CASL sequence by inserting a post-tagging time delay (w) between the end of the labelling period and the image acquisition. With this delay, quantification of perfusion is more complex, and requires the knowledge of some extra parameters (Alsop and Detre, 1996):

$$f = \lambda\left(\frac{M_b^{cont} - M_b^{inv}}{2\alpha M_b^0}\right) C(T_{1ns}, T_{1s}, T_{1a}, \delta, \delta_a) \tag{2.18}$$

where

$$\begin{aligned}\frac{1}{C} = T_{1ns} e^{-\delta / T_{1a}} &\left[\exp\left(\min(\delta - w, 0) / T_{1ns}\right) - \exp\left(-w / T_{1ns}\right)\left(1 - \frac{T_{1s}}{T_{1ns}}\right)\right] \\ &+ T_{1a}\left[\exp\left(\left(\min(\delta_a - w, 0) - \delta_a\right) / T_{1a}\right) - \exp\left(\left(\min(\delta - w, 0) - \delta\right) / T_{1a}\right)\right]\end{aligned} \tag{2.19}$$

where two transit times are defined: δ_a represents the time required for blood to flow from the tagging plane to the arteries within the vascular compartment, and δ is the transit time from the tagging plane to the capillary exchange sites of the vasculature, i.e., the point at which exchange between blood water and tissue water can occur. T_{1s} is the apparent T_1 in the presence of off-resonance radiation, T_{1ns} is the apparent T_1 in the absence of off-resonance radiation. Although the delay reduces the signal difference between the control and labelled images and complicates the quantification procedure, for the cases where the delay is greater than the arterial transit times across the image, the resulting CBF maps will be almost completely insensitive to variations in transit time (Alsop and Detre, 1996). Furthermore, this sequence allows almost all of the labelled

blood to either exchange with the tissue or 'wash through' the vasculature during the post-tagging delay, and therefore suffers less from the associated errors of arterial signal contributions.

It is important to note that since transit time effects cause an underestimation of CBF and intravascular signal causes an overestimation, the two effects can tend to cancel one another out. However, this will only be true under very specific circumstances, and both sources of systematic error need to be addressed for an accurate quantification of perfusion. It has been suggested that a combination of delayed acquisition (Alsop and Detre, 1996) and flow-crushing gradients (Ye et al., 1997a) is sufficient to account for both effects (Ye et al., 1997b).

2.3.2.1.1.3 Multi-slice CASL imaging

Magnetisation transfer complicates the extension of the above methods to multi-slice acquisition, since the control image must experience exactly equivalent MT effects as the spin labelled image. This means that the control 'plane' must be symmetrically opposite the inversion plane with respect to the imaging slice, which can only be true for a single imaging slice, and limits the slice orientation to being perpendicular to the arteries in which spin labelling is performed.

One possible solution involves the use of a two-coil set-up to avoid the saturation of macromolecular spins (Zhang et al., 1995, Zaharchuk et al., 1999). In this set-up, a small surface coil is used for the local labelling while a separate coil is used for the imaging. Extension of this approach to multi-slice perfusion imaging is straightforward, since the control image does not need to contain any MT information (Silva et al., 1995). However, specialised hardware is needed to implement this method, and flow quantification is still complicated by the need to account for a large range of arterial transit times. Alternatively, Alsop and Detre (1998) have recently proposed a sequence modification which allows multi-slice perfusion imaging with standard hardware to be

measured. Rather than acquiring the control image by changing the frequency and/or gradient polarity of the RF inversion pulse, the amplitude of the pulse is sinusoidally modulated at a frequency φ. Fourier transformation of an RF waveform of base frequency φ_0 with sinusoidal amplitude modulation of frequency φ results in a pair of inversion planes at frequencies $\varphi_0 \pm \varphi$. The result is that as spins flow through, they are inverted and then immediately 'uninverted', thereby losing their label. The MT effects of the sinusoidally modulated waveform have been shown to be equivalent to those of the standard labelling RF pulse (except very close to plane of inversion), thus enabling multi-slice perfusion imaging with any image orientation. However, some concerns remain regarding the efficacy of the double inversion pulse (Alsop and Detre, 1998).

2.3.2.1.2 Pulsed arterial spin labelling (PASL)

2.3.2.1.2.1 Basic theory

As mentioned in the previous section, CASL techniques suffer from two major problems: magnetisation transfer effects, caused by the application of a long off-resonance RF pulse prior to image acquisition, and the loss of the spin label by the blood water as it travels from the labelling plane to the imaging slice. In PASL techniques, these sources of error are minimised in an attempt to facilitate flow quantification. This is achieved by using a short (typically ~ 10 ms) RF pulse to label spins, and minimising the distance between the labelling region and the imaging slice.

Several different PASL techniques have been proposed, such as EPISTAR (*E*cho *P*lanar *I*maging and *S*ignal *T*argeting with *A*lternating *R*adiofrequency) (Edelman et al., 1994), FAIR (*F*low-sensitive *A*lternating *I*nversion *R*ecovery) (Kwong et al., 1995; Kim, 1995), PICORE (*P*roximal *I*nversion with *C*ontrol for *O*ff-*R*esonance *E*ffects) (Wong et al., 1997) and UNFAIR (*UN*-inverted *F*low-sensitive *A*lternating *I*nversion *R*ecovery) (Helpern et al., 1997). They are all equivalent in so far as they involve the acquisition of

pairs of images, one of which has inverted blood water flowing into the imaging slice and the other of which has fully relaxed blood water flowing in. In these techniques, the state of the static tissue magnetisation may be different at the time of image acquisition (e.g., FAIR images derive from an inversion recovery process, whereas in EPISTAR the tissue is saturated prior to the application of the inversion tag). However, since the static component of the signal is removed by subtraction of the spin labelled image from the control image, the behaviour of the difference signal with inversion time is the same in all these techniques (Calamante et al., 1999).

The relationship between the difference signal and perfusion can be obtained by solving the Bloch equation with the appropriate initial conditions (Kwong et al., 1995; Calamante et al., 1996; Buxton et al., 1998):

$$\Delta M(TI) = 2\alpha M_b^0 \frac{f}{\lambda}\left[\frac{\exp\left(-\frac{TI}{T_{1app}}\right)-\exp\left(-\frac{TI}{T_{1a}}\right)}{\frac{1}{T_{1a}}-\frac{1}{T_{1app}}}\right] \qquad (2.20)$$

where *TI* is the time between spin inversion and image acquisition (inversion time), and *ΔM(TI)* is the difference in magnetisation per unit mass between the labelled and control images. Quantification of blood flow therefore requires the acquisition of a set of image pairs at different TIs, and the differences in signal to be fitted to the biexponential in Eq. (2.20). If $T_{1a} \sim T_{1b}$, Eq. (2.20) reduces to

$$\Delta M(TI) = 2\alpha M_b^0 \frac{f}{\lambda} TI \exp\left(-TI / T_1\right) \qquad (2.21)$$

This theoretical signal difference is less than that of CASL by a factor of $(TI/T_{1app})exp(-TI/T_1)$, although the SNR efficiency $\Delta M/\sqrt{TR}$ is similar (Wong et al., 1998b).

As with CASL techniques, there are some effects that influence the accuracy of the perfusion quantification:

a) Transit time

b) 'Inflow time'

c) Intravascular signal

a) *Transit time effects.* In principle transit time effects should not be a problem in PASL. However, in practice there is some interaction between the edges of the inversion slice and the imaging slice (Frank et al., 1997). In order to minimise the interaction between the inversion and imaging slice profiles, it is necessary to move the edges of the inversion slice away from the imaging slice, e.g., the inversion slice is shifted away from the imaging slice for EPISTAR and widened for FAIR. As a result of this, a transit time is introduced during which the inflowing blood is not in the state assumed by the standard model (e.g., fully relaxed for FAIR, fully inverted for EPISTAR). Although generally less than in CASL, the transit time in PASL can be quite large, and still may introduce significant errors.

b) *'Inflow time' effects.* A second practical point to consider is the width of the inverted slab of spins. If the bolus width is insufficiently wide, fresh spins that have not been inverted will flow into the imaging slice during the inversion time. In EPISTAR, this width is defined in the pulse sequence by the bandwidth of the inversion pulse and the slice-select gradient; in FAIR, the range of spins affected by the non-selective inversion pulse is defined by the physical extent of the RF coil. If inflow of fresh spins occurs, the perfusion signal will be less than predicted by the standard ASL model (Calamante et al., 1996; Kim et al., 1997b; Pell et al., 1999).

c) *Intravascular signal effects.* As with CASL, the contribution of blood water signal needs to be considered in the quantification of the PASL difference signal. The inclusion

of a bipolar gradient in the imaging sequence has been shown to reduce the perfusion signal and cause a lengthening of the measured transit time (Wong et al., 1998b). This is interpreted as a reduction in the amount of spin labelled blood water signal present in the subtraction images, since the rapid motion of the intravascular water should cause its signal to decay rapidly in the presence of a field gradient. However, the choice of the magnitude of the gradient strength (i.e., *b*-value) is rather arbitrary, and is generally empirically determined as the point at which a further increase in *b*-value does not alter the calculated perfusion value.

Some of these effects can be included in the perfusion model by taking into account a finite transit time and limited bolus width. However, this further complicates the quantification procedure (Kim et al., 1997b; Pell et al., 1999; Buxton et al., 1998). Alternatively, PASL pulse sequences can be modified to reduce their sensitivity to transit time effects and allow the acquisition of a purely perfusion-dependent subtraction image. Wong et al. (1998a) have recently proposed two sequences: QUIPSS (*QU*antitative *I*maging of *P*erfusion using a *S*ingle *S*ubtraction) and QUIPSS II. In QUIPSS, a saturation pulse is applied to the imaging slice at a time TI_1 after application of the labelling or control RF pulse, and the image is acquired at a later time TI_2. By doing this, any signal difference which evolves during TI_1 is destroyed, and only spins which enter during the subsequent period ΔTI (= TI_2 - TI_1) prior to image acquisition contribute to the perfusion difference signal. Under these circumstances, perfusion quantification is independent of transit time as long as TI_1 is longer than the longest transit time of the system, and ΔTI is less than the temporal width of the spin labelled bolus. In QUIPSS II, a saturation pulse is applied to the labelled region at time TI_1, effectively 'clipping' the trailing edge of the bolus and thus giving it a well-defined temporal width, and the image is again acquired at TI_2. For this sequence, the conditions for transit time insensitivity are: (i) TI_1 must be less than the width of the labelled bolus, and (ii) ΔTI must be greater than the longest transit time of the system, so that the entire bolus enters the imaging slice before the image acquisition. The conditions for QUIPSS II are more easily met than for QUIPSS, and QUIPSS II also has the advantage of allowing some washout of labelled

intravascular signal during the ΔTI period. Contamination of the perfusion signal by the signal from labelled blood in large vessels is minimised, resulting in a more accurate measurement of tissue perfusion. The drawback of the technique is a reduction of the perfusion signal difference compared to standard PASL techniques due to T_1 decay during ΔTI.

2.3.2.1.2.3 Multi-slice PASL imaging

The introduction of a PASL sequence which is insensitive to different transit times has allowed the extension of the technique to multi-slice acquisitions. Initially, FAIR was implemented in a multi-slice mode by merely increasing the width of the slice-selective inversion so that several slices were contained within the inversion slab (Kim et al., 1997a). Also, EPISTAR has been used to obtain multi-slice perfusion data by acquiring several image slices adjacent to the inversion slab (Edelman and Chen, 1998). However, in this approach, a range of transit times is automatically introduced by the different physical distances between each imaging slice and the closest edge of the inversion slice, thus making accurate quantification difficult. QUIPSS II is a natural choice for multi-slice PASL due to its inherent transit time insensitivity. The main problem for QUIPSS II is the need to limit the second inflow time ΔTI to a length that is not much longer than tissue T_1, to prevent the decay of a significant proportion of the perfusion label. Since the condition for transit time insensitivity is that ΔTI is longer than the longest transit time present, a limitation on the length of ΔTI limits the robustness of the sequence and, therefore, limits the number of slices which can be obtained in a single acquisition.

2.3.2.2 Perfusion imaging using MR contrast agent

Paramagnetic contrast agents have been used for the past ten years to obtain information about different physiological parameters related to CBF, cerebral blood volume (CBV) and the mean transit time (MTT) of blood through a volume of tissue. This technique,

usually referred to as dynamic susceptibility contrast (DSC) MRI, involves the injection of a bolus of contrast agent and the rapid measurement of the MRI signal loss due to spin dephasing (i.e., decrease in T_2 and T_2*) during its fast passage through the tissue (Villringer et al., 1988). Although the vascular space is only a small fraction of the total tissue volume (~5% in the human brain), the compartmentalisation of contrast agent within the intravascular space leads to a significant transient drop in signal because it results in a susceptibility effect that extends beyond the vascular space (Gillis and Koenig, 1987; Villringer et al., 1988). In regions with an intact blood:brain barrier (BBB), this effect dominates over the more local T_1 relaxation enhancement (Fig. 2.10).

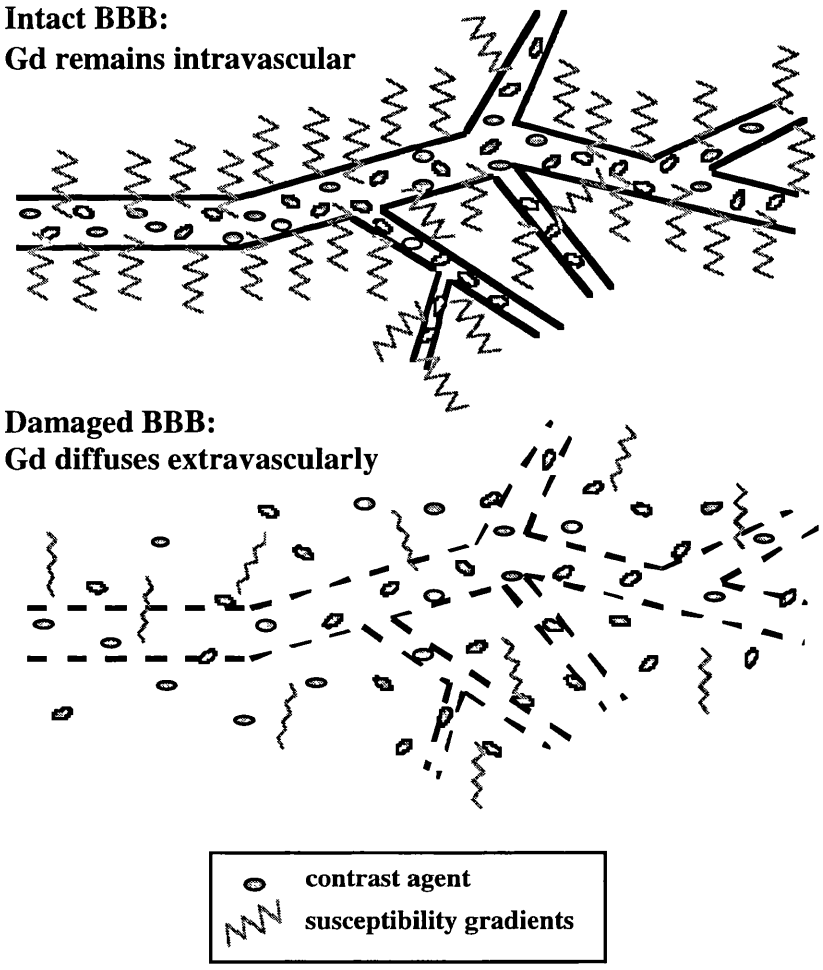

Figure 2.10.

Figure 2.10. Schematic representation of the effect of the injection of an MR contrast agent (e.g., Gd-DTPA) on the T_1 and T_2 relaxation times. The top figure shows the case when the BBB is intact. In this case, the contrast agent remains intravascular, generating large susceptibility gradients which significantly reduce the T_2 and T_2^* relaxation times

(decreased signal intensity). This effect extends beyond the intravascular space. The bottom figure shows the case when the BBB is damaged: there is leakage of the contrast agent outside the intravascular space. In this case, the contrast is distributed both in the intra and extravascular spaces, reducing the induced susceptibility gradients (and therefore reducing the T_2/ T_2^* effect). This distribution of the contrast agent over a larger region introduces significant signal enhancement (via T_1 shortening) in T_1-weighted images.

Since the transit time of the bolus through the tissue is only a few seconds, a fast imaging technique is required to obtain sequential images during the wash in and wash out of the contrast material (Fig. 2.11). The practicability of DSC-MRI was greatly increased with the widespread availability of EPI (see Chapter 3). This fast imaging technique allows an improved characterisation of the passage of the bolus, and facilitates the acquisition of multi-slice data, thus increasing the regional coverage of the technique. However, the choice of the imaging technique for each particular application depends on many factors, such as region of the brain, regional coverage, time resolution, hardware specifications, etc.

2.3.2.2.1 Basic theory

The model used for perfusion quantification in DSC-MRI is based on the principles of tracer kinetics for non-diffusable tracers (Zierler, 1962; Zierler, 1965; Axel, 1980), and relies on the assumption that, in the presence of an intact BBB, the contrast material remains intravascular.

The concentration $C_{VOI}(t)$ of tracer in a given volume of interest (VOI) can be described in terms of three functions (Axel, 1995; Østergaard et al., 1996a; Calamante et al., 1999):

- *Transport function, h(t):* probability density function of transit time *t* through the VOI following an ideal instantaneous unit bolus injection. This reflects the distribution of transit times through the voxel, which is dependent upon the vascular structure and flow.

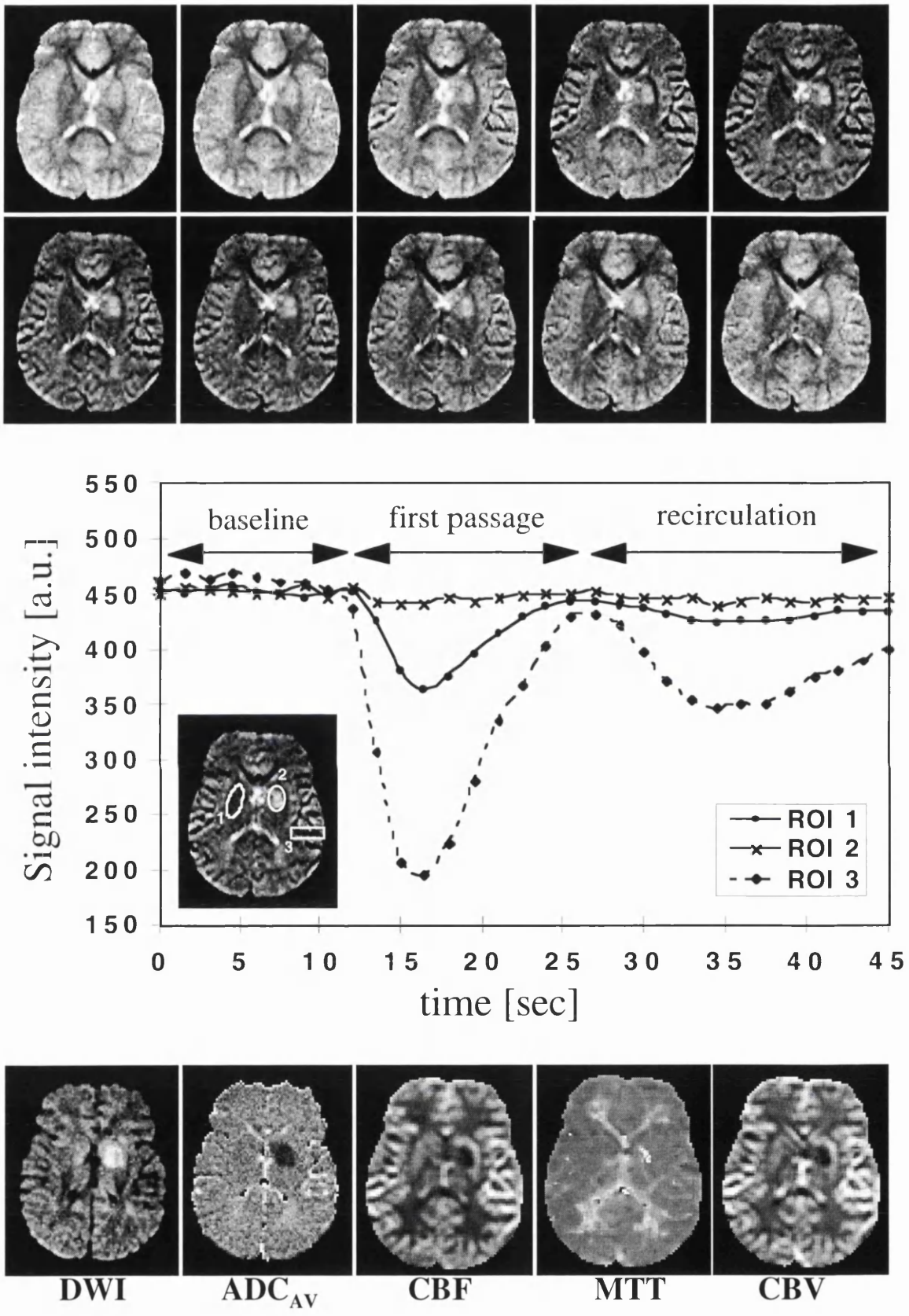

Figure 2.11.

Figure 2.11. DSC-MRI in a 4 year old child 12 h after a stroke in the left basal ganglia (right side of the images). Sequential SE echo-planar images during the passage of a

bolus of contrast agent (TR=1.5 sec), together with the signal intensity time course (in arbitrary units) for three ROIs (ROI 1: right basal ganglia, ROI 2: left basal ganglia, ROI 3: peripheral branch of the right MCA). The top left and bottom right images correspond to t=12 sec and 25.5 sec, respectively. The images show the signal intensity decrease associated with the passage of the bolus. Three different periods can be identified in the time course data: the baseline (before the arrival of the bolus), the first passage of the bolus, and the recirculation period (in this case, a second smaller peak, more clearly seen in the arterial region (ROI 3)). Note that the stroke region (ROI 2) shows almost no contrast agent passage due to the very low CBF to that area. The images in the bottom row are (from left to right): diffusion-weighted image, ADC_{AV}, CBF, MTT and CBV maps. All of them clearly show the ischaemic region.

- *Residue function, R(t):* fraction of injected tracer still present in the VOI at time t following an ideal instantaneous unit bolus injection at time t = 0. By definition, $R(t) = \left[1 - \int_0^t h(\tau)d\tau\right]$, where the integral term represents the fraction that has left the VOI, and $R(t=0)$ = 1, i.e., all the tracer is present at time t = 0.
- *Arterial input function (AIF), $C_a(t)$:* concentration of contrast agent that enters the VOI at time t.

The concentration $C_{VOI}(t)$ can be written in terms of a convolution of the residue function and the AIF (Calamante et al., 1999):

$$C_{VOI}(t) = \frac{\rho}{k_H} \cdot F_{VOI} \cdot \left(C_a(t) \otimes R(t)\right) = \frac{\rho}{k_H} \cdot F_{VOI} \cdot \int_0^t C_a(\tau)R(t-\tau)d\tau \qquad (2.22)$$

where F_{VOI} is the CBF in the VOI, ρ is the density of brain tissue (needed to provide the correct flow units), and $k_H=(1-H_{art})/(1-H_{cap})$ accounts for the difference in hematocrit (H) between capillaries and large vessels, since only the plasma volume is accessible to the tracer. This expression can be interpreted by considering the AIF as a superposition of consecutive ideal boluses $C_a(\tau)d\tau$ injected at time τ. For each ideal bolus, the concentration still present in the VOI at time t will be proportional to $C_a(\tau)R(t-\tau)d\tau$, and

the total concentration $C_{VOI}(t)$ will be given by the sum (or integral) of all these contributions. Therefore, in order to calculate CBF, Eq. (2.22) must be deconvolved to extract $F_{VOI} \cdot R(t)$, and the flow obtained from its value at time $t = 0$.

As mentioned above, CBV can be also obtained from DSC-MRI data. For an intact BBB, CBV is proportional to the normalised total amount of tracer,

$$CBV = \frac{k_H}{\rho} \bullet \frac{\int C_{VOI}(t)dt}{\int C_a(t)dt} \tag{2.23}$$

The normalisation to the AIF takes account of the fact that, independent of the CBV, if more tracer is injected, a greater concentration will reach the VOI.

The third physiological parameter which can be calculated, MTT, is the average time required for any given particle of tracer to pass *through* the tissue, following an ideal instantaneous bolus injection. By using the definition of the transport function, MTT can be written as the ratio of the first moment of the transport function to its zeroth moment:

$$MTT = \frac{\int t \cdot h(t)dt}{\int h(t)dt} \tag{2.24}$$

In the classical outflow experiment (where the concentration in the venous output, $C_{OUT}(t)$, is measured instead of the concentration at the VOI), the MTT can be directly calculated from the first moment of the tracer concentration (Axel, 1995). However, as pointed out by Weisskoff et al. (1993), this MTT is distinct from the first moment of $C_{VOI}(t)$. Therefore, calculation of MTT cannot be performed without solving first Eq. (2.22), and the first moment of $C_{VOI}(t)$ is just an approximation and depends on the topology of the vasculature.

These three physiological parameters are related through the central volume theorem (Stewart, 1894; Meier and Zierler, 1954): MTT=CBV/F_{VOI}. Therefore, once CBF and CBV are known, MTT can also be calculated directly. Conversely, some studies have used the central volume theorem to estimate a 'perfusion index' ("CBF_i") from the ratio of the CBV to the first moment of concentration-time curve (used as an *approximation* to MTT). However, apart from the previously mentioned dependency on the underlying vascular structure, this 'perfusion index' is influenced by the shape of the bolus, since the first moment contains contributions from both the MTT and the first moment of the AIF (Axel, 1995). This extra contribution becomes more important as MTT becomes shorter and therefore one does not expect a simple linear relationship between F_{VOI} and "CBF_i", particularly at high flow values (Wittlich et al., 1995).

2.3.2.2.2 DSC-MRI quantification issues

To use this model with MRI data it is necessary to convert the observed MR signal intensity variations to changes in contrast agent concentration. Since MRI is not able to directly measure the tracer concentration, it must be measured indirectly through its effect upon signal intensity. It has been shown, both empirically (Villringer et al., 1988; Rosen et al., 1990; Hedehus et al., 1997) and using Monte Carlo simulations (Fisel et al., 1991; Weisskoff et al., 1994; Boxerman et al., 1995; Kennan et al., 1994), that the tracer concentration is approximately proportional to the observed change in the relaxation rate $R_2=1/T_2$ (or R_2*) in normally perfused tissue. By assuming a single exponential relationship, the change in relaxation rate (ΔR_2) can be obtained from the change in signal intensity from the baseline signal before contrast administration (S_0),

$$C_{VOI}(t) = \kappa_{VOI} \bullet \Delta R_2 = -\frac{\kappa_{VOI}}{TE} \bullet \ln\left(\frac{S_{VOI}(t)}{S_0}\right) \qquad (2.25)$$

where $S_{VOI}(t)$ is the signal intensity measured in the VOI at time t, and TE is the echo time of the sequence. The proportionality constant κ_{VOI} is a constant that depends on the tissue,

the contrast agent, the field strength and the pulse sequence parameters. An equivalent relationship is assumed for the concentration of the tracer in the arterial input (with a proportionality constant κ_{an}).

There are a number of assumptions in the model described above, apart from the already mentioned intact BBB. First, the flow is stable during the measurement, and the contrast agent is really a tracer (i.e. it has no effect on the CBF and has negligible volume itself). Second, the effects of any change in T_1 relaxation are negligible. Third, the recirculation of the tracer (Fig. 2.11) is negligible or eliminated. This can be achieved, either by truncating the curve, or by fitting a portion of the curve to an assumed bolus shape function, typically a gamma-variate function (Starmer and Clark, 1970; Berninger et al., 1981). Fourth, since the AIF is estimated from a major vessel (such as the MCA), the dispersal and delay of the bolus as it reaches the VOI must not be significant. This last assumption is likely to be invalid during ischaemia and, as will be discussed in Chapter 6, can produce a significant underestimation of the calculated perfusion.

Although deconvolution methods allow regional CBF, CBV and MTT to be calculated, quantification using more simplistic approaches has commonly been used. These different approaches to the quantification of data obtained using DSC-MRI can be divided in three main categories:

a) Quantification of *absolute* CBF
b) Quantification of *relative* CBF (relCBF)
c) Quantification using *summary parameters*, such as time-to-peak (TTP), bolus arrival time (BAT), maximum peak concentration (MPC), full width at half maximum, peak area, first moment of the peak ($C^{(1)}_{VOI}$), etc.

The first two approaches are very technically demanding since they require an accurate characterisation of the AIF and its deconvolution from the residue function. The AIF depends not only on the shape of the injected bolus, but also on the cardiac output, the

vascular geometry and the cerebral vascular resistance. However, the AIF can be estimated by measuring the signal loss in a region of interest positioned on a feeding cerebral artery, such as the carotid artery or the middle cerebral artery (MCA) (Porkka et al., 1991; Rosen et al., 1991; Perman et al., 1992), and it has been shown to be proportional to measurements obtained invasively by arterial blood sampling in animals (Porkka et al., 1991; Rosen et al., 1991).

The determination of summary parameters, on the other hand, does not require the deconvolution of the measured signal and they have been widely used, both in animal and human studies, due to the much simpler and less time consuming processing. However, there is no simple relationship between the summary parameters and CBF. They also depend on other factors, such as CBV, MTT, bolus volume and shape, injection rate and cardiac output. This makes their interpretation less straightforward, and in general it will depend on assumptions about the underlying vascular structure (Weisskoff et al., 1993; Gobbel et al., 1991). Furthermore, accurate comparisons between subjects, or repeated measurements in follow-up studies, are not possible. However, when no information about the AIF is accessible, summary parameters are the only quantitative option and, in many cases, they can be useful in helping to distinguish between various pathological and physiological situations.

2.3.2.2.3 Deconvolution of the concentration time curve

Several methods to deconvolve Eq. (2.22) have been proposed. Østergaard et al. (1996a; 1996b) have compared the performance of some of them, both using Monte Carlo simulations and experimental data. They analysed two main categories of deconvolution approaches: model dependent (Jacquez, 1972) and model independent techniques (Gobbel et al., 1994; Rempp et al., 1994). In the first, an empirical analytical expression is chosen to describe the tracer vascular retention, i.e., a specific analytical expression for $R(t)$ is assumed. The most common model is to consider the vascular bed as one single, well

mixed compartment, and therefore $R(t)=\exp(-t/MTT)$ (Bassingthwaighte and Goresky, 1984; Lassen et al., 1984). In the second, the model independent approach, both CBF and $R(t)$ are determined by non-parametric deconvolution, i.e., the residue function is *also* treated as an unknown variable. This approach itself can be further subdivided in two categories. In the Transform approach, the convolution theorem of the Fourier transform is used to deconvolve Eq. (2.22):

$$F_{VOI} \bullet R(t) = \mathcal{F}^{-1}\left\{\frac{\mathcal{F}[C_{VOI}(t)]}{\mathcal{F}[C_a(t)]}\right\} \tag{2.26}$$

where $\mathcal{F}^{-1}$ denotes the inverse of the Fourier transform $\mathcal{F}$. In the other category, the algebraic approach, Eq. (2.22) is rewritten as a matrix equation (Østergaard et al., 1996a):

$$\begin{pmatrix} a_{11} & a_{12} & \cdots & a_{1N} \\ a_{21} & a_{22} & \cdots & a_{2N} \\ \vdots & \vdots & \ddots & \vdots \\ a_{N1} & a_{N2} & \cdots & a_{NN} \end{pmatrix} \bullet \begin{pmatrix} R(t_1) \\ R(t_2) \\ \vdots \\ R(t_N) \end{pmatrix} = \begin{pmatrix} C(t_1) \\ C(t_2) \\ \vdots \\ C(t_N) \end{pmatrix} \tag{2.27}$$

where

$$a_{ij} = \begin{cases} \dfrac{\rho}{k_H} F_{VOI} \Delta t\left(C_a(t_{i-j-1}) + 4C_a(t_{i-j}) + C_a(t_{i-j+1})\right)/6 & 0 \le j \le i \\ 0 & \text{else} \end{cases} \tag{2.28}$$

and solved either by a regularisation approach or by using singular value decomposition (SVD) techniques (Press et al., 1992).

From the methods studied, Østergaard et al. (1996a; 1996b) concluded that the model independent approach using SVD was the most accurate in the quantification of DSC-MRI data, independent of the underlying vascular structure ($R(t)$) and volume (CBV).

To obtain CBF in absolute units (ml/100g/min), fixed values for the relevant proportionality constants need to be assumed (Rempp et al., 1994; Schreiber et al., 1998; Gückel et al., 1996). For example, uniform values for hematocrit in the capillaries and large vessels are assumed (typically, H_{art}=0.45 and H_{cap}=0.25), 1.04 g/ml is assumed for the density of brain tissue (ρ), and a *single uniform* proportionality constant for tissue and the AIF is assumed in Eq. (2.25), i.e., $\kappa_{VOI} = \kappa_{art}$ for *any* tissue. With these assumptions, absolute CBF values which agree with published data using other techniques, have been reported in normal subjects (Rempp et al., 1994; Schreiber et al., 1998). However, the validity of these assumptions in pathological conditions, or a complete analysis of the error introduced by these assumptions, remains to be determined. An alternative approach for the calculation of absolute CBF involves cross-calibration with another technique which is used as a gold standard (Østergaard et al., 1998a; 1998b), and where a *common* empirical conversion factor (to absolute flow units) is obtained. However, the validity of the same conversion factor in patients with altered haemodynamics, and for different tissue types remains to be shown.

2.3.2.3 Do ASL and DSC-MRI measure the 'same' perfusion?

When in the late 1980s and early 1990s the MRI technique known as intravoxel incoherent motion (IVIM) imaging (Le Bihan et al., 1986) was used in an attempt to measure perfusion, a debate was raised (Henkelman, 1990; Le Bihan and Turner, 1992). Henkelman argued that IVIM could not measure perfusion in the 'classical sense' (Henkelman, 1990): classically, perfusion refers to tracer terminal deposition (in isotopic deposition techniques) or uptake of tracers (in washout techniques) in tissues, which can be measured with conventional methods. Although it was suggested (Le Bihan and Turner, 1992, Henkelman et al., 1994) that IVIM could provide information on perfusion, with the addition of knowledge about the capillary network organisation, the

technique did not prosper due to the lack of sufficient dynamic range for the useful quantification of perfusion (King et al., 1992).

Similarly, the question arises as to whether the two MRI techniques described in this chapter measure the 'same' perfusion. Blood perfusion is used both for the delivery of oxygen and nutrients, as well as for the elimination of the waste products. The process of delivery and elimination depends on two major factors: blood microcirculation and the blood-tissue exchange process.

Measurement of perfusion using ASL is based on the assumption that water is a freely diffusible tracer, while DSC-MRI assumes that the injected contrast agent remains intravascular (nondiffusible tracer). Therefore, there is an important difference between the 'perfusion' measured by these two techniques. Measurements using ASL (freely diffusible tracers) rely on the exchange of the tracer (labelled water) between the capillaries and the tissue and thus reflect only the fraction of microscopic blood flow which actively contributes to the process of supply and elimination of metabolites to the tissue. This becomes more important at higher CBF values, since it has been shown that the higher the flow the less exchange there is between labelled blood and tissue (Silva et al., 1997a; 1997b). Measurements employing intravascular tracers, on the other hand, measure the total microscopic blood flow, including blood in pathological arteriovenous systems bypassing the capillaries and thus the physiologically important exchange process. This extra contribution is especially important when gradient-echo (GE) techniques are used instead of spin-echo (SE) methods, because the susceptibility contrast in GE images arises from both large and small vessels, whereas in SE images it is dominated by small, capillary sized vessels, where exchange takes place (Weisskoff et al., 1994; Boxerman et al., 1995; Kennan et al., 1994). Therefore, any study attempting to compare these two techniques should consider all the above issues, and not only those relating to the intrinsic limitations of each technique (Calamante et al., 1999).

3. Introduction to the *k*-space formalism and echo-planar imaging

3.1 THE CONCEPT OF K-SPACE

Early in the 1970s, Mansfield and Grannell (1973) demonstrated that the free induction decay (FID) in an MR experiment, when plotted in a space corresponding to the time integral of the magnetic field gradient (G(t)) applied to the object during acquisition, can be regarded as the 'diffraction pattern' of the object:

$$S(t) = C\int_V \rho(\boldsymbol{r})\exp(i\boldsymbol{k}\cdot\boldsymbol{r})d^3r \tag{3.1}$$

where C is a constant (depending on T_2^*), $\rho(\boldsymbol{r})$ is the density of nuclear spins in the object of volume V, and

$$\boldsymbol{k}(t) = \gamma\int_0^t G(t')dt' \tag{3.2}$$

where γ is the gyromagnetic ratio. The vector $\boldsymbol{k}(t)$ (in the space commonly referred to as '*k*-space') has units of inverse distance, and corresponds to the 'reciprocal space' used in X-ray crystallography. Commonly, by using an RF excitation pulse containing a limited range of frequencies in the presence of a magnetic field gradient (the 'slice select gradient') only a slice of spins in the object is excited, and the volume integral in Eq. (3.1) reduces to a two-dimensional integral:

$$S(t) = Cd\int_A \rho(\boldsymbol{r})\exp(i\boldsymbol{k}\cdot\boldsymbol{r})d^2r \tag{3.3}$$

where d is slice thickness selected, and A is the area of the section of the sampled.

In either case, the FID is revealed as the Fourier transform, or 'diffraction pattern', of the spin density $\rho(\boldsymbol{r})$. This allows a simple visual interpretation of the different MRI pulse sequences: they can be regarded as different ways of sampling the FID data in *k*-space, by means of various strategies for varying the gradients (see Eq. (3.2)). With increasing t, the function $\boldsymbol{k}(t)$ describes a trajectory scanning the *k*-space, the value of the Fourier transform $\rho(\boldsymbol{k})$ of the spin density being given by the value S(t) at each point of the trajectory (Ljunggren, 1983).

With increasing value of $|\boldsymbol{k}|$, the value of $\rho(\boldsymbol{k})$ tends to zero. This decay with growing $|\boldsymbol{k}(t)|$ is usually very rapid. However, as long as the spins have not been irreversibly defocused by T_2^* relaxation the signal can always be recalled by causing the trajectory to return to the region of small $|\boldsymbol{k}|$ values, thus giving rise to an 'echo'.

Figure 3.1 shows the *k*-space trajectory for a gradient-echo pulse sequence.

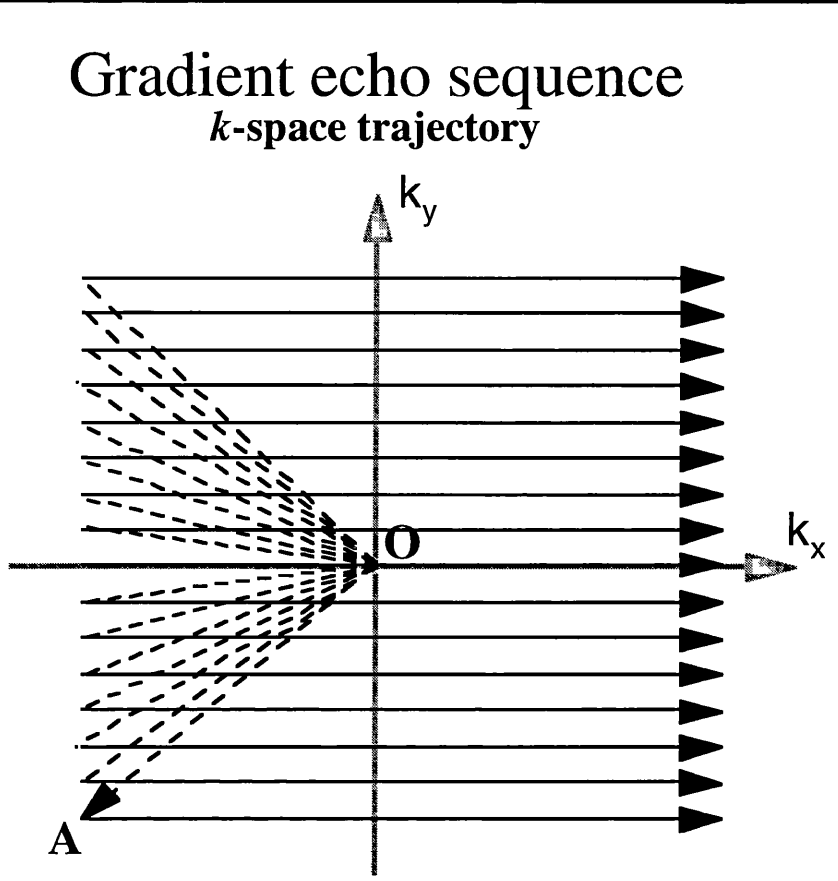

Figure 3.1.

Figure 3.1. Conventional gradient echo pulse sequence. Schematic representation of the *k*-space trajectory. k_x corresponds to the read direction of *k*-space, while k_y, the phase encoding direction. Multiple RF excitations are needed to cover *k*-space. After each RF excitation, gradient pulses in the read (usually called 'read dephasing gradient') and phase encoding direction ('phase encoding step gradient') are applied to move the *k*-space trajectory away from the centre ('O' in the figure), towards the origin of each line (e.g., dotted line to 'A' in the figure). A single line of *k*-space is read following each RF excitation.

3.1.1 Spatial resolution and field of view

As mentioned in the previous section, the MR signal measured in *k*-space is the Fourier transform of the spin density in the domain of $\boldsymbol{r}$ ('real space'). As a consequence, the spin density can be calculated from the signal by inverse Fourier transformation. The

accuracy of this calculation depends on how many points have been sampled in k-space and on what coordinate range has been covered. In the case of equidistant sampling, the resolution (Δx) and the field of view (FOV) in a given direction are related to the sample spacing (Δk_x) and range (k_{max}) as follows:

$$\Delta x = \frac{2\pi}{(2k_{max})} \tag{3.4}$$

$$FOV_x = \frac{2\pi}{\Delta k_x} \tag{3.5}$$

As in the diffraction process in optics, the spatial resolution in MR is 'diffraction limited' by a pseudo-wavelength given by $\lambda=\Delta x$. Therefore, to increase resolution (decrease Δx) a larger portion of k-space must be sampled. The central part of k-space contains low spatial frequencies that determine image contrast, whereas the outer part contains high spatial frequencies that determine image detail, as illustrated in Fig. 3.2.

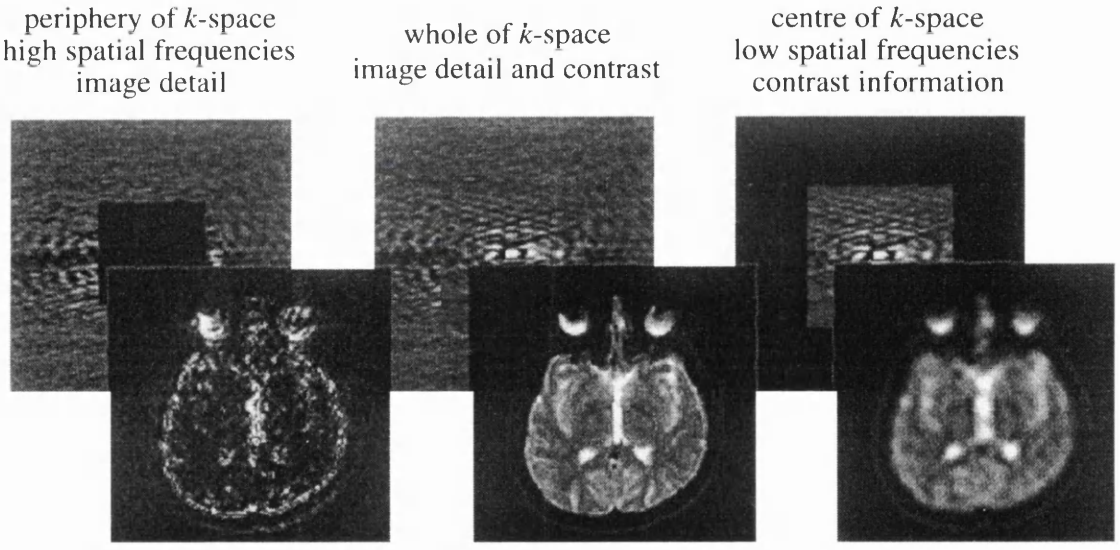

Figure 3.2.

Figure 3.2. Image information in k-space. The top figures are the k-space raw data (from an EPI scan), and the bottom figures are the corresponding images. Data acquired near the origin of k-space contain low spatial frequency information about the image, while data acquired towards the k-space periphery represent high spatial frequencies. If

the data from the low values of k are zeroed as in the left figure, only the high spatial frequencies remain, and the resulting image contains mostly thin lines, with little contrast information. When only the low spatial frequency data are used (right figure), a low resolution image is produced, but with the correct broad image contrast. (Reprinted from Schmitt et al., 1998a).

3.2 ECHO-PLANAR IMAGING

In 1977 Mansfield introduced a very important new idea to create an MR image (Mansfield, 1977). In contrast to the techniques available until that time (e.g., that shown in Fig. 3.1), which required multiple RF excitations to create an MR image, Mansfield proposed sampling the whole of k-space in a single, continuous trajectory. However, this method, termed echo-planar imaging (EPI), was going to require 10 more years to produce high quality images due to the practical difficulties surrounding its implementation (Schmitt et al., 1998a).

In the following years, many variations of the original idea were proposed. The echoes to sample k-space could either be formed as gradient echoes, as in true EPI sequences (such as MBEST (Howseman et al., 1988), BEST (Doyle et al., 1986), FLEET (Chapman et al., 1987), spiral EPI (Ahn et al., 1986)), or as spin echoes (RARE (Hennig et al., 1986)), or a combination of both (GRASE (Oshio and Feinburg, 1991)).

The two most commonly used variations of the EPI sequences are those using an oscillatory (e.g., trapezoidal, sinusoidal, or a combination of both) 'read' switched gradient and either a series of blipped 'phase encoding' gradients (to sweep horizontally across k-space (Fig. 3.3)) or a constant 'phase encoding' gradient (to 'zig-zag' through k-space (Fig. 3.4)).

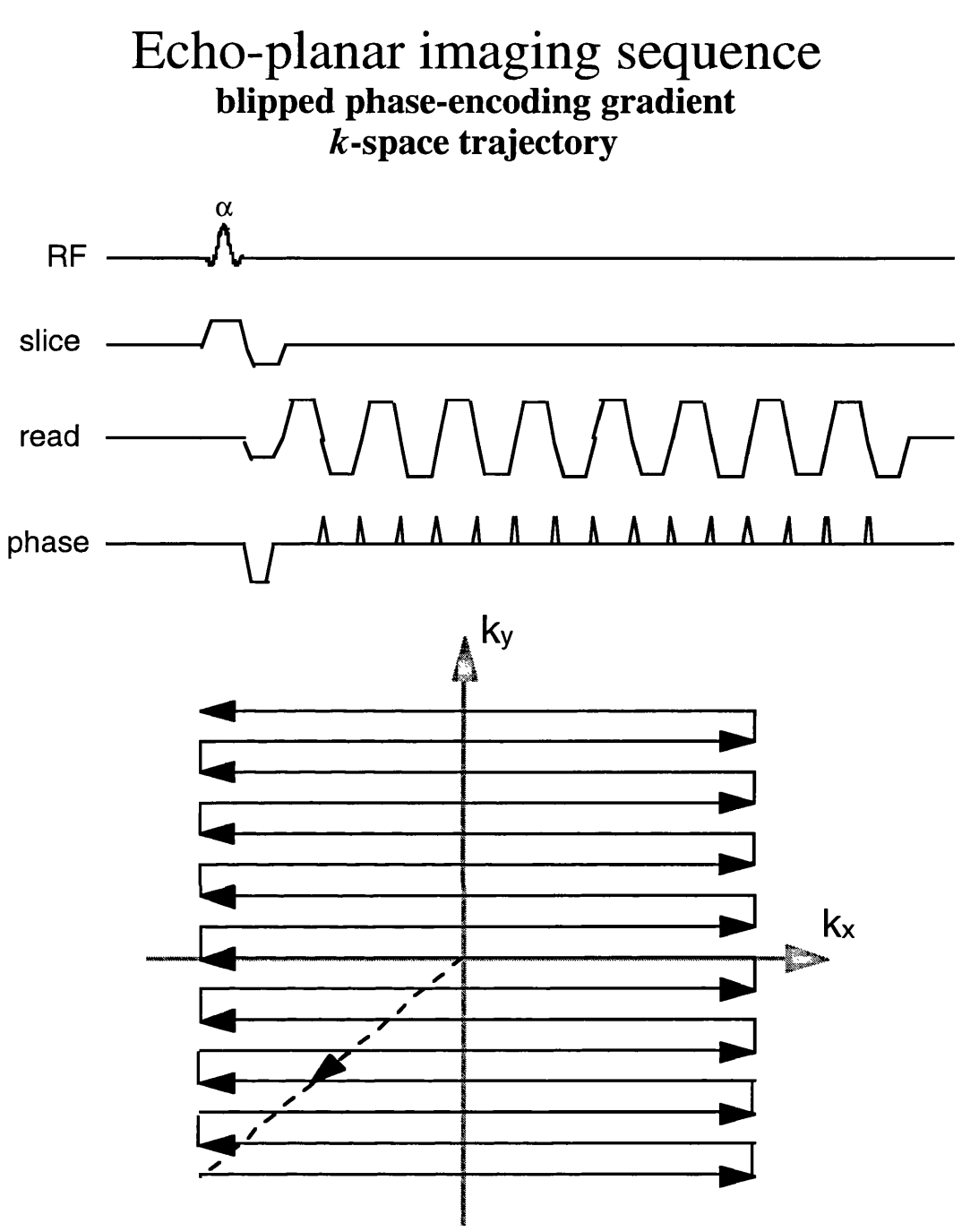

Figure 3.3.

Figure 3.3. EPI pulse sequence with blipped phase-encoding gradient. The top figure shows a simplified representation of the pulse sequence. The oscillatory read gradient generates multiple echoes, which are encoded differently by the successive phase encoding blips. The bottom figure shows a schematic representation of the corresponding *k*-space trajectory. A single RF excitation (flip angle=α) is used to scan the entire *k*-space. In contrast to the *k*-space trajectory shown in Fig. 3.1., even and odd lines of *k*-space are traversed in opposite directions.

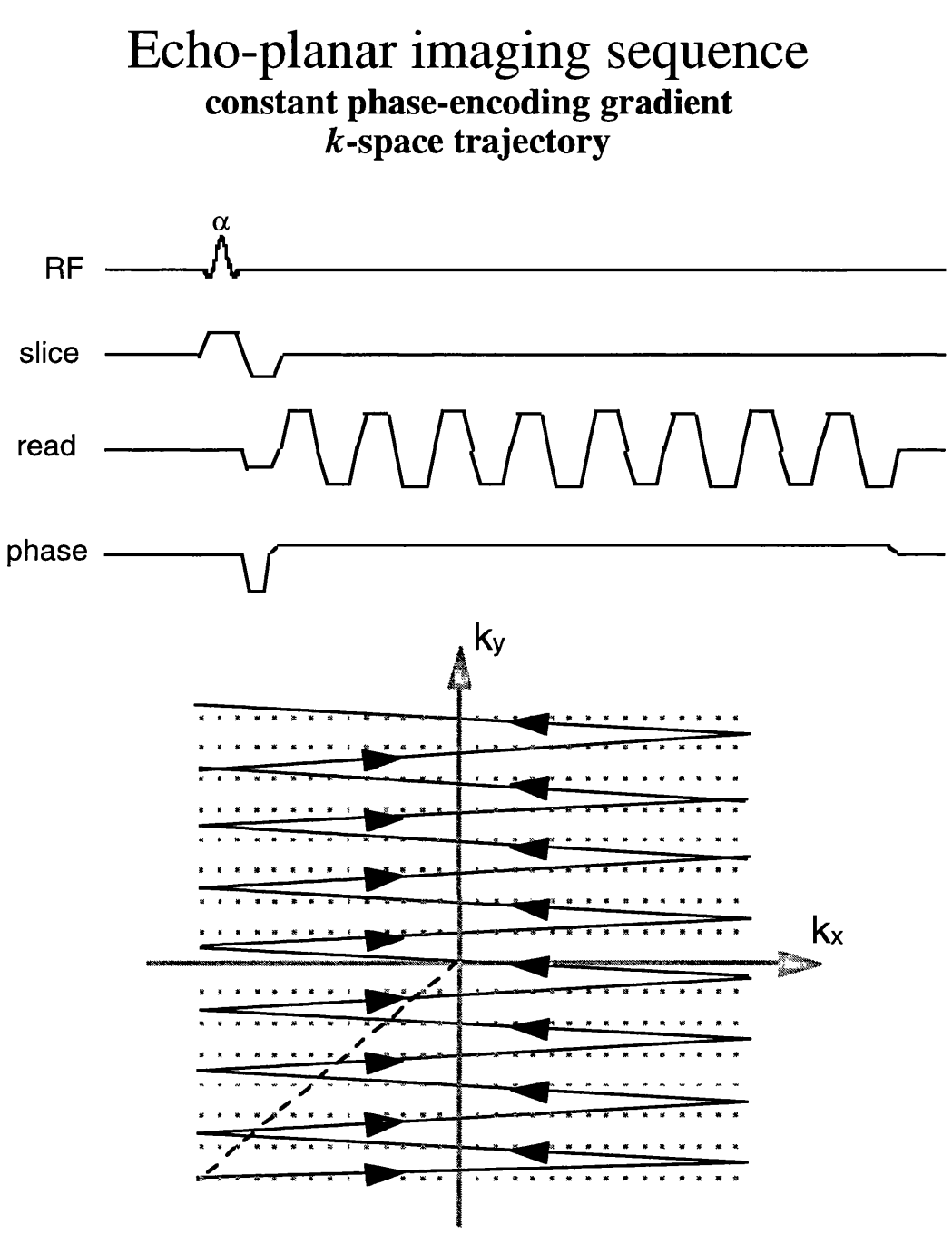

Figure 3.4.

Figure 3.4. EPI pulse sequence with constant phase-encoding gradient. The top figure shows a simplified representation of the pulse sequence. The oscillatory read gradient generates multiple echoes, which are encoded differently by the continuous application of the phase encoding gradient. The bottom figure shows an schematic representation of the *k*-space trajectory. A single RF excitation (flip angle=α) is used to scan the entire *k*-space. Similarly to the *k*-space trajectory shown in Fig. 3.3., even and odd lines of *k*-space are traversed in opposite directions, although the trajectory describes a zig-zag pattern not collinear with the cartesian grid.

3.2.1 Data acquisition and image reconstruction

3.2.1.1 Sampling of S(t)

In order to increase the speed of image acquisition, EPI often samples the signal not only under a constant 'read' gradient, but also under a varying gradient such as during the gradient ramp times.

There are two approaches that can be taken to sample S(t) under a varying readout gradient (Fig. 3.5). A linear sampling in time can be used, using a constant sampling interval Δt during the readout period (leading to a variable Δk_x, i.e., non-linear sampling in k-space). Alternatively, the sampling can be performed non-linearly in time, using a varying sampling interval during the readout (leading to constant Δk_x, i.e., linear sampling in k-space).

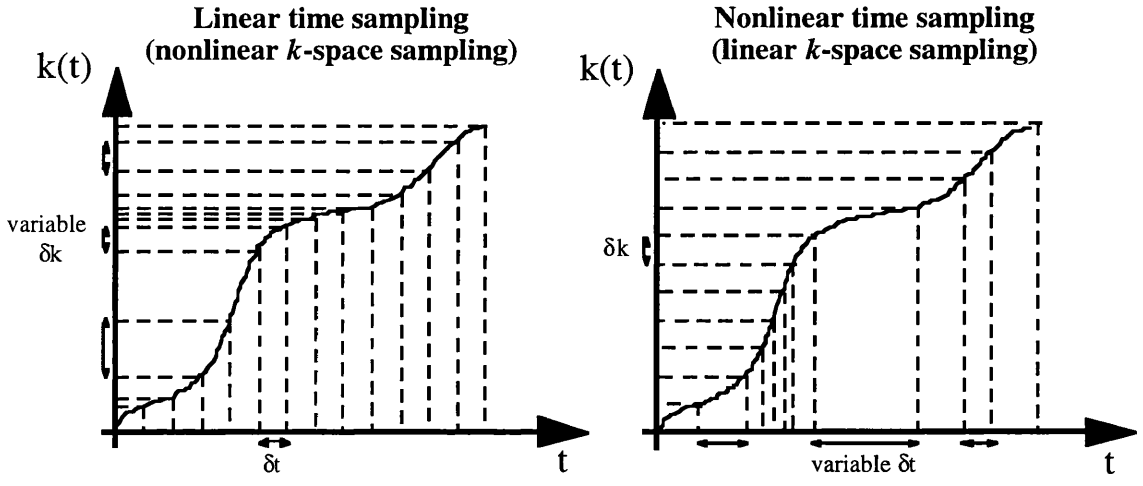

Figure 3.5.

Figure 3.5. Linear vs. non-linear sampling in time. The graphs show the k-space coordinate (k(t)~'area under the gradient' (see Eq. (3.2)) as a function of time for a variable gradient G(t). The left graph corresponds to the case of linear sampling in time (at a constant rate δt), and the graph on the right, the case of non-linear sampling in time

(with a variable δt). In the first case, the linear sampling in time generates non-linear sampling in *k*-space (variable δk). In the second case, the signal is sampled at a variable δt time interval such as to produce a linear sampling in *k*-space (constant δk spacing).

An important issue of data sampling is the Nyquist criterion (Bracewell, 1978). This describes how fast and how many data points must be sampled to avoid aliasing effects. The sampling rate must be at least twice the frequency of the highest frequency component in the waveform being sampled. This is of special importance for non-uniform *k*-space sampling (linear sampling in time), where the condition must be satisfied for all the values of Δk used. For example, when a pure sinusoidal readout gradient is used, the Nyquist condition must be satisfied for the 'worst' case (Δk_{max}, i.e., at the maximum value of the read gradient), and then the rest of the data is oversampled. For a given maximum gradient amplitude (and therefore a longer readout for the same FOV), linear sampling in time requires a larger number of samples than with a constant gradient. Similarly, for a constant readout period, the maximum gradient amplitude must be increased. The resultant decreased Δt, for the same Δk_{max}, therefore increases the number of samples again. In either case, a $\pi/2$ times larger number of samples is required, corresponding to the ratio between the unit area defined by a constant readout and the unit area of the varying gradient waveform (Schmitt and Wielopolski, 1998b).

3.2.1.2 Image reconstruction

Conventional MR image reconstruction is based on two-dimensional Fourier transformation, which requires equidistance between the sampled data. This can be achieved in two ways:

a) the data can be sampled non-equidistantly in time (the non-linear sampling method mentioned above) such that equidistance in *k*-space results. In a graphic representation this means that the data are sampled in Δt_i intervals such that the area under the readout gradient between any two consecutive measurements is the same.

b) the data can be sampled non-equidistantly in *k*-space and interpolated to equidistant *k*-space locations during image reconstruction (linear sampling).

In this regard, there is an important difference between the two EPI approaches mentioned above (Section 3.2). The EPI sequence with blipped 'phase encoding' gradients produces a 'rectilinear' *k*-space trajectory (apart from at the edges of each line), and therefore is more suitable for combination with a non-linear time sampling scheme (option (a), above). On the other hand, the EPI sequence using constant 'phase encoding' gradient produces a 'zig-zag' trajectory in *k*-space and, since interpolation is already required, it is usually combined with the much simpler approach of linear sampling in time (option (b) above). Therefore, in what follows, two sequences will be considered:

I. EPI sequence *I*: using blipped 'phase encoding' gradients and non-linear sampling in time (linear in *k*-space).

II. EPI sequence *II*: using constant 'phase encoding' gradient and linear sampling in time (non-linear in *k*-space).

Each sequence has advantages and disadvantages (Schmitt and Wielopolski, 1998b). For example, EPI sequence *I* has a much faster image reconstruction time, since it does not require the time consuming process of interpolation onto a uniform grid. Therefore, it is more appropriate for dynamic studies where a large number of images must be acquired (e.g., functional MRI, dynamic susceptibility contrast MRI, etc.). However, it poses some demands on the data-acquisition system, since the analog-to-digital converter must be triggered with an accuracy of about 100 ns to avoid degradation in the final image (Schmitt and Wielopolski, 1998b). Furthermore, due to the variable sampling interval it would be optimal to have the bandwidth of the analog filter to match that of each sampling interval (to maximise SNR). This is not usually possible since most analog filters maintain a fixed filter bandwidth during the entire EPI readout (Wielopolski et al., 1998). This is not a problem in EPI sequence *II*, where there is a single Δt value, although its reconstruction time is much longer (not only due to the regridding process,

but also due to the larger number of samples acquired (see Section 3.2.1.1), which must be transferred through the data bus of the image processor (Schmitt and Wielopolski, 1998b)).

Since the signal is acquired during both positive and negative read gradients, it is necessary to reverse the temporal order of data points in every other echo to make use of all echoes. As will be shown below (Section 3.2.2), this echo-reversing is an important source of image artefacts.

While the reconstruction of the images acquired using EPI sequence *I* is, in principle, straightforward (the data are already in a rectangular equidistant grid), the situation is very different for the EPI sequence *II*. Apart from the already mentioned interpolation in the read direction of *k*-space, the data are not equidistantly distributed in the phase encoding direction. These data can be reconstructed also by interpolation to the rectangular grid, or directly by using the 'interlaced Fourier transform' method (Schmitt and Wielopolski, 1998b). This method splits the original data set into two, which are sampled equidistantly (with twice the sampling width). These sets are independently reconstructed, and the final image is retrieved from them (Sekihara and Kohno, 1987).

3.2.2 EPI image artefacts

EPI is more sensitive to image artefacts than conventional MRI primarily for two reasons: the echo reversal of every second echo and the long readout period. These account for most of the artefacts described in this section.

3.2.2.1 Artefacts associated with echo reversing - N/2 ghost

Due to the reversal of every other line before image reconstruction, any imperfections in the acquired signal leads to an alternate line variation in the raw data. Echo asymmetry

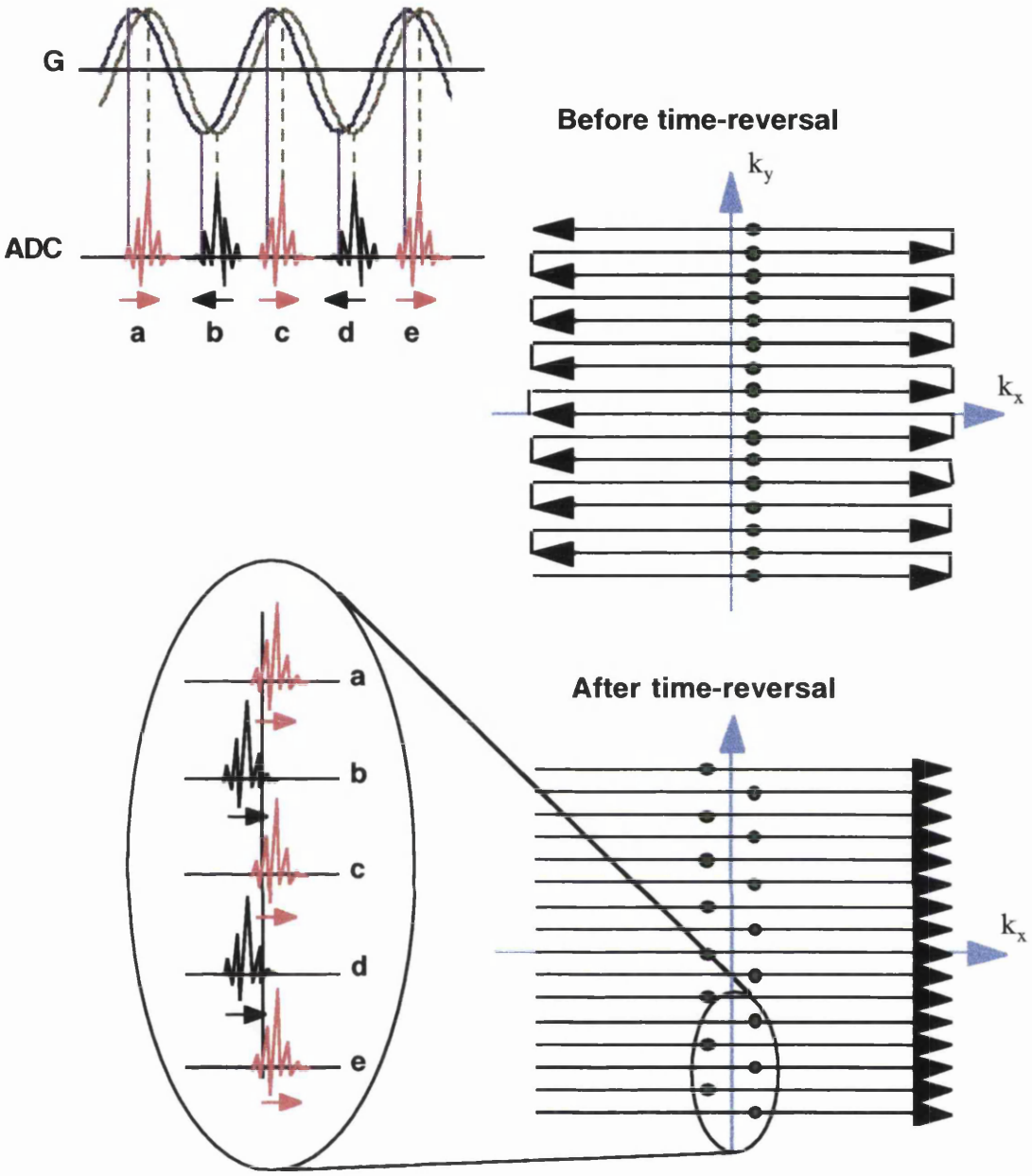

Figure 3.6.

Figure 3.6. Echo asymmetry caused by the time-reversal of alternate echoes during image reconstruction. Schematic representation of the effect of a delay between the gradient waveform (green sinusoid) and the analog-to-digital converter sampling (purple sinusoid). The *k*-space data *before* time-reversal of even lines show a series of 'delayed', but aligned echoes (represented by the filled circles). *After* time-reversal, the echoes are not aligned any more, and the signal is modulated from line to line.

can arise, for example, from the conjunction of the time-reversal of alternate echoes during image reconstruction with non-ideal features of the acquisition, such as timing errors between data sampling and gradient waveform (see for example Fig. 3.6), eddy currents, analog filter characteristics, and frequency offsets related to field inhomogeneity, susceptibility and chemical shift (Buonocore and Gao, 1997; Reeder et al., 1997; Fischer and Ladebeck, 1998). Alternate line variations in the raw *k*-space data lead to a signal modulation with half the Nyquist frequency, causing the so-called 'N/2 ghost' in the phase encoded direction (a ghost image shifted by half of the FOV after Fourier transformation (Fig. 3.7))

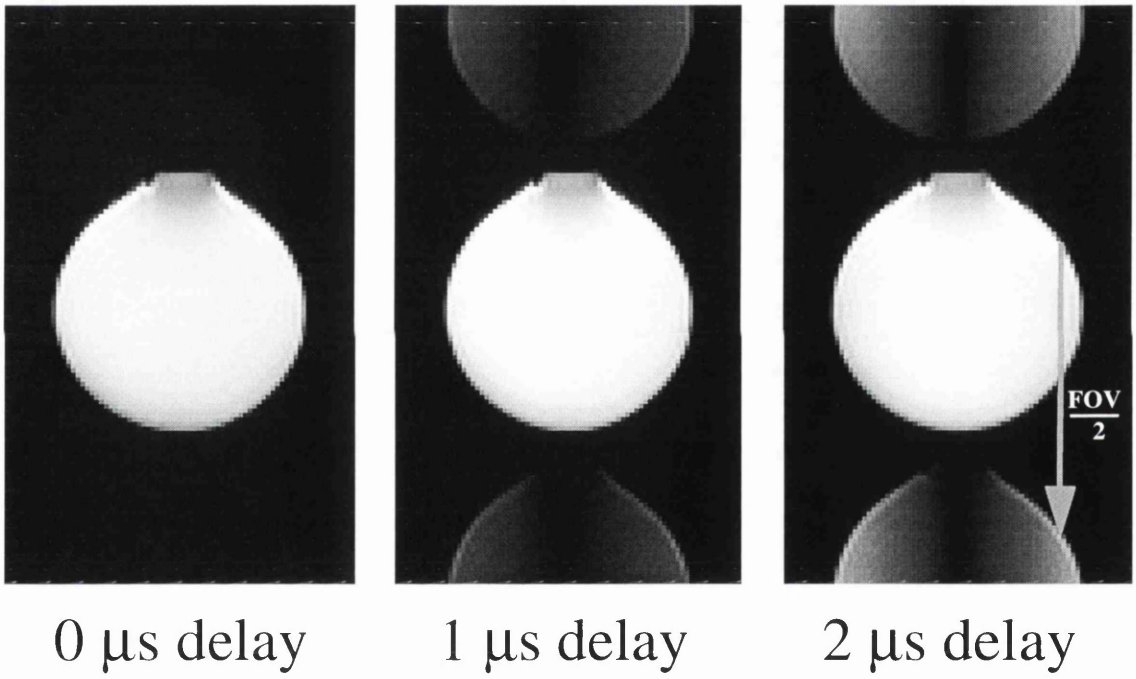

Figure 3.7.

Figure 3.7. Nyquist ghost artefact in EPI. A ghost image is clearly seen displaced half the FOV from the main image. In this case, the source of the ghost is mainly a small misalignment (delay) of gradient waveform and analog-to-digital converter timing: no delay (left image), 1 µs delay (middle image), and 2 µs delay (right image). As can be seen, the intensity of the ghost increases with increasing delay.

3.2.2.1.1 Sources of N/2 ghost

Eddy currents can cause a time delay (or also an advance) between the current in the coil and the gradient field, as well as a reduction in the amplitude of the gradient field. This delayed gradient field causes the magnetisation to refocus late. Due to the time reversal, the echo in each second line is shifted by the same time delay in the opposite direction, introducing a 'zig-zag' pattern along the phase-encoding direction of *k*-space. If there is a B_0 field eddy current, the MR signal differs from even to odd lines, although not due to an echo shift but to an alternating phase value. In either case, the signal modulation will be the source of N/2 ghost (Fischer and Ladebeck, 1998).

A similar phase alternation can be present whenever there is a *frequency offset*, such as those due to chemical shift or field inhomogeneity. However, in the latter case, the inhomogeneity may be spatially dependent, and therefore the phase values between even and odd lines may vary in different regions of the image. In this case, a perfect compensation (as described in the next section) cannot be achieved.

Due to the cut-off characteristic of the analog *low pass filter*, the output signal is distorted asymmetrically (convolution of the signal with a filter-dependent convolution kernel). This is a further source of time shift which may cause problems after time-reversal of every other line (Fischer and Ladebeck, 1998).

3.2.2.1.2 Correction methods - Reference scan

The echo shifting introduced by the time reversal can in principle be corrected either by:

- an exact adjustment of the analog-to-digital converter raster to the readout gradient field, or
- a post-processing phase correction. According to the Fourier-shift theorem (Bracewell, 1978) a timing error (*k*-space shift) is equivalent to a linear phase error in the 'projection' (the 1-D Fourier transformed echo). This information can be measured

from 'reference scans'. These are raw data sets (consisting of at least two echoes) acquired without phase encoding before, during, or after data acquisition (Schmitt and Wielopolski, 1998b). The phase information in these reference scans can be used to correct the MR signal alternation in the image data (echo position and phase alternation) in many different ways, for example by constant, linear or non-linear phase corrections, modulation transfer function deconvolution, etc. (Bruder et al., 1992).

As mentioned previously (*Sampling of S(t)*, Section 3.2.1.1), the Nyquist criterion must be satisfied. This influences the selection of correction method (post-processing or exact adjustment of the analog-to-digital converter) for the EPI sequence, depending on the sampling scheme used (linear or non-linear in time). The first case (post-processing) should be used when linear sampling in time is performed. In this case, shifting the raw data can be performed before interpolation and no undersampling occurs (the sampling interval Δt was chosen to satisfy the Nyquist condition at the maximum value of the read gradient, and the data are oversampled for the other values of the gradient). On the other hand, when non-linear sampling in time is used, the non-linearity is designed for a *synchronised* sampling raster (by requiring equal gradient areas between samples). Therefore, a non-synchronised raster could violate the Nyquist theorem, and therefore shifting the data by post-processing would not solve the Nyquist sampling problem. In these cases, an accurate adjustment of the analog-to-digital converter must be performed. Therefore, the N/2 correction for the EPI sequence *I* defined in Section 3.2.1.2 is usually performed by adjusting the analog-to-digital converter, while the EPI sequence *II* uses a post-processing correction. Thus, although the reconstruction time is much shorter with the first sequence, its 'preparation time' is longer because it requires an exact synchronisation of the sampling raster and the actual gradient before collecting the reference and image data.

3.2.2.2 Artefacts associated with the long readout period

The EPI acquisition time is longer than that in conventional MRI (typically ~30-100 ms compared to ~5-15 ms), although in this time the whole information necessary to reconstruct an image is acquired. The effective acquisition times in the read and phase encoded directions are different, as are the gradient amplitudes used by each gradient. Expressed in bandwidth per pixel in the image (BW/pix), the bandwidth in the phase encoding direction is smaller than the BW/pix in the read direction by a factor which is approximately the number of lines of *k*-space scanned (i.e., number of echoes in the EPI echo train). Typical values of BW/pix (for a 128x128 matrix) are ~1300 Hz in the read direction and ~10 Hz in the phase encoded direction. It is this very small BW/pix in the phase encoded direction that is the main cause of many of the artefacts seen in EPI. These artefacts are effectively only seen in this direction, while the effects in the read direction are usually negligible (Johnson and Hutchison, 1985; Farzaneh et al., 1990; Fischer and Ladebeck, 1998).

3.2.2.2.1 Geometric distortions - B_0 inhomogeneities

The presence of field inhomogeneities (due to magnet imperfections, or introduced by the patient) produces significant artefacts in low BW/pix EPI images. These are manifested as local signal displacement, due to the local 'erroneous' frequency. Thus, the information appears in the wrong physical location in the image, and since this displacement is spatially dependent, a local geometric distortion arises (Fig. 3.8).

Furthermore, linked with this local distortion, which is a stretching or compressing of an image voxel, there is a non-uniformity in the image. The brightness of a pixel is proportional to the volume to which it corresponds. Therefore, the signal is reduced in regions where the image is stretched and increased in those regions which are compressed (see Fig. 3.8).

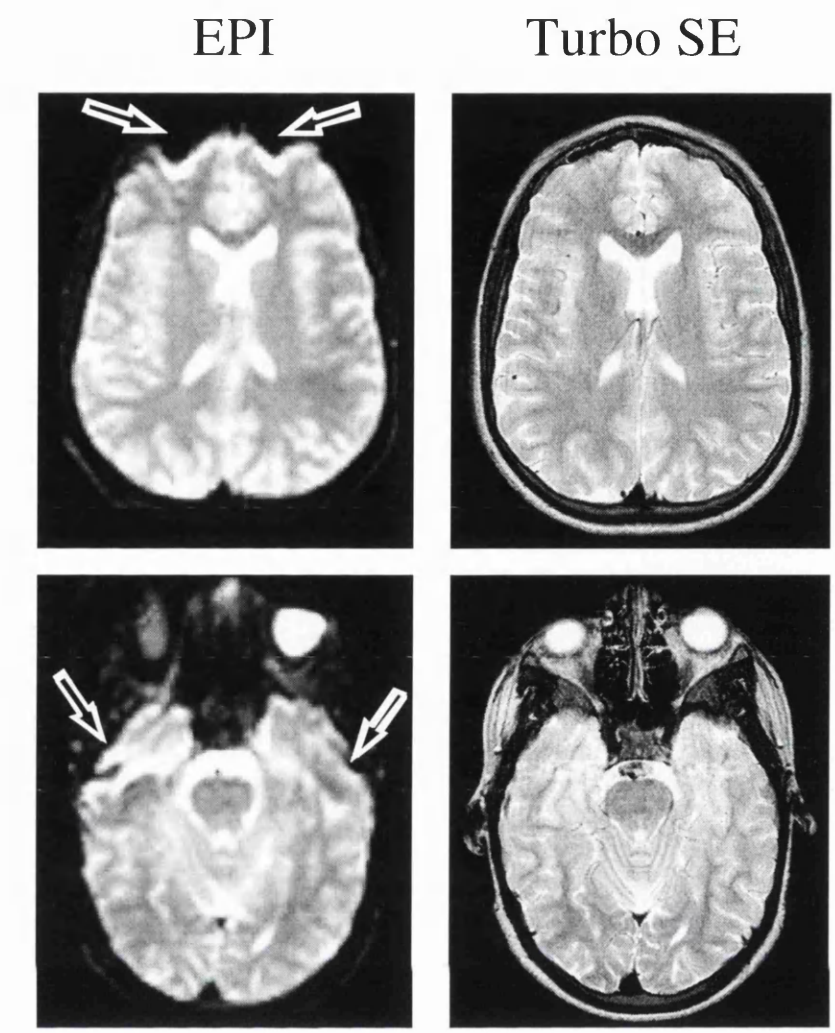

Figure 3.8.

Figure 3.8. Image distortion in EPI ('susceptibility artefact'). The figure shows typical echo-planar images (128x128 matrix) on the left, and the corresponding Turbo SE images on the right. Image distortions can be observed in the images acquired using EPI (arrows), as compared to the Turbo SE images. There is also a 'redistribution' of the signal, with regions of increased signal intensity, and regions of reduced signal.

3.2.2.2.2 Geometric distortions - Eddy currents

Image shifts or distortions can also be generated by magnetic field perturbations due to the presence of eddy currents (see Chapter 4). However, these distortions are not local as with the susceptibility artefacts described in Section 3.2.2.2.1. Instead, they usually

affect the image globally, since the main eddy current effects are linear field gradients and B_0 (spatially invariant) eddy currents.

3.2.2.2.3 Chemical shift artefacts

Due to the low BW/pix in the phase encoding direction, signals with a different chemical shift from water will appear shifted in the phase encoding direction. In contrast to the off-resonance effects described in Section 3.2.2.2.1 (B_0 inhomogeneities), the chemical shift is spatially constant (similar to a B_0 eddy current). In these cases, no distortion is introduced, and the image is simply uniformly shifted. The most common case is the shifted signal from the fat (Fig. 3.9). Since there is ~3.3 ppm chemical shift difference between fat and water (~210 Hz at 1.5 T), the fat image appears displaced by several pixels (~20 pixels at 1.5 T). Therefore, to avoid the interference between the water and the displaced fat signals, fat suppression is essential when EPI is used *in vivo* (Fig. 3.9).

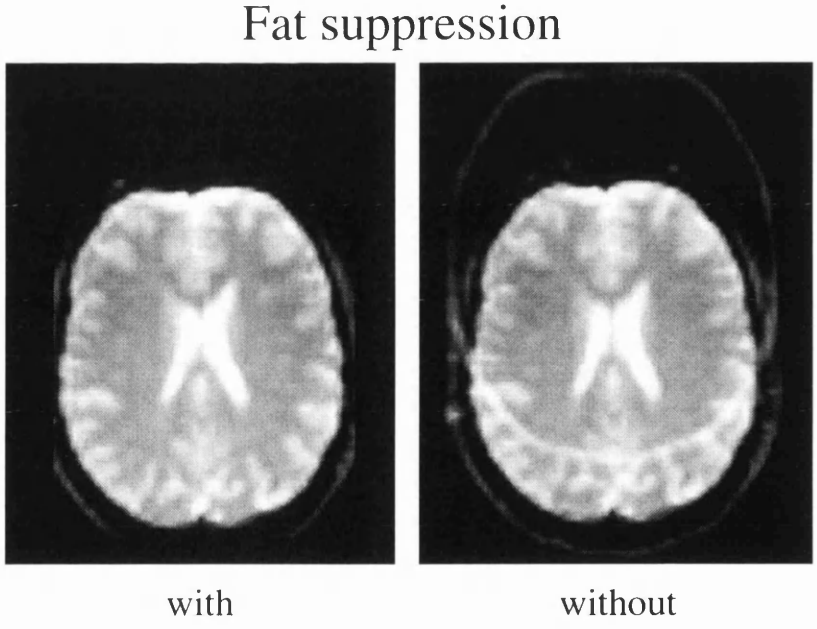

Figure 3.9.

Figure 3.9. Fat artefact in EPI. The figure shows an example of an echo-planar image acquired with (left) and without (right) fat suppression. In the absence of fat

suppression, the signal from the fat is visible and can be seen to be displaced in the phase encoding direction (vertical direction) due to its different chemical shift.

3.2.2.2.4 T_2^* Filtering - Loss of resolution and signal loss

Since EPI data are acquired under a decaying T_2^* envelope for the echoes, some blurring (filtering of the high spatial frequencies) is introduced along the phase encoded direction in the image, reducing the spatial resolution. The blurring can be expressed mathematically as a convolution of the real signal with a point spread function (Farzaneh et al., 1990; Fischer and Ladebeck, 1998). This convolution spreads the signal (and consequently decreases its intensity) from each pixel.

3.2.2.3 Other artefacts

Since the duration of the readout period must be kept short to minimise the T_2^* decay and resultant blurring, the maximum matrix size used is limited in practice (typically 64x64 or 128x128). Furthermore, due to limitations in the peak gradient amplitude availability, the minimum FOV is also limited (typically 20-25 cm). Therefore, EPI usually generates images with low spatial resolution (spatial resolution is 'sacrificed' for time resolution). This leads to two well known artefacts in low spatial resolution imaging: partial volume contamination and ringing artefacts. The first one is present whenever the macroscopic structures of the object are comparable to the pixel size. As a consequence, for example, pixels with pure cortical grey matter are very difficult to image because there is usually significant contamination from CSF. The second artefact, also called edge ringing or Gibbs phenomenon, is related to the truncation of the signal from limited sampling. This is specially important in structures with long T_2^* (such as CSF), and is usually evident as low intensity, parallel striations adjacent to interfaces between high and low signal (such as between CSF and tissue (Fig. 3.10)). These two artefacts can be reduced by using a fluid attenuated inversion recovery (FLAIR, Hajnal et al., 1992) preparation to suppress the fluid signal from the CSF.

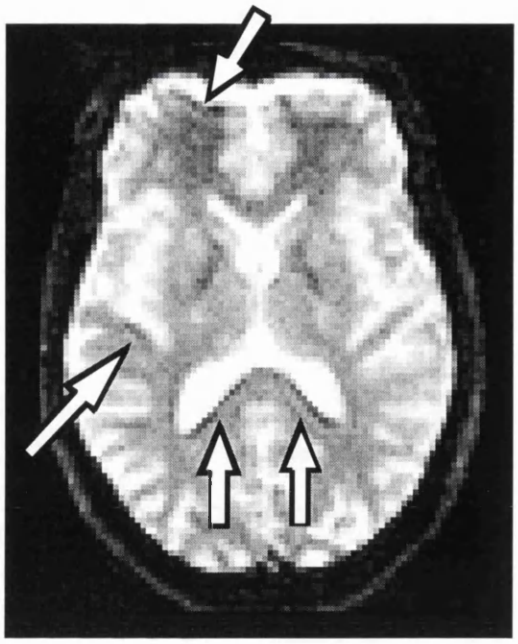

Figure 3.10.

Figure 3.10. Ringing artefact in EPI. The figure shows an echo-planar image (128x128 matrix). The arrows show the ringing artefacts arising from the interface between regions with two very different signal intensities (e.g., CSF and tissue).

4. Correction for Eddy Current Induced B_0 Shifts in Diffusion-Weighted Echo-Planar Imaging

4.1 INTRODUCTION

4.1.1 Quantitative diffusion imaging in clinical systems

The signal intensity changes that are observed in diffusion-weighted images have been used successfully over the last decade for the detection of cerebral ischaemia (Baird and Warach, 1998). Although they often provide good visualisation of stroke lesions, it is now generally accepted that more quantitative measurements, in the form of maps of the apparent diffusion coefficient (ADC), offer a number of advantages (Ulug et al., 1997). In particular, they remove confounding relaxation effects, and provide an objective means of defining diffusion abnormalities. However, initial experience with clinical MRI systems indicates that the calculation of artefact-free ADC maps from a series of diffusion-weighted echo-planar images is not necessarily straightforward.

4.1.2 Eddy current effects

As mentioned in Section 3.2.2.2.2 (Chapter 3), one limitation to single-shot EPI is its sensitivity to the magnetic field perturbations resulting from eddy currents. The very low bandwidth per pixel in the phase-encode direction (typically ~10 Hz/pixel) means that small changes in magnetic field, which would not affect conventional imaging sequences, can significantly degrade EPI images. These induced eddy currents do not cause a significant distortion of the image in the read direction (typically ~1000 Hz/pixel bandwidth), and mainly affect the image in the phase-encode direction. The effect on the image depends on the nature of the field perturbation (Fig. 4.1):

a) *Uniform translation:* a uniform field offset caused by a B_0 eddy current produces a uniform image shift in the phase encode direction. Each pixel is shifted by the same amount regardless of its position.
b) *Non-uniform translation*: a field gradient in the slice direction (Z) produces an image shift that is dependent on slice position. Each pixel is shifted in the phase encoded direction by an amount that is linearly related to the Z position.
c) *Shear*: a field gradient in the read direction (X) produces a shearing of the image. Each column in the image is shifted (in the phase encode direction) by an amount that is linearly related to the X position.
d) *Scaling*: a field gradient in the phase-encode direction (Y) produces a scaling (stretch or contraction) of the image in the same direction. Each pixel is shifted in the phase direction by an amount that is linearly related to the Y position, independent of X.

These effects can be further complicated by the time dependence of the eddy currents, which introduces blurring in the image. In diffusion-weighted (DW) EPI sequences the diffusion gradients produce eddy currents which vary according to their magnitude and direction. Consequently, DW-EPI images which use different b-values may suffer different levels of distortion, leading to artefacts in the ADC map that is calculated from a combination of such images. In addition, when the trace of the diffusion tensor is

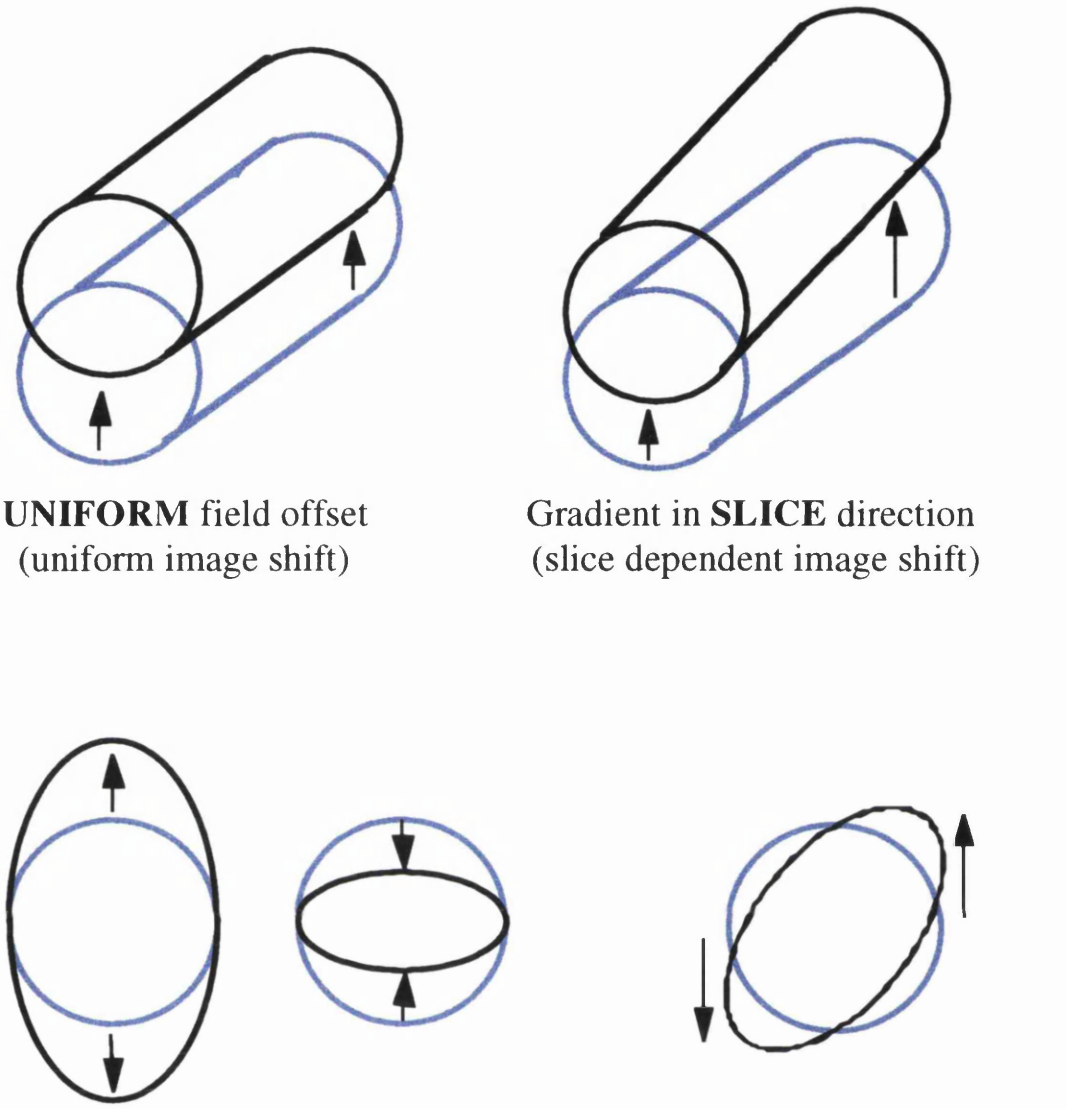

Figure 4.1.

Figure 4.1. Schematic representation of the different induce image shifts and distortions (equivalent to local shifts) due to the presence of eddy currents. The blue drawings represent the undistorted objects, while the black lines, their distorted versions. The arrows highlight the shifts or distortion in each case. 'P.E.' stands for phase encoded.

estimated by averaging the ADC measurements along three orthogonal axes (ADC_{AV}), the eddy current artefacts would typically be different for each of these ADC maps, leading to further errors. Such image misregistration not only introduces artefacts at the edge of the brain, but also results in an effectively lower spatial resolution in the calculated ADC maps. This leads to an inaccurate estimation of the diffusion parameters, especially at boundaries between tissues that have different diffusion or MR relaxation properties. Although many modern clinical MRI scanners use actively-shielded gradient coils in addition to eddy current compensation to minimise eddy currents, DW-EPI images from these systems nevertheless are often affected by considerable eddy current artefacts. In particular, on many clinical systems the primary problem is an image shift due to an uncompensated B_0 eddy current. It is this type of image artefact that is addressed in this chapter.

4.1.3 Correction of eddy currents effects

One approach to correcting the distortions in DW-EPI has been to apply a post-processing algorithm for spatial realignment of the images (Haselgrove and Moore., 1996). This is achieved by deriving a series of parameters which describe the translations, scaling and shearing of the images with respect to each other. Although this method has been shown to deal adequately with B_0 shifts as well as with the other types of artefacts, it may provide erroneous results when the images have very different intensity contrast, such as in a slice with a large infarct or when there is a large amount of CSF around an atrophic brain. Acute infarcted regions have less attenuation than the surrounded tissue, while chronic infarcted regions and CSF are highly attenuated. In such cases, the different diffusion weightings produce images with very dissimilar contrast. This correction method also requires a time consuming off-line processing step, which may not be convenient for providing ADC or trace maps for immediate assessment in a clinical examination. Alternatively, the B_0 problem can be addressed by applying pre-emphasis pulses to a Z_0 coil. However, the necessary hardware is not usually available on standard clinical equipment, and would constitute a difficult and expensive

modification. Another hardware solution, which would also be difficult to implement on clinical systems, is to modulate the transmitter and receiver reference frequencies to track the time-dependent B_0 shift (Crozier et al., 1992; 1994). A number of solutions that do not require hardware modifications have been suggested which use modified DWI sequences to minimise the size of the eddy currents that are induced (Fig. 4.2). In general, they involve gradient switching that is designed to produce mutual cancellation of eddy currents. One of these approaches is to introduce the diffusion weighting by using bipolar gradients (Fig. 4.2b) (Alexander et al., 1997). However, due to the shorter diffusion time of this sequence, a much longer TE (and associated smaller SNR) is required for a given *b*-value. More recently, another sequence modification was proposed, in which each monopolar diffusion gradient was replaced by a bipolar gradient with a 180° RF pulse in the middle (Fig. 4.2c) (Reese et al., 1998). Another approach involves adding 'dummy' gradient pulses which do not affect the basic sequence characteristics but generate eddy currents which oppose those produced by the original diffusion gradient pulses in the sequence (Fig. 4.2d) (Boesch et al., 1991). However, all these methods involving only sequence modifications will not necessary produce a complete correction in every case.

The problem of time dependent B_0 shifts is well known in localised spectroscopy and is typically addressed by applying a post-acquisition phase correction algorithm to the free induction decay (FID) (Ordidge and Cresshull, 1986; Jehenson and Syrota, 1989; Klose, 1990). The algorithm uses a reference signal, such as that from a separate acquisition performed without water suppression, to measure the phase at each sample point. These measured phase values are then used to correct the original FID.

In this chapter a B_0 shift correction procedure for DW-EPI is described, which is based on the spectroscopy phase correction technique described above. The method uses a non-phase-encoded (nPE) reference scan to correct the phase of each echo in the EPI echo-train, and is similar in principle to the method proposed by Jezzard et al (1998). The purpose of the work was to develop a correction method that would allow the collection

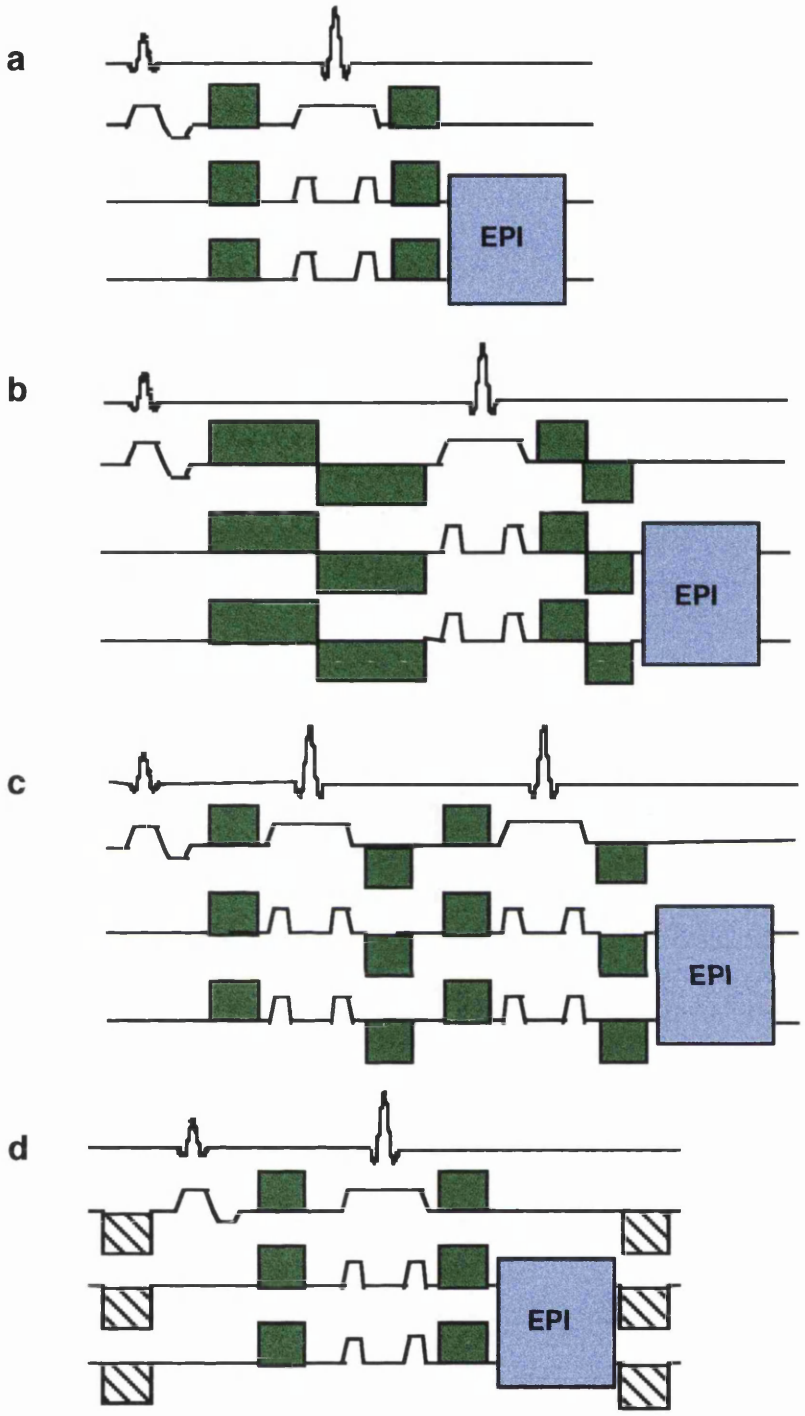

Figure 4.2.

Figure 4.2. Schematic diagram of the DW pulse sequence used to minimise the effect of eddy currents. (a) Conventional monopolar sequence (with a pair of Stejskal-Tanner diffusion gradients); (b) bipolar DW sequence (the sizes of the bipolar gradients on each side of the inversion pulse are not necessary the same); (c) twice-refocused spin-echo sequence; (d) DW sequence with 'dummy' gradients. The green boxes represent diffusion gradients, the diagonal hatched boxes the 'dummy' gradients, and the blue boxes the EPI readout.

of data as part of clinical investigations on children, some of whom are acutely ill. One of the main objectives was the calculation of average ADC maps that are free of misregistration artefacts, for their immediate interpretation. Therefore, on-line correction of the data is performed as part of the image reconstruction process, allowing ADC maps to be calculated immediately for clinical evaluation, without the need for off-line post-processing.

4.2 METHODS

4.2.1 MRI sequence

Experiments were performed on a 1.5 T whole body imaging system (Vision Magnetom, Siemens AG, Erlangen, Germany) using shielded gradients with a maximum gradient strength of 25 mT/m, and a minimum ramp time of 300 μs.

A DW-EPI sequence was used (see Fig. 4.3), which consisted of a spin echo EPI sequence with a pair of Stejskal-Tanner diffusion gradients (green boxes in Fig. 4.3), one on each side of the 180° refocusing pulse. In order to reduce the effects of the eddy currents, 'dummy' gradients were also added to the sequence. These were of the same amplitude but opposite polarity to the diffusion gradients, and are represented by diagonal hatched boxes in Fig. 4.3. The centre of *k*-space was sampled at the centre of the SE which was positioned at the 33rd echo of the 128 echo readout. This 'asymmetric' echo-train is commonly used in DW-EPI (especially in clinical systems with limited gradient strength) since it allows a shorter TE to be used for a given *b*-value (Fig. 4.4). In this way, SNR is increased, although some blurring is introduced in the images (Fig. 4.5, middle row). In principle, this blurring can be eliminated by a 'half-Fourier'-type reconstruction (HF), which generates an image with higher resolution, but lower SNR (Fig. 4.5c, bottom row). Compared to small possible patient movements during the acquisition of the full data set for the calculation of ADC_{AV} maps, a small image blurring

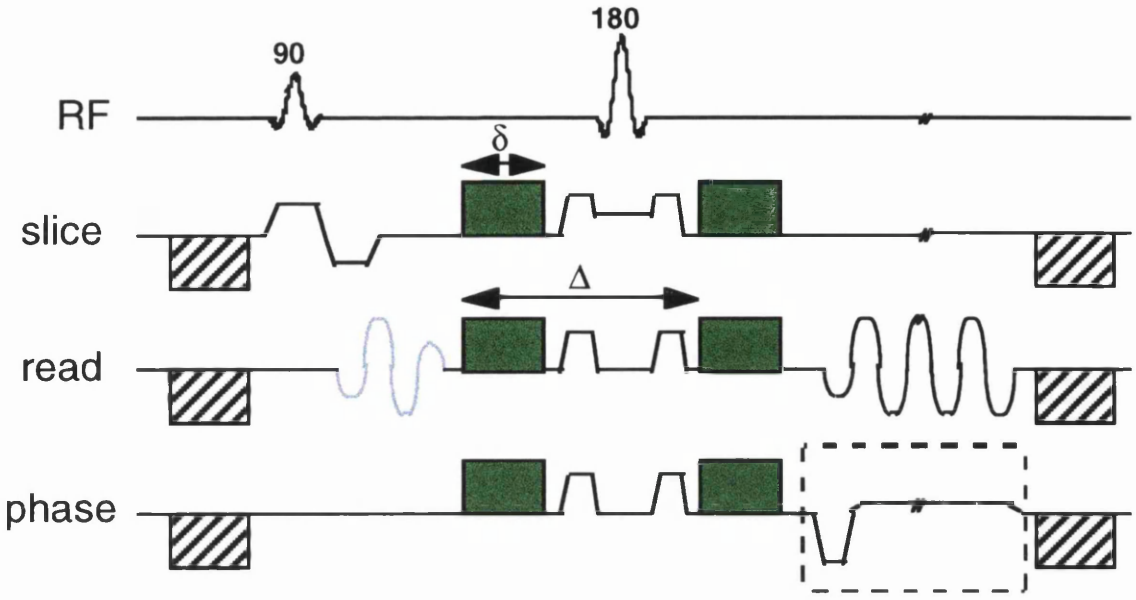

Figure 4.3.

Figure 4.3. Diagram of the DW-EPI pulse sequence used in this work. The green filled boxes represent the Stejskal-Tanner diffusion gradients and the diagonal hatched boxes the 'dummy' gradients. The nPE data were acquired without the gradients indicated by the dashed box. The data for the correction of the Nyquist ghost were acquired during the blue sinusoidal part.

is not a major problem, and the higher SNR was favoured, therefore using the 'asymmetric' echo-train without 'half-Fourier' reconstruction. Linear data sampling was performed throughout the echo train using a constant phase encode gradient in conjunction with a read gradient with sinusoidal ramps of duration 300μs and a plateau of duration 120μs (720μs echo-spacing, 10.85 Hz/pixel in the phase-encoded direction); 180 data points were acquired for each echo and the data were interpolated to a 128 matrix before Fourier transformation. Imaging parameters were: TE=98 ms; 128x128 matrix; 24 cm FOV, corresponding to 1.9x1.9 mm^2 in plane resolution; 5 mm slice thickness; time interval between slices = 240 ms; delay between multi-slice acquisitions = 4 s. Data for Nyquist ghost correction were obtained during each scan by sampling two non-phase-encoded echoes after the 90° excitation pulse (indicated in blue in Fig. 4.3); these data were used to apply a standard non-linear phase correction to all echoes in the

echo train after Fourier transformation in the read direction (Bruder et al., 1992). This procedure will be referred as "N/2 correction".

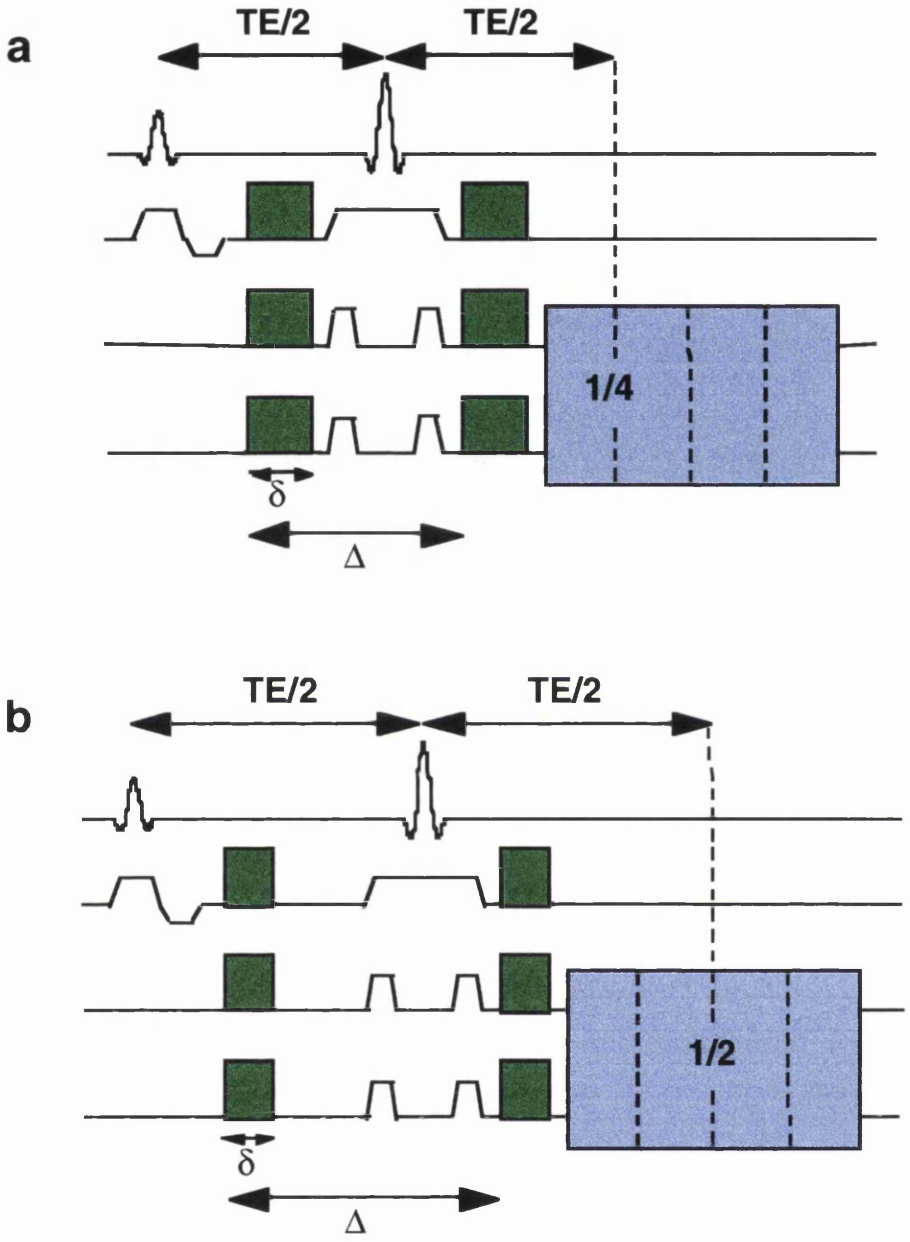

Figure 4.4.

Figure 4.4. Schematic diagram of the DW-EPI pulse sequences using an 'asymmetric' (a), or a 'symmetric' echo-train readout (b). In the 'asymmetric' case, the SE is sampled at the centre of *k*-space which is typically positioned at 1/4 of the echo-train. In the 'symmetric' case, the SE is positioned in the middle of the echo-train, increasing, therefore, the TE. The green boxes represent diffusion gradients, and the blue boxes the EPI readout.

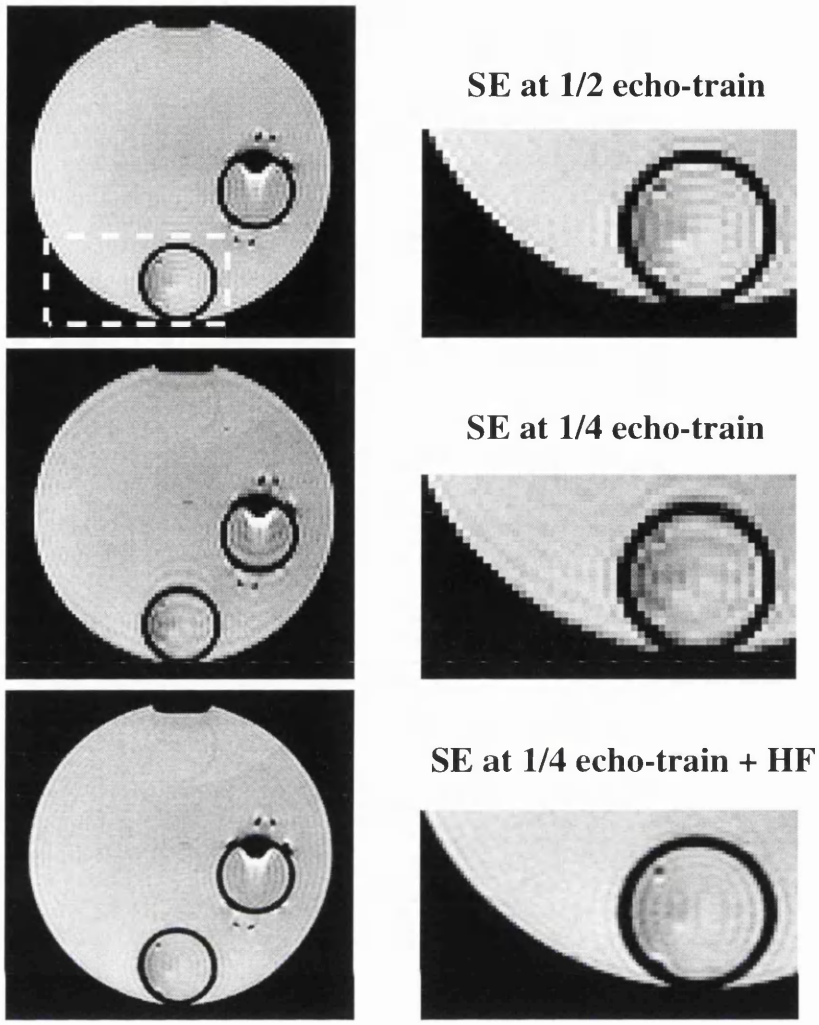

Figure 4.5.

Figure 4.5. Echo-planar images acquired with a 'symmetric' echo-train (top row), an 'asymmetric' echo-train (middle row), and an asymmetric echo-train with a 'half-Fourier' type reconstruction (HF) (bottom row). The images on the right show magnified versions of the portion marked in dotted lines in the top left image. These magnified versions show the blurring in the middle image, and the higher resolution in the bottom image.

The diffusion parameters were: δ/Δ = 21.1/46.3 ms (diffusion time = 39.3 ms), and gradient strengths of 0 and 22 mT/m using a linear ramp of duration 600 μs. The diffusion gradients were applied in three orthogonal directions (along the phase, read and slice directions respectively). The *b*-values were calculated neglecting the contribution of imaging gradients. The sequence was designed to minimise the cross-terms by

refocusing all imaging gradients immediately after they were applied (Pierpaoli et al., 1996b), and short crusher gradients, 1 ms long and 8 mT/m in amplitude, were used to spoil unwanted magnetisation (the estimated cross-term contribution from the crusher gradients was < 2 s/mm^2 (Mattiello et al., 1994)). As mentioned in Section 2.2.4.3, since the contribution of the imaging gradients is minimised, the ADC_{AV} represents a good approximation to the trace. The contribution from eddy current gradients to the *b*-value was also neglected. Although they can produce significant distortions and shifts to the echo-planar image due to the very low bandwidth per pixel in the phase encoded direction, the induced gradients are very small (~μT/m) and do not have a significant effect on the diffusion sensitivity of the sequence.

4.2.2 Characterisation of the eddy current effects (phantom studies)

In order to characterise the phase evolution during the echo train, the DW-EPI sequence was used without the phase encoding gradient (dashed box in Fig. 4.3) to acquire data from a spherical phantom (diameter 18 cm) containing doped water (approximately 5 mM $NiSO_4$). These non phase-encoded (nPE) data were transformed to the frequency domain to obtain a series of projections of the object. The standard N/2 correction was then applied to these projection data. In the absence of eddy currents, the phase of these projections should be constant or have a fixed linear time dependence due to a frequency offset (Fig. 4.6). On the other hand, the presence of eddy currents can lead to frequency shifts that vary according to the magnitude and orientation of the diffusion gradients. It is this phase error (δ in Fig. 4.6) that needs to be corrected.

The phase evolution was determined by using a cross-correlation method to calculate the phase difference $\Delta\varphi_{jr}$ between each projection $\mathbf{P}_j$ and a reference projection $\mathbf{P}_r$:

$$e^{i\Delta\varphi_{jr}} = n(\mathbf{P}_r^{\dagger} \cdot \mathbf{P}_j) \qquad (4.1)$$

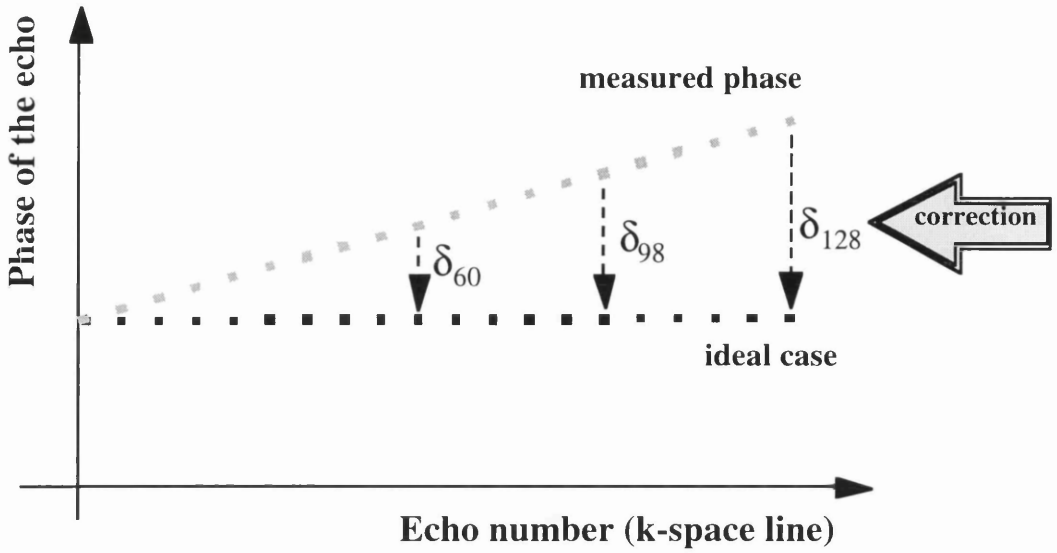

Figure 4.6.

Figure 4.6. Schematic representation of the phase evolution along the echo-train. The black dotted line represents the phase for each echo in the echo-train in the ideal case (e.g., constant phase), while the grey dotted line represents the measured phase in the presence of eddy currents (e.g., time independent eddy current gradient). The difference for each echo (or *k*-space line) is the phase error δ that must be corrected (examples for the 60th, 98th and 128th lines are shown in the figure).

where $\mathbf{P}^{\dagger}$ is the transpose of the complex conjugate of **P**, and n is a normalisation factor. This phase difference $\Delta\varphi_{jr}$ reflects the change induced by the eddy currents between the measurement of the *j-th* echo and the reference echo. The cross-correlation method was found to give a more robust estimate of $\Delta\varphi$ than using more simple methods, such as the phase at the maximum of the echo (which relies on the measurement in a single point), or the average phase for each echo (which gives the same contribution from any phase value along the projection, regardless of its amplitude). These two methods are more sensitive to the presence of noise in the data.

In order to properly characterise the phase evolution with a reduced sensitivity to erroneous isolated phase measurements (particularly for echoes at the end of the echo train in regions with high susceptibility variations), the nPE data were smoothed along

the lines dimension before the calculation of $\Delta\varphi$. This was performed by applying an additional Fourier transform along the lines dimension (i.e., for each column), followed by a symmetric Hanning filter and inverse Fourier transform back to the projection space. This provided a robust estimate of the slow phase variation of the $\Delta\varphi$ evolution. However, due to the finite extent of the nPE data, this convolution procedure produced distortions at the start and end of the echo train where there were artefactual discontinuities in the measured $\Delta\varphi$ values. Therefore, the filter was empirically selected in order to restrict the errors to the first line and last line only, while still producing enough smoothing to the data (Fig. 4.7). For this reason, these lines were corrected using the $\Delta\varphi$ value obtained from the second and penultimate projections, respectively.

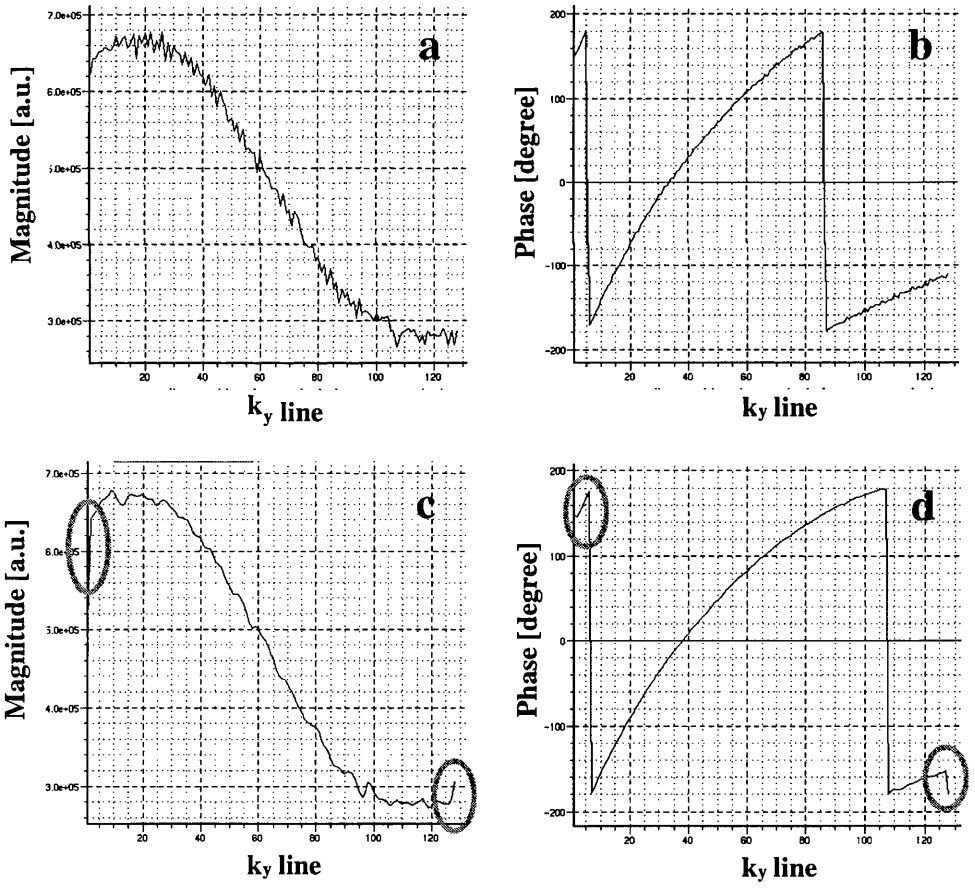

Figure 4.7.

Figure 4.7. Effect of smoothing the nPE data. Magnitude (a) and phase (b) data as a function of k_y line (i.e., echo position in the echo-train) without smoothing, but after N/2 correction (see Fig. 4.8). Magnitude (c) and phase (d) data when smoothing was applied to the nPE data. As can be seen, the smoothing reduces the high frequency variations in

the data, but produces erroneous values at the beginning and end of the echo-train (shown by the oval regions in (c) and (d)).

Since the nPE data set is also acquired under an alternating read gradient, it suffers from odd and even echo misregistration (Fig. 4.8). Therefore, it is necessary to perform the N/2 correction on the nPE data before the smoothing step. Otherwise, the smoothed data would not represent the real phase variations during the echo-train.

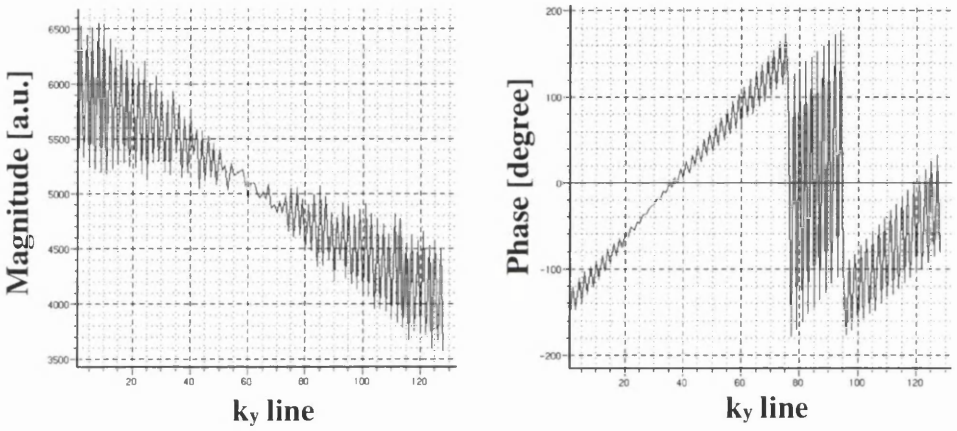

Figure 4.8.

Figure 4.8. Magnitude (left) and phase (right) data as a function of k_y line without N/2 correction or smoothing. An obvious magnitude and phase alternation between even and odd lines can be seen. If this alternation were not corrected, the smoothing of the data could produce an erroneous characterisation of $\Delta\varphi$.

4.2.3 Image correction

The proposed correction method is illustrated in the flow chart in Fig. 4.9 and consists of the following steps:

1) Acquisition of nPE data.
2) Fourier transformation of the nPE data to the frequency domain (projection space).
3) N/2 correction of nPE data and smoothing of these data along the lines dimension.
4) Calculation of the phase difference $\Delta\varphi_{jr}$ between each projection and a reference projection (where j is the line number, and r the reference line).

5) Application of phase correction to the raw *k*-space data for each line *j* of the image data with the $\Delta\varphi_{jr}$ value obtained from the same line of the nPE data, except in the case of the first and last lines, where $\Delta\varphi_{2r}$ and $\Delta\varphi_{127r}$ are used.

6) Calculation of the corrected image (N/2 correction and 2D-FFT).

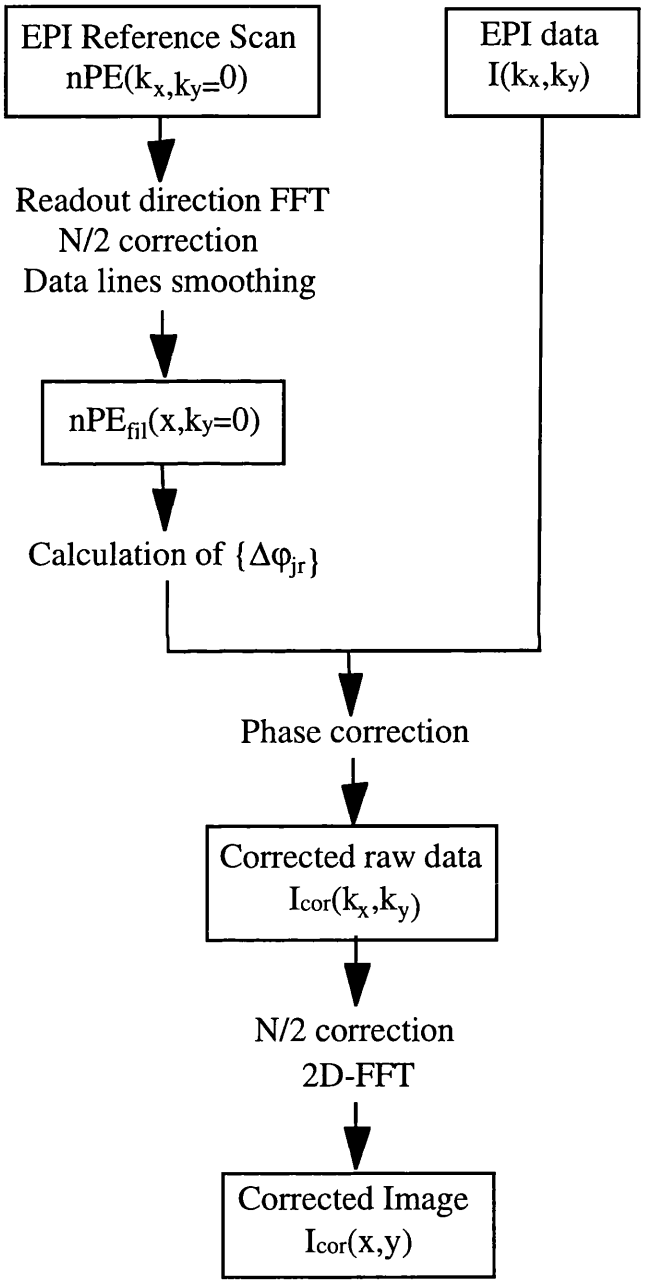

Figure 4.9.

Figure 4.9. Schematic flow chart of the proposed correction method.

In this work, the line at the centre of *k*-space (line 33, corresponding to the SE centre) was chosen as the reference line. However, any line can be used; the only difference will be a different global phase value for the data (which is not relevant in a magnitude image). The correction procedure was performed on the scanner using the Siemens on-line signal processing language (SPL) as part of the image reconstruction process.

4.2.4 Validation

For the validation of the proposed correction method, axial slices of the spherical phantom were acquired. Diffusion gradients were applied along the *Z*-axis, which was found to be the direction that produced the largest shift in the image. For each diffusion gradient two images were acquired: one using a gradient strength of +22 mT/m, the other using a strength of -22 mT/m. A subtraction of these two images was used to assess the influence of the diffusion gradient on the image shift. The procedure was performed for sequences with and without 'dummy' gradients. A standard image realignment algorithm (SPM, (Friston et al., 1995)) was used to measure the image displacement before and after the correction method was applied (see below).

In order to show the effectiveness of the method *in vivo*, ADC maps in three orthogonal directions and the corresponding ADC_{AV} map were calculated for a normal volunteer. Imaging parameters were the same as before, and 3 *b*-values (0, 300 and 606 s/mm^2) were used for each orientation.

The correction method and the calculation of the ADC_{AV} map were also implemented on-line and validated in a 10-year-old stroke patient. Two *b*-values (0 and 606 mm^2/s) in three orthogonal directions were acquired in 20 axial slices, with a total scan time of 1 min. The imaging parameters were as described for the phantom and volunteer studies.

4.2.5 Image shift measurement

Finally, to characterise the effect of eddy currents on the actual image shift, the SPM image realignment algorithm was used to measure the image displacement as a function of slice position and measurement protocol. Due to the difficulties in realigning images with different diffusion weighting, image shifts were obtained by realigning the uncorrected image to the corresponding image generated from the application of the correction method described above; the same raw data were used for both corrected and uncorrected images. This approach is based on the assumption that the correction method provides an accurate repositioning of the image. Multi-slice axial images were acquired using a cylindrical water phantom (length = 18 cm, diameter = 18 cm). Images were acquired with diffusion gradient strengths of 0 mT/m and 22 mT/m along the *Z* axis, both with and without 'dummy' gradients. Twenty-five slices were acquired in ascending and descending order to study the potential cumulative effect of successive gradient pulses on the induced shift.

4.3 RESULTS

4.3.1 Characterisation of the eddy current effects

The beneficial effect of the presence of 'dummy' gradients can be seen in Fig. 4.10, where the phase evolution of the nPE data is plotted for 6 consecutive acquisitions from the *same* axial slice position; a diffusion gradient strength of 22 mT/m in the slice direction was used with a TR of 240 ms. This TR was the same as the time interval between slices in the multi-slice acquisition, thereby ensuring that the timing between each pair of diffusion gradient pulses is equivalent to that in a multi-slice acquisition. When no 'dummy' gradients are used in the sequence (Fig. 4.10a) there is a progressive increase in the frequency offset shown by the increase in the slope of the phase evolution. This indicates a long time constant eddy current that has a cumulative effect on

successive acquisitions. When 'dummy' gradients are put in the sequence (Fig. 4.10b) this cumulative effect is much reduced and all acquisitions have a similar phase evolution during the echo train.

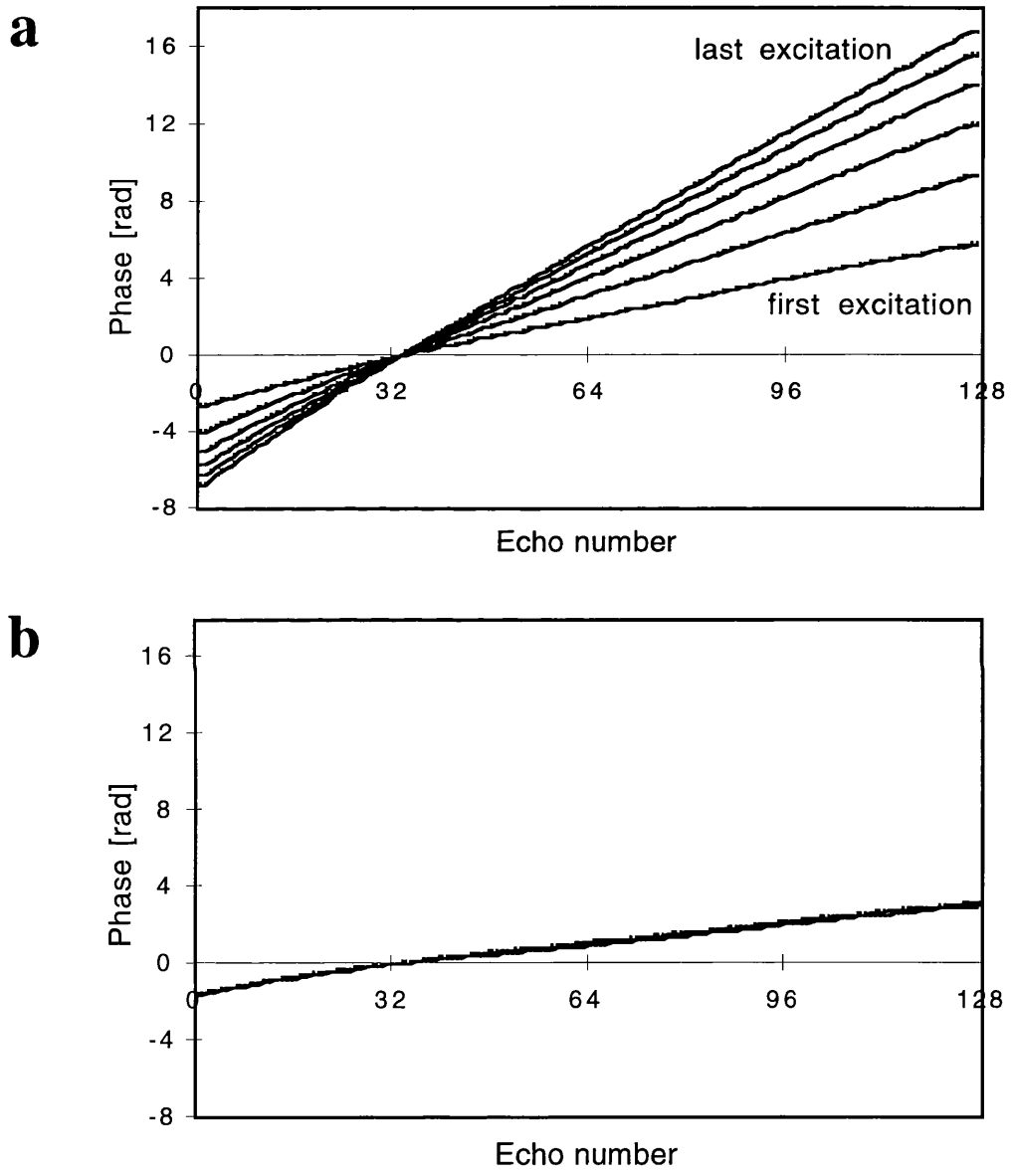

Figure 4.10.

Figure 4.10. Effect of the presence of 'dummy' gradients on the phase evolution during the echo train for 6 consecutive acquisitions from the *same* slice position. (TR=240 ms, diffusion gradient strength = 22 mT/m in the z-axis). (a) In the absence of 'dummy' gradients; (b) in the presence of 'dummy' gradients. The phase of each echo is calculated relative to a reference echo (line 33).

Figures 4.11a and 4.11b show the behaviour of the phase evolution (in the presence of 'dummy' gradients) during the echo train for 7 different slices (slice separation = 7.5 mm) using diffusion gradients of 11 mT/m or 22 mT/m in the slice direction. It can be seen that the phase evolution is dependent not only on the gradient amplitude, but also on

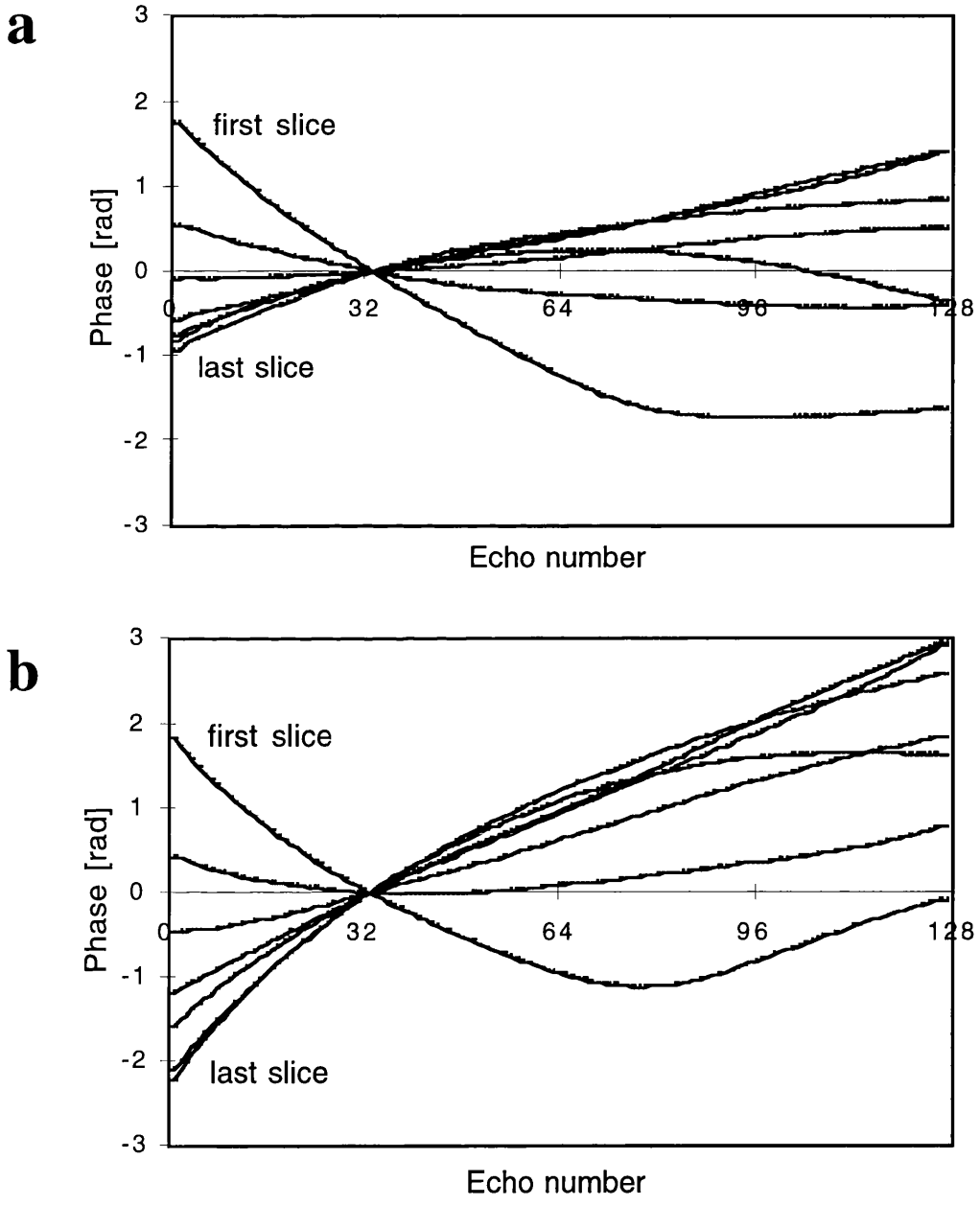

Figure 4.11.

Figure 4.11. Phase evolution during the echo train for 7 different slices in the presence of 'dummy' gradients. (a) Diffusion gradient strength = 11 mT/m, (b) 22 mT/m.

the slice position. Since the data were acquired using the 'dummy' gradients, the cumulative effect was minimised, and the slice dependence of the phase evolution reflects the presence of an eddy current gradient in the slice direction. Moreover, the phase evolution remained slice dependent even when a single slice acquisition was performed at different slice positions (data not shown). It should also be noted that the high non-linearity of the phase evolution for some slices makes it impossible to characterise the time dependence without measuring the phase at a large number of points during the echo train.

4.3.2 Validation (phantom studies)

Figure 4.12 shows the subtraction obtained from axial images acquired using diffusion gradients of ±22 mT/m in the slice direction. A clear shift induced by the eddy currents can be seen (top row of images) that depends on slice position. The maximum image shift (top-right image) measured using SPM was 18 mm (approximately 9 pixels). The shift is reduced by the presence of the 'dummy' gradients (middle row), although a significant misregistration is still present (maximum measured shift: 4.6 mm (approximately 2.5 pixels)). This shift is effectively eliminated after the phase correction is applied (bottom row). After correction, the image shift was less than the nominal pixel size of 1.9 mm and was estimated to be 0.3 mm using SPM. A very small shear can be seen in some slices after the image shift was corrected (e.g., bottom right image). This minor distortion was originally masked by the much more important image shift and, in general, it was found to be almost negligible for axial slices.

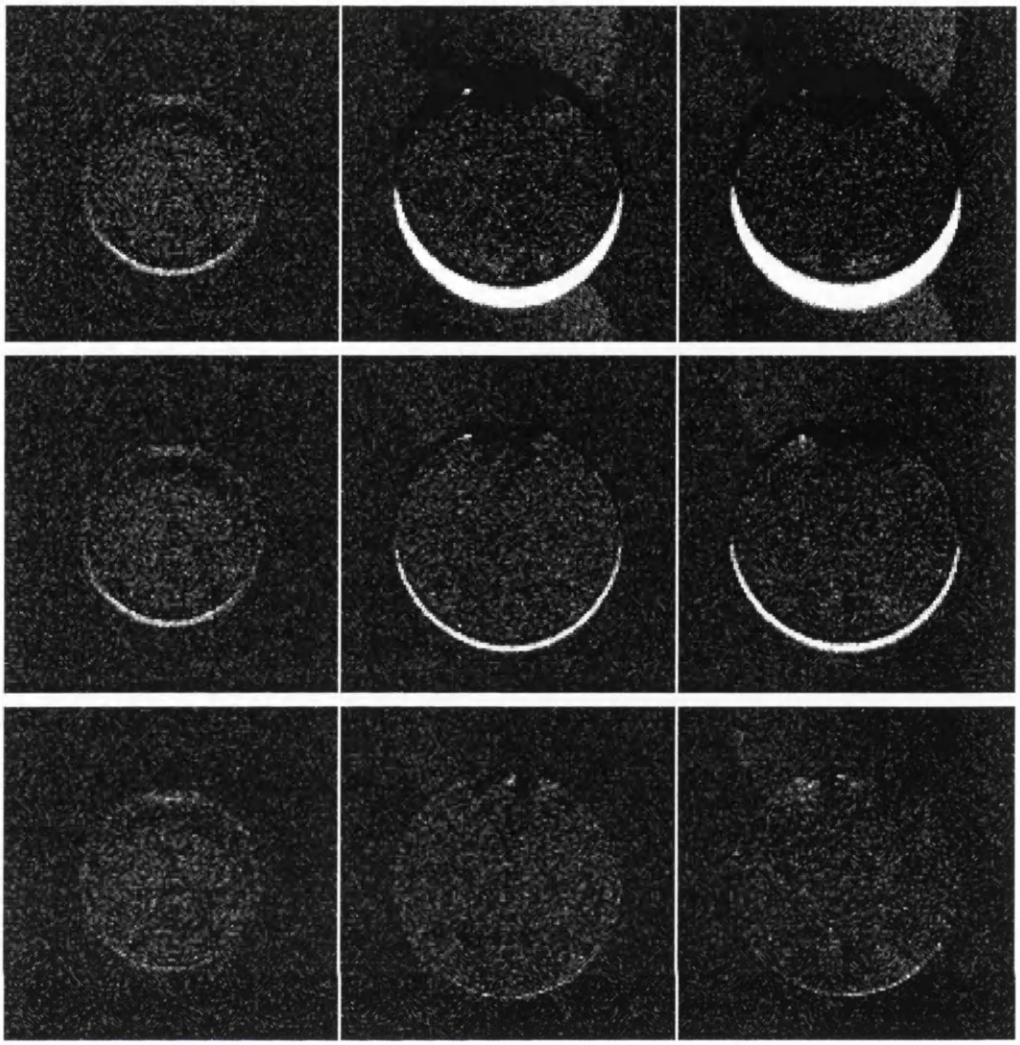

Figure 4.12.

Figure 4.12. Difference images resulting from the subtraction of data acquired using +22 mT/m and -22 mT/m diffusion gradients along the *Z*-axis. The three columns contain data from three different slice positions. Top row, uncorrected data in the absence of 'dummy' gradients; middle row, uncorrected data in the presence of 'dummy' gradients; bottom row, corrected data in the presence of 'dummy' gradients.

4.3.3 Image shift measurement

Figure 4.13 shows the measured shift of diffusion-weighted echo-planar images relative to the corresponding images without diffusion-weighting, when 22 mT/m diffusion gradients were applied along the *Z* axis. A linear dependence on the slice position can be seen when the data were acquired with 'dummy' gradients (solid lines); this confirms the

presence of an eddy current gradient in the slice direction. Since the bandwidth per pixel in the phase encoded direction was 10.85 Hz, the linear frequency offset is equivalent to an eddy current gradient amplitude of approximately 0.004 mT/m (i.e., more than 5000 times smaller than the applied diffusion gradient). The behaviour was independent of whether the slices were acquired in ascending or descending order, and the maximum relative frequency shift was approximately 25 Hz. When no 'dummy' gradients were used (dashed lines), the induced shift was larger and non-linear, with a maximum value of approximately 60 Hz. Furthermore, the pattern of image shifts was dependent on whether an ascending or descending slice order was used. These results demonstrate the effect of the 'dummy' gradients in reducing the shift and avoiding the cumulative effect of successive gradient pulses. When the diffusion gradients were applied along the X or Y axes, the relative shift was restricted to less than 1.5 mm, corresponding to a frequency shift of less than 8.5 Hz (data not shown).

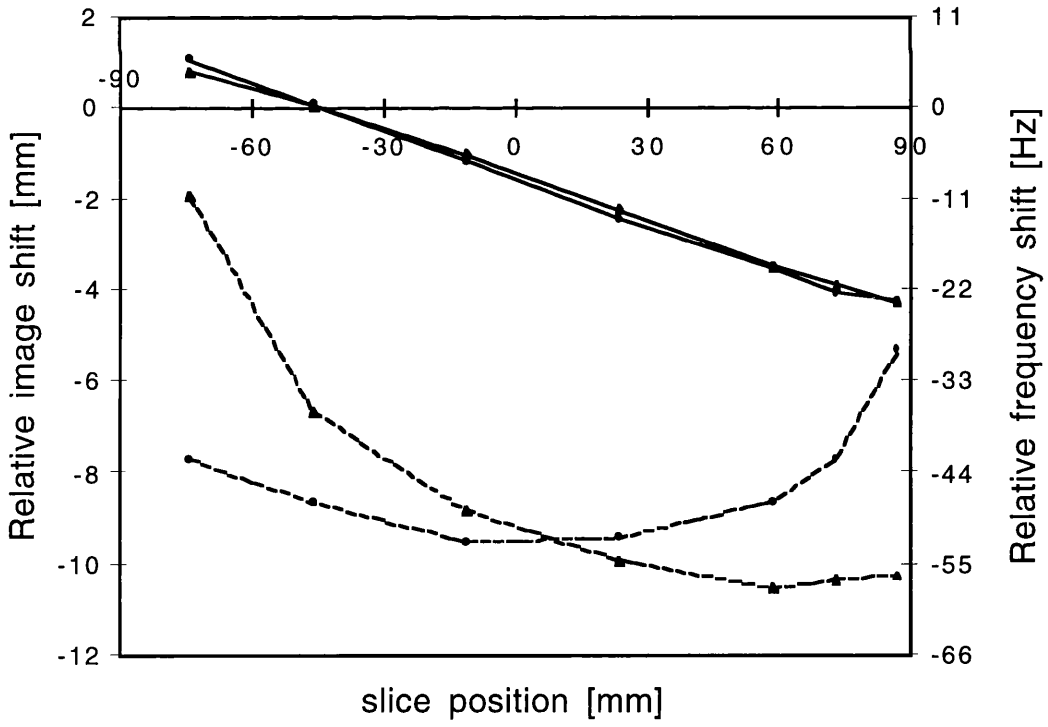

Figure 4.13.

Figure 4.13. Relative shifts between images acquired using Z-axis diffusion gradients of 22 mT/m and 0 mT/m as a function of slice position. Solid lines represent data

acquired in the presence of 'dummy' gradients, dashed lines in their absence. Slice data were acquired both in ascending (▲) and descending (●) order. Slice positions are measured relative to the centre of the magnet (0 mm). The data from only 7 of the 25 measured slices are displayed. The relative frequency shifts were estimated from the measured image shifts.

4.3.4 Validation (volunteer and patient studies)

To demonstrate the utility and validity of the proposed method *in vivo*, Fig. 4.14 compares ADC maps with and without correction for a normal volunteer. Each row in the figure shows ADC maps for three orthogonal directions together with the associated ADC_{AV} map. The maps in the top row were calculated from uncorrected raw data acquired without 'dummy' gradients, and the maps in the bottom row were derived from corrected raw data acquired in the presence of 'dummy' gradients. The most striking effect is seen in the ADC_Z map obtained from the uncorrected data. Not only is there a significant effect at the edge of the brain (shown by the arrow in Fig. 4.14) but there is also artefactual structure throughout the brain due to the misalignment of tissue interfaces. These artefacts are not apparent when the map is obtained from the corrected raw data acquired in the presence of 'dummy' gradients. Similarly, the uncorrected ADC_{AV} map has a severe edge effect which is not seen in the corrected map, and is less uniform than that derived from corrected data.

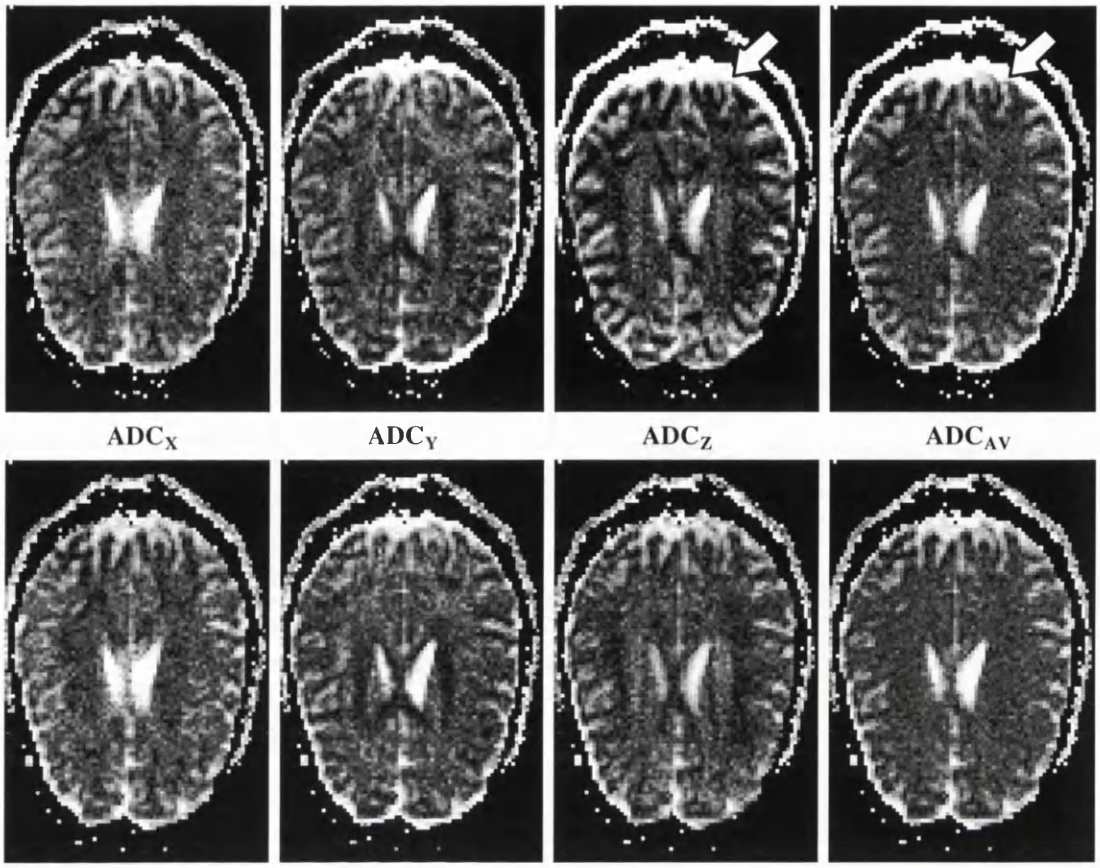

Figure 4.14.

Figure 4.14. ADC maps for a normal volunteer. Top row, calculated from uncorrected data acquired in the absence of 'dummy' gradients; bottom row, from corrected data in the presence of 'dummy' gradients. The arrows indicate the large artefact seen at the edge of the brain in the uncorrected maps.

Figure 4.15 shows the corrected and uncorrected ADC_Z maps for 8 slices in the same volunteer. It can be seen that the correction method produces unshifted images even in regions with large susceptibility gradients, such as the temporal lobes, where EPI suffers from large image distortions. Furthermore, no blurring is observed in those regions.

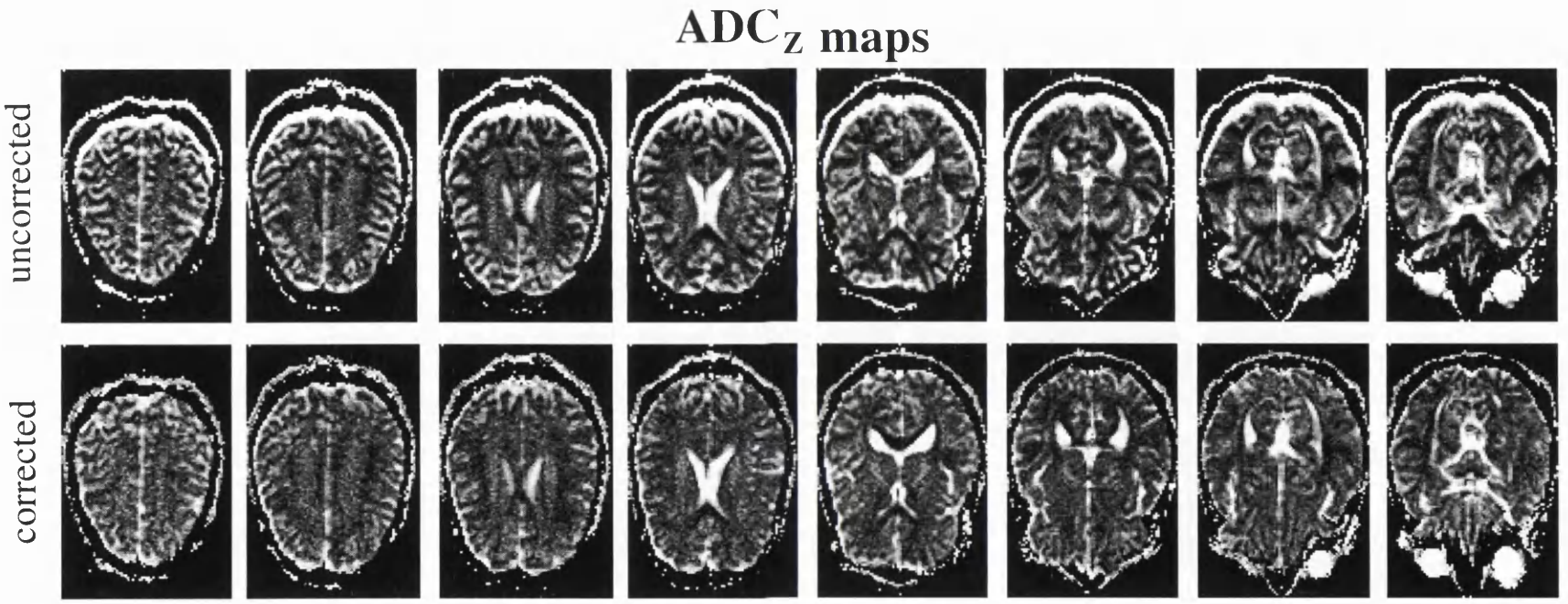

Figure 4.15.

Figure 4.15. ADC_Z maps for the same volunteer as in Fig. 4.14. Eight different slices showing the maps calculated from uncorrected data acquired in the absence of 'dummy' gradients (top row), and the maps calculated from corrected data in the presence of 'dummy' gradients (bottom row). The correction method produces maps without image misregistration even in slices with large susceptibility induced distortions.

Figure 4.16 shows ADC maps acquired approximately 24 hours after the onset of stroke in a 10-year-old female. This figure shows one slice from a 20 slice data set. Each ADC map was created on-line from corrected diffusion weighted images, and the ADC_{AV} map calculated as the average of the three ADC maps. There are no artefacts associated with image shifts in the calculated ADC maps. The ADC_{AV} map shows a clearly delineated region of reduced diffusion in the left basal ganglia (right side of the image). The lesion is less well-defined on the individual ADC maps due to the confounding effects of anisotropy.

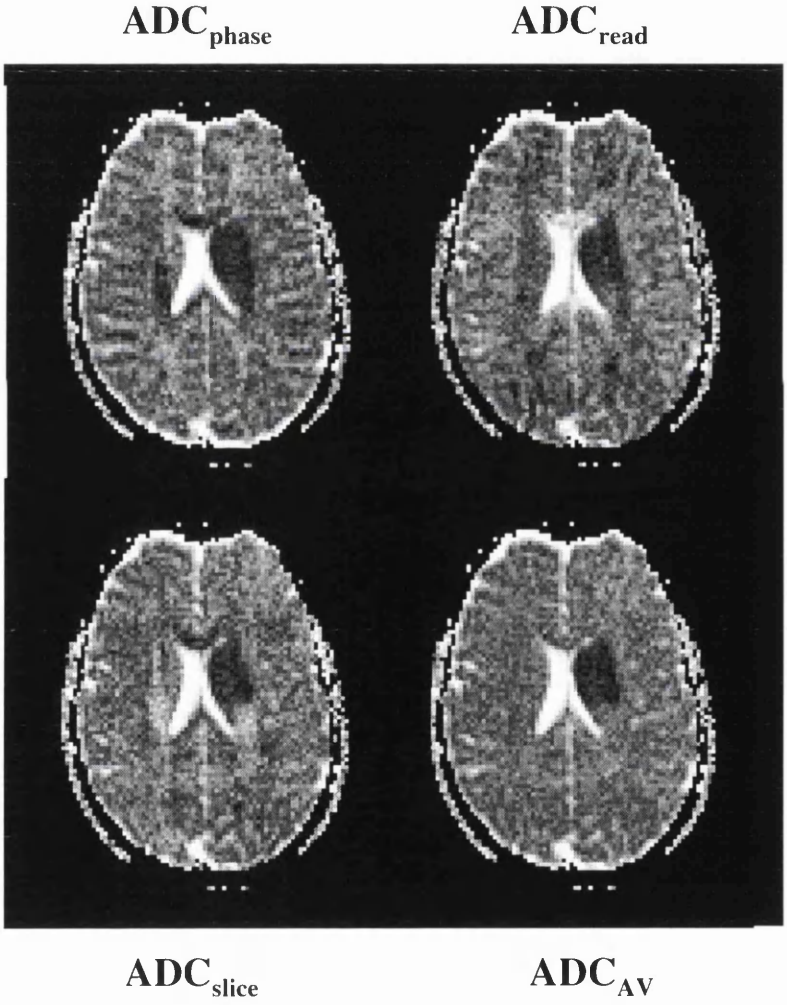

Figure 4.16.

Figure 4.16. ADC maps acquired approximately 24 hours after the onset of stroke in a 10-year-old female. This figure shows one slice from a 20 slice data set. Each ADC map was created from corrected diffusion weighted images, and the ADC_{AV} map calculated as the average of the three ADC maps. No artefacts resulting from image shifts were

observed. The ADC_{AV} map shows a clearly delineated region of reduced diffusion in the left basal ganglia. The phase encoding direction is along the vertical direction.

4.4 DISCUSSION

An on-line method that eliminates eddy current induced image shifts in DW-EPI has been described. The characteristic shifts for the particular 1.5 T MR system used in this work have been established, and the method has been validated both in phantom and human studies.

An advantage of the present method is that no assumption is made about the functional dependency of the phase evolution during the echo train, i.e., no fitting of the data is necessary. Moreover, since a different nPE data set is acquired for each slice, it can correct not only for B_0 shift effects, but also for eddy currents which induce a frequency shift that is dependent on slice position. This allows the correction of the shift, even in cases of slice-dependent and non-linear phase evolution, as in the particular MR system used here.

Although the method is very general, one disadvantage is that the acquisition time is doubled, since it is necessary to acquire nPE data for each slice and *b*-value. However, in systems where the phase evolution is simpler or more linear, it might be possible to characterise it with only 2 or 3 points by acquiring extra non-phase-encoded echoes before and after the echo train, and using the echo at the centre of *k*-space (non-phase-encoded). This would half the acquisition time, because it would be unnecessary to acquire the nPE reference scans. It would also be possible to reduce the total acquisition time when the phase evolution is similar for different slice positions, corresponding to a true B_0 shift, with no *Z*-gradient eddy current and no cumulative effects. In that case, acquisition of only *one* nPE reference scan from a single slice would be enough to correct for the shift. As suggested by Jezzard et al (1998), an alternative approach to reducing the acquisition time is to perform a pre-calibration using a phantom, avoiding the need to

collect the nPE data for each acquisition. However, it should be noted that exactly the same protocol and imaging parameters should be used for the acquisition of this pre-calibration and any subsequent *in vivo* examination, i.e., the same number of slices, slice locations, slice acquisition order, TR, diffusion gradient strength, etc. Moreover, the pre-calibration method depends on the long time stability of the eddy currents, which can be affected by the cryogen levels.

Although 'dummy' gradients are not necessary for the image shift correction, they may decrease the effect of magnetic field gradients induced by eddy currents, that is, they may help to minimise the scaling and shear, which is not corrected by the method described here. Indeed, in the current work they were found to reduce the small image scaling effect in our system (Fig. 4.17), and for this reason 'dummy' gradients were used in the final sequence. However, on systems with more severe image scaling or shear problems, the addition of 'dummy' gradients may not provide complete compensation for such effects.

Figure 4.17.

Figure 4.17. Difference images resulting from the subtraction of data acquired using +22 mT/m and -22 mT/m diffusion gradients along the *Z*-axis, from corrected data in the *absence* of 'dummy' gradients. The three columns contain data from three different slice positions. Although the image shift is corrected, there is a small remaining scaling effect (see Fig. 4.12).

Although the phase correction method described does not correct for image scaling and shear, it will still correct for any induced B_0 shift even in the presence of these other image distortions. However, it should be noted that an uncorrected scaling may lead to

erroneous ADC values, since a *b*-value dependent change in pixel size (due to eddy currents) would translate to a *b*-value dependent change in pixel intensity. That is, if due to the induced eddy currents, a pixel of area A is effectively scaled to an area A', the intensity will change to $I'=(A/A')\cdot I$, and the error in the ADC will be $\Delta ADC=(1/b)\cdot Ln(A'/A)$. For example, a 5% pixel contraction (in the phase encode direction) would produce ~5% increase in signal intensity, which would represent ~9% error in the ADC (for a 600 s/mm^2 *b*-value and a 0.9 x10^{-3} mm^2/s diffusion coefficient).

Since the main induced eddy current gradient in our system is along the Z direction, the distortion is primarily a slice dependent image shift (for axial slices). This type of artefact is successfully eliminated by the proposed correction method. However, when other image orientations are used, the induced eddy current gradient along the new phase and read directions may become significant. In this case, if the 'dummy' gradients are not enough to compensate the scaling and shear, further corrections may be also needed. In principle, it is possible to correct them without introducing major modifications to the methodology presented here. For the correction of the scaling, an empirical pre-calibration can be performed to increase (or decrease) the size of the phase-encoded gradient. This change effectively decreases (or increases) the FOV in the phase-encoded direction ($FOV_y \sim 1/\Delta k_y \sim 1/G_{pe}$), thereby compensating, the stretch (or contraction) induced by the eddy currents. For the case of a shear, the same nPE data can be used to calculate the eddy current gradient in the read direction as described by Jezzard et al (1998), although this method is very susceptible to noise errors at high *b*-values, long echo-trains or short T_2^* values.

In order for the method to work, some assumptions need to be valid. First, it is assumed that the effects of the eddy currents are reproducible so that the frequency shifts induced in the nPE data are the same as in the image data. This was facilitated by the use of 'dummy' gradients and a 4 s delay between acquisition of image data and nPE data, which helped to avoid a cumulative effect and allowed for the decay of the eddy currents. Secondly, the effect produced by the eddy currents induced by the phase encoding

gradient during the readout is neglected. However, the small phase encoding gradient in EPI is an unlikely source of eddy currents, particularly in our case in which a constant phase encoding gradient was used (~0.07 mT/m in our EPI sequence). The fact that the method produced a good correction supports the validity of the assumptions made.

Since the correction method involves the modification of the phase of the raw image data, it is possible in principle to introduce some artefacts to the image if the measurement of $\Delta\varphi$ is imprecise. In our case, it was found that, when imaging slices *in vivo* with short T_2^* (e.g., poor shimming, regions with significant geometric distortions, etc.), blurring artefacts were introduced unless smoothing was applied to the nPE data as described above (see *Methods* (Section 4.2.2)). This can be seen in Fig. 4.18, where the DW image (22 mT/m diffusion gradient along the read direction) was corrected with (right) and without (left) smoothing the nPE data. An obvious blurring is introduced in the image corrected without smoothing the nPE data.

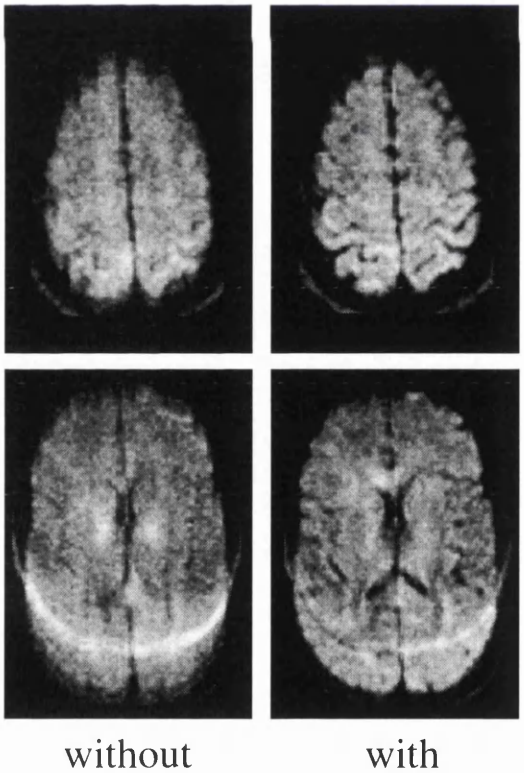

Figure 4.18.

Figure 4.18. Example of image blurring at two slice positions on a normal volunteer. Corrected DW images with (right) and without (left) smoothing of the nPE data. A clear blurring can be seen on the left images.

In summary, a method to correct slice dependent frequency shifts for DW-EPI has been described, which allows the on-line calculation of maps of the trace of the diffusion tensor with an acquisition time of about 1 min for a typical clinical study of 20 slices, 2 b-values, in three orthogonal directions. This allows the immediate assessment of calculated trace maps in clinical examinations. As described, the correction technique makes no assumptions concerning the B_0 eddy current characteristics of any particular MR system, and is therefore of general applicability. In addition, the proposed correction method is not restricted to DW-EPI, but could also be used with other techniques that suffer from eddy current problems, such as perfusion imaging (Kwong et al., 1995; Kim, 1995).

5. The Effect of Residual Nyquist Ghost in Quantitative Echo-Planar Diffusion Imaging

5.1 INTRODUCTION

As was mentioned in Chapter 3 (Section 3.2.2.1), EPI is susceptible to a Nyquist ghost artefact arising from an asymmetry between odd and even echoes when positive and negative read gradients are used to sample alternate lines of *k*-space (Bruder et al., 1992; Fischer and Ladebeck, 1998). This signal modulation in the raw data produces a ghost in the image domain which is displaced by half the field of view (FOV) in the phase encode direction relative to the correct image position. Although hardware developments and the application of post-processing routines have minimised the problem, a residual Nyquist ghost is often produced when the current generation of commercial equipment is used to perform EPI. The intensity of this residual ghost is typically 2-4% of the intensity of the object (Franconi et al., 1997). In most applications, including non-quantitative diffusion-weighted imaging (DWI), the Nyquist ghost is easily identified and does not impair image interpretation. However, this chapter reports the observation of artefacts in EPI-based ADC maps which are less easy to identify. The problem is associated with Nyquist ghosts of highly mobile spins (particularly those in the orbits), and results from the

relatively high signal intensity which is produced at low *b*-values. For typical T_2-weighted sequence parameters used in clinical examinations, the relative signal intensity of the orbit (or cerebrospinal fluid, CSF) to white matter is ~370%. Therefore, even a small (2-4%) remaining ghost of the fluid high signal intensity would represent a significant proportion of the intensity in white matter (~8-15%). These artefacts are seen as regions of apparently low ADC which are indistinguishable on the ADC maps from regions of reduced diffusion (Fig. 5.1) and can be generated from base EPI images with no obvious artefact and with a low level of Nyquist ghost.

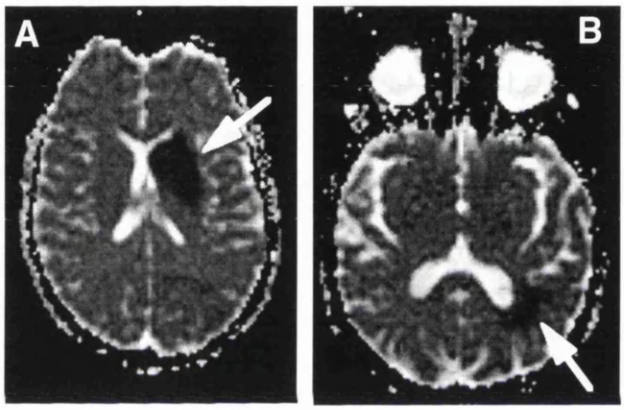

Figure 5.1.

Figure 5.1. Average ADC maps of a patient with an acute stroke (a) and a normal volunteer (b). Both maps show a region with a similar reduction in diffusion (arrows). While the area in the left basal ganglia in the patient corresponds to a true reduction in the ADC, the intensity in the region in the volunteer is artefactually reduced.

In the studies described on this chapter, data acquired *in vivo* were used to demonstrate that these artefacts can be avoided by including standard methods of spatial pre-saturation or fluid-suppression in the diffusion-weighted EPI protocol. In addition, phantom studies were used to illustrate how phase and amplitude variations in the ghost generate the artefacts, and theoretical expressions derived elsewhere were used to provide a detailed understanding of the artefacts observed in vivo. The removal of Nyquist ghost

artefacts in the ADC maps will increase the reliability of image interpretation, which is essential if quantitative diffusion studies are to be used in clinical investigations.

5.2 METHODS

Experiments were performed on the 1.5 T Siemens Vision whole body imaging system described in Chapter 4. Multi-slice data were acquired using a similar DW single-shot SE-EPI sequence as used for the diffusion studies described in Chapter 4 (Section 4.2.1), but with TE extended to 118 ms to allow for the use of higher *b*-values. Eddy current induced image shifts were corrected by using a multi-slice reference scan without phase encoding as described in Chapter 4.

Following the observation of regions of artefactually low ADC in a number of subjects, the effect was investigated in healthy volunteers and phantoms by performing the series of experiments described below.

5.2.1 Pre-saturation of the signal from the orbits

The first experiment in a healthy subject used the same sequence as that used in clinical studies to acquire four axial images at each slice position: one image without diffusion-weighting and three images with diffusion gradients applied along phase, read and slice directions respectively. The diffusion parameters were δ/Δ = 21.1ms/46.3ms (diffusion time = 39.3 ms) using a gradient strength of 22mT/m, corresponding to a *b*-value of 606 s/mm^2. The acquisition was performed twice; for the second acquisition oblique slab pre-saturation was applied to reduce the level of signal intensity in the orbits. The position and angle of the pre-saturation region were selected with reference to a sagittal T_2-weighted fast spin-echo image and chosen to minimise the effect of the pre-saturation on signal from brain tissue (Fig. 5.2). This technique has been used previously in echo-planar functional MRI acquisitions to remove stimulus-correlated Nyquist ghost artefacts

caused by eye movement (Chen and Zhu, 1997). An alternative method for reducing the effect of the Nyquist ghost of the orbit would be to apply the switched readout gradient along the anterior-posterior (AP) axis of the head instead of left-right as in this study; however, this is not a desirable option on many systems with whole-body gradients, such as the one used in this study, due to the increased likelihood of neuromuscular stimulation by time-dependent gradients when they are applied along the AP axis. ADC maps were calculated from each set of four base images and comparisons were made between the average ADC (ADC_{AV}) maps obtained from the two acquisitions. To prevent the background noise in the base images from appearing as random values in the calculated maps, an arbitrary fixed threshold was used to assign a value of zero to voxels with a low signal in the unweighted base image.

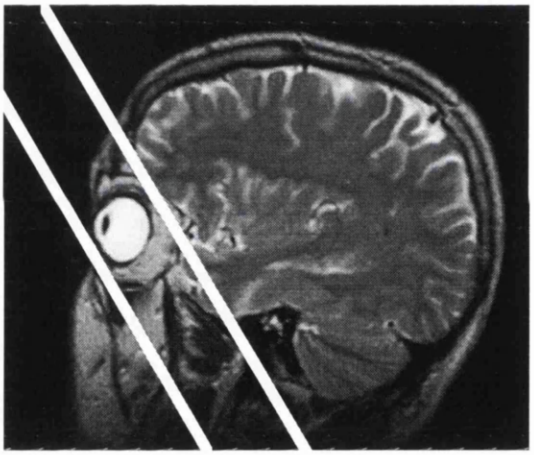

Figure 5.2.

Figure 5.2. Sagittal T_2-weighted fast spin-echo image, showing the typical position and angle of a pre-saturation region which was used to reduce the signal from the orbits in echo-planar diffusion studies. The parallel white lines indicate the outer limits of the pre-saturation region. This procedure was used to remove Nyquist ghost contributions from the orbits which can interfere with brain tissue signals to produce focal regions with erroneous ADC values.

A second experiment was used to provide a more detailed characterisation of the *b*-value dependence of signal in the regions of the brain that showed artefacts in ADC maps. The experiment was performed on the same subject as the first experiment and carried out

during the same imaging session. Images were acquired at identical slice positions to those in the first experiment using 4 different *b*-values (0, 141, 565 and 1272 s/mm^2) and diffusion parameters δ/Δ = 31.1ms/56.3ms (diffusion time = 45.9 ms). Separate acquisitions were performed with diffusion gradients applied along phase, read and slice directions respectively. As above, acquisitions were performed with and without pre-saturation.

5.2.2 Fluid suppression using FLAIR

Suppression of signal from fluid in the orbits can also be achieved using the FLAIR method (Hajnal et al., 1992). This approach was used in a third experiment in which the sequence was modified to include a slice-selective adiabatic inversion pulse and data were acquired from a separate healthy volunteer. FLAIR has been used previously in diffusion-weighted EPI studies to examine the effect of CSF partial-volume averaging on ADC calculation (Kwong et al., 1991; Falconer and Narayana, 1997). For the implementation used in the current study, an inversion time (TI) of 2400 ms was used in conjunction with a TR of 9000 ms, which were empirically optimised. The complete multi-slice data set was obtained in two separate acquisitions in which first the even- and then the odd-numbered slices were acquired. This allowed a relatively wide slice profile to be used for the inversion pulse to ensure a good inversion across the entire slice thickness and to minimise the effects of CSF flow. The diffusion parameters were the same as those used in the first experiment. For comparison, images without the inversion pulse were acquired at the same slice positions.

5.2.3 Level of Nyquist ghost of the orbit

The level of Nyquist ghost from the orbits was estimated in the above subject by using the non-FLAIR sequence with a pre-saturation region positioned over the occipital lobes so that only the ghost of the orbits was visible in that part of the image. Seven signal

averages were obtained to improve the signal-to-noise ratio of the ghost. The mean signal intensity for a region of interest (ROI) within each orbit was then compared with corresponding measurements in the ghost to calculate the 'ghost to image' ratio.

5.2.4 Pattern of interference in a phantom

Images of a phantom sample were acquired to investigate the phase properties of the Nyquist ghost which result in the particular artefacts observed *in vivo*. The study used a similar EPI sequence to that used for the previous experiments, but no diffusion-weighting was applied. A single transverse image of the manufacturer's standard spherical head phantom was acquired with a FOV of 240 mm. In order to exaggerate the Nyquist ghost for demonstration purposes, a 1μs delay (corresponding to approximately 1/4 of the dwell time) between gradient waveform and data sampling was introduced during the acquisition of the image data. This has the effect of increasing the first-order phase error which is present in the projection data after Fourier transformation of each echo along the frequency-encode direction (a shift in k_x represents a linear phase in x). However, the non-phase-encoded signals for Nyquist ghost correction were acquired without the delay so that they did not include information about this additional phase error, leading to an incomplete phase correction during image reconstruction and a final image with an increased level of Nyquist ghost. As described in Chapter 4 (Section 4.2.1), the centre of k-space was sampled at the 33rd echo in the echo train; direct Fourier transformation of these data results in a complex image with a large first-order phase variation along the phase encode direction. Under these conditions it is difficult to appreciate the phase relationships which underlie the artefacts observed in ADC maps (see *Discussion* (Fig. 5.12b)). To avoid this problem, a cyclic shift was applied along the k_y direction before Fourier transformation; it should be noted that this procedure does not affect the way in which the Nyquist ghost signals produce artefacts in the modulus image (see *Discussion* (Section 5.4)). Two complex images were reconstructed from the same data set; in one case a zero-order phase error was introduced to both image data and phase correction data to simulate the effect of a frequency offset of 1 ppm.

5.3 RESULTS

5.3.1 Pre-saturation of the signal from the orbits

Figure 5.3 shows the results from the first experiment on a healthy subject. Figure 5.3a shows an echo-planar image without diffusion-weighting which was acquired without a pre-saturation pulse. Figure 5.3c shows the corresponding ADC_{AV} map, showing a region of apparently low ADC_{AV} near the occipital horn of the left ventricle with a value of $0.35\pm0.13 \times 10^{-3}$ mm^2/s (mean ± SD), which is typical for tissue affected by acute stroke (Figs. 5.1a and 5.4a). The low ADC_{AV} region follows the tissue contours, giving the impression of a genuine diffusion abnormality associated with the white matter in that part of the brain. A less obvious abnormality is present in the unweighted base image (Fig. 5.3a), in which there is a corresponding region of hypointensity that is difficult to identify with conventional window settings; no corresponding signal abnormalities were observed in the diffusion-weighted images (Fig. 5.3b). The image in Fig. 5.3d was acquired with a pre-saturation region to suppress orbit signal, and the corresponding ADC_{AV} map is shown in Fig. 5.3f. The low ADC_{AV} region, seen in Fig. 5.3c, is absent from this second map, in which the measured ADC_{AV} for the same region is $0.75\pm0.14 \times 10^{-3}$ mm^2/s.

For comparison with the maps derived from healthy subjects, Fig. 5.4a shows an ADC_{AV} map from a patient with a genuine region of reduced diffusion. The patient was a 10-year-old female who had suffered a stroke approximately 24 hours before the scan. The ADC_{AV} in the affected region is $0.42\pm0.07 \times 10^{-3}$ mm^2/s which is similar to that in the artefact region of Fig. 5.3c. However, in this case, there is a corresponding region of hyperintensity in the DWI (Fig. 5.4b), consistent with a true region of ischaemia.

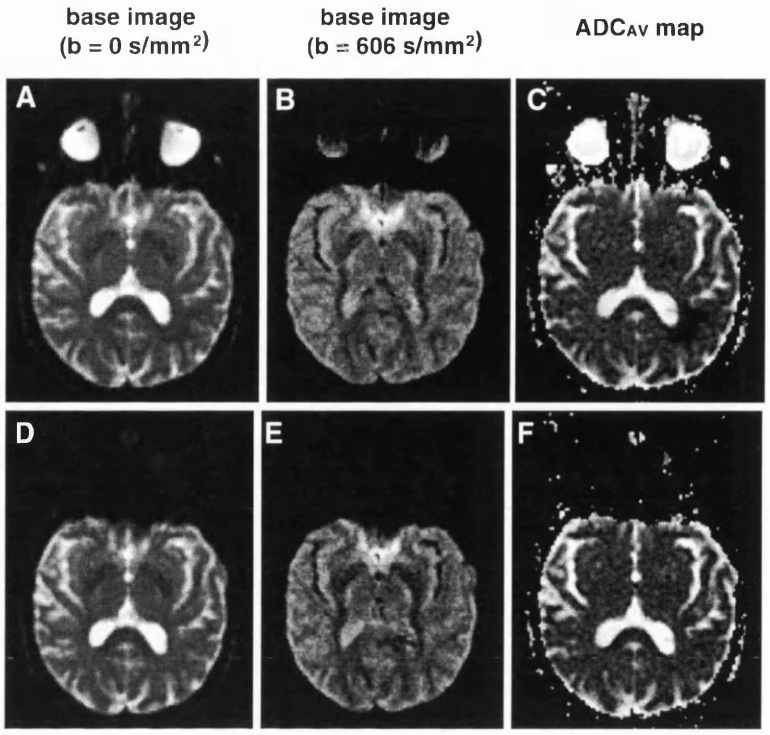

Figure 5.3.

Figure 5.3. Single-shot echo-planar images and ADC_{AV} maps from a healthy subject. Each map was derived from four acquisitions: one without diffusion weighting and three with the diffusion gradient applied successively along orthogonal directions with a b-value of 606 s/mm^2. (a) Image acquired without diffusion-weighting. (b) Image acquired with a b-value of 606 s/mm^2. (c) Corresponding ADC_{AV} map which has a region of apparently low ADC_{AV} near the occipital horn of the left ventricle. Images acquired without diffusion-weighting (d) and with a b-value of 606 s/mm^2 (e), both with a pre-saturation region to suppress signal from orbits. (f) Corresponding ADC_{AV} map which does not have a region of low ADC_{AV}.

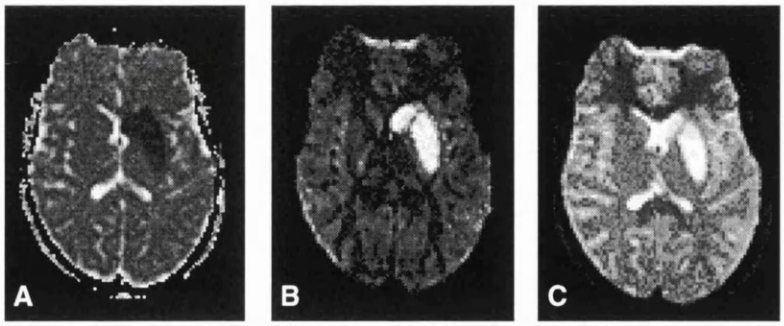

Figure 5.4.

Figure 5.4. ADC_{AV} map (a), diffusion-weighted image (b), and echo-planar image without diffusion-weighting (c) from a 10-year-old female with a stroke showing a

region of reduced diffusion in the left basal ganglia. The examination was performed 24 hours after the onset of clinical symptoms. The region of reduced diffusion is associated to a region of hyperintensity in the DW image.

Figure 5.5 shows the *b*-value dependency of the signal intensity for a region of tissue corresponding to the artefact region of Fig. 5.3c. Figure 5.5a shows the region of interest selected, while Fig. 5.5b shows its signal intensity as a function of *b*-value. Diffusion gradients were applied in the read direction, corresponding to the left-right axis of the head. A similar behaviour was observed when diffusion gradients were applied in phase and slice directions. For the data acquired with pre-saturation, the signal variation is close to the expected mono-exponential behaviour. However, without pre-saturation the signal shows similar behaviour at high *b*-values, but relatively low signal at low *b*-values. This signal dependence provides further evidence for the origin of the artefactually low ADC_{AV} values shown in Fig. 5.3c.

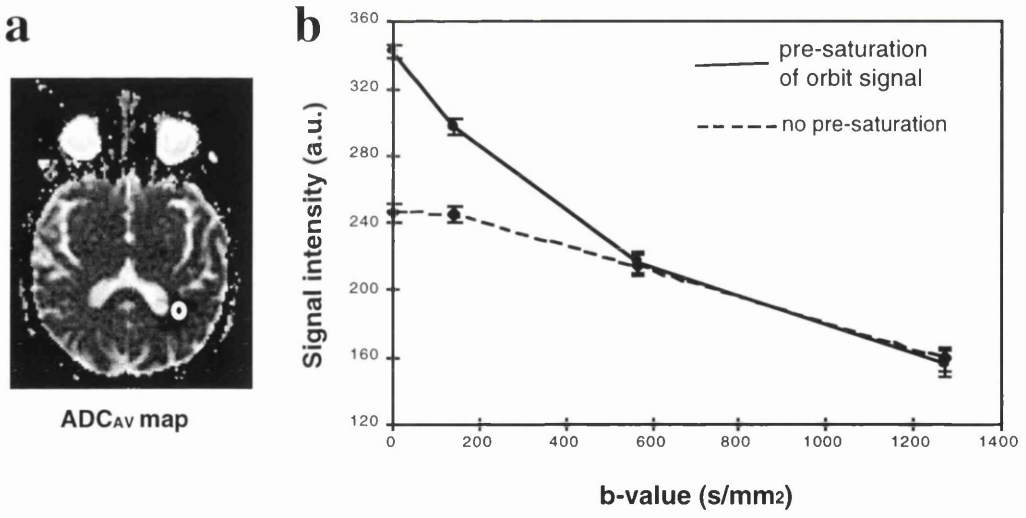

Figure 5.5.

Figure 5.5. (b) Signal intensity as a function of *b*-value for a ROI (shown in (a)) corresponding to the artefact in Fig. 5.3c for acquisitions with (solid line) and without (dashed line) pre-saturation of orbit signal. When no pre-saturation is applied the Nyquist ghost of the orbit interferes with brain tissue signal to produce a region in which there is a signal reduction at low b-value.

5.3.2 Fluid suppression using FLAIR

As shown in Fig. 5.6, fluid-suppression can also be used to avoid the erroneous ADC calculations caused by Nyquist ghosts. Figure 5.6a shows a standard EPI image without diffusion weighting from a second healthy subject and Fig. 5.6b shows the corresponding ADC_{AV} map which has a region of apparently low ADC_{AV} in the left occipital lobe. The measured ADC_{AV} in the region is $0.45\pm0.18 \times 10^{-3}$ mm^2/s and its location is consistent with its being caused by the Nyquist ghost of the orbit. As in Fig. 5.3a, the corresponding region of the unweighted base image (Fig. 5.6a) has reduced signal level. The fluid-suppressed image is shown in Fig. 5.6c, demonstrating a large reduction in signal intensity from both CSF and orbits. The corresponding ADC_{AV} map (Fig. 5.6d) shows that the low ADC_{AV} region did not appear when the base images were acquired with an inversion pulse to suppress fluid. The measured ADC_{AV} in this map in the region which corresponds to the low ADC_{AV} region in Fig. 5.6b is $0.83\pm0.15 \times 10^{-3}$ mm^2/s. Despite achieving a high level of CSF signal suppression, some CSF contributions are still seen in the ADC_{AV} map of Fig. 5.6d. This can be attributed to voxels in which the residual CSF signal is above the fixed threshold used during data processing. It is likely that voxels with partial-volume signal contributions from both CSF and parenchyma contribute to this effect.

5.3.3 Level of Nyquist ghost of the orbit

An analysis of images acquired from the same subject with pre-saturation of the occipital lobes showed that the magnitude of the ghost of the left orbit was 6% of the corresponding value measured at the correct image location. However, the Nyquist ghost of the right orbit was not detectable above the noise (Fig. 5.7c).

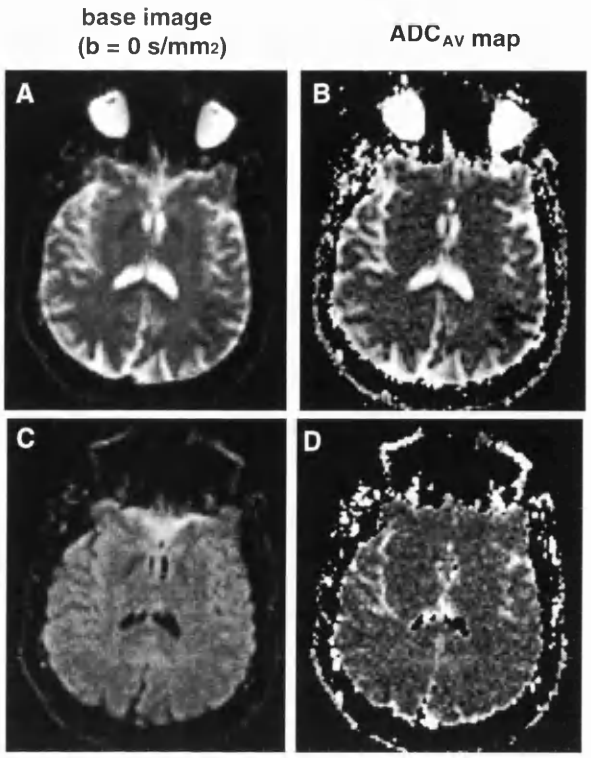

Figure 5.6.

Figure 5.6. Echo-planar images and ADC_{AV} maps from a healthy subject. The maps were generated from acquisitions with *b*-values of zero and 606 s/mm^2 along orthogonal axes. (a) Image acquired without diffusion-weighting. (b) Corresponding ADC_{AV} map showing a region of apparently low ADC_{AV} in the left occipital lobe. (c) Image acquired without diffusion-weighting using an inversion pulse to reduce the signal from CSF and orbits. (d) Corresponding ADC_{AV} map which does not have a region of low ADC_{AV}. Some CSF contributions are still seen in this map due to residual CSF signals which were above the fixed threshold used during data processing.

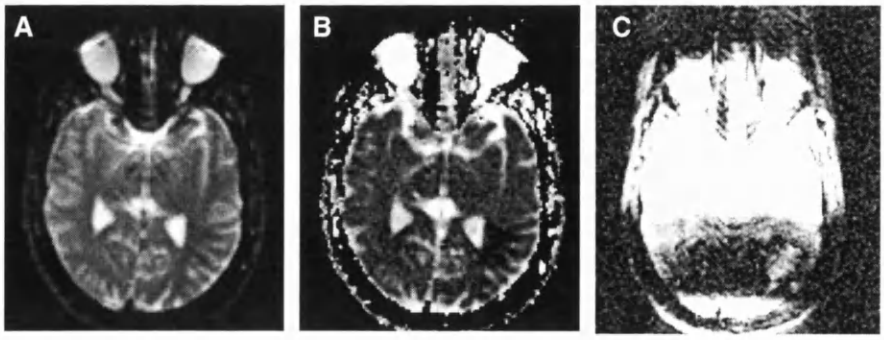

Figure 5.7.

Figure 5.7. Images and ADC_{AV} map for a healthy volunteer. (a) Image without diffusion-weighting. (b) Corresponding ADC_{AV} map. (c) Image acquired without

diffusion-weighting with a pre-saturation region to suppress signal from the occipital lobes. The image in (c) was windowed to show the ghost from the orbit.

5.3.4 Pattern of interference in a phantom

The phase properties of the Nyquist ghost observed *in vivo* were investigated using a phantom sample. Figure 5.8a shows the modulus image for the phantom study in which the Nyquist ghost produced by the EPI sequence was exaggerated by adding an acquisition delay. The figure shows a 'parent' image at the correct location in the centre of the FOV and a ghost image displaced by half the FOV from the 'parent' image. The amplitude of the ghost varies as a function of position along the frequency-encode direction (from left to right in the image). The ghost is symmetrical about the centre of the image, at which point there is no visible ghost. In regions of the image where the ghost image is superimposed on the 'parent' image the pattern of interference varies. Where the ghost of the top-right of the phantom overlaps with the 'parent' image of the bottom-right of the phantom the amplitude is decreased in a similar way to the effect observed in non-diffusion-weighted scans acquired in vivo (highlighted in Fig. 5.8b). However, where the ghost of the bottom-right of the phantom overlaps the 'parent' image of the top-right of the phantom the amplitude is increased (highlighted in Fig. 5.8c). On the left of the image the situation is reversed; there is an increased amplitude at the bottom of the 'parent' image and a decreased amplitude at the top (highlighted in Fig. 5.8d).

The corresponding phase map in Fig. 5.8e demonstrates the underlying cause of these interference phenomena. Firstly, considering the ghost image in a region where there is no overlap with the 'parent' image, there is an asymmetry between the left and right (highlighted in Fig. 5.8f). In fact, there is a phase difference of approximately π radians between the two sides. No such variation is seen in the region of the 'parent' image where there is no overlap (highlighted in Fig. 5.8g). When the phase of a pixel in a non-overlapping region of the 'parent' image is compared with the corresponding pixel in the ghost, a phase difference of about $\pm\pi/2$ is observed; the sign of this phase difference

depends on whether the pixels are on the left or right of the image (highlighted in Fig. 5.8h). Lastly, there is a linear phase variation along the *y* direction which has the same gradient in both 'parent' and ghost images; in the case of the 'parent' image, this variation produces a phase-wrap at the centre of the image. The combination of these effects results in the spatially dependent interference behaviour observed in the modulus image.

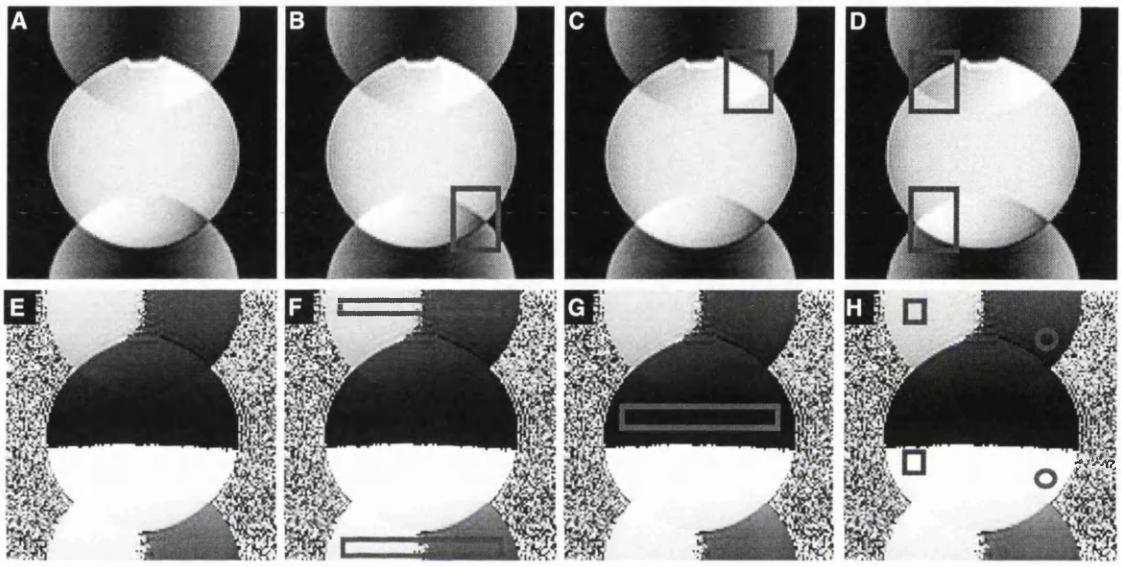

Figure 5.8.

Figure 5.8. Images of a phantom sample acquired with an EPI sequence without diffusion-weighting, demonstrating the appearance of the Nyquist ghost when an acquisition delay is used to generate a first-order phase error. These images show how the ghost and 'parent' images can interfere constructively and destructively in different regions of the image leading to signal modulations which are the underlying cause of ADC artefacts observed in data acquired in vivo. As described in the text (see discussion), this spatial variation in behaviour can be understood by considering theoretical expressions for the complex image domain signal in single-shot EPI. (a) Modulus image. (e) Corresponding phase image. Figures (b-d) are the same as the modulus image (a) but with the areas described in *Results* (Section 5.3.4) highlighted. Figures (f-h) are the same as the phase image (e) but with the areas described in the *Results* (Section 5.3.4) highlighted.

The phantom images in Figs. 5.9c and 5.9d illustrate the amplitude and phase behaviour when the same data are modified to simulate a frequency offset. The positional shift of

the overall image that would normally be associated with a frequency offset has been removed to allow a direct comparison with Fig. 5.8 (repeated in Figs. 5.9a and 5.9b). The modulus image of Fig. 5.9c is similar to that of Fig. 5.9a (or Fig. 5.8a), but the axis of symmetry for the spatial dependence of the ghost has shifted to the left of the image; importantly, the zero signal intensity band of the ghost has shifted to the left. As a consequence of this, interference effects are now more obvious on the right of the image. In the corresponding phase map of Fig. 5.9d the point where the phase of the ghost changes by π can also be seen to shift to the left.

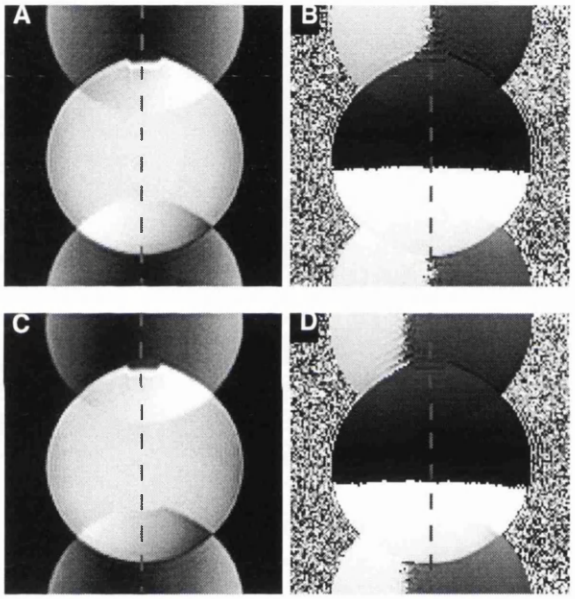

Figure 5.9.

Figure 5.9. Images of a phantom sample acquired with a EPI sequence without diffusion-weighting, demonstrating the appearance of the Nyquist ghost when first-order (a-b), and both zero- and first-order phase errors occur in the raw data (c-d). The first-order error was present in the acquired data and the zero-order error was simulated during image reconstruction. (a) Modulus image and (b) phase image as in Fig. 5.8 (first-order phase error). (c) Modulus image and (d) corresponding phase image when both zero- and first-order phase errors are present. The dotted lines show the position of the axis of symmetry for the spatial dependence of the ghost for the case of no zero-order phase error (a-b). Note that the zero signal intensity region of the ghost image has shifted to the left in the presence of a frequency offset. Together with Fig. 5.8, these data can be used to explain the observation of a systematically left-sided artefact in the ADC maps acquired in vivo.

5.4 DISCUSSION

This study demonstrates that residual Nyquist ghosts of the orbits in echo-planar images can lead to severe artefacts in ADC maps. The focal nature of the affected regions and their relationship to anatomical structure means that they could easily be misinterpreted as genuine diffusion abnormalities. It has also been shown that the artefacts can be avoided by including regional pre-saturation pulses or fluid attenuation in the acquisition protocol.

The ADC_{AV} artefacts seen in Figs. 5.3 and 5.6 are clearly related to the Nyquist ghost of the high signal from the orbit at low *b*-values. The measured level of Nyquist ghost on the MRI system used in this study is within the range of values reported for other commercial scanners (Bruder et al., 1992; Franconi et al., 1997). It should also be noted that the ghost level elsewhere in the image is generally less than that measured for the orbit. Although this level of ghost is acceptable for many EPI applications, it is too high for brain diffusion studies in which the relatively high signal from the orbit can produce b-value dependent ghost signals which are significant when compared to signal from brain tissue. Interference between these two signals modifies the level of signal which is attributed to brain tissue. For the MRI system used in this study the Nyquist ghost of the orbit was found to systematically reduce (due to destructive interference) the apparent signal from a region of tissue in the left occipital region of the brain in a number of subjects. Because the orbit signal is highly attenuated at high *b*-values, this reduction in signal was more significant at low *b*-values, resulting in the *b*-value dependence shown in Fig. 5.5 which produces an artificially low ADC estimate. As the problem is particularly severe in tissues with a low relative signal intensity such as white matter, the resulting artefact follows tissue contours. Such an artefact is easily mistaken for infarcted tissue as it does not appear as a recognisable ghost of the orbit.

One possible way of avoiding these artefacts would be the use of a minimum *b*-value (b_{min}) large enough to produce sufficient attenuation to the fluid signals, such that their Nyquist ghost signals are negligible compared to the signal from the tissue. From our

results, this does not represent a practical solution. Firstly, the use of a non-zero b_{min} would require its acquisition for the three orthogonal directions, increasing the total acquisition time. Secondly, and more importantly, even a b-value of ~150 s/mm^2 was found to be insufficient (see Fig. 5.5b) and therefore the maximum b-value (b_{max}) would have to be extremely large to still provide an accurate estimation for the ADC (see *Appendix* (Section 5.5)).

In principle, the observed behaviour for the signal from the orbit is common to all fluid signals so Nyquist ghosts of CSF may cause similar effects. These CSF related artefacts would be less easy to identify as they would not be restricted to such a specific region of the brain (Fig. 5.10). Therefore, although pre-saturation is effective at removing artefacts caused by orbit signals, it does not offer a general solution to the problem. However, by using the FLAIR protocol, artefacts from both orbit and CSF signals could be avoided. It should be noted that the artefact signal problem becomes more severe with increasing echo time as a result of an increase in the orbit or CSF signal relative to that of brain tissue; this echo time dependence means that T_2 maps generated from EPI data may also be susceptible to artefacts.

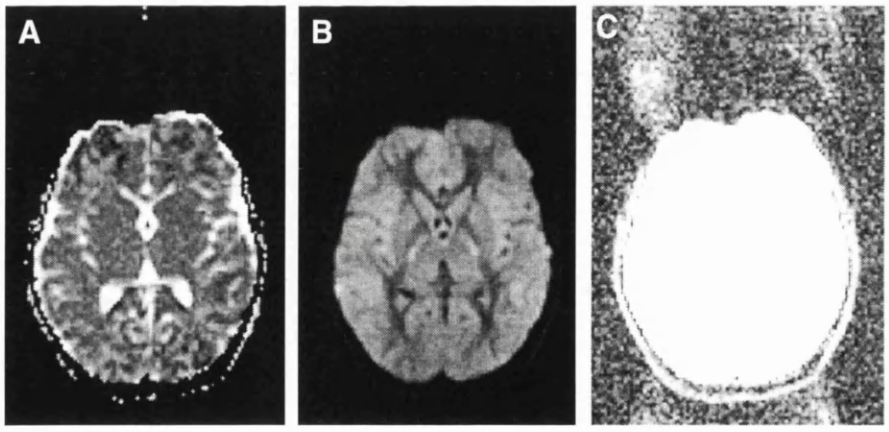

Figure 5.10.

Figure 5.10. Data from a patient scanned with a standard diffusion-weighted EPI sequence using b-values of zero and 606 s/mm^2. (a) ADC_{AV} map showing focal regions of reduced ADC_{AV}, primarily in the frontal lobes. No hyperintensity was seen in the corresponding diffusion-weighted images (e.g. (b)). (c) Image without diffusion weighting showing the position of the residual Nyquist ghost relative to the main image.

The apparently low ADC_{AV} values in (a) are interpreted as an artefact resulting from interference between CSF signals in the ghost and brain tissue signals in the main image.

The phase and amplitude variations demonstrated in the phantom images provide an explanation for the interference patterns which are the underlying cause of the ADC artefacts. In turn, the signal behaviour in the phantom images can be understood with reference to a previous theoretical analysis of the Nyquist ghost in single-shot EPI (Buonocore and Gao, 1997). The complex image domain signal resulting from an echo-planar acquisition can be described in terms of a contribution from the 'parent' image at the correct position ($\hat{M}_{parent}$) and a contribution from the ghost ($\hat{M}_{ghost}$):

$$\hat{M}_{parent}(x,y) = M(x,y)\cos\theta(x) \tag{5.1}$$

$$\hat{M}_{ghost}(x,y) = iM(x,y-N/2)\sin\theta(x) \tag{5.2}$$

where $M(x,y)$ is the object being reconstructed (note that $M(x,y)$ is not necessarily a real number), N is the matrix size, i is the square root of -1, x and y specify spatial co-ordinates along read and phase-encode directions respectively, and $\theta(x) = \theta_0 + x\theta_1$. This angle $\theta(x)$ is the frequency-dependent phase error at the echo centre which is equal in magnitude, but opposite in sign for odd and even echoes. A simplified form of θ is used here to describe only zero- and first-order effects. The zero-order term θ_0 is associated with frequency offsets (Buonocore and Gao, 1997; Heid, 1997) and the first-order term θ_1 is caused by a temporal shift of the echo in the acquisition window (Buonocore and Gao, 1997). This linear phase error is sufficient to explain the observations reported in this study, but in general a more complex spatial dependence is required for a complete description of the Nyquist ghost. When there is a first-order phase error, but no zero-order error, Eq. (5.2) describes a ghost image amplitude which is zero at $x=0$ and varies sinusoidally with x. This is consistent with the pattern of Nyquist ghost shown in Fig. 5.8a. Similarly, non-zero θ_0 and θ_1 terms in $\theta(x)$ produce a minimum amplitude at some

other point along x as shown in Fig. 5.9c. Equations (5.1) and (5.2) also show a $\pi/2$ phase shift (given by the i factor in Eq. (5.2)) between corresponding points in 'parent' and ghost images as demonstrated in the phantom study. The phase change in the ghost between the left and right sides of the image seen in Figs. 5.8e and 5.8b corresponds to a change in the sign of $sin\theta(x)$ in Eq. (5.2).

If there were no zero-order phase error, the reduction of ADC in the artefact region would be smaller as a result of a change in position of the minimum point of the ghost; however, an additional artefact would occur in the right hemisphere in which an elevated ADC would result from a constructive interference between ghost and 'parent' images at low b-values (see Fig. 5.8a).

The artefact reported in this study was found to appear systematically in the right of the image, corresponding to the left side of the brain, and was reproduced when scans were repeated in separate imaging sessions. This asymmetry can be attributed to a slice-dependent frequency offset and to the fact that the slice through the orbits was shifted with respect to the isocentre of the magnet. Figure 5.11a shows the image shifts (and frequency shifts) as a function of slice position calculated using the SPM image realignment algorithm (Friston et al., 1995), as described in Chapter 4. The images were acquired without diffusion weighting using a cylindrical water phantom. A positive frequency shift can be seen, which is approximately quadratic with the slice position. This frequency shift produces an asymmetric Nyquist ghost for any slice, apart from the slice position ~10 mm above the isocentre (towards the top of the head). Figure 5.11b shows the phantom (and Nyquist ghost) images for 9 slices. The axis of symmetry of the ghost is shifted in accordance with the frequency shift in that slice, that is, it starts as a large shift to the left, which is reduced towards the isocentre, and it is increased again to the left as the slices are further away from the isocentre.

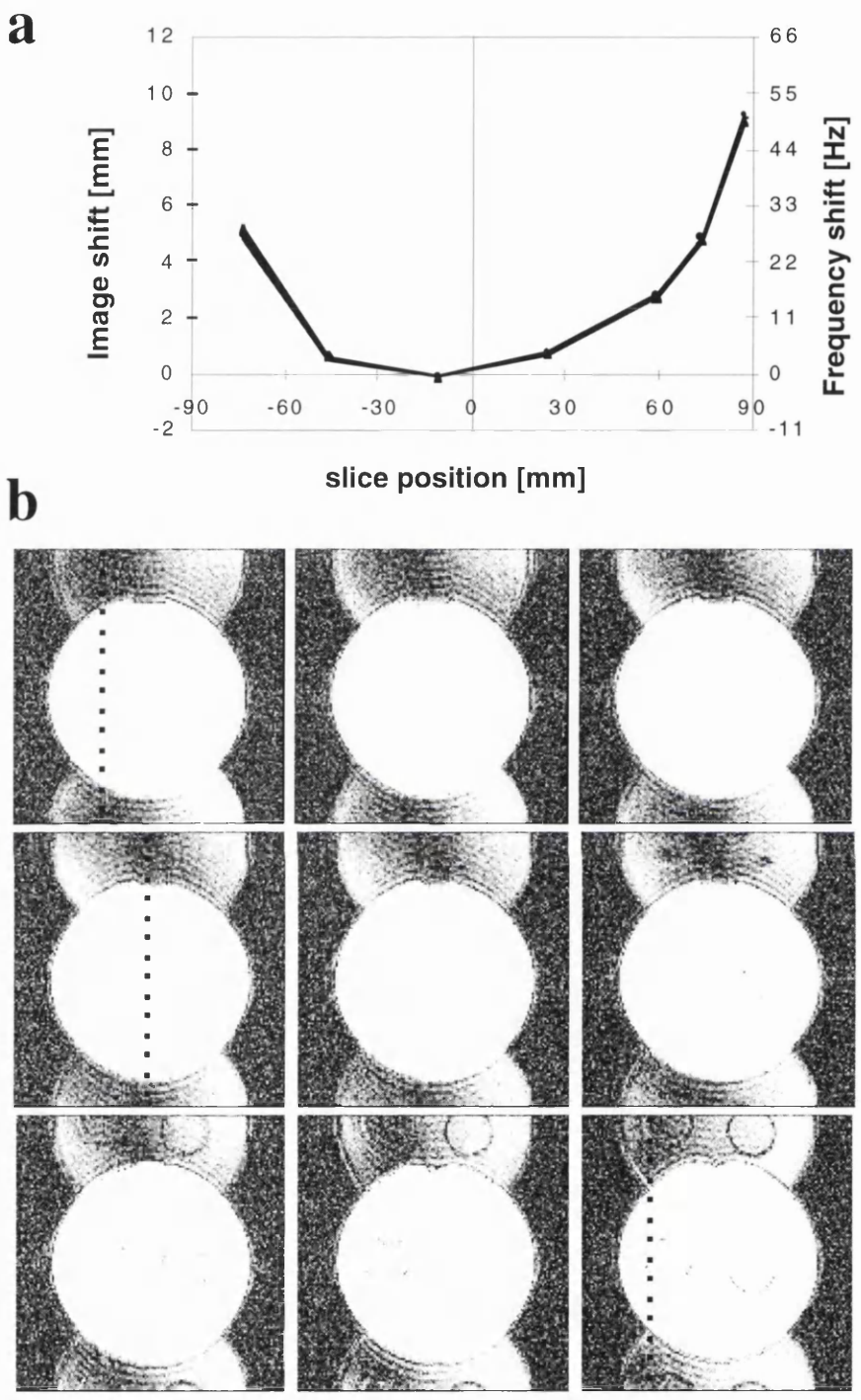

Figure 5.11.

Figure 5.11. Data from a cylindrical water phantom showing the asymmetry in the Nyquist ghost. (a) Calculated image shifts (and frequency shifts) as a function of slice position for images acquired without diffusion weighting. Slice data were acquired both in ascending (▲) and descending (●) order. Slice positions are measured relative to the centre of the magnet (0 mm). The data from only 7 of the 25 measured slices are displayed. The relative frequency shifts were estimated from the measured image shifts.

(b) Images for 9 different slices. The axis of symmetry of the ghost (with zero signal intensity) is shifted to the left in the top left slice (dotted line), the shift is reduced towards the isocentre (dotted line), and it is increased again to the left as the slices are further away from the isocentre (bottom right image). The two circles in the bottom row of images correspond to two cylindrical compartments inside the phantom.

A further factor that affects the specific interference pattern seen in this study is the phase variation along the phase-encode direction shown in Figs. 5.8e and 5.9b. This is another reproducible feature of the acquisition and reflects a small offset of the true $k_y=0$ point along the k_y axis in the raw data. Without an offset along k_y there would be no phase variation along y and the phase difference between ghost and 'parent' signals would be $\pm\pi/2$ at all points in the image so that any overlap between the two would produce constructive interference resulting in ADC estimates which were artificially high (Fig. 5.12a). If there were a k_y offset equal to an integral multiple n of the sampling interval Δk_y there would be an additional phase error of $2n\pi$ across the FOV and, therefore, $n\pi$ between 'parent' and ghost in the overlapping region (a distance FOV/2 apart). As a result, the net difference between the two would still be $\pm\pi/2$ and the interference effects in the modulus image would be the same as the case without a k_y offset. Consequently, echo-planar imaging strategies which shift the centre of k-space by an integral number of echoes do not have an effect on the pattern of interference (Fig. 5.12b). However, if the k_y shift is not a multiple of Δk_y there is an effect. In particular, a k_y shift of $\Delta k_y/2$ produces an additional phase difference of $\pi/2$ between 'parent' and ghost in the overlapping region (a phase error of π across the FOV); this has the effect of producing a net phase difference of either zero or π depending on the position in the image and generates the bright and dark regions seen in the modulus images of Figs. 5.8e and 5.9a. This k_y shift is the source of the linear phase variation observed along the y direction (Fig. 5.8e). The phase in the image can then be written as:

$$\phi_{parent} = \phi_p^{(o)} + \alpha_p y_p \tag{5.3}$$

$$\phi_{ghost} = \phi_g^{(o)} + \alpha_g y_g \tag{5.4}$$

where $\alpha_p = \alpha_g$, since the gradient of the phase variation was found to be the same in both 'parent' and ghost images (see *Results* (Section 5.3.4)). The y_p position of the 'parent' image will interfere with the $y_g = y_p \pm N_y/2$ position of the ghost (positive sign for the bottom and negative sign for the top half of the 'parent' image), where N_y is the number of pixels in the phase-encoded direction. Therefore, the phase difference between 'parent' and ghost images (which determined the type of interference) will be:

$$\Delta\phi = \left(\phi_p^{(0)} - \phi_g^{(0)}\right) \mp \alpha N / 2 = \Delta\phi^{(0)} \mp \alpha N / 2 . \qquad (5.5)$$

This explains why it is possible to have different types of interference between the bottom (destructive in Fig. 5.8b) and the top (constructive in 5.8c) part of the 'parent' image.

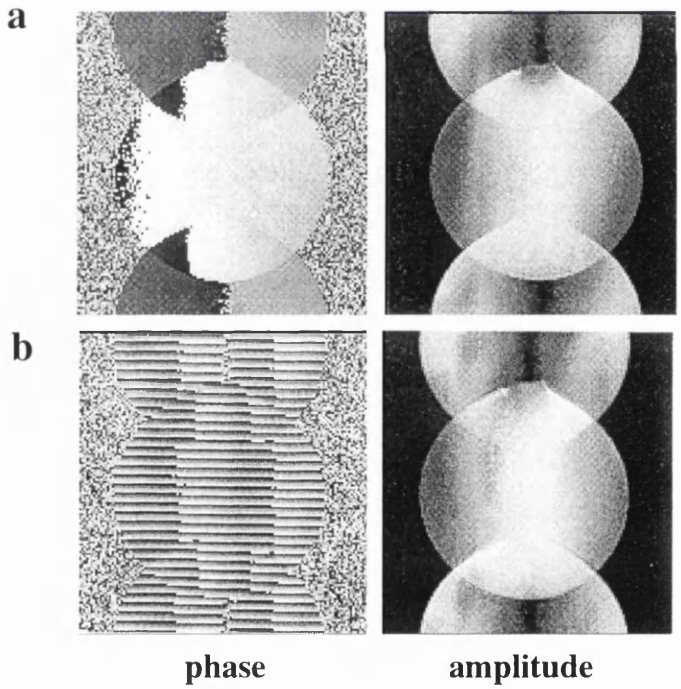

Figure 5.12.

Figure 5.12. Data from a phantom sample showing the effect of an offset of the true $k_y=0$ point along the k_y axis in the raw data. Without an offset (a) produces constructive interference. With an offset equal to an integral multiple n (33 in the figure) of the sampling interval Δk_y (b) the same interference pattern is observed.

It is interesting to observe that one way of eliminating the effect of the zero-order term θ_0 is by using a recently proposed method for the correction of Nyquist ghost, in which three non-phase-encoded echoes are acquired instead of two (Heid, 1997). Any zero-order phase error is corrected by this new N/2 correction, and the asymmetry in the Nyquist ghost is eliminated. Figure 5.13 shows phantom data acquired in the same slice positions as in Fig. 5.11b, but where the three non-phase-encoded echo correction was used. It can be seen that this N/2 correction eliminates the frequency offset, and the ghost is symmetric for all the slices.

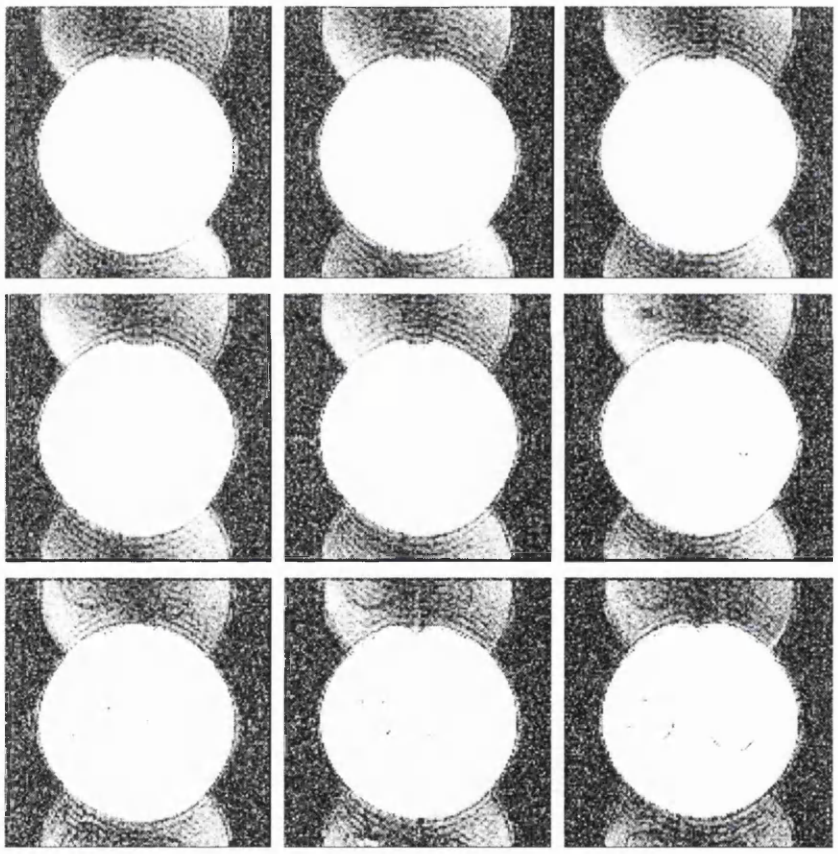

Figure 5.13.

Figure 5.13. Images from a phantom acquired in the same slice positions as in Fig. 5.11b, but using a correction method based on three non-phase-encoded echo (Heid, 1997). When this correction is used, the shift in the axis of symmetry of the ghost is eliminated and the ghost is symmetric for all the slices.

On other MR systems the pattern of interference may be different from that described in this study, with different consequences for the resulting ADC measurements. However, the potential corruption of quantitative diffusion data by Nyquist ghost signals is a general phenomenon which should be considered in all EPI-based diffusion studies. In practice, low ADC values that result from a genuine reduction in brain water ADC would usually have a corresponding hyperintensity on the diffusion-weighted images. Consequently, the presence of the artefacts described in this study could often be recognised with reference to the original EPI images; this emphasises the dangers of relying solely on calculated ADC maps without considering the appearance of signal in the base images. However, in other circumstances, such as in the calculation of the full diffusion tensor (Pierpaoli et al., 1996), it may not be possible to identify other manifestations of these artefacts. In general, the removal of such artefacts will increase the reliability of image interpretation, which is essential if quantitative diffusion studies are to be used in clinical investigations.

5.5 APPENDIX

In this appendix, analytical expressions for the interference between the image and the ghost are developed.

5.5.1 Interference between ghost and image

If there is no Nyquist ghost in the image, the relationship between the signal intensity and the ADC will be given by:

$$S_i = S_0 e^{-bADC_i} \qquad \text{for} \quad i = x, y, z \tag{5.6}$$

where S_i is the signal intensity for the DW images with diffusion gradients along the x, y or z axis, S_0 is the unweighted image (b-value = 0), and ADC_i is the ADC values along the x,y or z directions. Therefore, the average ADC can be written as:

$$ADC_{AV} = \frac{1}{3}\sum_i ADC_i = \frac{1}{3b}\sum_i \ell n\left(\frac{S_0}{S_i}\right). \tag{5.7}$$

On the other hand, in the presence of an overlapping Nyquist ghost, the signal intensities would be modified. In our case, the effect is mainly a modification of the signal intensity in the unweighted image, that is, the new signal intensity (S_0^*) is

$$S_0^* = \xi S_0 \tag{5.8}$$

with ξ a positive number less than 1 for a destructive interference (as in the *in vivo* data shown in this chapter) and greater than 1 for constructive interference. Therefore, the calculated ADC (ADC^*) will be

$$ADC_{AV}^* = \frac{1}{3}\sum_i ADC_i^* = ADC_{AV} + \frac{1}{b}\ell n(\xi) \tag{5.9}$$

Figure 5.A1 shows the percentage error in the calculated average a ADC as a function of ξ, for b-values of 400, 600, 800 and 1000 s/mm^2, and a 0.80 x 10^{-3} mm^2/s ADC_{AV}. This figure shows that large errors are introduced even for small signal intensity changes due to interference. For example, a 10% reduction in signal intensity in the unweighted image (ξ=0.9) produces a 22% error in the ADC_{AV} for the b-value used in this chapter. As expected from Eq. (5.9), the effect becomes more important the smaller the b-value used. If an error larger than 10% were considered unacceptable, the reduction in signal intensity should be less than 5%. For the extreme case of a 180° phase difference between overlapping 'parent' and 'ghost' images (complete destructive interference), this 5% reduction in the signal of white matter would require a ghost/image ratio for the orbit

(or CSF) of less than ~1.5% (ghost/CSF = $0.05S_0^{(WM)}/3.70S_0^{(WM)} = 0.013$, for the typical values of relative signal intensity between the orbit (or CSF) and white matter of ~370%, as mentioned in the Introduction).

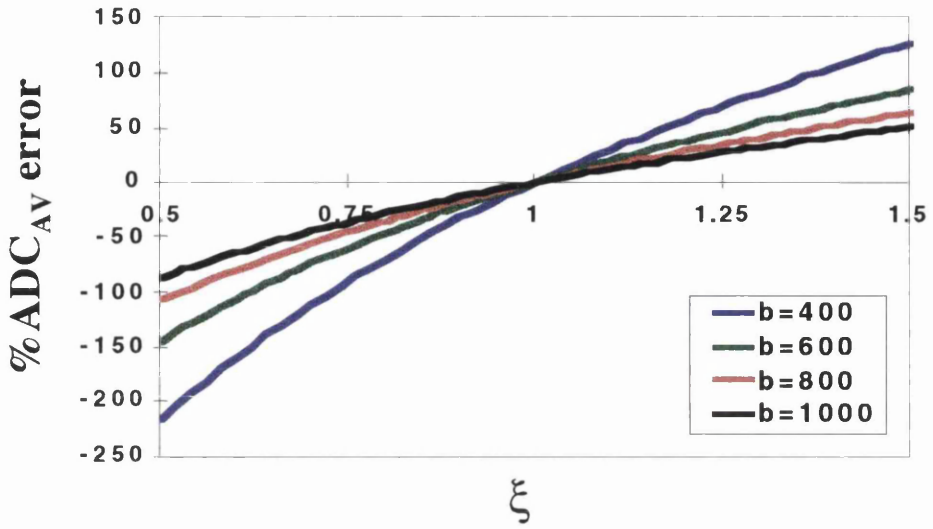

Figure 5.A1.

Figure 5.A1. Percentage error in the calculated average ADC as a function of ξ (see Eq. (5.9)). Four different *b*-values were used: 400 s/mm^2 (blue), 600 s/mm^2 (green), 800 s/mm^2 (red), and 1000 s/mm^2 (black), and a 0.80 x 10^{-3} mm^2/s ADC_{AV} was assumed.

5.5.2 Nyquist ghost interference with $b_{min} \neq 0$

When two *b*-values greater than zero are used for the calculation of the ADC, the expression for the average ADC in the absence of ghost is:

$$ADC_{AV} = \frac{1}{3}\sum_i ADC_i = \frac{1}{3(b_{\max} - b_{\min})}\sum_i \ell n\left(\frac{S_i(b_{\min})}{S_i(b_{\max})}\right). \qquad (5.10)$$

If there were a ghost contribution, the measured DW signal intensities would be:

$$S_i^*(b_{\min}) = \xi_i S_i(b_{\min})$$
$$S_i^*(b_{\max}) \approx S_i(b_{\max}) \tag{5.11}$$

where $i = x$, y or z, and it is assumed that the b_{max} is large enough to attenuate the signal intensity from the orbits (or CSF), making the contribution from the ghost negligible for the maximum diffusion-weighting.

In this case, the error in the calculated average ADC would be:

$$ADC_{AV}^* - ADC_{AV} = \frac{1}{3(b_{\max} - b_{\min})} \ell n(\xi_x \xi_y \xi_z) \tag{5.12}$$

Figure 5.A2 shows the percentage error in ADC_{AV} as a function of (b_{max}-b_{min}) for different values of ξ_i. It can be seen that the smaller the ξ_i (more interference), the larger the error, and the underestimation becomes more important the smaller the difference in b-values. For example, if an error larger than 10% were considered unacceptable, the b-values should be separated at least 640 s/mm^2 for ξ_i = 0.95 (5% reduction in the signal intensity), and 1300 s/mm^2 for ξ_i = 0.90 (10% decrease in signal intensity). As mentioned in the *Discussion* (section 5.4), the b_{min} should be larger than 150 s/mm^2 (ξ~0.86 for the ~150 s/mm^2 b-value used in Fig. 5.5b) and, therefore, b_{max} becomes too large for typical clinical systems.

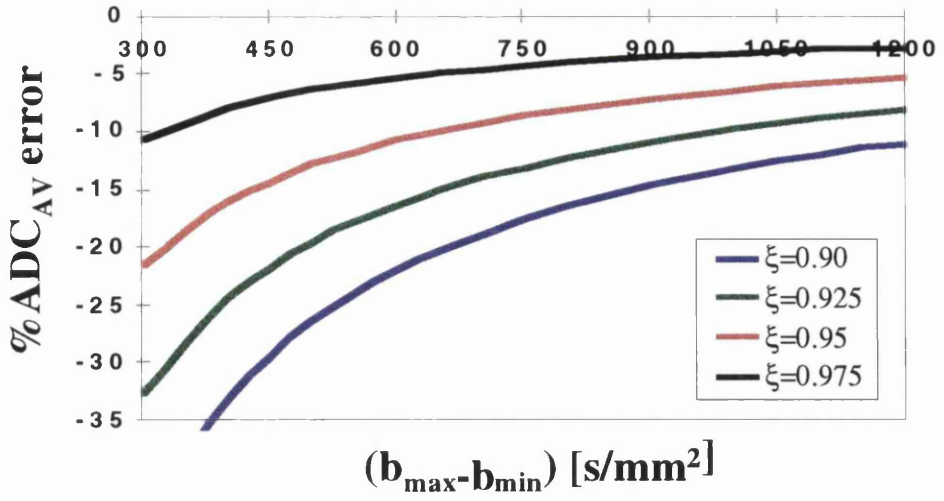

Figure 5.A2

Figure 5.A2 Dependency of the $\%ADC_{AV}$ error on the distance between *b*-values (b_{max}-b_{min}). Four different values of ξ_i are plotted: 0.90 (blue), 0.925 (green), 0.95 (red), and 0.975 (black). The smaller the ξ_i (more interference) the larger the error, and the underestimation becomes more important the smaller the difference in *b*-values is chosen.

5.5.3 Interference as a function of the ghost/image ratio

The interference between the image (e.g., white matter) and the overlapping ghost (Nyquist ghost from the orbit or CSF) will modify the signal intensity in the image as:

$$S^*_{WM} = \left\| S_{WM} + S_{ghost} \right\| = \sqrt{(S_{WM})^2 + (S_{ghost})^2 + 2S_{WM}S_{ghost}\cos(\phi)} \qquad (5.13)$$

where the parallel vertical bars represent the amplitude of the complex number, and ϕ the phase difference between the overlapping parts of the image (S_{WM}) and the ghost (S_{ghost}).

For a given ghost/image ratio (GIR) the signal intensity in the ghost will be given by

$$S_{ghost} = GIR \cdot S^{(\alpha)} \qquad (5.14)$$

where α = 'orbit' or 'CSF' (depending on the source of the Nyquist ghost). Thus, Eq. (5.10) can be written as

$$ADC^{*}_{AV} = \frac{1}{3\Delta b}\sum_{i} \ell n\left(\frac{\sqrt{\left(S_i(b_{\min})\right)^2 + \left(GIR\cdot S^{(\alpha)}(b_{\min})\right)^2 + 2GIR\cdot S^{(\alpha)}(b_{\min})S_i(b_{\min})\cos(\phi)}}{S_i(b_{\max})}\right) \tag{5.15}$$

where $\Delta b=(b_{max}-b_{min})$, and it is assumed that the diffusion in the orbit and CSF is isotropic, that is, $S^{(\alpha)}$ is independent of the gradient direction *i*.

For the particular case of a 180° phase difference between overlapping 'parent' and 'ghost' images (complete destructive interference), Eq. (5.15) can be simplified to

$$\begin{aligned} ADC^{*}_{AV} &= ADC_{AV} + \frac{1}{3(b_{\max}-b_{\min})}\sum_{i} \ell n\left(1-\frac{GIR\cdot S^{(\alpha)}(b_{\min})}{S_i(b_{\min})}\right) \\ &= ADC_{AV} + \frac{1}{3(b_{\max}-b_{\min})}\sum_{i} \ell n\left(1-GIR\frac{S_0^{(\alpha)}}{S_0}e^{-b_{\min}(ADC_{\alpha}-ADC_i)}\right) \end{aligned} \tag{5.16}$$

Figure 5.A3 shows the percentage error in the calculated average ADC as a function of $(b_{max}-b_{min})$ for different values of b_{min} (0, 100, 200, and 300 and s/mm^2) and GIR (0.025, 0.05, and 0.075). The signal intensity ratio between orbit (or CSF) and white matter was assumed to be 3.7, the ADC_α 3.0 x 10^{-3} mm^2/s, and two white matter 'fibres' were considered as extreme cases: an isotropic 'fibre' (with ADC_{WM}=0.80 x 10^{-3} mm^2/s for each direction *i*), and a cylindrical 'fibre' ($ADC_x=ADC_y$=0.30x10^{-3} mm^2/s and ADC_z=1.80x10^{-3} mm^2/s). The percentage error increases rapidly with increasing GIR, and is more relevant with smaller b_{min}. For example, for a GIR=0.05, even a b_{min}= 300 s/mm^2 would require a Δb= 1200 s/mm^2 for a percentage error in ADC_{AV} less than 10%. The results are almost indistinguishable for the two 'fibre' geometries studied, with the anisotropic case producing slightly larger errors for increasing b_{min}.

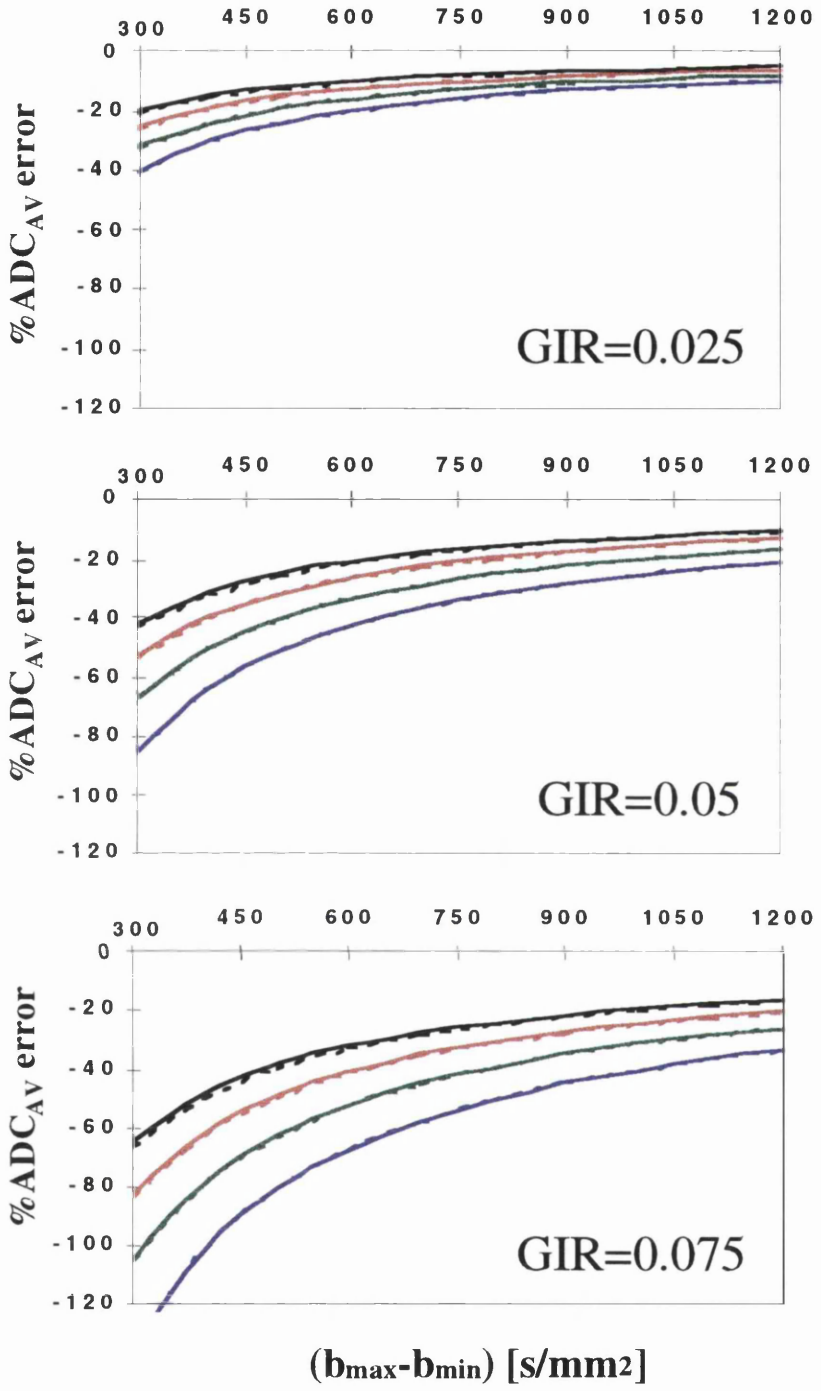

Figure 5.A3

Figure 5.A3 Percentage error in the calculated average ADC as a function of (b_{max}-b_{min}) for different values of GIR: 0.025 (top) , 0.05 (middle), and 0.075 (bottom). Four different b_{min} were plotted: 0 s/mm^2 (blue), 100 s/mm^2 (green), 200 s/mm^2 (red), and 300 s/mm^2 (black). The signal intensity ratio between orbit (or CSF) and white matter was assumed to be 3.7, the ADC_α 3.0 x 10^{-3} mm^2/s, and two white matter 'fibres' were considered as extreme cases (see *Appendix* (Section 5.5.3)): an isotropic 'fibre' (solid lines), and a cylindrical 'fibre' (dotted lines). The percentage error increases rapidly with increasing GIR, and is more relevant with smaller b_{min}.

6. Delay and dispersion effects in DSC-MRI: simulations using Singular Value Decomposition

6.1 INTRODUCTION

The model for dynamic-susceptibility contrast MRI (DSC-MRI) quantification described in Chapter 2 (Section 2.3.2.2.1) assumes that there is no delay or dispersion of the bolus between the site where the arterial input function (AIF) is measured and the most distant tissue; that is, the model assumes that the AIF reflects the *exact* input to the tissue. However, as mentioned in Section 2.3.2.2.2, the AIF is typically estimated in a major artery such as the middle cerebral artery (MCA), and this single measurement is usually used as the AIF for the whole brain. Therefore, delay and dispersion can be present, and the quantification using the model described in Section 2.3.2.2.1 may be inaccurate. Such delay and dispersion occur primarily in patients with cerebrovascular diseases, but they may also be present in healthy volunteers (Østergaard et al., 1998a), and it has been suggested that the transit time can be tissue dependent, with a longer time for white matter than grey matter (Jackson et al., 1998; Zhu et al., 1999).

This chapter describes the simulations performed to evaluate the effect of delay and dispersion on the quantification of DSC-MRI data using singular value decomposition (SVD).

6.2 METHODS

6.2.1 Simulations

Two different approaches for performing DSC-MRI simulations are possible. Both rely on model assumptions for the shape of the AIF and/or the concentration time curve, but they differ in the way the effect of the noise is simulated. In one of these approaches, the so-called Monte Carlo simulations, the noise is introduced into the simulated data by adding, for example, random Gaussian noise to generate different data sets for a given signal-to-noise ratio (SNR). This procedure is repeated many times (typically ~1000 times), and mean values for the desired parameters are calculated. In the other approach, samples of real noise are obtained, and then added to the simulated data. This second approach was chosen for the simulations described here since it makes no assumption regarding the noise distribution, and it can be directly compared to our real data.

The following sections describe the simulation of the AIF, the tissue concentration time course, the effect of delay and/or dispersion, and the generation of the image data sets.

6.2.1.1 Simulated AIF

Simulations were performed using AIFs with a shape and size that typically could be obtained using a standard injection scheme. This was done by adjusting the parameters of a gamma-variate function

$$C_a(t) = \begin{cases} 0 & t \le t_0 \\ C_0 (t - t_0)^r e^{-(t-t_0)/b} & t > t_0 \end{cases} \qquad (6.1)$$

to resemble the averaged arterial bolus size and shape observed in large vessels in typical human studies. The gamma-variate function has four free parameters to adjust the desired bolus AIF: C_0 is a scaling factor, r determines the rate of initial rise of the function, b the subsequent decay, and t_0 (usually called 'bolus arrival time', BAT), determines the time at which the bolus arrives at that region. If the bolus is injected at t=0, t_0 represents the delay of arrival (see below).

The gamma-variate function is typically used to fit the AIF and/or the tissue signal to eliminate the presence of signal change resulting from contrast recirculation. In our simulations, the contribution of recirculation was not included in the data. Since long delays and large dispersions were simulated, the presence of recirculation would have complicated the determination of the individual contributions to the error.

Since the injected dose is proportional to body weight, the amount of injected contrast agent is much smaller in children than in adults. Furthermore, the heart rate in children is faster. Therefore, much narrower peaks are usually observed in DSC studies in children. For these reasons, two different AIFs were used in the simulations: one that reflected typical data in children ($C_a^{(child)}$), and the other data in adults ($C_a^{(adult)}$). The measured $C_a^{(child)}$, together with the corresponding gamma-variate function, can be seen in Fig. 6.1. The values used were representative of typical data-sets obtained at the Great Ormond Street Hospital for Children (GOSH):

$$C_a(t) \propto \begin{cases} 0 & t \le 12 \\ (t-12)^{3.26} e^{-(t-12)/1.02} & t > 12 \end{cases} \qquad (6.2)$$

Figure 6.1 also shows the gamma-variate function for the $C_a^{(adult)}$, which was obtained from published values from normal volunteers participating in a clinical test (Østergaard et al., 1996a):

$$C_a(t) \propto \begin{cases} 0 & t \le 12 \\ (t-12)^{3.0} e^{-(t-12)/1.5} & t > 12 \end{cases} \tag{6.3}$$

The scaling factors in Fig. 6.1 were arbitrarily chosen for comparison purposes. As expected, a much wider peak can be seen for the adult case.

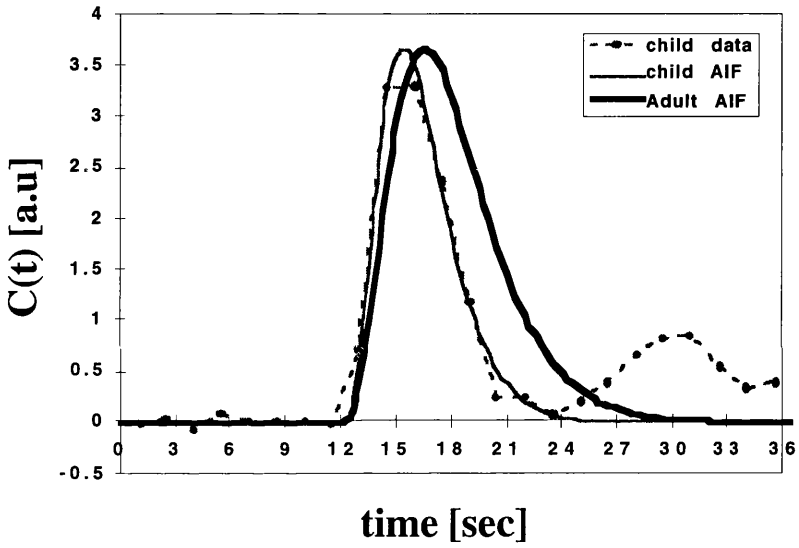

Figure 6.1.

Figure 6.1. Typical AIF data from a child (dotted line), together with the corresponding gamma-variate fitting as shown in Eq. (6.2) (solid line). The bold solid line shows the gamma-variate function used as a representative case for adult data (Eq. (6.3)).

6.2.1.2 Simulation of the noise contribution

As mentioned above, instead of simulating the noise contribution as a Gaussian distribution, real data-sets of noise were acquired using the same sequence as that used for the perfusion measurements. The manufacturer's standard spherical head phantom

was used, together with a cylindrical loading ring. This ring is designed to load the coil to a similar level to that found *in vivo*. The slices were positioned outside the phantom, and since amplitude data were used, a constant offset was added to the complex data to preserve the noise distribution (see Fig. 6.2). In this way, both the noise distribution within an image and between images in the data-set (i.e., the noise in the time course for each pixel) reflected typical noise found in real DSC-MRI measurements. Figure 6.2 shows 5 images from the set of 50, and the time course for a 3x3 region of interest (ROI).

6.2.1.3 Simulated tissue signal (C(t))

For the simulation of the tissue data set, Eq. (2.22) from Section 2.3.2.2.1 (Chapter 2) was used with the simulated AIF and a residue function R(t). This method requires the assumption of a given model for the tissue. A well known model is the use of an exponential decay as a general model for the residue function. This is based on a simple model of the vasculature bed as one single, well-mixed compartment (Bassingthwaighte and Goresky, 1984; Lassen et al., 1984). Then, as a first-order model, a single exponential function is used to describe the residue function:

$$R(t, MTT) = e^{-t/MTT} \tag{6.4}$$

According to Eq. (2.22) from Section 2.3.2.2.1, the simulated tissue signal will be given by

$$\begin{aligned} C(t) &= F\int_{t_0}^{t} C_0(\tau - t_0)^r e^{-\frac{(\tau - t_0)}{b}} e^{-\frac{(t-\tau)}{MTT}} d\tau \\ &= FC_0 e^{-\left(\frac{t}{MTT} - \frac{t_0}{b}\right)} \int_{t_0}^{t} (\tau - t_0)^r e^{-\tau\left(\frac{1}{b} - \frac{1}{MTT}\right)} d\tau \end{aligned} \tag{6.5}$$

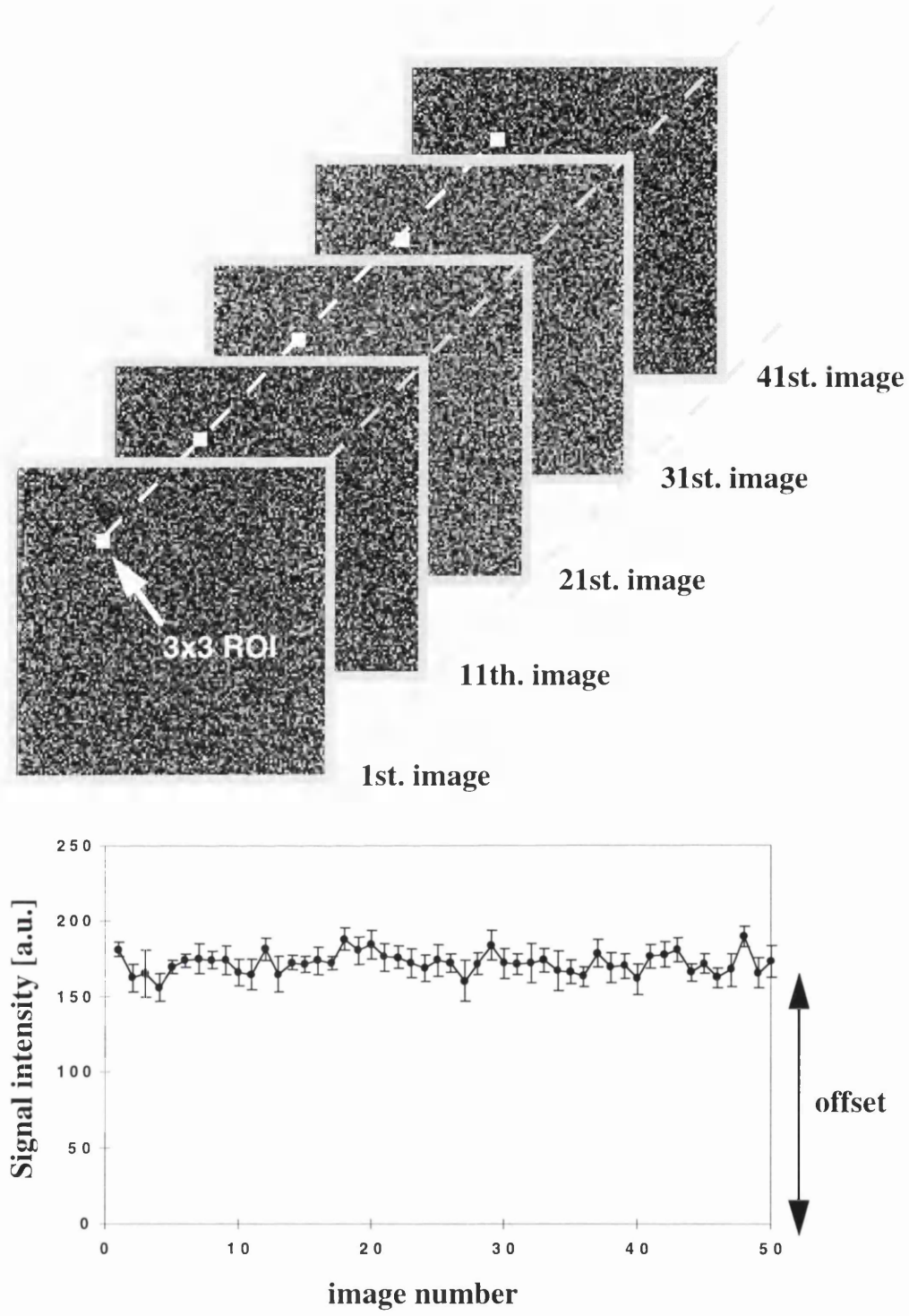

Figure 6.2.

Figure 6.2. Noise data set used in the simulations. Top: five representative images from the set of 50. Bottom: time course for a 3x3 ROI (shown as a white square box in the images). The error bars represent the ±SD within the ROI. Notice the offset added to the data to preserve the noise distribution.

For simplicity, a value of 1 for ρ and k_H is assumed throughout the rest of the simulations.

By making the appropriate change of variables, an analytical expression can be obtained for the above integral, for the case of b<MTT:

$$\begin{aligned} C(t) &= FC_0 e^{-(t-t_0)/MTT}\left(\frac{1}{b}-\frac{1}{MTT}\right)^{-(r+1)}\int_0^{(t-t_0)(1/b-1/MTT)}\xi^r e^{-\xi}d\xi \\ &= FC_0 e^{-(t-t_0)/MTT}\left(\frac{1}{b}-\frac{1}{MTT}\right)^{-(r+1)}\Gamma(r+1)\cdot\Gamma_I\left(r+1,(t-t_0)(1/b-1/MTT)\right) \end{aligned} \tag{6.6}$$

where $\Gamma(x)$ is the Gamma function

$$\Gamma(x)=\int_0^\infty \xi^{x-1}e^{-\xi}d\xi, \tag{6.7}$$

and $\Gamma_I(a,x)$ is the incomplete Gamma function:

$$\Gamma_I(a,x)=\frac{\int_0^x \xi^{a-1}e^{-\xi}d\xi}{\Gamma(a)}. \tag{6.8}$$

The scaling factor C_0 can be determined from the desired peak drop in the simulated signal intensity. According to Eq. (2.25) in Section 2.3.2.2.2, the drop in signal intensity will be given by

$$\Delta=\frac{\Delta S}{S_0}=\frac{S_0-S_{\min}}{S_0}=1-e^{-\kappa C_{\max}TE} \tag{6.9}$$

where S_0 and S_{min} are the baseline and minimum signal intensities respectively, C_{max} is the maximum concentration, and κ is a proportionality constant (Section 2.3.2.2). Assuming

κ=1 for the simulations, and typical signal drops (from GOSH data and Østergaard et al (1996a)) for grey matter (Δ_{gm}=40%) and white matter (Δ_{wm}=17%), the peak concentration will be (for the 101 ms TE used at GOSH):

$$C_{max} = \begin{cases} 5.11 & \text{gray matter} \\ 1.86 & \text{white matter} \end{cases} \tag{6.10}$$

Figure 6.3 shows simulated concentration time curves using Eq. (6.6) with a TR=1.5 s, for different flow values for grey (a) and white matter (b). For the final simulation of delay and dispersion effects, the values indicated in Table 6.1 were chosen as representative of typical values for CBF, CBV, and MTT (MTT=CBV/CBF) for grey and white matter (Schreiber et al., 1998; Rempp et al., 1994; Koshimoto et al., 1999; Calamante et al., 1999). The corresponding concentration time curves are shown in blue in Fig. 6.3.

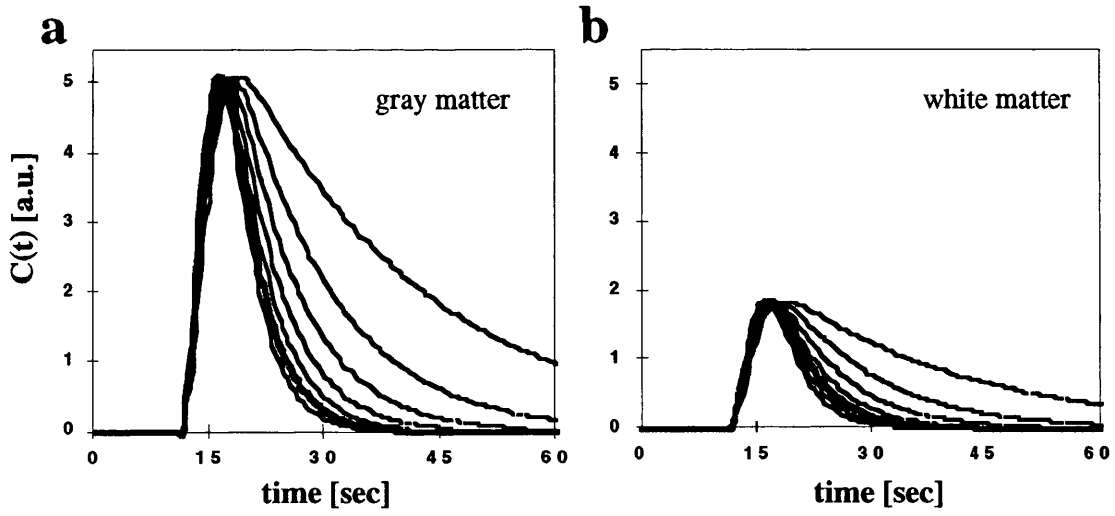

Figure 6.3.

Figure 6.3. Simulated concentration time curves without delay or dispersion (Eq. (6.6)) with a TR=1.5 s, for different flow values. (a) Grey matter (10-70 ml/100g/min). (b) White matter (5-35 ml/100g/min). The curves shown in blue correspond to the values used in the subsequent simulations of delay and dispersion.

Table 6.1.

Tissue type	CBF [ml/100g/min]	CBV [ml/100g]	MTT [sec]
grey matter	60	4	4
white matter	25	2	4.8

Table 6.1. Values of CBF, CBV and MTT assumed for the simulation of the tissue signal intenstity.

The time concentration curves were then converted to the simulated MRI signal intensity time curves by using the single exponential relationship

$$S(t) = S_0 e^{-\kappa C(t) TE} \tag{6.11}$$

where the baseline S_0 was scaled to the real noise data according to typical *SNR* values obtained *in vivo* at GOSH (SNR_{gm}=36 and SNR_{wm}=30):

$$S_0 = SNR \cdot SD_{noise} \tag{6.12}$$

and SD_{noise} was determined from the real noise data.

6.2.1.4 Simulation of delay and dispersion

Since it is not possible in practice to measure the *true* AIF (C_a) for each pixel, this is usually estimated from a major vessel, such as the MCA. Therefore, as mentioned in the Introduction (Section 6.1), the *estimated* AIF ($C_a^{(est)}$) may undergo delay and/or dispersion during its passage from the point of measurement (MCA) to the particular pixel of tissue.

A delay can be easily simulated by increasing the bolus arrival time (t_0 replaced by $t_0+\delta t_0$), which effectively shifts the concentration time curve (Fig. 6.4).

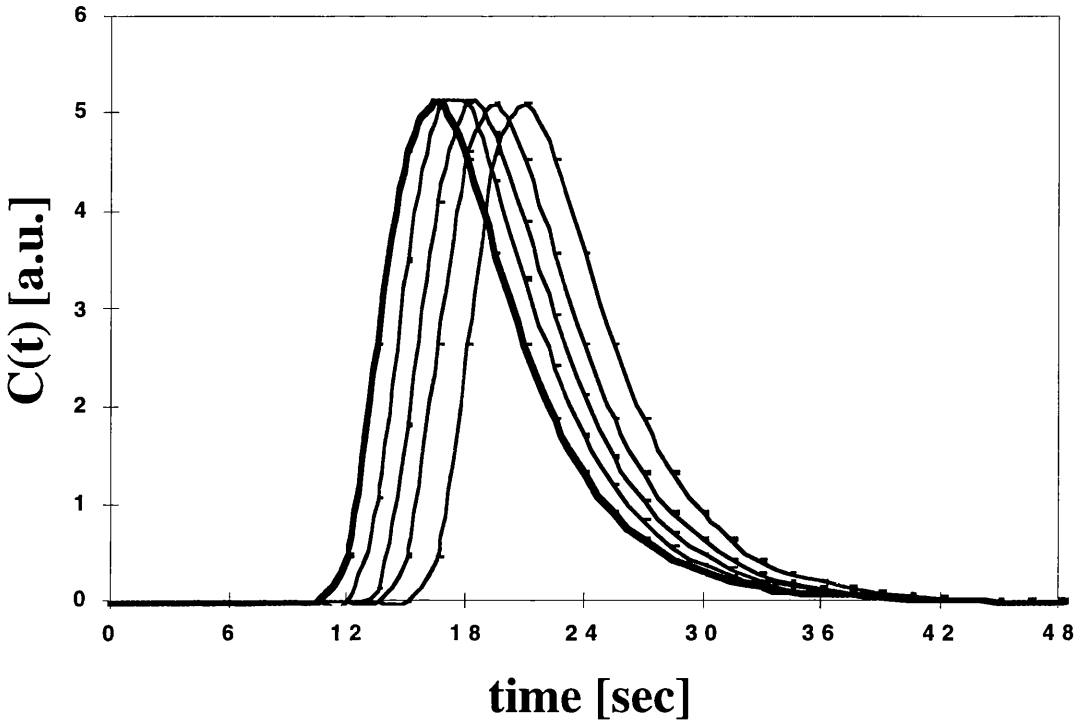

Figure 6.4.

Figure 6.4. Simulated tissue concentration time curve (child case) for different delay values. The bold curve shows the case without delay, while the other curves were simulated with delays of 1.0, 2.0, 3.0 and 4.5 s. As can be seen, the simulated delay simply shifts the curve to the right.

The dispersion can be described in terms of a transport function. Since the transport function gives the probability distribution for each transit time (see Section 2.3.2.2.1), the dispersion can be described mathematically as a convolution with a vascular transport function $h^*(t)$ from the site of measurement to the given pixel, i.e.

$$C_a(t) = C_a^{(est)}(t) \otimes h^*(t) \tag{6.13}$$

with the resulting tissue concentration expressed as:

$$\begin{aligned} C(t) &= F \cdot C_a(t) \otimes R(t) = F \cdot \left(C_a^{(est)}(t) \otimes h^*(t)\right) \otimes R(t) = \\ &= F \cdot C_a^{(est)}(t) \otimes \left(h^*(t) \otimes R(t)\right) \end{aligned} \tag{6.14}$$

Therefore, it is equivalent to a convolution of the estimated AIF with an effective residue function (Østergaard et al., 1996a): $R^{(eff)} = h^* \otimes R$.

The particular vascular transport function depends on several factors, such as the topology of the vasculature, the tissue type, the site where the AIF was estimated, CBV, etc. As a first approximation, the same assumption, namely a well-mixed compartment, was also used for the vasculature, and the transport function will be given by (see Eqs. (6.4) and the definition of the residue function (Section 2.3.2.2.1))

$$h^*(t) = -\frac{dR^*(t)}{dt} = \beta \cdot e^{-\beta t} \tag{6.15}$$

where $1/\beta$ corresponds to the effective "MTT" from the site of AIF measurement to the input to the particular pixel (see Eq.(6.4)). Therefore, the larger the $1/\beta$, the larger the dispersion, and in the limit of $1/\beta \to 0$, h^* tends towards the Dirac delta function.

With this model, the effective residue function will be

$$\begin{aligned} R^{(eff)}(t) &= \int_0^t \beta e^{-\beta(t-\tau)} e^{-\tau / MTT} d\tau \\ &= \frac{\beta}{\left(\frac{1}{MTT} - \beta\right)} \left(e^{-\beta t} - e^{-t / MTT}\right) \end{aligned} \tag{6.16}$$

Figure 6.5 shows the grey matter effective residue function for a range of values of $1/\beta$ together with the assumed single exponential model (Eq. (6.4)). As can be seen, with increasing dispersion the resemblance of effective residue function to the original single exponential $R(t)$ diminishes.

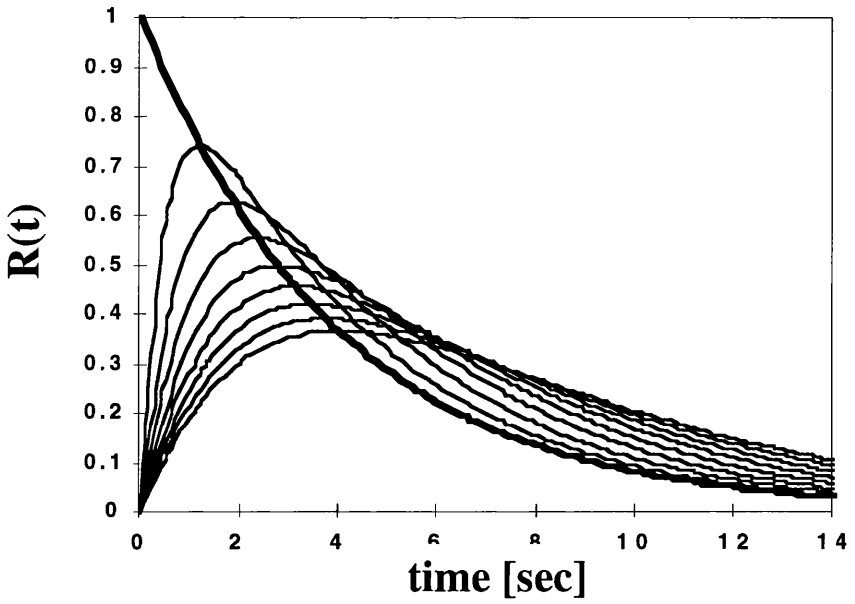

Figure 6.5.

Figure 6.5. Effect of dispersion on the residue function for grey matter. The bold line shows the case without dispersion (single exponential), while the rest of the curves show the effective residue function for a range of values of 1/β (0.5, 1.0, 1.5, 2.0, 2.5, 3.0, 3.5 and 4.0 s). Similar results are obtained for white matter.

The dispersed tissue concentration time curve will be given by the convolution in Eq.(6.14). For the case when b<MTT (valid for the parameters chosen in the simulations) and b<1/β, the following analytical expression can be obtained:

$$C(t) = \frac{\beta F C_0 \Gamma(r+1)}{\left(\frac{1}{MTT} - \beta\right)} \left[\frac{e^{-\beta(t-t_0)}}{\left(\frac{1}{b} - \beta\right)^{r+1}} \Gamma_I\left(r+1, (t-t_0)(1/b - \beta)\right) \right. \\ \left. - \frac{e^{-(t-t_0)/MTT}}{\left(\frac{1}{b} - \frac{1}{MTT}\right)^{r+1}} \Gamma_I\left(r+1, (t-t_0)(1/b - 1/MTT)\right) \right] \tag{6.17}$$

For the case when b>1/β, the second term is still the same (because b<MTT), but the first term needs to be evaluated by numerically solving the integral:

$$C(t)=\frac{\beta F C_0}{\left(\frac{1}{MTT}-\beta\right)}\left[\frac{e^{-\beta(t-t_0)}}{\left(\beta-\frac{1}{b}\right)^{r+1}}\int_0^{(t-t_0)(\beta-1/b)}\xi^r e^{\xi}d\xi\right.$$

$$\left.-\frac{e^{-(t-t_0)/MTT}}{\left(\frac{1}{b}-\frac{1}{MTT}\right)^{r+1}}\Gamma(r+1)\cdot\Gamma_I\left(r+1,(t-t_0)(1/b-1/MTT)\right)\right] \tag{6.18}$$

This dispersed tissue concentration is shown in Fig. 6.6 for a range of values of 1/β together with the original non-dispersed tissue curve. A clear spread of the peak and decreasing of its height can be seen with increasing dispersion (increasing 1/β).

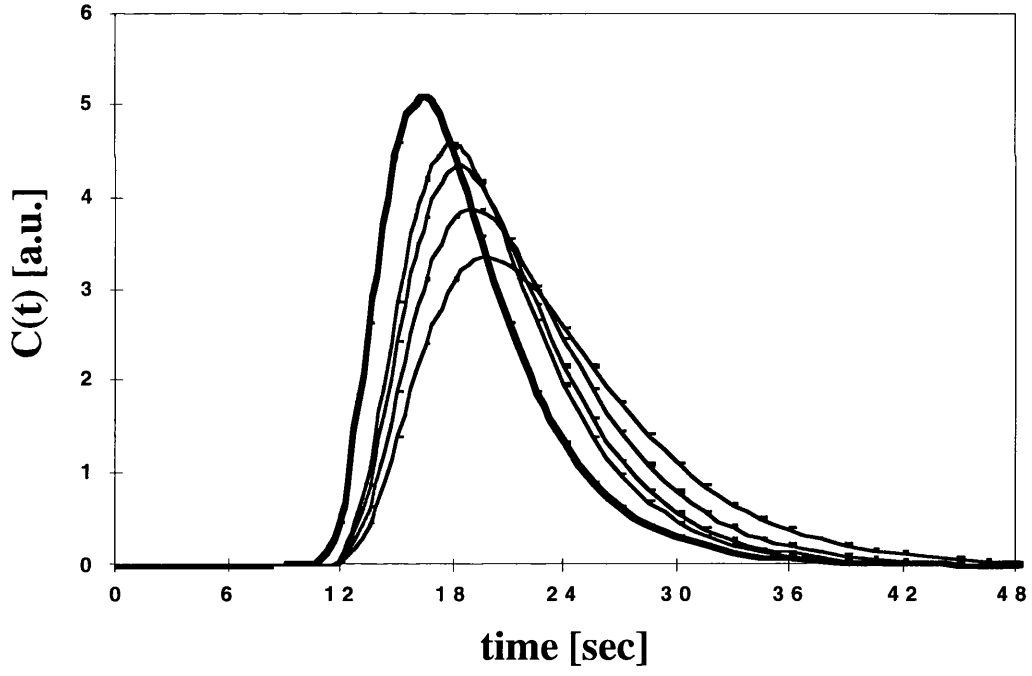

Figure 6.6.

Figure 6.6. Effect of dispersion on the tissue concentration for grey matter in the child case. The bold line represents the non-dispersed case (Eq. (6.6)), while the other curves show the concentration for a range of values of 1/β (1.5, 2.0, 3.0 and 4.5 s).

6.2.1.5 Simulation of image data set

For the generation of images, 4 different time courses were simulated:

A. Time course for a typical grey matter pixel (using Eq. (6.6) together with the grey matter values from Table 6.1).

B. Time course for a typical white matter pixel (using Eqs. (6.6) together with the white matter values from Table 6.1).

C. Time course for the delayed and/or dispersed grey matter pixel (using Eqs. (6.17) and (6.18)).

D. Time course for the delayed and/or dispersed white matter pixel (using Eqs. (6.17) and (6.18)).

Each of these time courses was added to one of the four quadrants of the images in the noise data-set (Fig. 6.7):

- Time course for a typical grey matter pixel → top left side of the image.
- Time course for a typical white matter pixel → bottom left side of the image.
- Time course for the delayed and dispersed grey matter pixel → top right side of the image.
- Time course for the delayed and dispersed white matter pixel → bottom right side of the image.

Before combining the time course of the pixels with the noise data, the positive offset added to the amplitude noise data (see *Simulation of the noise contribution* (Section 6.2.1.2)) was subtracted to bring the noise distribution back around its zero mean.

Therefore, this simulation creates a data-set of 50 images of 128x128 pixels, similar to the one obtained in a typical real DSC-MRI study. Each simulated image consists of four uniform regions (Fig. 6.7): two 'normal' regions (left side of the image) and two 'abnormal' regions (right side of the image). This simulated data-set was processed with the same software as that used for the real DSC patient data. By comparing the results

from corresponding regions from the images on the left and the right, the effect of different delays and/or dispersions can be evaluated.

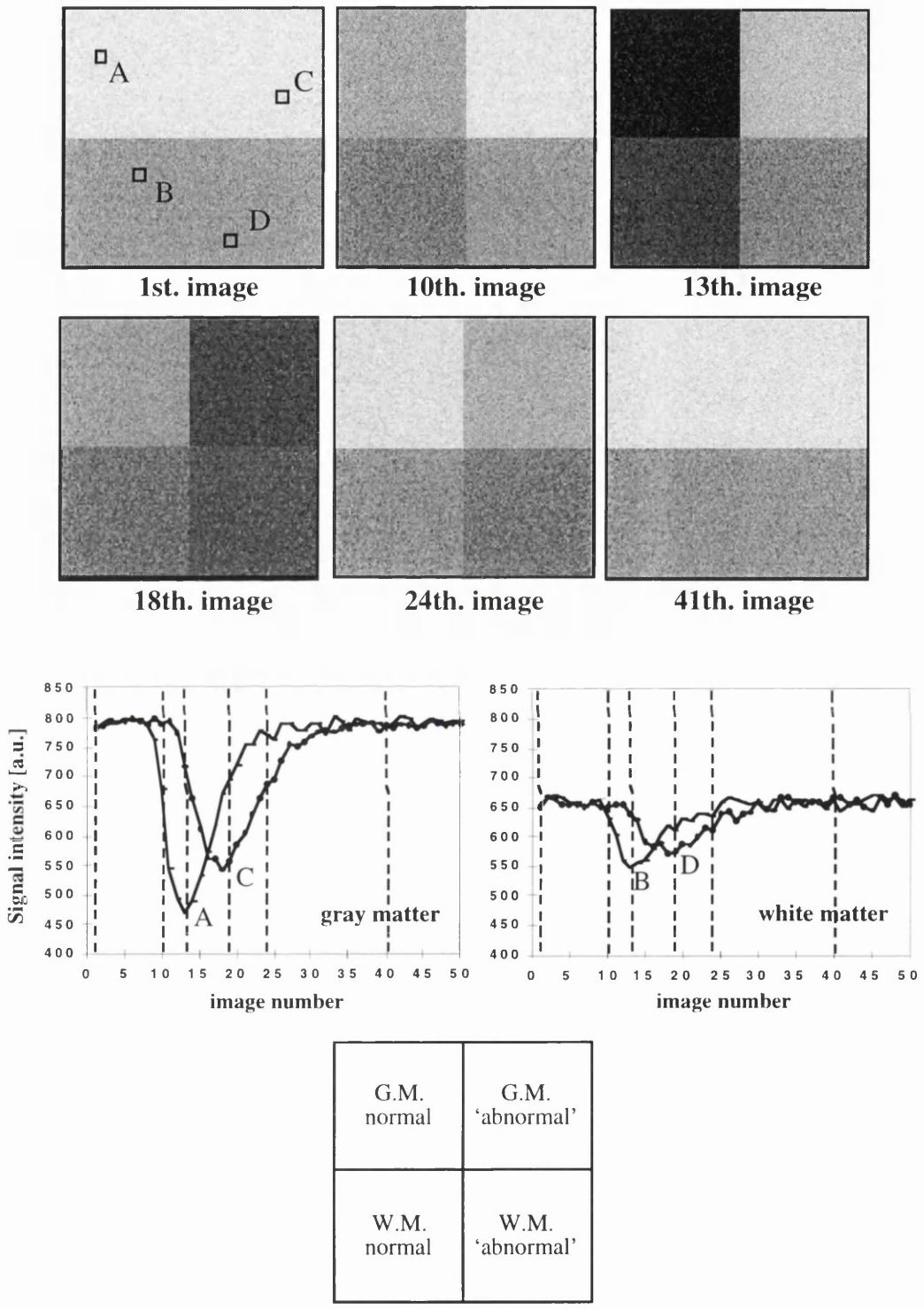

Figure 6.7.

Figure 6.7. Simulated images for the case of the adult data with a 3.0 s delay and $1/\beta$=4.5 s. The figure shows 6 representative images from the set of 50, as well as the time courses from four 3x3 ROIs (as shown by the squares in the 1st. image): region A

(grey matter without delay or dispersion), region B (white matter without delay or dispersion), region C (grey matter with 3.0 s delay and 4.5 s dispersion), region D (white matter with 3.0 s delay and 4.5 s dispersion). The vertical dotted lines in the time course graphs show the positions for the 6 images displayed.

6.2.2 Implementation of the simulations

The simulated data-sets were created using routines written with IDL software (RSI, Boulder, Colorado). A 3x3 uniform smoothing kernel was applied to the simulated raw image data before deconvolution (Østergaard et al., 1996a), and maps of CBF, CBV and MTT were calculated on a pixel by pixel basis. The SVD analysis of these data was performed using the *SVD_new* software written by Leif Østergaard (see *Appendix* (Section 6.5)). The simulations and SVD analysis were performed on a 170 MHz Sun UltraSparc.

The simulations were repeated for a range of delays between 0-6 s. From our experience, delays between 2-3 s are not uncommon in patients, and the 6 s delay limit was chosen to include all delays that we have observed in practice. For the dispersion, data were simulated with values of $1/\beta$ up to 6 s. This maximum effective "MTT" was taken as an extreme case. A combination of delay and dispersion within these ranges was simulated to evaluate their effect in the quantification of DSC data using SVD. A region of interest in each quadrant of the image was drawn, and the ratios of the 'abnormal' to the corresponding normal side were computed for each case. These are plotted as mean±SD over the ~3800 pixels in each region (62x62; the border 2 pixels in each quadrant are not included due to 3x3 kernel used for smoothing). In the absence of delay and dispersion the ratio would be 1, while a ratio <1 represents an underestimation, and a ratio >1 represents an overestimation of the corresponding parameters (CBF, CBV, or MTT) due to the presence of delay or dispersion. The SD of the ratio $y=x_1/x_2$ was calculated according to Armitage et al (1987) as:

$$SD_y^2 = \frac{SD_{x1}^2}{x_2^2} + \frac{x_1^2}{x_2^4} SD_{x2}^2 \qquad (6.19)$$

which is valid if x_2 (the 'normal' CBF, CBV or MTT value in the simulations) has a small coefficient of variation (typically 2-4% for grey matter, and 6-10% for white matter in practice).

6.3 RESULTS

6.3.1 Delay effects (without dispersion)

Figure 6.8 shows an example (delay = 3 s) of the time courses for typical 3x3 ROIs in each quadrant of the simulated images.

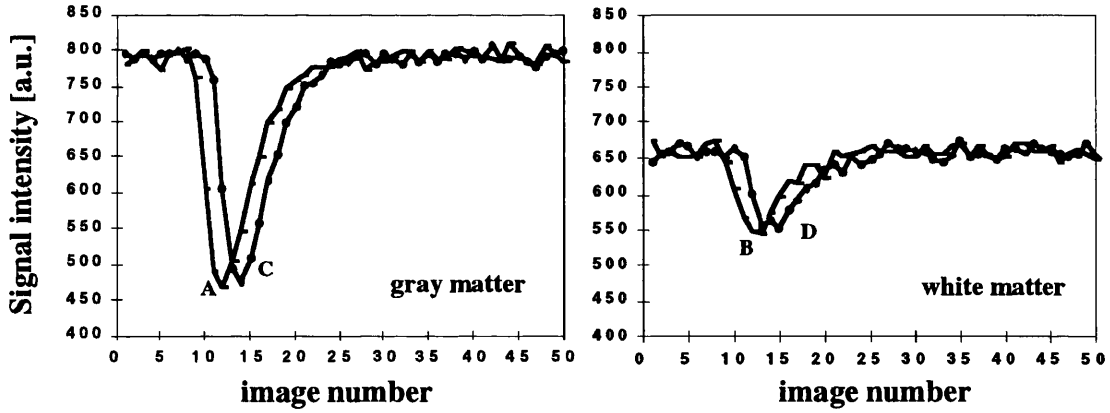

Figure 6.8.

Figure 6.8. Time courses for 4 typical 3x3 ROIs for simulated data with 3.0 s delay in the absence of dispersion. The 4 ROIs were defined in similar positions to those in Fig. 6.7.

The effect of the simulated delays on the quantification of DSC using SVD can be seen in Fig. 6.9. This figure shows the ratio of the value in the right region ('abnormal') to the value in the left region ('normal') for the three different parameters (CBF, CBV and

MTT). The three parameters are plotted, although only two of them are linearly independent (central volume theorem (Section 2.3.2.2.1)). Figure 6.9a shows the results for the data using the AIF for children (Eq. (6.2)), while Fig. 6.9b shows the equivalent results for the adult case (Eq. (6.3)). The behaviour is qualitatively similar for both adult and child cases, regardless of the tissue type. However, the error bars are larger for white matter due to its lower SNR.

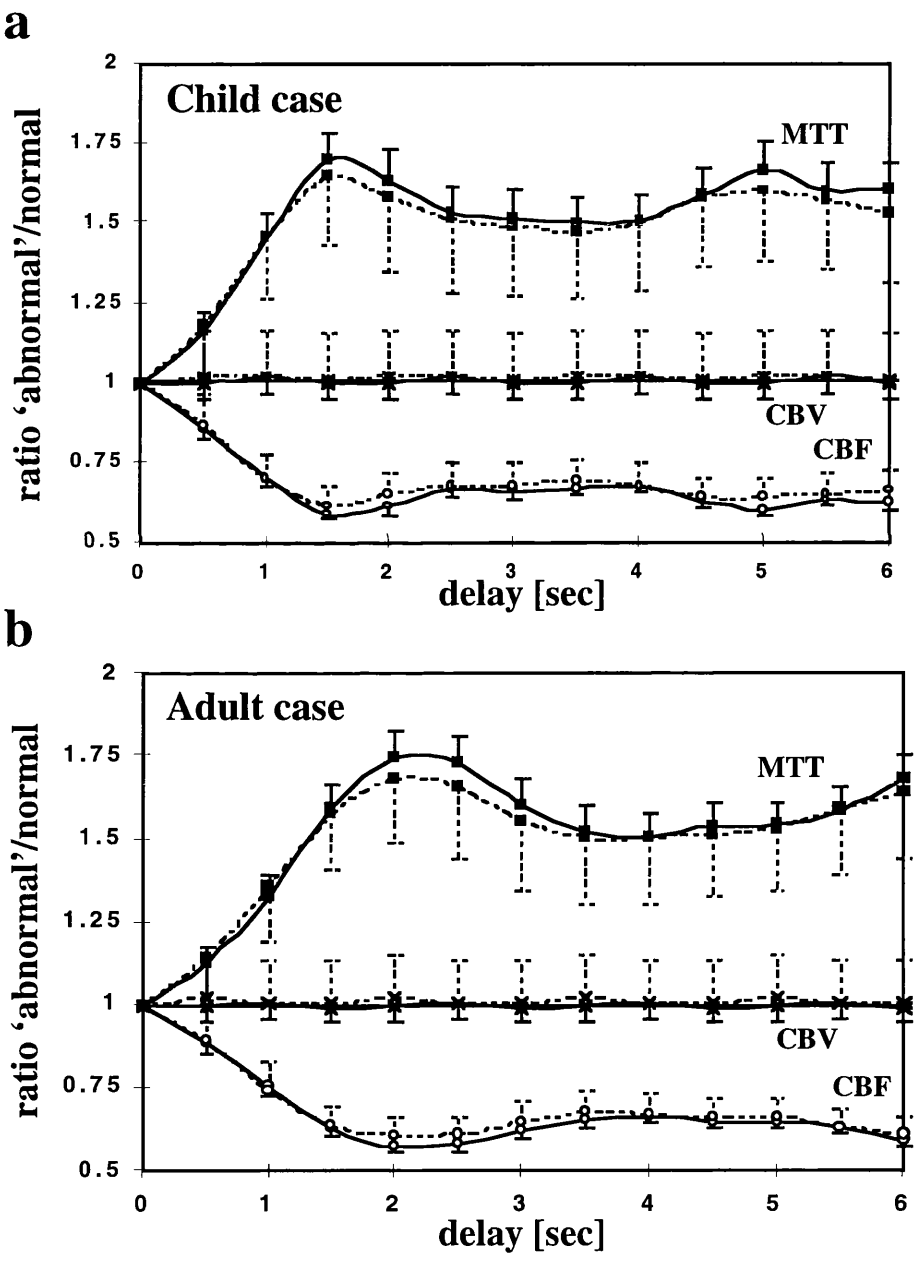

Figure 6.9.

Figure 6.9. Effect of delay (without dispersion) on the quantification of DSC-MRI data. The figures show the ratio of the value in the 'abnormal' side to the value in the

'normal' side. The solid lines represent the values for grey matter, while the dotted lines, the white matter cases. (a) Child case. (b) Adult case. CBF ratios are labelled with open circles, CBV ratios with crosses, and MTT ratios with filled squares. The error bars represent the SD of the ratio, and only one side of the error bars is displayed to avoid the superposition of the bars from grey and white matter.

As expected, the CBV (which is proportional to the area under the peak) is not affected by the simulated delay, since a delay only shifts the peak, without modifying its shape or size. On the other hand, the CBF is underestimated (ratio<1) but, interestingly, the flow ratio decreases approximate linearly until a delay of ~1.5-2.0 s, then oscillates around an asymptotic value of ~0.65, i.e., a 35% underestimation. Correspondingly, the MTT is overestimated, with the ratio increasing very rapidly until delays ~1.5-2.0 s, and oscillating around an asymptotic value of ~1.6 (i.e., an approximately 60% overestimation).

Figure 6.10 shows examples of calculated maps for simulated delays of 0.5, 1.0 and 1.5 s. The underestimation in CBF (decreased signal intensity in the right quadrant compared to the intensity in the corresponding left quadrant), and overestimation of the MTT (increased signal intensity) are clearly seen. On the other hand, the intensity in the CBV maps is approximately the same on both sides.

As described in the *Appendix* (Section 6.5), if there is a significant recirculation peak and a gamma-variate fit to the tissue data is not used to remove its contribution, a fixed time window for the analysis must be used. In this case, the first-passage peak would be shifted partly outside the window by the presence of a delay and its effect, in principle, can be much more important. This situation was simulated by fixing the upper limit for the window for the SVD analysis to the time when recirculation typically occurs (~14 s from the arrival of the bolus in the child case; see Fig. 6.11). The results of a fixed time window are shown in Fig. 6.12 for the data using the AIF for children. The most obvious effect is on the calculated CBV (cross symbols), which is underestimated, since the area within the selected window is less than the total area under the peak.

Interestingly, a fixed time window does not seem to modify the results for the CBF calculation (open circles) provided the maximum of the peak is within the window (delay ~7.5 s in Figs. 6.11 and 6.12). For longer delays, the CBF is further underestimated, because the part of the function inside the window is no longer in the form of a peak. However, such very long delays are unlikely to happen in real situations. For the MTT (filled squares), the initial overestimation is very quickly overcompensated by the fast decrease in CBV, therefore producing an underestimation for delays longer than ~4-5 s.

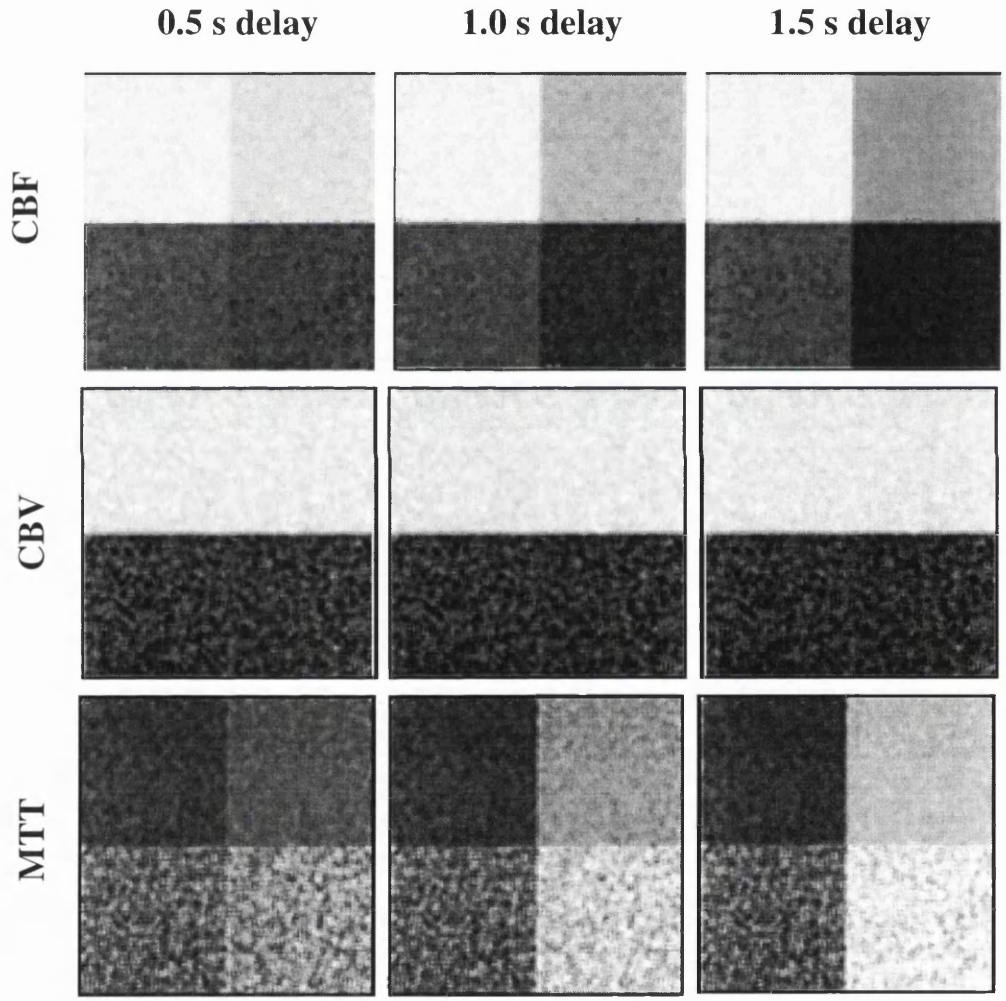

Figure 6.10.

Figure 6.10. CBF (top row), CBV (middle row) and MTT maps (bottom row) calculated using SVD in the presence of a delay = 0.5 s (left column), 1.0 s (middle column), and 1.5 s (right column).

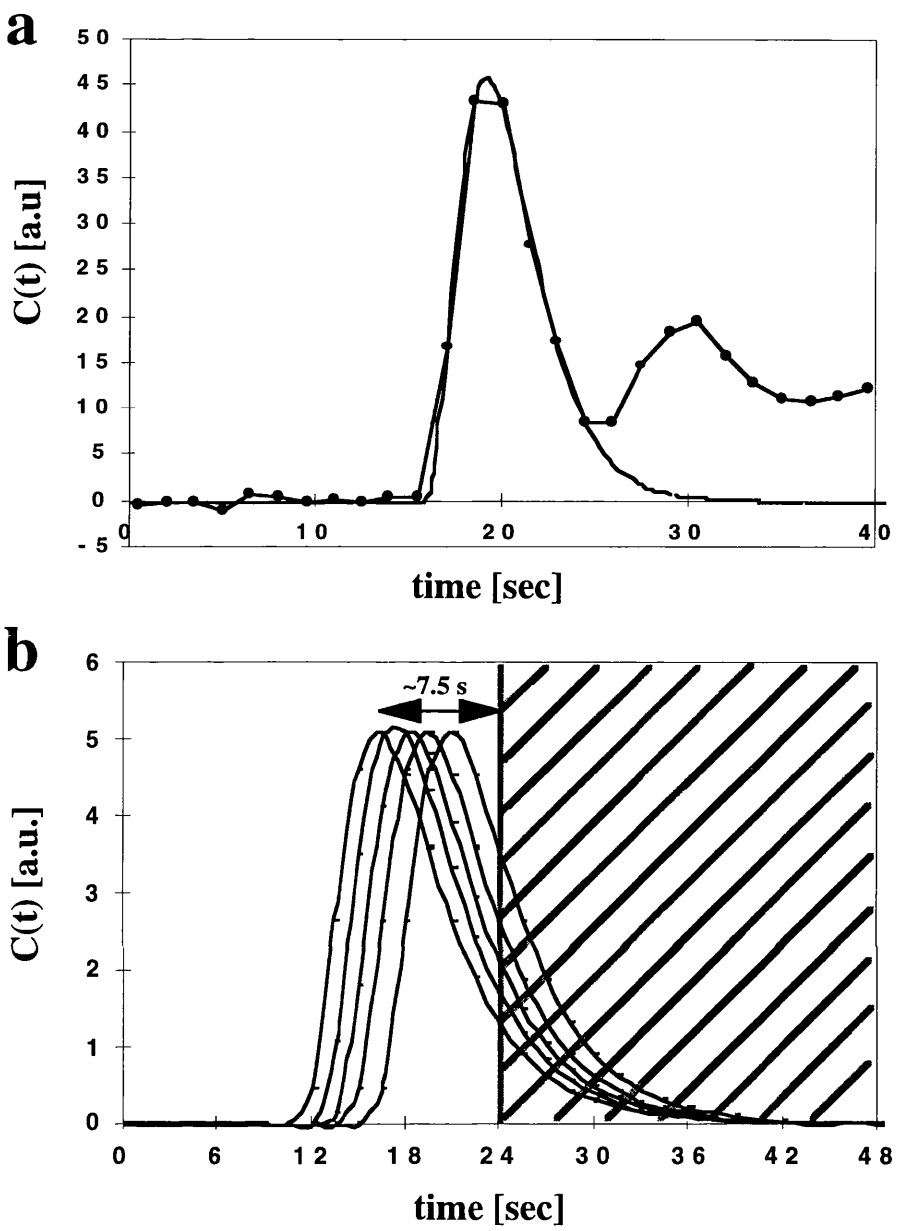

Figure 6.11.

Figure 6.11. (a) Concentration time curve for a typical data set with recirculation of the tracer obtained at GOSH. The filled circles represent the measured values, while the solid line the corresponding gamma-variate fitting. (b) Simulated concentration time course in the presence of a delay (see Fig. 6.4). The diagonal hatched area shows the part not included when the fixed time window was used in the SVD analysis. As can be seen, a delay longer than 7.5 s would move the maximum of the peak outside the window for analysis.

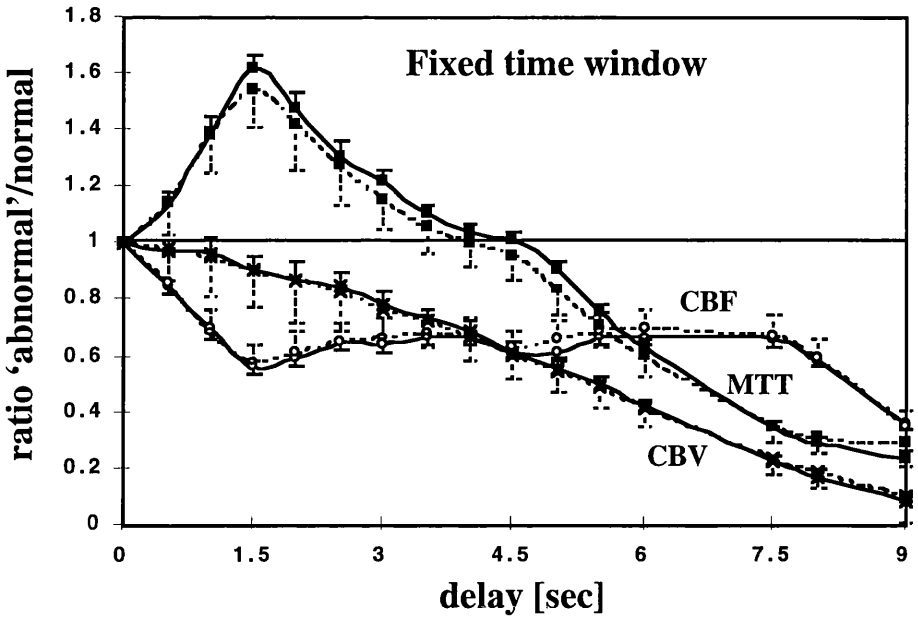

Figure 6.12.

Figure 6.12. Effect of delay (without dispersion) on the quantification of DSC-MRI data when a fixed time window is used for the SVD analysis. The figure shows the ratio of the value in the 'abnormal' side to the value in the 'normal' side for the child case. See legend of Fig. 6.9 for details.

As a real example of the effect of delay, Fig. 6.13 shows the DSC data from a 6 year old child who had a right internal carotid artery stenosis with probable dissection, and who presented with multiple episodes of transient ischaemic attacks. The CBF map (Fig. 6.13a) shows apparently reduced perfusion in the right hemisphere (left side of the image). Figure 6.13b shows the concentration time curves for two regions (one in each hemisphere). It can be seen that there is a delay of ~2 s in the arrival of the bolus to the right side, and although the peak is much wider, its height is similar to that on the left side. Given the simulation data presented in Fig. 6.9a, the CBF map shown in Fig. 6.13a is potentially misleading in that the presence of delay (and possibly dispersion) has introduced an approximately 40% underestimation in the perfusion quantification.

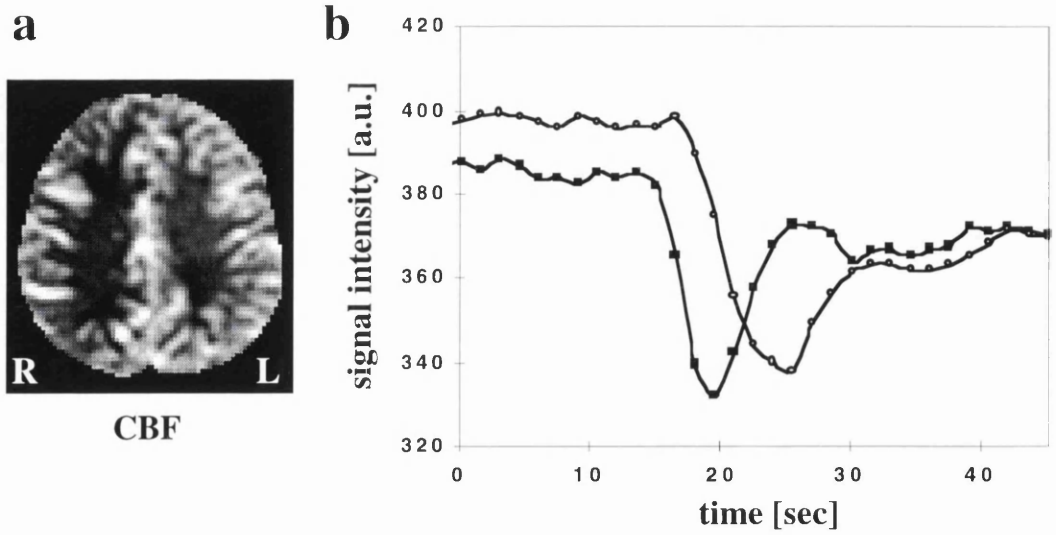

Figure 6.13.

Figure 6.13. DSC data from a 6 year old child who had a right internal carotid artery stenosis with probable dissection. (a) CBF map. (b) Signal intensity time curves for two regions (one in each hemisphere). A clear delay of ~2 s in the arrival of the bolus can be seen in the right side. The presence of such delay (and possibly dispersion) introduced a significant underestimation in the CBF map.

6.3.2 Dispersion effects (without delay)

Figure 6.14 shows an example ($1/\beta$ = 3 s) of the time courses for typical 3x3 ROIs in each quadrant of the simulated images.

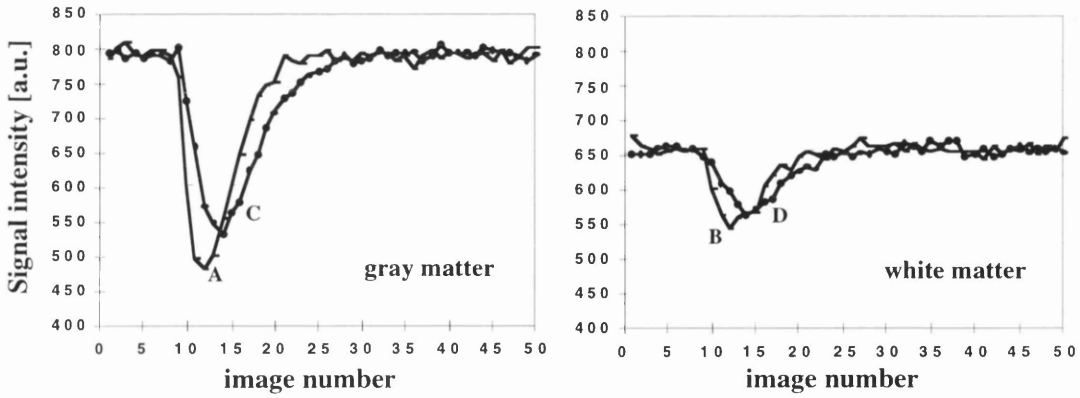

Figure 6.14.

Figure 6.14. Time courses for 4 typical 3x3 ROIs for simulated data with $1/\beta$ = 3.0 s in the absence of delay. The 4 ROIs were defined in similar positions as in Fig. 6.7.

The effect of the simulated dispersion on the quantification of DSC using SVD can be seen in Fig. 6.15. This figure shows the ratio of the value in the right region ('abnormal') to the value in the left region ('normal') for the CBF (open circles), CBV (crosses) and MTT (filled squares). Figure 6.15a shows the results for the data using the AIF for children (Eq. (6.2)), while Fig. 6.15b shows the equivalent results for the adult case (Eq. (6.3)). As with the delay simulations, the behaviour is qualitatively similar for both cases.

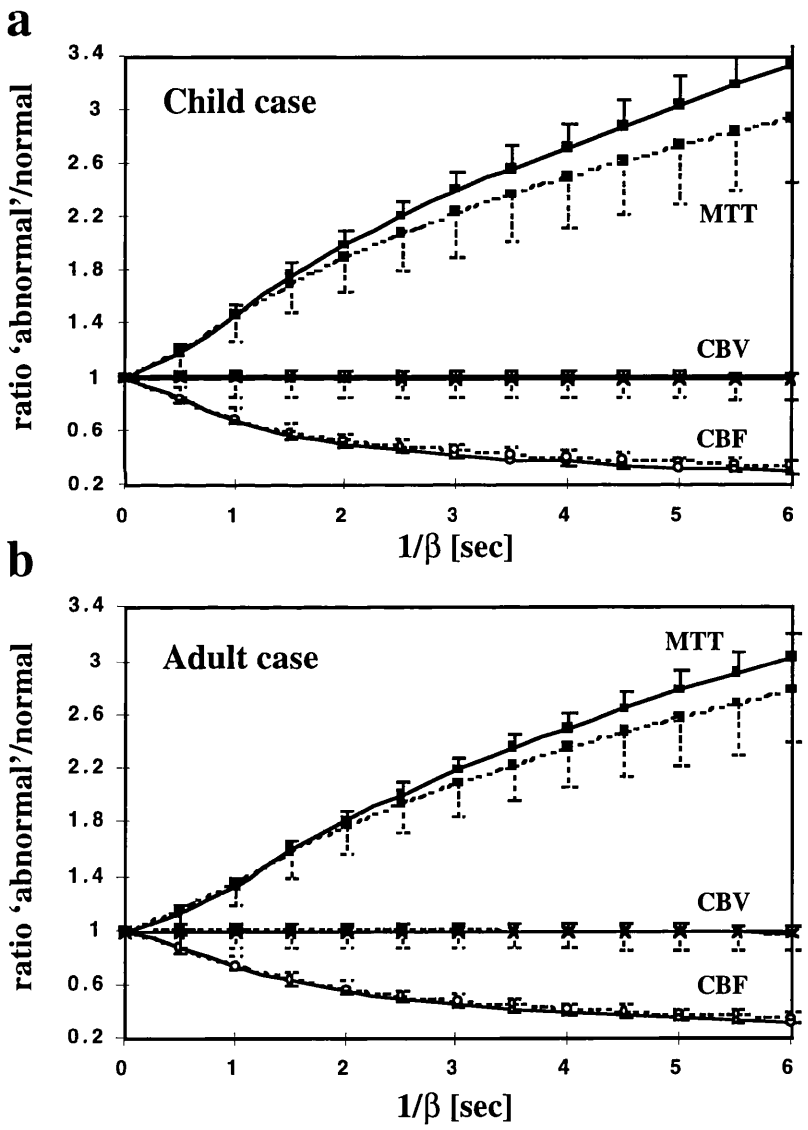

Figure 6.15.

Figure 6.15. Effect of dispersion (without delay) on the quantification of DSC-MRI data. The figure shows the ratio of the value in the 'abnormal' side to the value in the 'normal' side for the child case (a) and adult case (b). See legend of Fig. 6.9 for details.

Similarly to the delayed cases, the CBV is not affected (although the shape of the peak changes, the total area under the peak remains the same). The CBF is increasingly underestimated (ratio<1) with larger dispersion and, therefore, the MTT is overestimated. The effect is larger in the grey matter than in the white matter region, especially with increased dispersion.

The maximum CBF underestimation obtained with the simulated delayed data was ~40% (ratio ~0.6), for a delay of approximately 2 s. An equivalent underestimation is very quickly reached with a dispersion of $1/\beta$ ~1.5-2, but in the case of dispersion, this continues to increase further thereafter as $1/\beta$ increases.

6.3.3 Delay and dispersion effects

The effect of the combined effect of delay and dispersion into the quantification of DSC using SVD can be seen in Fig. 6.16. This figure shows the ratios of the value in the right region ('abnormal') to the value in the left region ('normal') as a function of dispersion, for different delays (0.5, 1.0, 1.5 and 3.0 s). The results for the CBF ratios are shown in Fig. 6.16a, and the results for the MTT ratios in Fig. 6.16b. The behaviour is qualitatively similar for the child (left graphs) and adult (right graphs), although the errors (underestimation of CBF and overestimation of MTT) are slightly larger for the former. As may be expected, for small dispersion, the contribution of the delay is significant, while it becomes less important with increasing dispersion. Furthermore, the ratio is almost independent of the delay value for delays longer than ~1.5 s, as was found for the simulated delays without dispersion (see Fig. 6.9).

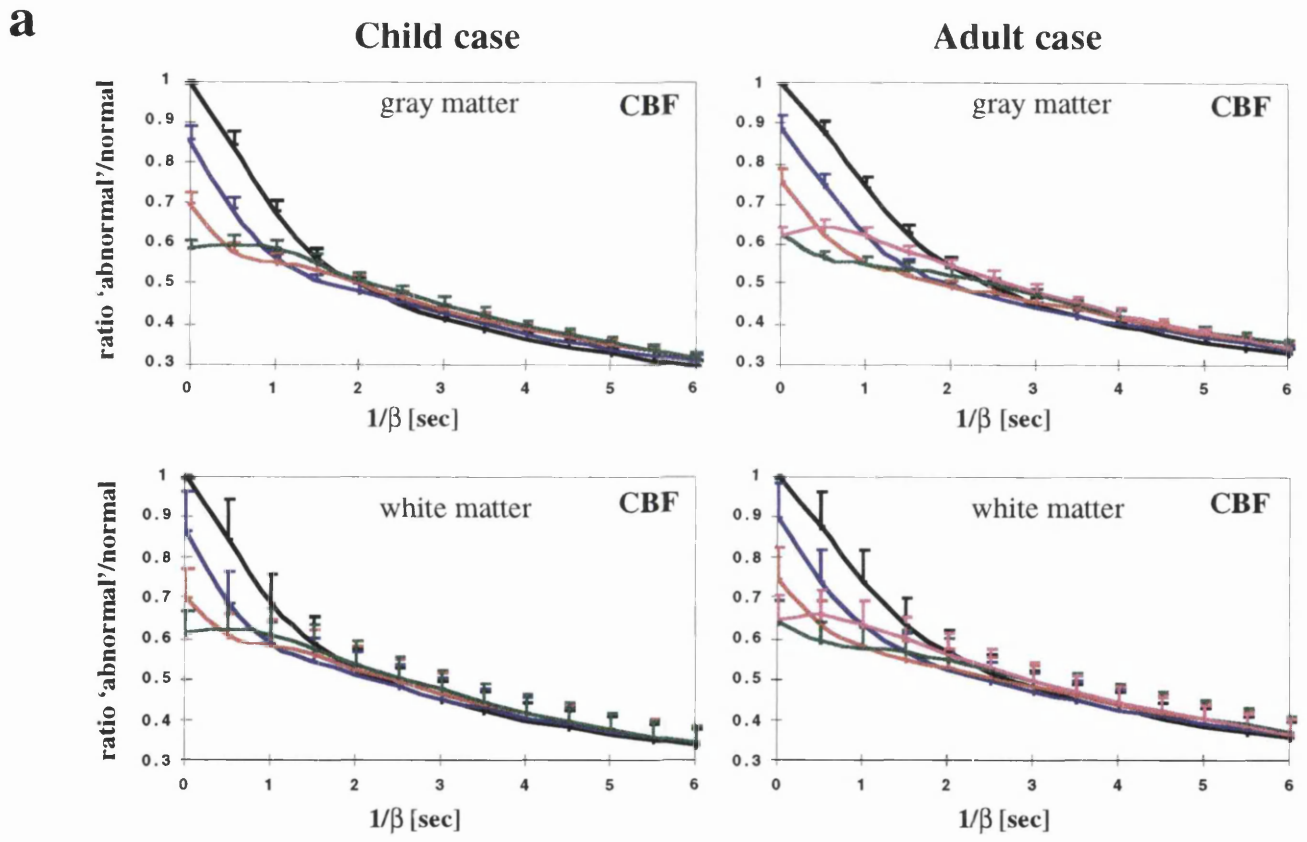

Figure 6.16.

Figure 6.16. Effect of delay and dispersion on the quantification of DSC-MRI data. The figure shows the ratio of the value in the 'abnormal' side to the value in the 'normal' side as a function of dispersion (1/β) for different delays. (a) CBF, (b) MTT. The top row graphs show the grey matter case, and the bottom row graphs the white matter data. The different delays are plotted in different colours: black (0.0 s), blue (0.5 s), red (1.0 s), green (1.5 s) and pink (3.0 s).

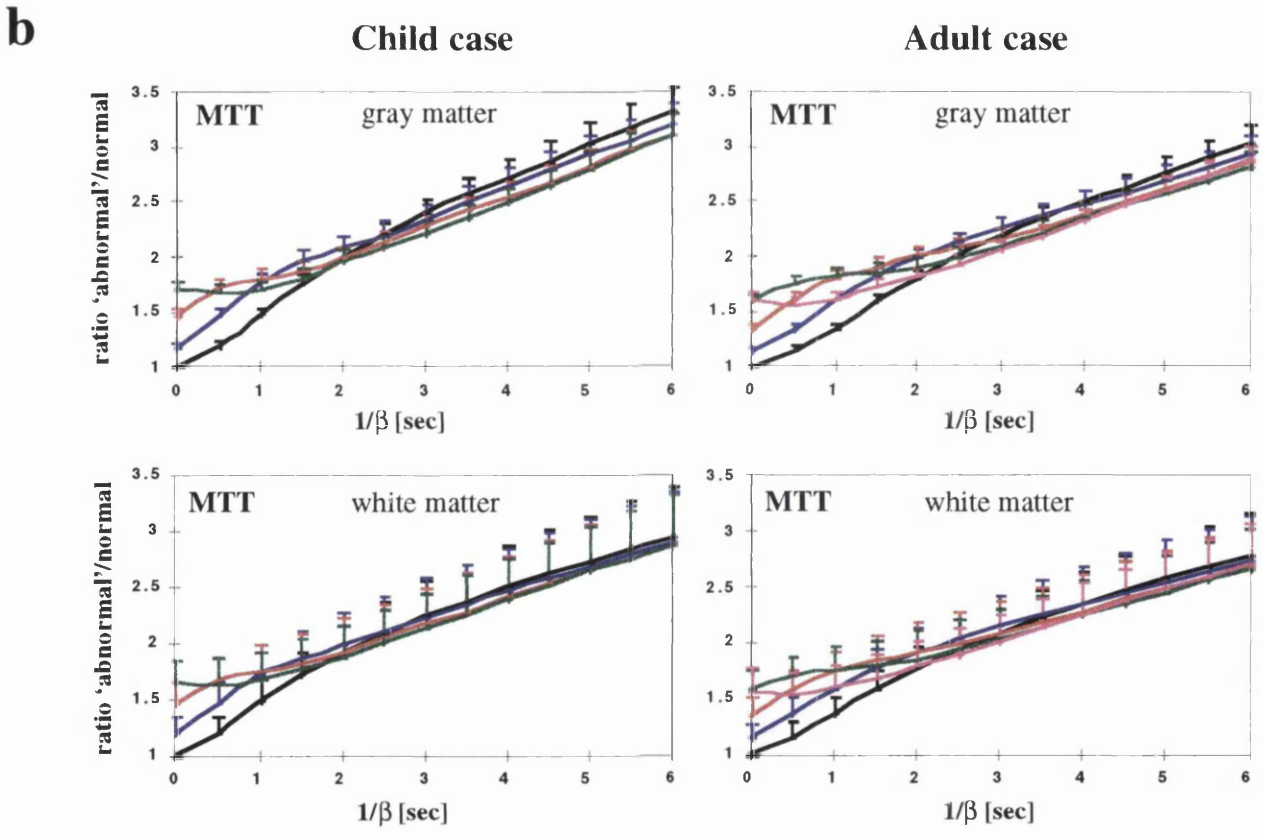

Figure 6.16.

Figure 6.16. Effect of delay and dispersion on the quantification of DSC-MRI data. The figure shows the ratio of the value in the 'abnormal' side to the value in the 'normal' side as a function of dispersion (1/β) for different delays. (a) CBF, (b) MTT. The top row graphs show the grey matter case, and the bottom row graphs the white matter data. The different delays are plotted in different colours: black (0.0 s), blue (0.5 s), red (1.0 s), green (1.5 s) and pink (3.0 s).

6.4 DISCUSSION

The effect of various delays and/or dispersions on the SVD analysis of DSC-MRI data were evaluated using computer simulations. Although our patient population consists mainly of children, it also includes young adults. Therefore, two different AIFs were simulated to evaluate the effects of delay and dispersion in both children and adults. By using hand injection for the delivery of the bolus of contrast agent, very different shapes of AIF can be obtained. However, an increasing number of research groups are now using MR compatible power injectors. This allows not only a faster injection rate, but also a more reproducible and controlled injection. The simulated AIFs used in this chapter were representative of data from children and adults obtained using a power injector.

The model of vascular transport function assumed for these simulations is one that is commonly used. There are some other simpler models (Østergaard et al., 1996a; 1996b), such as a box-shaped residue function (representative of a vascular bed with 'plug flow'), a triangular function or the decreasing portion of a Gaussian residue function (as intermediate models between the single, well-mixed compartment and the model of parallel capillaries with equal transit times and 'plug flow'). Some authors have also suggested the use of linear combination of exponentials (Jacquez, 1972). More recently, Østergaard et al. have incorporated a more complicated mathematical vascular model into the DSC analysis to try to account for the effect of delay and dispersion (Østergaard et al., 1999). In that study, the vasculature was modelled as a major feeding artery (with fixed relative dispersion and a delay determined by its volume fraction) in series with small parallel vessels (considered as simple delay lines) with relative flows and weights according to a given flow heterogeneity. For the simulations in this chapter, the single exponential model was taken as a first approximation for the vascular model. Further studies are needed to verify the validity of the present results with other models, as well as a comparison of the different models. Further work is also necessary to determine the

best vascular operators that describe a wide variety of vascular residue functions in the brain.

The simulations used samples of real noise data. This approach was chosen because it has the advantage that no assumption is made regarding the noise distribution (in contrast to Monte Carlo simulations), and it can be directly compared to our real data. Since the measurements were performed in a standard whole-body clinical system using the manufacturer's RF coil, the results should reflect those obtained in many other typical clinical systems. Furthermore, since the results were qualitatively similar for grey and white matter but with larger error bars in the latter, the results are probably qualitatively true for other SNRs as well.

6.4.1 Delay effects

The presence of a delay in the data was found to introduce large errors in the quantification of CBF and MTT, although it did not affect the CBV. The calculated overestimation of MTT was apparently larger than the underestimation of CBF. A relatively short delay of 1-2 s (not unlikely in ischaemic areas) produced approximately a 35% error in CBF and a 60% error in the MTT. The apparently larger effect in MTT is due to the inverse relationship between CBF and MTT (for a constant CBV), that is, if δMTT and δCBF are the overestimation and underestimation of MTT and CBF respectively, then (central volume theorem (Section 2.3.2.2.1))

$$MTT + \delta MTT = \frac{CBV}{CBF - \delta CBF} \tag{6.20}$$

and therefore

$$\frac{\delta MTT}{MTT} = \frac{\frac{\delta CBF}{CBF}}{\left(1 - \frac{\delta CBF}{CBF}\right)} > \frac{\delta CBF}{CBF} \tag{6.21}$$

for a positive δCBF, that is a CBF underestimation (note negative sign in Eq. (6.20)).

These errors could be corrected, in principle, by shifting back the peaks by δt_0, although this requires knowledge of the delay for each pixel. An estimation of this delay can be obtained by fitting the concentration time curve to a gamma-variate function on a pixel by pixel basis, although this method is very sensitive to noise.

The qualitative behaviour was the same for the two AIFs simulated. However, the delay for which the maximum error was introduced was longer for the adult case (~2-2.5 s) than for the child case (~1.5 s). This most likely reflects the much wider peak for the adult example.

The oscillation about an asymptote of the ratios of CBF and MTT for large delays was an unexpected result. The reasons for this oscillation are not clear, and further work is needed to clarify its origin.

As mentioned in *Results* (Section 6.3.1), a gamma-variate fitting is not performed in many practical cases. The SNR often is not high enough to allow an accurate fitting on a pixel by pixel basis, and therefore a fixed time window must be used for the analysis. The simulations showed that the error in the calculated CBF (underestimation) is not greatly affected by the presence of a fixed time window, but that a large error (underestimation) is introduced in the CBV, reducing, therefore, the initial overestimation in the MTT.

6.4.2 Dispersion effects

The simulated dispersions introduced large errors in the quantification of CBF and MTT, while CBV was not affected. In contrast to the effects of delay, the error continued to increase with increasing dispersion, introducing errors of over 200% in the MTT and 50% in the CBF for $1/\beta$ larger than ~2.5 s. This larger error with increasing dispersion can be interpreted in terms of the failure of the DSC model to distinguish between dispersion in the feeding vessels (from the place where the AIF was estimated to the VOI) and intravoxel dispersion by tissue microvasculature within the VOI (Østergaard et al., 1999, Schreiber et al., 1998; Calamante et al., 1999). An unaccounted dispersion produces spreading of the peak (see Fig. 6.6) which is interpreted by the DSC model as an increase in the MTT through the tissue (the wider the peak, the longer the MTT). However, this apparent increase in MTT is not related to true intravoxel dispersion.

The qualitative behaviour was the same for the two AIFs simulated, although the effect was slightly larger for the child case. The induced error was larger in the grey matter than in the white matter region, with the difference increasing with increasing dispersion.

Unlike the case for a delay, there is no simple way of correcting for dispersion. This requires modelling of the vasculature. As mentioned above, Østergaard et al. have recently incorporated a mathematical vascular model into the DSC analysis (Østergaard et al., 1999). By analysing data from 6 normal volunteers, they showed that the vascular model approach is less sensitive to vascular delay and dispersion than the conventional SVD approach. This method could potentially be used to correct for the dispersion observed in cerebrovascular disease. Their results are very promising, but further validation on a large number of patients with cerebrovascular diseases is needed. Another possibility would involve the use of the information from the graphs shown in Fig. 6.16 as a correction. However, this method would also be dependent on the assumed model for the vasculature (one single, well mixed compartment) and it would require an estimation of β (for example, $1/\beta$~delay). Regardless of the correction method, the

simulations performed in this chapter show that the presence of an unaccounted dispersion introduces very significant errors in the quantification of DSC-MRI data.

6.4.3 Delay and dispersion effects

The combined effect of delay and dispersion were found to introduce large errors in the quantification of DSC data using SVD. The induced error is not simply the addition of the separate errors. For example, a combined delay of 1 s and a dispersion of $1/\beta$=1.5 s produced a CBF underestimation of ~46% for the grey matter in the adult case. For comparison, the individual underestimation introduced by the delay and the dispersion alone were ~24% and 37%, respectively. It is interesting that for $1/\beta$ larger than ~1.5-2.0s, the ratios are almost independent of the delay value. Therefore, the effect of correcting *only* for the delay (by shifting back the peak) would reduce only slightly the error in those cases.

In most real situations, delays are likely to have an associated dispersion. Perfusion delays usually occur as a consequence of long arrival delays for the arterial blood to the VOI, for example as a result of collateral circulation. In these cases, the extra path that the blood must take further spreads the bolus, introducing some dispersion. Therefore, the simulations with delay *and* dispersion are more likely to reflect the situations observed in patients. This has two important consequences. Firstly, a simple shifting of the peak to eliminate the delay is sometimes performed; this will probably only reduce the error but not eliminate it, because there is likely to be also an uncorrected dispersion. Therefore, the results in such cases must still be interpreted cautiously, because the CBF is likely to remain underestimated (see Fig. 6.16 with delay=0 s (black lines)). Since the error would exaggerate the perfusion deficit, it is not problematic if the CBF map is used mainly to identify abnormal regions. However, it becomes very relevant when regions are defined in terms of flow values, when flow thresholds are determined, or when comparison between patients or follow up studies are performed. In all these cases, the

conclusions can be erroneous due to the confounding effect of the unaccounted dispersion. Secondly, there is a problem related to the use of time-to-peak (TTP) maps as a summary parameter (see Section 2.3.2.2.2). These maps will reflect both the delay (time until the arrival of the bolus) and the dispersion (time from the start of the peak until its maximum). Therefore, they cannot be directly used to identify the regions with delayed perfusion, since a longer TTP could represent, in principle, an area with a dispersed peak but *without* delay. However, as for the previous case, the TTP maps are very useful for the identification of abnormal regions because the two effects (delay and dispersion) are additive. For the identification of regions with delayed perfusion, the obvious choice is the use of BAT maps. However, as mentioned before (see *Discussion* (Section 6.4.1)), these maps might be difficult to calculate accurately on a pixel by pixel basis due to low SNR.

Finally, it should be mentioned that another possibility for the simulation of the tissue concentration time curves (C(t)) consists of measuring the signal from typical grey and white matter pixels obtained from real data. These could be fitted to a gamma-variate function, and the fitted functions used for subsequent simulations of delay and dispersion. This method assumes that the gamma-variate function correctly describes the concentration of contrast agent in the tissue. Interestingly, the convolution of a gamma-variate function (model for the AIF) with an exponential function (model for R(t))

$$(t-t_0)^r e^{-(t-t_0)/b} \otimes e^{-t/MTT} \tag{6.22}$$

is not a gamma-variate function (Fig. 6.17). Figure 6.17a shows simulated data (open circles) using Eq. (6.6) with a TR=0.5 s, and the corresponding gamma-variate fitting (solid line). As can be seen, the gamma-variate function does not accurately represents the simulated data, producing underestimation of the peak and the tail of the concentration time curve. This may have important consequences for the use of gamma-variate function fitting for the elimination of contrast recirculation in tissue, since this function does not really represent the concentration time course. In practice, however, due to the presence

of noise and the low number of data points available, the two functions are likely to be indistinguishable. Figure 6.17b shows a subgroup of the simulated data from Fig. 6.17a, which represents more the data obtained *in vivo:* TR=1.5 s, and the concentration time curve until the time when recirculation usually occurs (~25 s in Fig. 6.17b). When only these data are considered (even in the absence of noise) the corresponding gamma-variate function better represents the data.

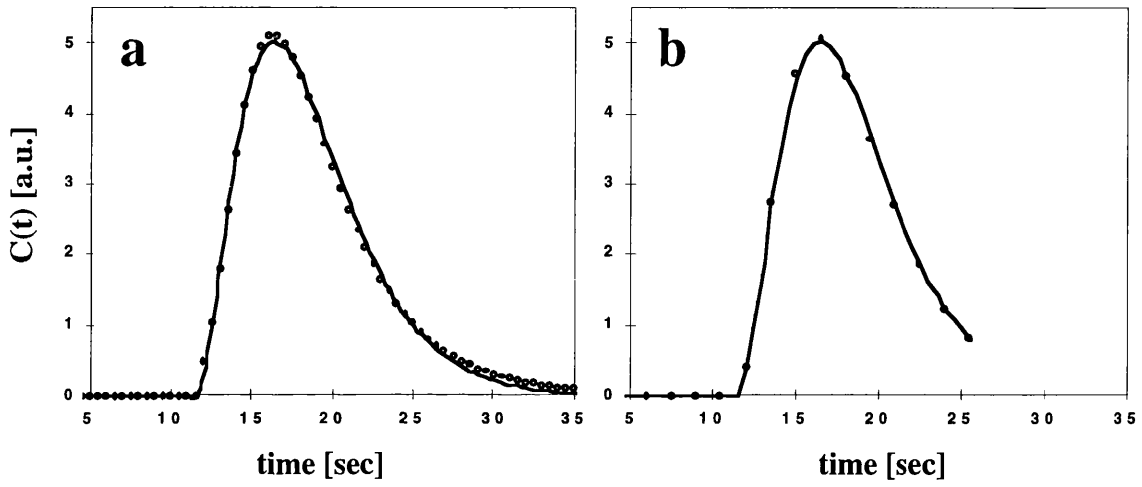

Figure 6.17.

Figure 6.17. (a) Comparison of simulated data (TR=0.5 s) in the absence of delay or dispersion (open circles) and the corresponding gamma-variate fitting (solid line). (b) Subset of the simulated data (TR=1.5 s) and its gamma-variate function.

In summary, the simulations performed in this chapter have shown that the unaccounted effect of delay and/or dispersion can have a very significant effect in the quantification of DSC data using SVD. When the SNR is large enough, the delay can be corrected by using the information from BAT maps. However, these corrected data can still be inaccurate due to the presence of an uncorrected dispersion. The correction of this dispersion is less straightforward and requires a model for the vasculature (Østergaard et al., 1999). Therefore, when no correction for delay and dispersion is performed, special care must be taken in interpreting the calculated CBF, CBV and MTT maps if these effects may be present.

6.5 APPENDIX

This appendix describes the steps required to analyse the DSC-MRI data using the programme *SVD_new* written by Leif Østergaard. The first step consists of the estimation of the AIF. This is usually obtained from pixels in the MCA in one of the slices (see Fig. 7.1 in Chapter 7). The pixels are selected in an interactive way, subject to the following criteria:

- reasonable anatomical location (e.g., MCA)
- time course with an earlier and larger peak (as compared to the tissue)
- reasonable shape (i.e., similar to a gamma-variate function)

The signal from the pixels satisfying this criteria is averaged, and is used as the AIF. Typically, between 5-10 such pixels can be easily selected. It should be noted that if the TE is very long or if a large dose is used (from the experience at GOSH, a dose larger than 0.2 mmol/kg of Gd-DTPA), the signal intensity in some of these pixels may fall below the background noise. These pixels must be avoided in order not to introduce an underestimation of the AIF (Ellinger et al., 1998).

The second step consists of selecting the images corresponding to the start and end of the peak, since these are used to limit the SVD analysis to that time interval. In cases when there is a significant contribution to the peak from recirculation, two alternatives can be chosen:

i) the analysis can be limited to the time prior to the start of recirculation, or

ii) a gamma-variate fitting can be used to eliminate the recirculation contribution.

Neither of these options is ideal. The first option has the disadvantage that the tail of the peak is not included in the analysis, while the second depends on an accurate fitting, which in turn relies on a good SNR.

Analogously to the AIF, the image corresponding to the end of the peak in the tissue must be obtained. This is more complicated than for the AIF, since the time when the tissue passage ends is generally not uniform throughout the slice. The best option, provided enough SNR is available, consists of a gamma-variate fitting on a pixel by pixel basis. However, this is not generally possible (particularly in white matter, where the SNR is very low for an accurate fitting). Furthermore, the fitting would require a pixel by pixel knowledge of the start of the recirculation ('end' of the peak), which is not straightforward to obtain. Therefore, the analysis is usually based on a 'fixed time window' approach, in which a global value for the start of the recirculation is selected.

This information (AIF, start and end of the AIF, start and end of the tissue peak) is then used as input to the *SVD_new* programme (together with the image data set). This programme performs the SVD (Østergaard et al., 1996a), and outputs three maps: CBF, MTT, and CBV.

There are some limitations in the analysis performed using the method described in this appendix. The first limitation is the use of a single AIF estimation for the whole brain. In principle, a different AIF can be used for each slice, although when the AIF is not obtained from a major vessel (e.g., in peripheral branches of the MCA) there can be a significant contribution from partial volume with the tissue, which introduces an underestimation of the AIF. The use of a single AIF is particularly relevant in stroke studies where there can be regional delays.

The second limitation is the already mentioned difficulty of accurately defining the beginning of the recirculation in the tissue (the model used in the quantification of DSC-MRI is based on the *first* passage of the contrast through the tissue). The use of a fixed time window for the analysis may introduce significant errors in regions with very prolonged MTT (very wide peaks).

As can be seen, the analysis is not automatic, and it requires substantial operator input. The main problem for a complete automated version of the analysis is the low SNR of the images at the pixel level. This makes the selection of a robust method for the detection of the start and end of the peak (particularly in white matter) very difficult. However, by performing the analysis in a semiautomatic way, the operator can qualitatively analyse the data by looking at the dynamic image data set.

7. Application of diffusion and perfusion MRI to the study of brain abnormalities in childhood

7.1 INTRODUCTION

Since the pioneering animal studies of Moseley and co-workers (Moseley et al., 1990), which showed an early decrease in the ADC of brain tissue water following an ischaemic insult, diffusion-weighted imaging (DWI) has found increasing use in the investigation of cerebral ischaemia, as well as in many other brain disorders, such as tumours and multiple sclerosis.

In cerebral ischaemia, the use of diffusion imaging has enabled the detection of ischaemic events before any abnormality is seen using conventional MRI, and it has allowed the distinction between acute and chronic lesions (see Section 2.2.5 from Chapter 2). The usefulness of a combined diffusion and perfusion analysis has in particular been greatly emphasised (Hossmann and Hoehn-Berlage, 1995; Baird and Warach, 1998; Calamante

et al., 1999), with one imaging modality complementing the other. Most of the present interest is in the mismatch between the area with diffusion abnormality and the area with perfusion disturbance. Any 'mismatch' area is believed to be tissue 'at risk' but potentially salvageable, and many studies have been performed to try to predict the final infarct size and to guide patient stroke therapy (Baird and Warach, 1998; Calamante et al., 1999).

At the Great Ormond Street Hospital for Children (GOSH) more than 400 patients have been scanned using diffusion MRI since early 1998, covering a large range of abnormalities, including stroke, epilepsy and tumours. Although dynamic susceptibility contrast (DSC) MRI has some limitations (see Chapter 6), it is still the most common MR technique for measuring perfusion in clinical studies (Calamante et al., 1999). At GOSH it has been in use since January 1999, and has been performed to assess the perfusion status in over 150 children with a large range of abnormalities.

This chapter describes some of the findings obtained at GOSH using quantitative diffusion and DSC-MRI, with the emphasis placed on the contribution of the diffusion and perfusion findings to diagnosis and to the management of the patients. The examples described here are restricted to cases where the diffusion and/or DSC-MRI data added relevant extra information to that obtained by conventional MRI.

The examples are taken from patients, who can be classified into four groups:

I. Patients with cerebral infarcts.
II. Patients with sickle cell disease.
III. Patients with moyamoya disease.
IV. Patients with other neurological disorders.

However, these groups are not mutually exclusive since, for example, some patients with sickle cell disease can develop moyamoya disease.

7.1.1 Patients with cerebral infarcts (Group I)

This is one of the most common groups of patients being studied using diffusion and perfusion MRI in many hospitals around the world. The aims of these studies include the discrimination of a new event in cases of multiple events, the identification of the area of mismatch between diffusion and perfusion abnormalities, and the evaluation of treatment. Some studies have been performed in stroke centres within 6 hours of the onset of an ischaemic event, when conventional MRI and CT are insensitive. Although none of the patients at GOSH was scanned before 12 hours from symptom onset due to practical limitations, a 'mismatch' can still be present since it has been shown that the ischaemic lesions may expand over periods of several hours, and even days, after the acute insult (Baird et al., 1997; Schwamm et al., 1998). Therefore, as will be shown, the cases of interest in this group of patients are not restricted to the hyperacute examples.

7.1.2 Patients with sickle cell disease (Group II)

This is a very important group of patients in the study of paediatric stroke, since sickle cell disease is the commonest single cause of childhood stroke (Earley et al., 1998). The incidence of stroke in children with sickle cell disease is approximately 250-fold higher than in a general paediatric population (Ohene-Frempong, 1991), and this incidence is similar to that in a general elderly adult population. Furthermore, approximately one quarter of the patients with homozygous sickle cell anaemia (HbSS) can be expected to be affected by the age of 40 (Ohene-Frempong et al., 1998). Sickle cell disease often involves stenosis or occlusion of segments of the internal carotid artery (ICA) or the proximal middle cerebral artery (MCA) and anterior cerebral artery (ACA), which predispose patients to stroke (Adams et al., 1992). Brain damage can be present in paediatric patients without clinical evidence of stroke. "Silent or covert infarction", defined as an ischaemic change in brain tissue in a patient with no clinical history of

stroke, is seen by conventional MRI in about 13% of all sickle cell disease patients (Moser et al., 1996; Armstrong et al., 1996).

The most common therapeutic approach in sickle cell disease is to delay aggressive stroke treatment until a primary stroke has occurred, and then use monthly blood transfusion therapy to prevent stroke recurrence (Piomelli, 1991). Blood transfusion therapy can reduce stroke recurrence by as much as 90% (Russell et al., 1984), and one stopped control trial has suggested that transfusion can prevent primary stroke (Adams et al., 1998). However, it is not an ideal treatment. Chronic transfusion of patients with sickle cell disease is associated with long term side effects such as iron overload syndrome. Bone marrow transplantation, which can result in disease-free survival as high as 91%, is not considered standard therapy because of the risk, difficulty, and expense of treatment (Walter et al., 1996). It is highly desirable to have a robust method for optimal patient selection and transfusion timing, and the possible role of diffusion and perfusion MRI has not yet been evaluated.

7.1.3 Patients with moyamoya disease (Group III)

Moyamoya disease is a rare and progressive cerebrovascular disease of unknown aetiology, with the highest prevalence reported in Japan (Takeuchi and Shimizu, 1957). Definitive diagnosis is made by catheter angiography, which reveals steno-occlusive disease at the ICA bifurcation and a characteristic "moyamoya" or "puff of smoke" angiographic appearance representing extensive net-like collateral vessels within the basal ganglia and thalami (Ukei et al., 1994). Childhood moyamoya disease differs from the adult form in that the disease typically occurs bilaterally, the moyamoya vessels are more prominent, there is higher incidence of symptomatic ischaemia, and there is a lower incidence of intracranial bleeding and aneurysms (Satoh et al., 1988; Suzuki and Kodama, 1983). Moyamoya patients have high incidence of recurrent stroke, transient ischaemic attack (TIA) and seizures.

Direct (external carotid-ICA bypass) or indirect revascularisation procedures appear to reduce the clinical symptoms, but the benefit of operation remains controversial. There is also debate over the relative merits of the direct and indirect procedures. PET and SPECT have a role in delineating areas of at-risk tissue, but they are not appropriate for repeated examinations. A non-invasive method of documenting change in tissue perfusion pre- and post-operatively would be of potential benefit in deciding whether patients would benefit from further procedures. It is possible that diffusion and DSC-MRI might prove a useful tool for pre-surgical assessment, as well as for the evaluation of different surgical techniques with respect to post-surgical brain tissue status.

It should be noted that since the patients from both Groups II and III have high risk of stroke, some of the diffusion and perfusion findings overlap with those from Group I. Therefore, the examples described in Group II and III will be restricted to cases directly related to the guidance and evaluation of the particular treatment for each case (blood transfusion in sickle cell disease, and revascularisation in moyamoya disease), while the other examples will be included as part of Group I.

7.1.4 Patients with other neurological disorders (Group IV)

This group included those patients for whom diffusion and perfusion MRI helped to explain both the presenting aetiology and the underlying mechanisms of other neurological disorders, such as in drug induced neurotoxicity or Sturge-Weber syndrome. In patients with neurological symptoms, it is very important to determine the underlying aetiology for the selection of the appropriate treatment.

Neurotoxicity is a common adverse effect of post-transplantation cyclosporin immuno-suppressive therapy. In most cases, the MR findings include lesions of increased signal intensity on T_2-weighted images affecting the subcortical white matter (Schwartz et al.,

1995; Truwit et al., 1991). These areas of T_2 abnormality are usually, but not invariably, reversible. Various hypotheses have been suggested to explain the pathophysiology of the induced neurotoxicity, including cerebral oedema (Schwartz et al., 1995) and ischaemia (Truwit et al., 1991), but the exact mechanism is still unknown. Quantitative diffusion studies may provide new information regarding the mechanism of neurotoxicity.

Sturge-Weber syndrome is a disease characterised by the presence of facial naevus ('port wine' stain), together with an ipsilateral leptomeningeal angioma, and choroidal angioma. These lead to a later calcification and cerebral atrophy. The most common neurological feature is the presence of seizures, although Sturge-Weber syndrome can be also associated to hemiplegia and impaired psychomotor development (Aicardi, 1998). The contributory factors to neurological deterioration are not yet clearly defined. In some patients, there is progressive cognitive impairment, while in others almost normal development takes place. In addition to the lesion, the hemisphere contralateral to the lesion is often haemodynamically compromised (Okudaira et al., 1997; Aylett et al., 1999).

The pathogenesis of Sturge-Weber syndrome is not fully understood, and there are several hypotheses for the progression of the neurological deterioration. It has been suggested that seizures may play a major role in such progression (Aicardi, 1998). In addition, investigations of cerebral blood flow and metabolism have suggested that cerebral ischaemia may contribute significantly (Maria et al., 1998; Reid et al., 1997). Further, some studies have suggested that the haemodynamic compromise of the tissue is responsible for the progression (Okudaira et al., 1997).

7.2.1 MRI studies

MRI was performed on the 1.5 T Siemens Vision whole body imaging system described in Chapter 4. Quantitative *diffusion* imaging was obtained using a FLAIR spin-echo EPI sequence, with a pair of diffusion gradients as described in Chapter 5 (Section 5.2.2). Imaging parameters were TE/TR/TI = 86/8700/2100 ms; 128x128 matrix; 24 cm FOV; 5 mm slice thickness. Diffusion parameters were δ/Δ=15/40.2 ms, *b*-values = 0 and 617 s/mm^2. A multi-slice reference scan was acquired for the on-line correction of B_0-eddy-current effects (see Chapter 4). ADC maps were calculated in three orthogonal directions, which were combined to calculate average ADC maps (ADC_{AV}). These three directions (labelled *'i'*, *'j'*, and *'k'*) were chosen in order to maximise the resultant diffusion gradient by applying diffusion gradients simultaneously along all three *'x'*, *'y'*, and *'z'* axes (Sorensen et al., 1996):

i = (-1,1/2,-1)

j = (1/2,-1,-1)

k = (-1,-1,1/2)

In this way, a 2.25 times larger *b*-value for a given maximum gradient strength could be obtained (due to the quadratic dependence of the *b*-value with the gradient strength (see Section 2.2.4 from Chapter 2)).

Perfusion MRI was performed using a multi-slice spin-echo EPI sequence. Imaging parameters were: TE/TR = 0.1/1.5 s; 128x128 matrix; 24 cm FOV; 5 mm slice thickness. Six slices were acquired (Fig. 7.1), with one of the slices including the MCA for the estimation of the arterial input function (AIF). A bolus of 0.15 mmol/kg-body-weight Gd-DTPA (Magnevist®, Schering AG, Germany) was injected intravenously (rate 2-6

ml/s) using an MR compatible power injector (Medrad Inc, Pittsburgh, PA), followed by a saline flush. The injection of the contrast began at the 15th multi-slice data set, and the passage of the bolus through the brain was sampled with a 1.5 s time resolution.

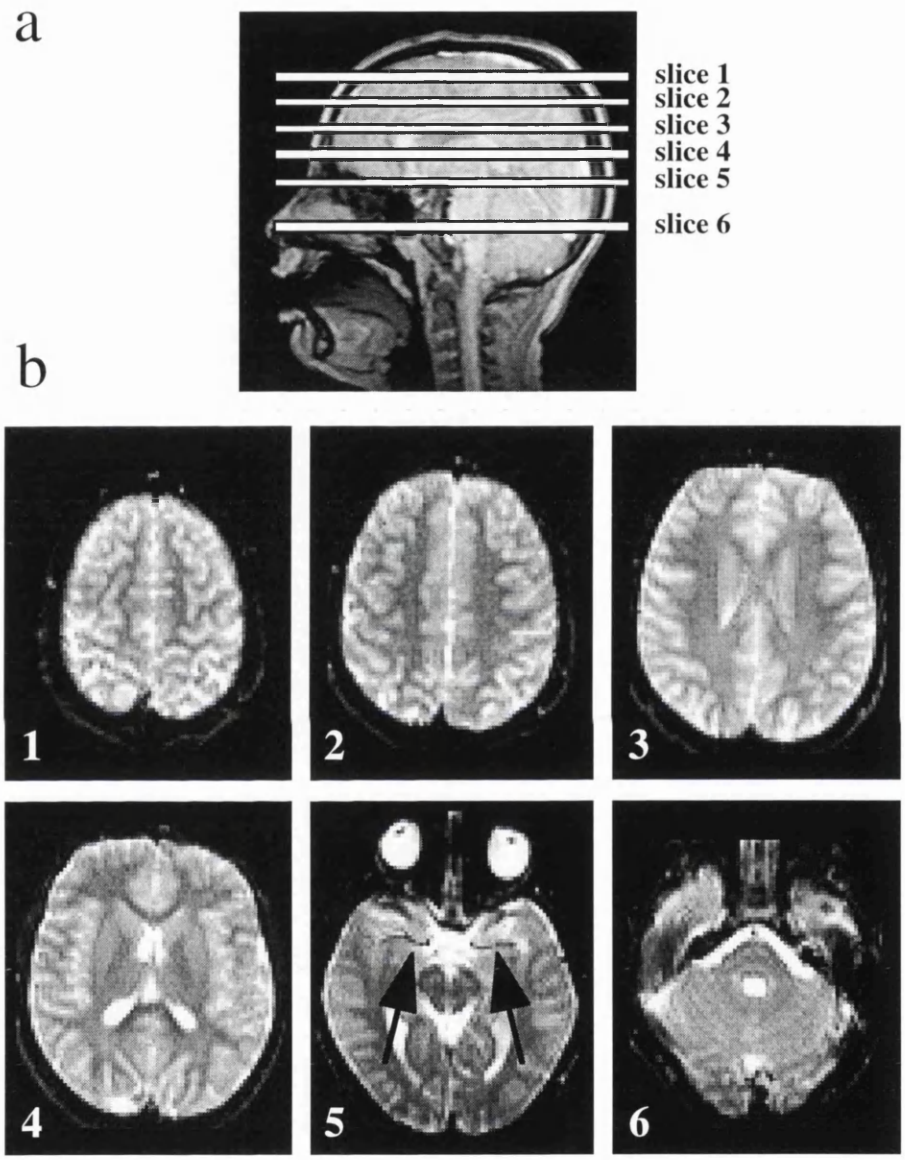

Figure 7.1.

Figure 7.1. Multi-slice SE-EPI data. (a) Sagittal scout image showing typical positions for the six slices used in DSC-MRI studies. (b) Typical axial multi-slice SE-EPI data set. Slice number 5 is usually positioned through the MCA (arrows).

7.2.2 MRI imaging analysis

7.2.2.1 Quantitative analysis of the diffusion data

When quantitative regional measurements of diffusion are performed, the partial volume with cerebrospinal fluid (CSF) can introduce a significant overestimation. Although a FLAIR preparation was used in the DWI sequence, some remaining CSF contamination may still be present (see Fig. 7.2). To avoid this partial volume contribution when a quantitative analysis was performed, a 'non-FLAIR' image was also used. This image was acquired using the same sequence, but without the adiabatic inversion pulse. An empirical threshold of 0.6 (for the ratio of the FLAIR image to the 'non-FLAIR' image) was defined to identify pixels with significant CSF contribution (ratio<0.6), and to mask the ADC_{AV} maps. Figure 7.2 shows a typical example of the FLAIR and 'non-FLAIR' images, as well as the corresponding ADC_{AV} maps for different thresholds. A clear elimination of the pixels with partial volume from CSF can be seen with increasing threshold, which allows a more accurate quantification of the diffusion of tissue.

7.2.2.2 Analysis of the perfusion data

The AIF was estimated from pixels within the MCA in one of the selected slices (see Fig. 7.1). These data were used to deconvolve the concentration time curve (see Eq. (2.22) of Chapter 2) using singular value decomposition (SVD) (Østergaard et al., 1996a). A 3x3 uniform smoothing kernel was applied to the raw image data before deconvolution. Maps of CBF, CBV and MTT were calculated on a pixel by pixel basis.

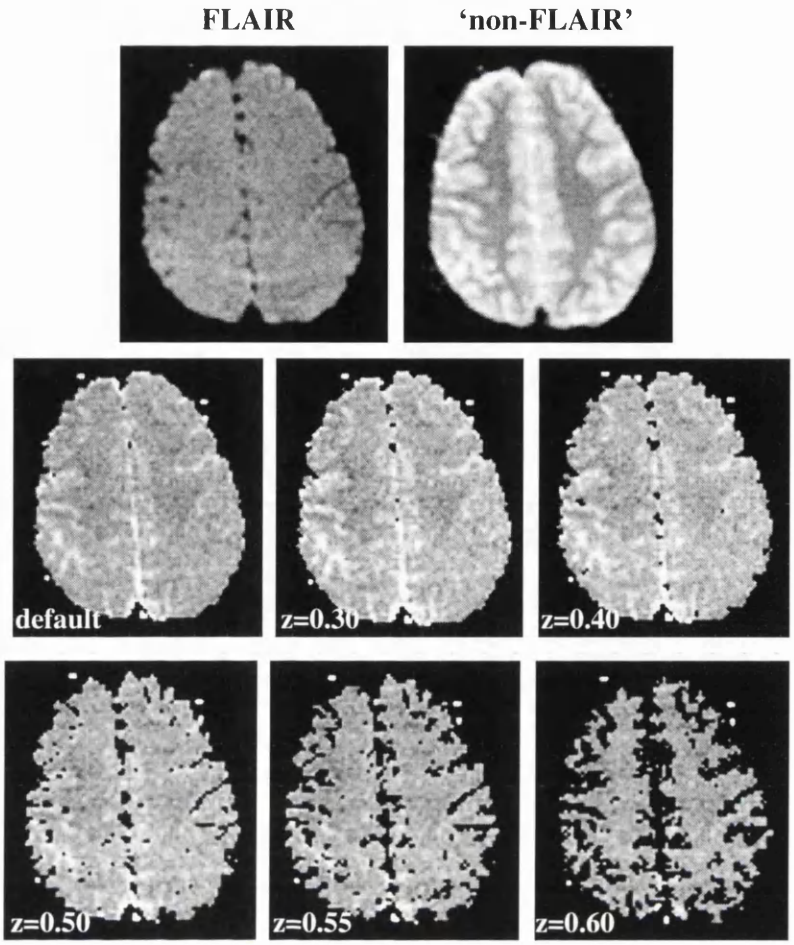

Figure 7.2.

Figure 7.2. Effect of CSF partial volume on ADC mapping. Top row: FLAIR and 'non-FLAIR' EPI images. The middle and bottom row show different ADC_{AV} maps created with different thresholds (z) for the ratio FLAIR/'non-FLAIR'. 'default' corresponds to the default threshold used during the on-line image processing. As can be seen, the larger the value of z, the more pixels with CSF partial volume are eliminated.

When long bolus arrival delays are present in the areas with perfusion disturbance, the quantification of DSC data using SVD produces very inaccurate results (see Chapter 6). In these cases, maps of summary parameters (such as 'time to peak' (TTP), and 'maximum peak concentration' (MPC)) were calculated on a pixel by pixel basis using routines written in IDL software (RSI, Boulder, Colorado). These maps were used to define regions of interest (ROIs), for which a more accurate quantitative analysis was performed as follows. 'Bolus arrival time' (BAT) was calculated for ROIs in the delayed area and in similar areas in the contralateral side. These were obtained by fitting a

gamma-variate function (see Eq. (6.1) from Chapter 6) to the corresponding time course data (Fig. 7.3), and the difference in arrival time ($\Delta BAT=BAT_{del}-BAT_{no\_del}$) was calculated for each case.

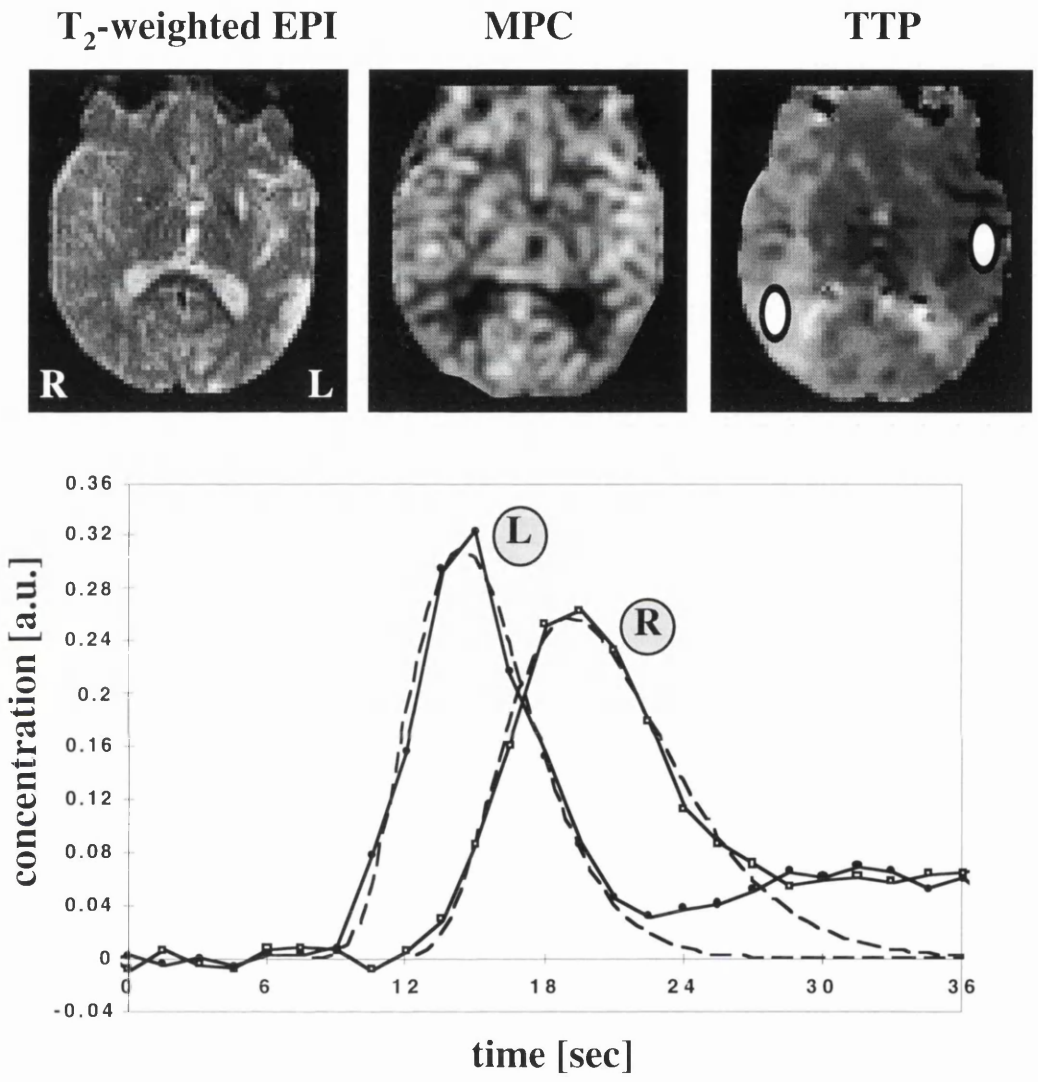

Figure 7.3.

Figure 7.3. Calculation of the BAT from the gamma-variate fitting. The figures show the T_2-weighted EPI image (left), MPC (middle) and TTP (right) maps for a child with moyamoya disease. The bottom graph displays the concentration time course for the cortical regions shown in the TTP map, together with the corresponding gamma-variate fittings (dotted lines). There is an ~4.5 s difference in the arrival of the bolus to the right region compared to the arrival time to the left region.

7.3.1 Patients with cerebral infarcts (Group I)

7.3.1.1 No diffusion/perfusion mismatch

As mentioned in Section 7.1, although much emphasis is currently placed on any mismatch in the extent and location of perfusion and diffusion abnormalities, those cases where the areas of increased T_2, reduction in diffusion, and low perfusion are all similar are also of considerable clinical relevance. Such data suggest that in these cases the affected tissue is restricted to the region already displayed by conventional MRI and, therefore, that there is no further tissue 'at risk'. One such example can be seen in Fig. 7.4, which shows the images from a scan performed 12 hours after symptom onset in a 4 year old child. An ischaemic region can be seen covering approximately a similar area in the left basal ganglia in all the images (right side of the images). The lesion is seen in the T_2-weighted image as a region of slight hyperintensity, while it is more clearly seen in the diffusion-weighted image (as hyperintensity) and the ADC_{AV} map (as decreased diffusion). The lesion is also readily seen in the CBF, MTT and CBV maps. In such cases, the final infarct is usually of the same size as in the initial study (Rordorf et al., 1998), and there is low risk of further extension of the lesion. Unless neuroprotective or reperfusion agents can be shown to reverse both DWI and T_2 abnormalities, such risky interventions may not be justified in these patients.

7.3.1.2 T_2 and ADC time evolution

Several studies have addressed the time evolution of T_2 and ADC (Warach et al., 1992; 1995; Welch et al., 1995; Marks et al., 1996; Lutsep et al., 1997; Nagesh et al., 1998;

Schlaug et al., 1997; Schwamm et al., 1998). It is well known that diffusion is reduced during the first few days following ischaemia, and that at some point later the ADC increases gradually to an abnormally high level, of necessity passing through 'normal' ADC values (usually referred as 'pseudonormalisation'). Figure 2.8 (see Chapter 2) shows a schematic representation of the time evolution of T_2 and ADC. The extra information obtained from diffusion, therefore, greatly adds to that from conventional MRI in the diagnosis of cerebral infarction.

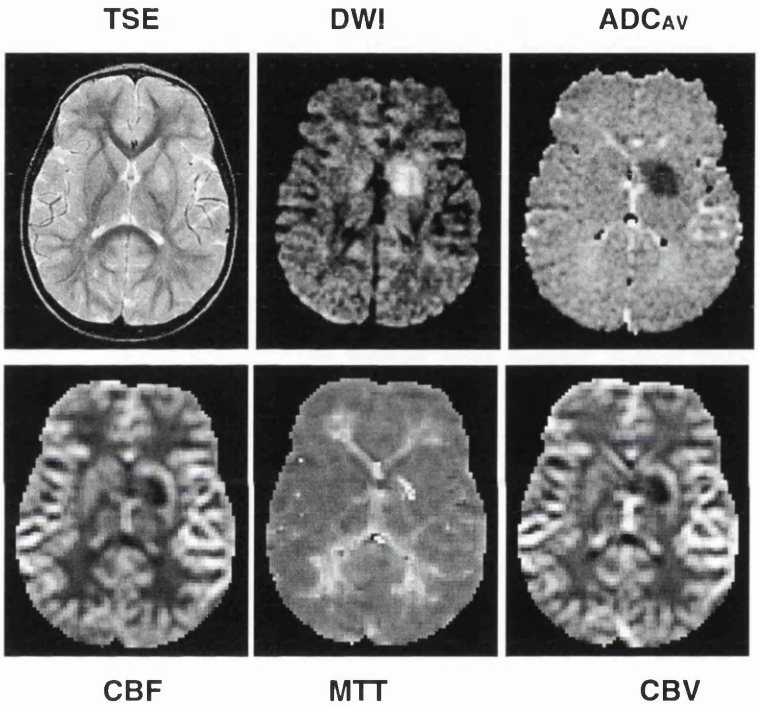

Figure 7.4.

Figure 7.4. Images of a 4 year old child, 12 hours after symptoms onset. The top row shows the axial T_2-weighted TSE image (left), diffusion-weighted image (middle), and ADC_{AV} map (right). The bottom row shows the CBF (left), MTT (middle) and CBV (right) maps. All of them show an abnormal region covering approximately a similar area in the left basal ganglia (right side of the images).

Such an evolution of the lesion can be seen in the images obtained 2 and 6 days after symptom onset in a 1 year old child (Fig. 7.5). The first scan shows a region of reduced diffusion in the right basal ganglia, consistent with the presence of an acute event. This lesion has gone through 'pseudonormalisation' to an abnormally high ADC value at the time of the second scan 4 days later.

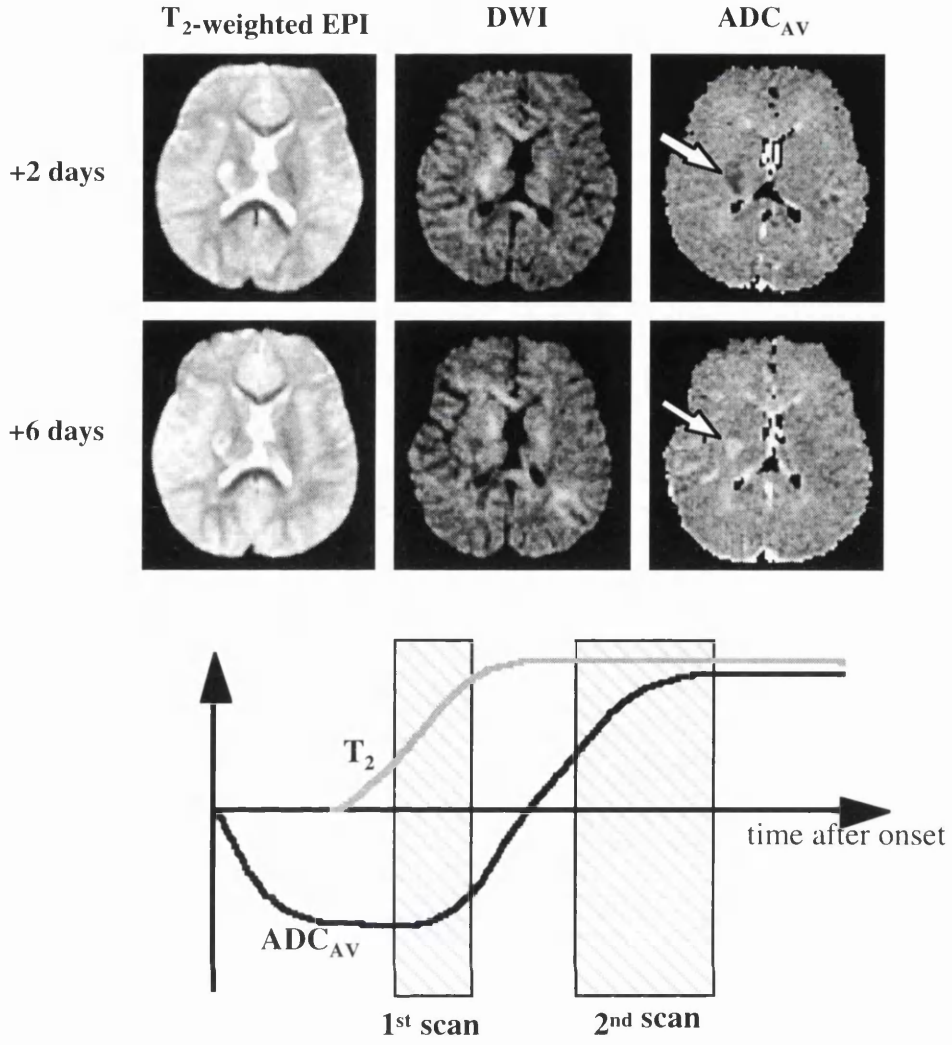

Figure 7.5.

Figure 7.5. Lesion evolution in a 1 year old child with a stroke in the right basal ganglia (left side of the images). The top row shows the axial T_2-weighted EPI image (left), diffusion-weighted image (middle), and ADC_{AV} map (right) acquired 2 days after symptoms onset. The bottom row shows the equivalent images for the follow up scan performed 4 days later. The lesion shows decreased diffusion in the first scan and increased diffusion in the second one (arrows). According to the images, the bottom graph shows an schematic diagram with the time course of the T_2 and ADC in the lesion, with the approximate stage of the two scans in this lesion evolution.

The time evolution of MR tissue characteristics also allows the differentiation of an acute event from a previously infarcted region. The 12 year old patient whose images are shown in Fig. 7.6 had a lesion in the left hemisphere several months before the onset of a second event in the same side. The images shown are from the scan performed 2 days

after the more recent event. The two lesions appear as hyperintense regions in the T_2-weighted image and, therefore, are not easily differentiated. However, they are very different in their diffusion properties, the area of reduced diffusion reflecting the acute event, and the area of increased diffusion reflecting the chronic event. The DSC-MRI data show a time delay to the maximum concentration, and reduced peak signal in the area corresponding to both lesions.

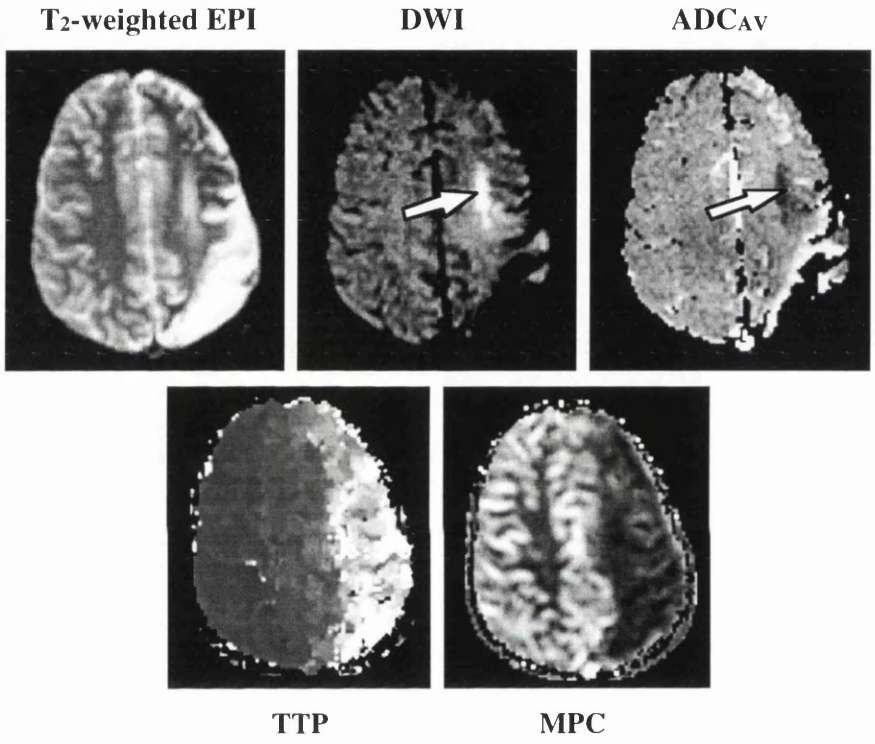

Figure 7.6.

Figure 7.6. Acute and chronic lesions in a 12 year old child. The MRI scan was performed 2 days after the last event. The top row shows the axial T_2-weighted EPI image (left), diffusion-weighted image (middle), and ADC_{AV} map (right). The bottom row shows the TTP and the MPC maps. There is a clear differentiation between the chronic (increased diffusion) and the acute (decreased diffusion (see arrows)) lesions. The DSC-MRI summary parameters maps show a large area with increased time to the peak maximum and decreased peak height, encompassing both the acute and chronic lesions.

More importantly, the time evolution as described above may allow the identification of multiple *acute* events. These are of great diagnostic importance since they suggest a source of multiple emboli and, therefore, the possibility of further events if no action is

taken. Figures 7.7 and 7.8 show an example from a 15 year old boy with an infarct in the right basal ganglia. Figure 7.7 shows the images from the scan performed 4 days after symptom onset. There are two lesions visible on T_2-weighted imaging (left image); the more posterior (P) shows very low diffusion, while the anterior (A) has already 'pseudonormalised'. This is suggestive of multiple acute ischaemic events, which was consistent with the observation of a further clinical event after the initial insult. These results were consistent with the MR angiography (MRA) findings of a right ICA dissection. Figure 7.8 shows the follow up scan (5 month later), where not only have both lesions evolved to a mature infarct (top row), but also there is a more extensive perfusion deficit in the right hemisphere (bottom row). This can be seen as a reduced CBF and increased MTT, especially in the watershed areas. The dissection was probably the source of the multiple emboli which caused the infarcts, as well as the low general perfusion in the right hemisphere. The mismatch between the infarcted area and the region with perfusion deficit suggests the presence of tissue 'at risk'.

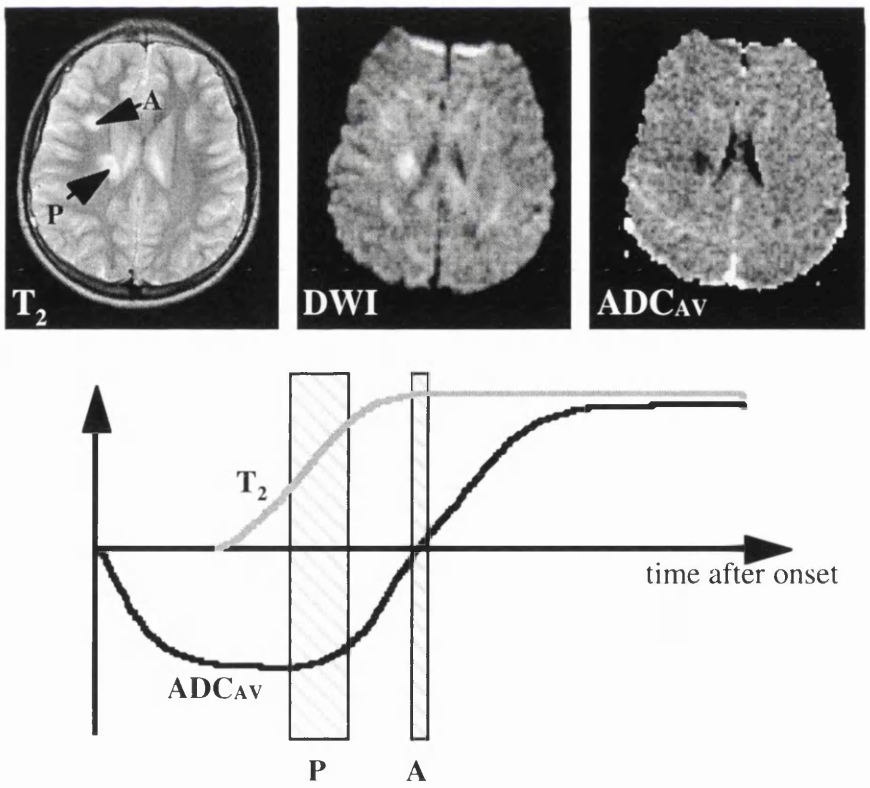

Figure 7.7.

Figure 7.7. Multiple acute events. MRI scan performed on a 15 year old child 4 days after symptoms onset. The top row shows the axial T_2-weighted TSE image (left),

diffusion-weighted image (middle), and ADC_{AV} map (right). Two regions of increased T2 can be seen in the right basal ganglia (left side of the images). While the more posterior (P) has decreased diffusion, the anterior (A) has already 'pseudonormalised'. The bottom graph shows a schematic diagram with the time course of the T_2 and ADC in the lesions, with the approximate stage of the two lesions.

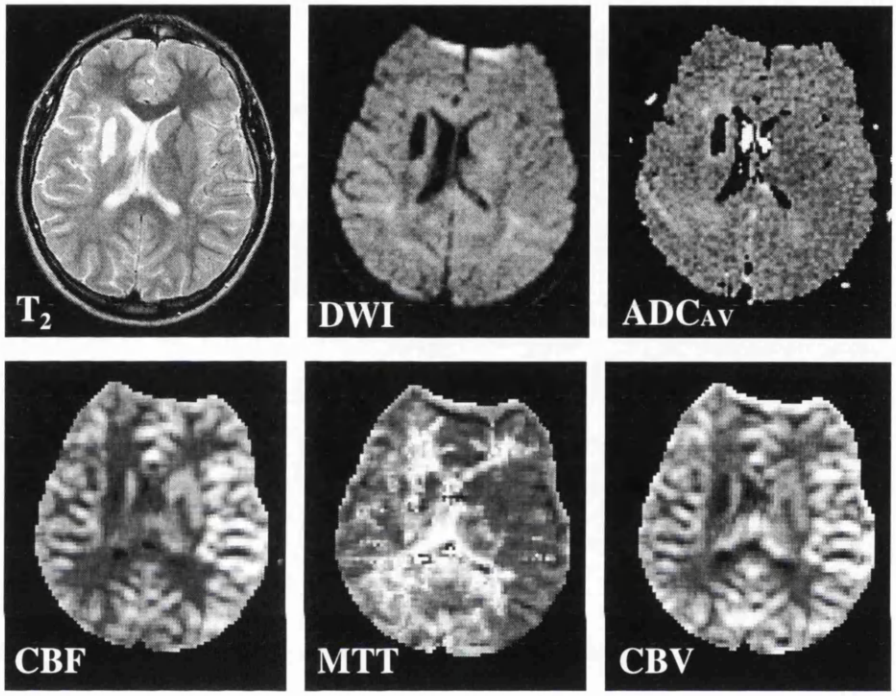

Figure 7.8.

Figure 7.8. Follow up MRI scan for the child in Fig. 7.7, performed 5 months later. The top row shows the axial T_2-weighted TSE image (left), diffusion-weighted image (middle), and ADC_{AV} map (right). The bottom row shows the CBF (left), MTT (middle) and CBV (right) maps. The two acute lesions in the previous scan (Fig. 7.7) evolved to a mature infarct (signal suppressed by the FLAIR preparation in the DWI sequence used). There is also a more extensive perfusion deficit in the right hemisphere (left side of the images), as can be seen as in the CBF and MTT maps.

There are still some issues concerning the time evolution of the diffusion coefficient which remain to be fully characterised. For example, it is not known if the evolution of the grey matter ADC is the same as that of white matter. Fig. 7.9 shows two examples where the diffusion was lower in the white matter areas than in the grey matter at the time of the scan. As mentioned before, this could suggest the presence of multiple acute

events. However, the absence of clinical evidence of such events favours the option of a tissue-dependent time evolution. This lesion heterogeneity has been previously reported (Nagesh et al., 1998), but it has not yet been fully characterised. Moreover, most of the published studies have been performed in adult patients, and further studies are needed to extend these results to children.

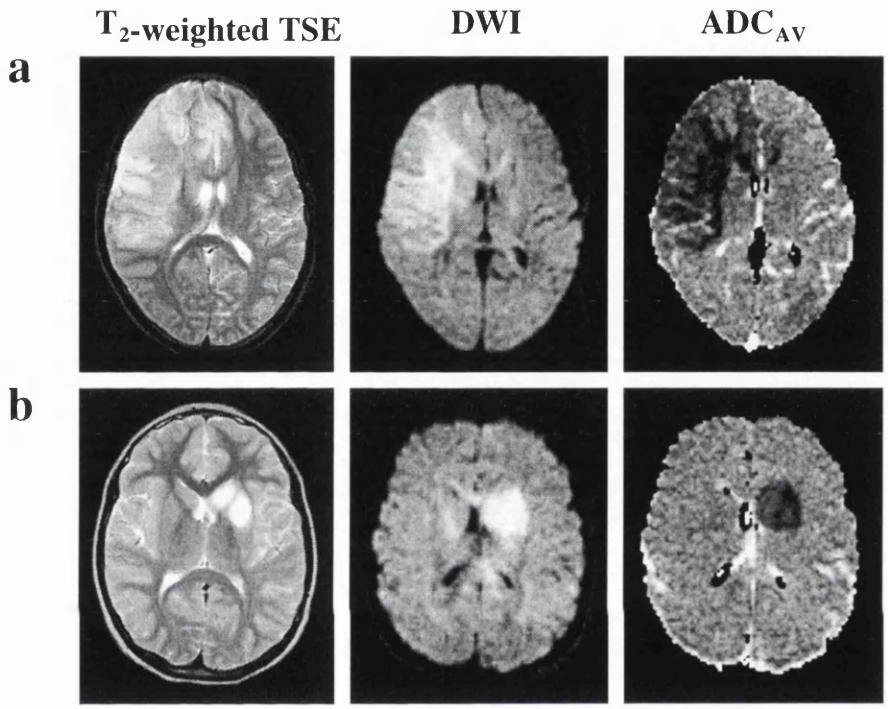

Figure 7.9.

Figure 7.9. White matter and grey matter lesion evolution. Axial T_2-weighted TSE images (left), diffusion-weighted images (middle), and ADC_{AV} maps (right) from two children. The top row shows the MRI scan (9 days after symptom onset) from a 12 year old with a lesion in the right MCA. The bottom row shows the MRI scan from a 13 year old child 2 days after symptom onset (lesion in the left basal ganglia). There is a markedly heterogeneity in the lesion in both cases, with the diffusion in the white matter lower than in the grey matter.

7.3.1.3 Diffusion/perfusion mismatch

There are some situations where there is a large mismatch between the perfusion and the diffusion/T_2 abnormalities (Figs. 7.10, 7.11 and 7.12), which is usually manifested as a relatively small area of diffusion abnormality, with a much larger region of perfusion

disturbance. This latter region often has long delays for the arrival of the contrast agent. Therefore, the 'conventional' analysis (deconvolution using the AIF) is not suitable (see Chapter 6), and summary parameters maps are more appropriate. The following examples illustrate both the important information that can be gained from such combined studies, and the difficulty in analysing the perfusion information.

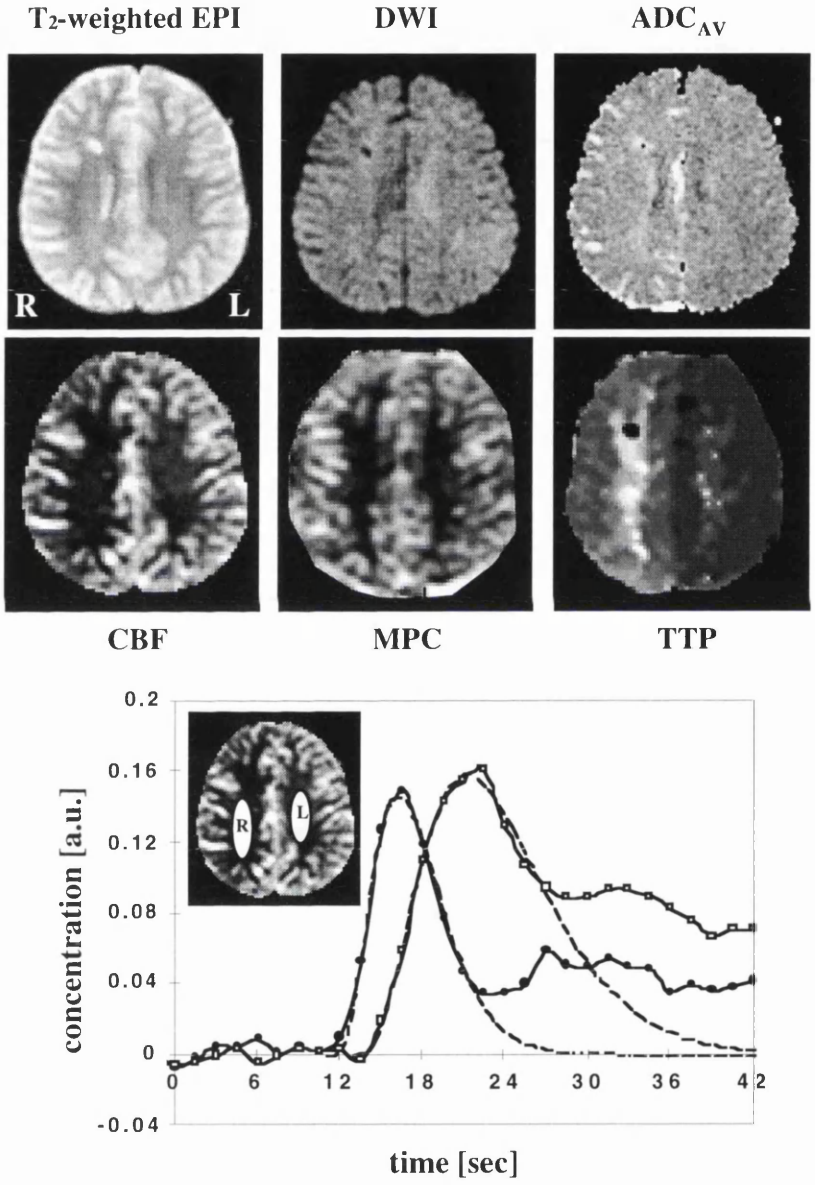

Figure 7.10.

Figure 7.10. Diffusion/perfusion mismatch in a 6 year old child with right ICA stenosis with probable dissection. The top row shows an axial T_2-weighted EPI image (left), diffusion-weighted image (middle), and ADC_{AV} map (right). The bottom row shows the CBF (left), MPC (middle) and TTP (right) maps. In the conventional MRI and diffusion imaging there was only a small mature infarction in the right frontal white

matter. On the other hand, the DSC-MRI data shows a more extensive perfusion abnormality in the right hemisphere. This can be seen as a prolonged time to maximum concentration (TTP map), although with approximately the same peak signal. The bottom graph shows the concentration time course for two white matter regions (L: filled symbols, R: open symbols), together with the corresponding gamma-variate fittings (dotted lines). There is an ~1.75 s delay to the arrival of the bolus between the two regions. This delay introduces an underestimation of the calculated CBF.

The first example (Fig. 7.10) is from a 6 year old patient who had a right ICA stenosis with probable dissection, and who presented with multiple episodes of TIAs. Both the T_2-weighted image and the ADC_{AV} map show only a small right frontal mature infarction, from an old event which occurred 4 months earlier. On the other hand, the DSC-MRI data show a much larger abnormality, with a long perfusion delay to the whole right hemisphere (ΔBAT= 1.75 s). Figure 7.10 shows the concentration time course for two ROIs, one in each hemisphere. By performing a gamma-variate fitting, the ratio of the right area to left area under the peak (proportional to CBV ratio) was ~1.7, which implies ~70% increase in the right CBV. It can be seen that although the peak height is not very different (see also the MPC map), it is much wider in the right hemisphere. These results suggest an autoregulatory response with increased CBV and MTT, keeping the CBF to approximately normal values.

The second example of a large mismatch between diffusion and perfusion abnormalities is from a 5 year old sickle cell disease patient (Fig. 7.11), who had an acute right hemiparesis 5 weeks before the first MRI examination. He presented with a bilateral motor deficit at the time of the scan. The T_2/diffusion data showed two mature infarctions, one in the left occipital lobe, and the other in a right frontal/parietal region (Fig. 7.11). However, the perfusion abnormality extends beyond that area, with reduced perfusion and prolonged MTT to a non-infarcted region in the right hemisphere (Fig. 7.11, arrows). The CBF ratio of the right side to the left side was ~0.55. To evaluate the possible CBF underestimation due to the presence of delay in the arrival of the bolus to this area, the regional concentration time course was evaluated (Fig. 7.11). The gamma-

variate fitting indicated that the contrast agent arrived at both regions at approximately the same time (ΔBAT~0.01 s). Therefore, the ~0.55 ratio is likely (provided there was not a significant contribution from dispersion) to reflect a true ~45% reduction in flow compared to the left side. This area of decreased perfusion and normal T_2 and diffusion is believed to represent compromised tissue.

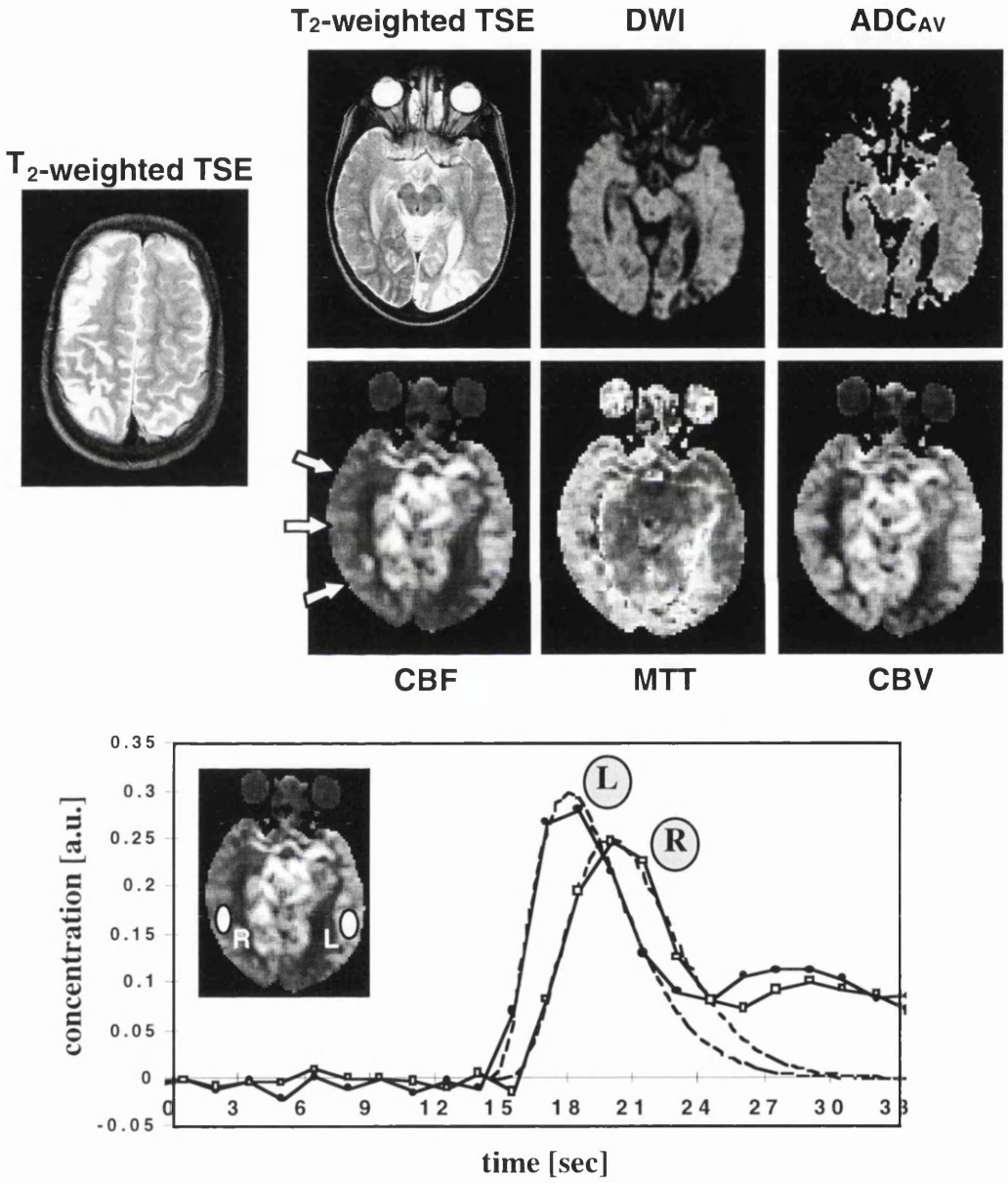

Figure 7.11.

Figure 7.11. Diffusion/perfusion mismatch in a 5 year old sickle cell disease patient. The T_2-weighted TSE data from two different slices show the mature infarctions. There is a large region of perfusion abnormality contralateral to the mature infarction in the bottom slice (arrows). This region appears normal in conventional MRI and diffusion imaging. The bottom graph shows the concentration time course for two regions together

with the corresponding gamma-variate fittings (dotted lines). One of the regions is on the side of the mature infarction (although with normal perfusion), and the other in the contralateral side, in the area of perfusion abnormality.

The last example of a much larger perfusion abnormality is from a 12 year old child with bilateral moyamoya disease (Fig. 7.12). This patient had old lesions involving the frontal watershed areas and the posterior left watershed area (white arrows). Although no abnormality was observed in the occipital areas using either diffusion or conventional MRI, this area has a perfusion abnormality (black arrows). A regional analysis of the concentration time course for two occipital regions and a normal region in the left basal ganglia showed that the contrast agent arrived at approximately the same time in the occipital regions, but was delayed ~2 s compared to the basal ganglia. Therefore, this delay introduced an underestimation in the calculated CBF in the occipital regions (Chapter 6). Although the delay to both sides was similar, the peak height and area were very different. The shape of the peak for the left occipital region (region 2 in the figure) is very similar to the basal ganglia region (ratio of the areas = 0.97), while it is much smaller for the right region (ratio of areas = 0.62). This suggests that perfusion is delayed to both occipital regions, but the deficit is more important in the right side, and therefore this region is at higher risk of stroke than the left.

7.3.2 Patients with sickle cell disease (Group II)

More than 50 children with sickle cell disease were scanned at GOSH using diffusion MRI, and a further 40 using diffusion and perfusion MRI. A qualitative analysis of the diffusion data (see *Future work* (Section 9.4 from Chapter 9)) suggests that diffusion alone is inadequate for the identification of tissue 'at risk' in this group of patients; there were some cases where diffusion MRI was unable to predict the region which later became infarcted, or to explain the clinical symptoms of the patient at the time of MR investigation. Figure 7.13 shows an example of a 12 year old sickle cell disease patient who presented with severe headaches and *left* hemiparesis. The scan performed 1 day

post symptom onset showed three haemorrhagic infarcts (one shown in the images) on the *left* side of the brain, without any evidence of recent abnormalities in ADC or T_2 on the *right* side. The follow up scan (3 days later) showed a new ischaemic infarct in deep watershed areas on the *right* side. Perfusion imaging was not available at the time of this patient's examination, but left sided symptoms suggest that it is likely there was a perfusion deficit on the *right* side at the time of the first scan, stressing the importance of a combined perfusion/diffusion evaluation.

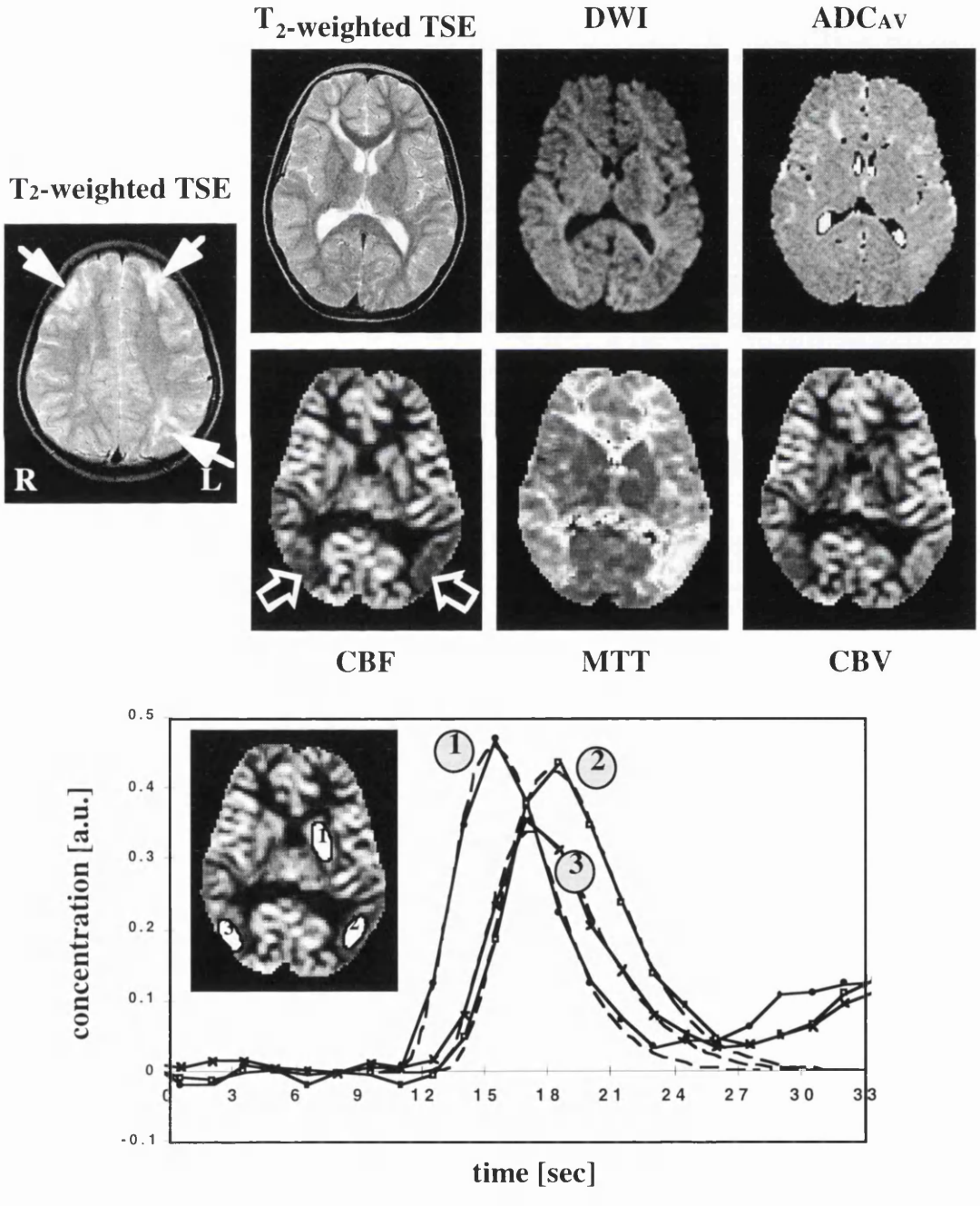

Figure 7.12.

Figure 7.12. Diffusion/perfusion mismatch in a 12 year old child with bilateral moyamoya disease. This child has mature infarctions involving the frontal watershed areas, and the posterior left watershed area (white arrows). The two rows show the MRI data from a different slice. Although no abnormality can be seen on conventional MRI or diffusion imaging in the occipital regions, there is a perfusion abnormality on both sides (open arrows). The bottom graph shows the concentration time course for the two occipital regions and a region in the left basal ganglia, together with the corresponding gamma-variate fittings (dotted lines). There is an ~1.5-2.0 s delay in the arrival of the bolus to the occipital regions compared to the arrival time at the basal ganglia.

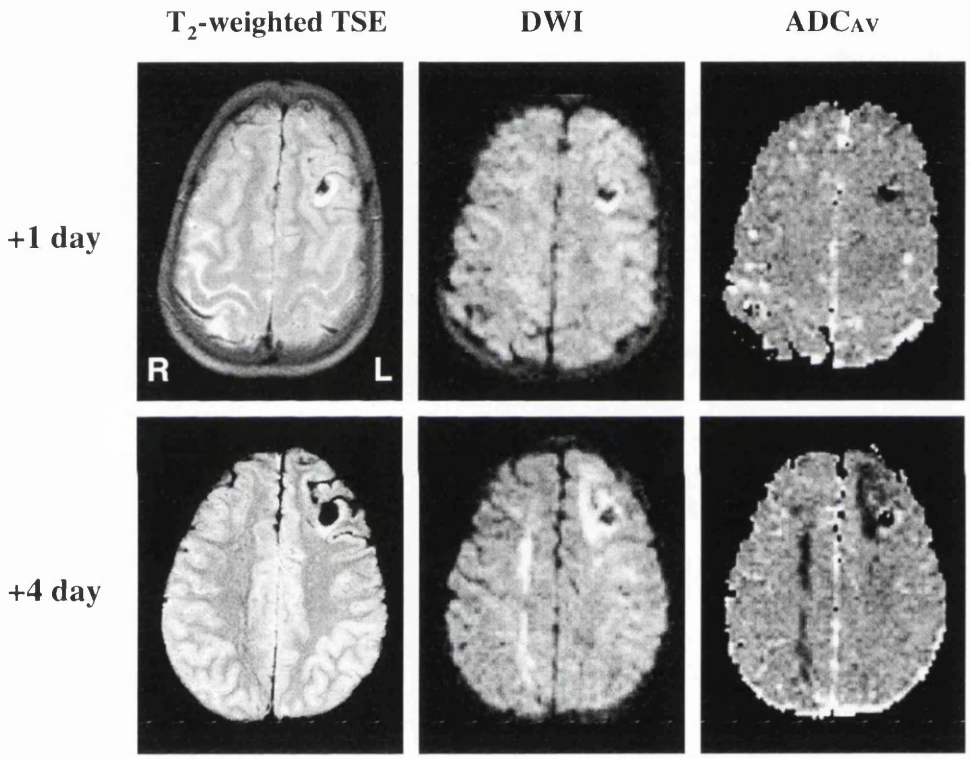

Figure 7.13.

Figure 7.13. MRI scans of a 12 year old sickle cell disease patient with *left* hemiparesis. Axial T_2-weighted TSE images (left), diffusion-weighted images (middle), and ADC_{AV} maps (right). The top row shows the images from the first scan (1 day post symptom onset). There is a haemorrhagic infarct on the left side of the brain (right side of the images). The bottom row shows the images from the second MRI scan (3 days later). A new ischaemic infarct in deep watershed areas on the *right* side can be seen as a region of decreased diffusion.

Although diffusion imaging alone was insufficient to predict further events in patients with sickle cell disease, combined diffusion/perfusion MRI was found to be of great help in the identification of tissue 'at risk' (as described in Section 7.3.1.3), as well as in the

contribution to patient management, and the evaluation of treatment outcome. These can be observed in the examples shown in Figures 7.14 and 7.15. The first example is from an 11 year old child with sickle cell disease who presented with severe headaches but otherwise normal neurology. No abnormalities were seen on conventional MRI and diffusion MRI (top row), but there was an extensive perfusion deficit on the right side (particularly in the anterior and posterior borderzones) and in a posterior region on the left. These are clearly seen as reduced CBF (arrows), and prolonged MTT (bottom row). This was consistent with the transcranial Doppler (TCD) findings; there was an abnormally high (>170 cm/sec) right MCA velocity of 203 cm/sec, consistent with a 40% risk of stroke in the next 40 months, and the left MCA velocity was 185 cm/sec, consistent with a 7% risk of stroke (Adams et al., 1998). These scans influenced management of the child, for on the basis of the diffusion/perfusion data, in conjunction with the high blood velocities, this child was considered to be at risk of stroke, and he was therefore treated by blood transfusion. A post-transfusion MRI scan has not yet been possible, but the post-transfusion MCA velocities measured with TCD were much lower (~150 cm/sec), and the child did not have a stroke.

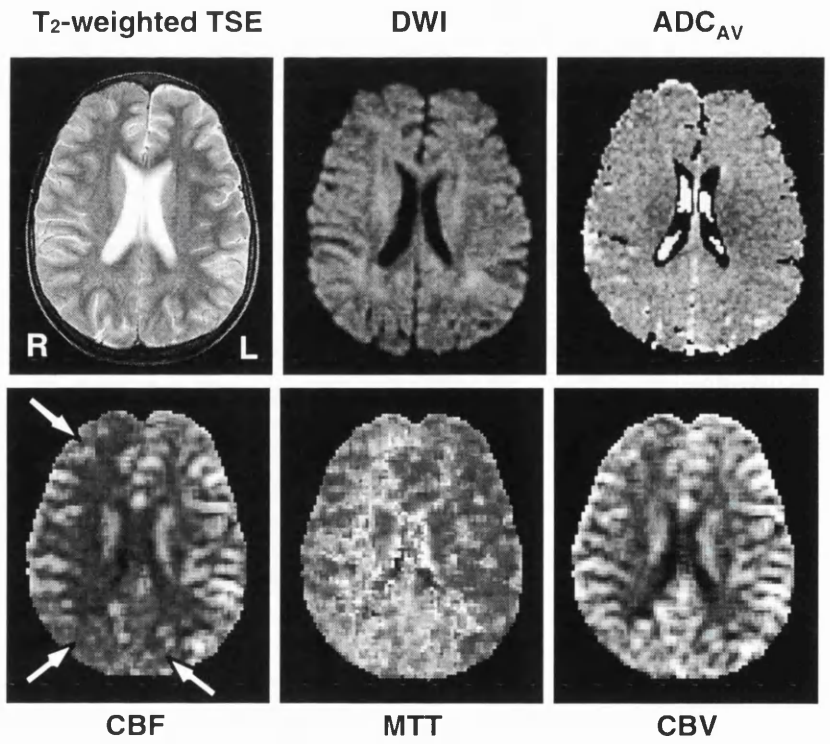

Figure 7.14.

Figure 7.14. MRI scans of an 11 year old sickle cell disease child who presented with severe headaches but otherwise normal neurology. The top row shows an axial T_2-weighted TSE image (left), diffusion-weighted image (middle), and ADC_{AV} map (right). The bottom row shows the CBF (left), MTT (middle) and CBV (right) maps. No abnormalities were seen on T_2 and diffusion MRI. There is an extensive perfusion deficit on the right side and in a posterior region on the left (arrows).

The next example shows a 15 year old boy who was scanned 1 day before (Fig. 7.15, top row) and 1 day after (bottom row) blood transfusion treatment. In this case, although diffusion/perfusion was not used in the decision to transfuse (the patient was already in ongoing treatment), it was of great help in evaluating the outcome of the treatment. Figure 7.15 shows a clear improvement in the perfusion deficit to the posterior right hemisphere, as compared to the scan performed before the transfusion (see arrows).

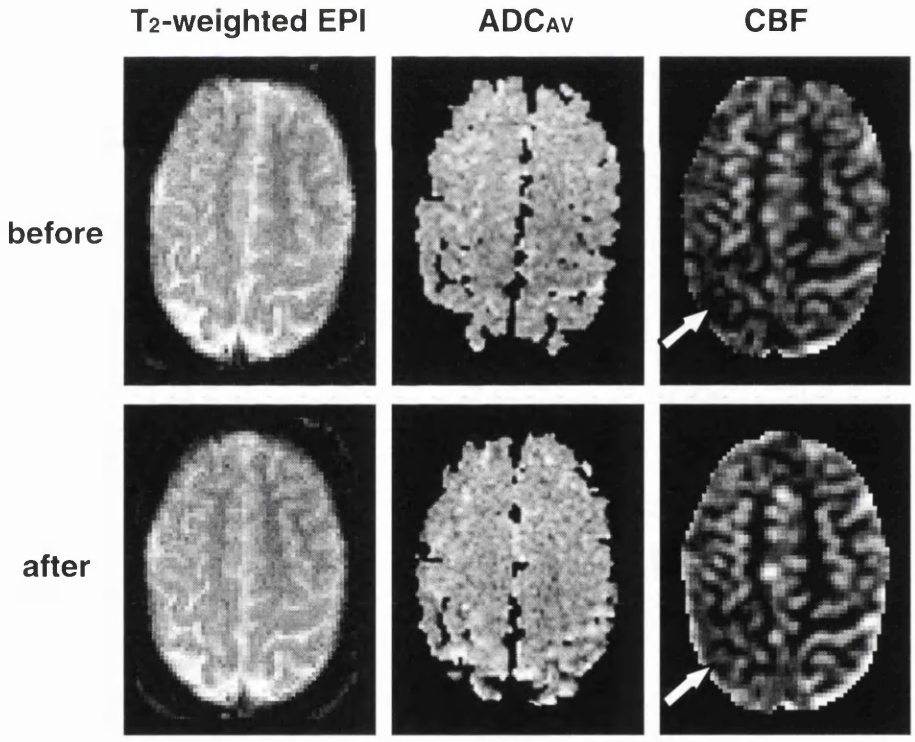

Figure 7.15.

Figure 7.15. MRI scans of a 15 year old sickle cell disease child 1 day before and 1 day after transfusion treatment. Axial T_2-weighted EPI images (left), ADC_{AV} maps (middle), and CBF maps (right). The top row shows the images from the MRI scan performed the day before blood transfusion, and the bottom row the images from the scan one day after. There is an improvement in the perfusion to a posterior region in the right hemisphere (arrows) after the transfusion.

It should be emphasised that the sickle cell disease patients represent an excellent group for the use of preventative therapy. In a normal elderly adult population, this is not possible in practice, and any therapy or treatment can be initiated only after an event has already occurred. The results presented above suggest that the combined use of MRI and TCD could be used to select patients with sickle cell disease at high risk of stroke who would be suitable for inclusion in the transfusion programme, even before a primary stroke has occurred. The simpler and quicker method of TCD, although it provides a more 'global' index (velocity in a large artery, reflecting the vascular supply of most of the corresponding hemisphere), may serve to pre-select patients for further investigation. A study is planned in which sickle cell disease patients with high velocities will be scanned using MRI to evaluate the degree and extension of the perfusion deficit associated with the particular TCD findings. MRI and TCD may also serve to evaluate the outcome of the treatment.

It should be noted that although in some of the cases presented above the only abnormality was observed in the perfusion data, the diffusion and T_2 information are still very important. With only the perfusion data it would not be possible to differentiate between tissue already infarcted (increased diffusion and prolonged T_2), cytotoxic oedema (decreased diffusion), and tissue 'at risk' (normal diffusion and T_2, but abnormal perfusion). Each of these cases is likely to require a different treatment approach (Barber et al., 1998), and therefore it is the combined T_2/diffusion/perfusion examination which makes MRI such a powerful tool.

7.3.3 Patients with moyamoya disease (Group III)

Ten children with moyamoya disease were scanned at GOSH using diffusion and perfusion MRI, of whom some were scanned both pre- and post-surgical treatment. Due to the particular cerebrovascular characteristics of moyamoya disease, a heterogeneous distribution of bolus arrival times was usually observed, with some areas displaying

large delays. Therefore, in most of the moyamoya disease cases, the conventional DSC-MRI analysis (deconvolution) is inappropriate, and the data should be analysed using summary parameters maps (Section 2.3.2.2.2). When revascularisation is performed, these delays are greatly reduced, and the deconvolution analysis might become more accurate, although some areas usually remain with long bolus arrival delays. One example of a child with moyamoya disease who was not revascularised was shown in Fig. 7.12. As discussed in Section 7.3.1.3, there is a large delay for the arrival of the bolus (ΔBAT~2 s) compared to normal regions.

As with the sickle cell disease group, diffusion/perfusion MRI made a significant contribution to patient management in moyamoya disease, as well as to the evaluation of the outcome of treatment. One such example can be seen in Fig. 7.16, which shows the images from an 8 year old child with bilateral moyamoya disease. This child had already been revascularised on the left (top row images), but there were still long delays to the right hemisphere, which was normal on conventional MRI and diffusion imaging. These findings suggested the presence of tissue 'at risk' of infarction. The child was then revascularised on the right side, and the middle row in Fig. 7.16 shows the images after this second surgical procedure. As can be seen, there is a significant improvement in the perfusion on the right: contrary to the scan pre-surgery, the bolus arrives even earlier than to the left (ΔBAT_{before} = 4.5 s, ΔBAT_{after} = -1.1 s). However, there are still delays (ΔBAT~4 s) to watershed areas (bottom row, see arrow).

The perfusion deficit to watershed areas was observed in most of the children who were scanned post-surgically. This suggests that the treatment is usually successful in improving the flow to the area directly affected by the surgery, although it seems unable to completely re-establish the perfusion to the watershed areas. Further follow up studies are needed to study the evolution of the perfusion status in these 'at risk' areas.

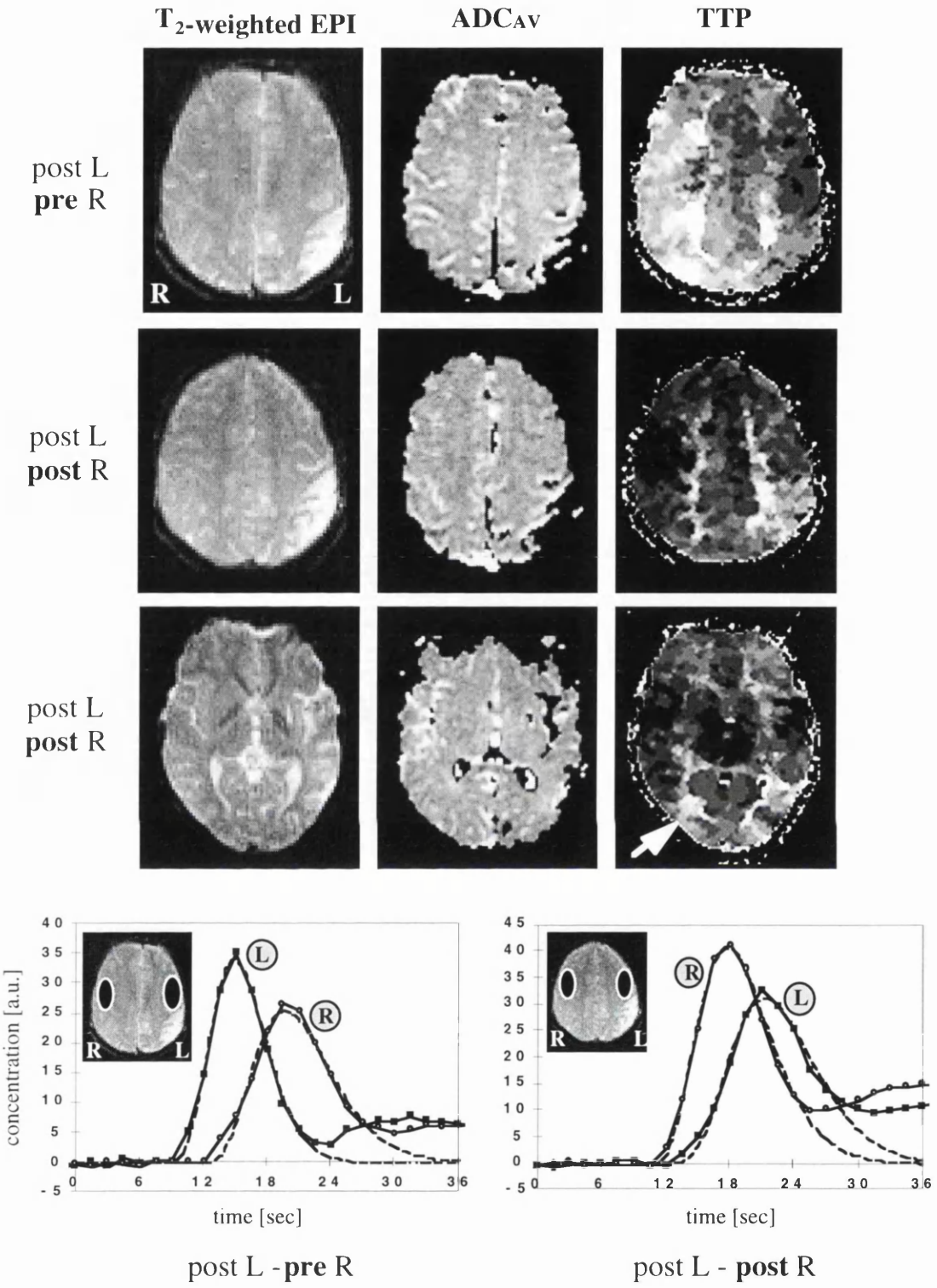

Figure 7.16.

Figure 7.16. MRI scans of a 8 year old child with bilateral moyamoya disease. T_2-weighted EPI (left images), ADC_{AV} (middle), and TTP maps (right). The top row images show the MRI data from the first scan (after surgery on the left and *pre* surgery on the right). There is a mature infarction in the left occipital lobe, and an extensive area of delayed perfusion of the contralateral side (which is normal on conventional MRI and diffusion imaging). The middle row shows the results after revascularisation on the right

side, with a significant improvement to the perfusion on the right. The bottom row shows the results from this second scan (post-surgery on the right) on a different slice, where there are still delays to watershed areas (arrow). The graphs at the bottom show the concentration time courses for two ROIs (one on each side) before (left) and after (right) the second surgery. There is a clear improvement to the perfusion on the right, which shows a bolus arrival even earlier than to the left.

However, revascularisation was not always successful in eliminating the clinical symptoms. One example is presented in Fig. 7.17, which shows the data obtained post-surgery (left and right) in a 13 year old child with bilateral moyamoya disease. Even after bilateral surgery, there were extensive areas with delayed perfusion (ΔBAT~2-4 s). The imaging findings were consistent with the clinical symptoms of multiple TIAs after surgery.

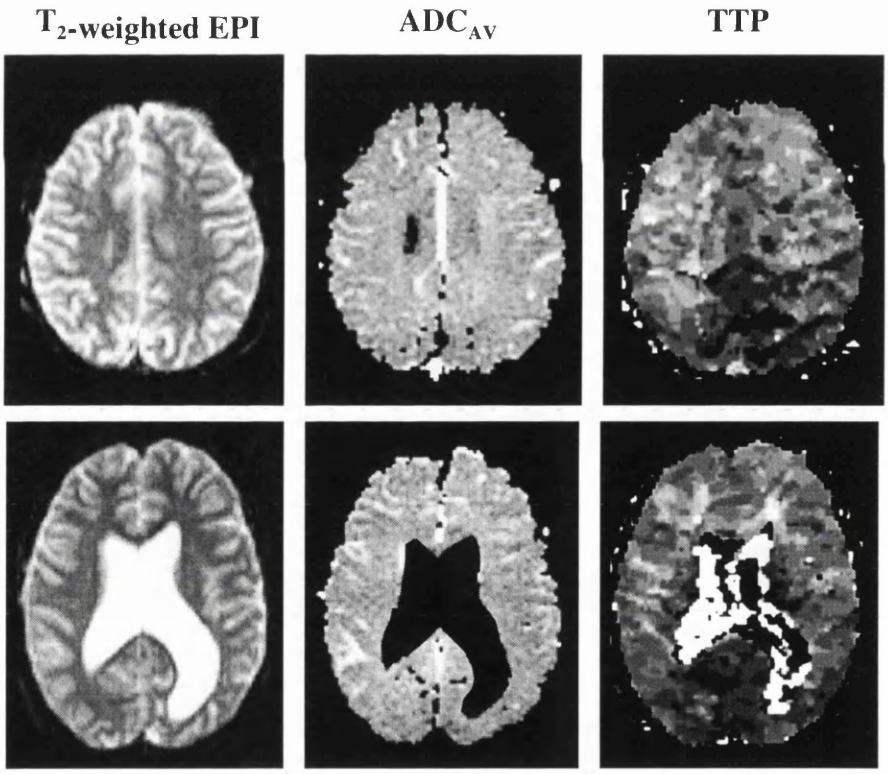

Figure 7.17.

Figure 7.17. MRI scans of a 13 year old child with bilateral moyamoya disease. The scan was performed after surgery on both sides, and the figure shows the result at two different slice positions. T_2-weighted EPI (left images), ADC_{AV} (middle), and TTP maps (right). There are extensive areas with delayed perfusion (fronto/parietal regions).

Therefore, the combined diffusion/perfusion study was found to be a very useful tool for the evaluation of the tissue status for pre-surgical treatment. Furthermore, DSC-MRI allows the assessment of the perfusion distribution after surgery. This can prove very important in the evaluation of treatment outcome, and in determining the optimal surgical technique.

7.3.4 Patients with other neurological disorders (Group IV)

As mentioned in Section 7.1.4, there are some cases in which diffusion and perfusion MRI help to establish aetiology and also to understand the underlying mechanisms of other neurological disorders. This section presents a description of longitudinal diffusion MRI measurements that aided understanding of (i) drug induced neurotoxicity and (ii) Sturge-Weber syndrome.

7.3.4.1 Cyclosporin neurotoxicity

A 9 year old child with sickle cell disease was administered cyclosporin after presenting with nephrotic syndrome. The child suffered a generalised seizure four days later, and several further events in the following three weeks. The diagnostic dilemma at that stage was whether this illness was a result of sickle cell disease requiring exchange transfusion.

MRI was performed at 2, 6, 21, 31, and 49 days after initial neurological symptoms, as well as before initiation of cyclosporin treatment (as part of the sickle cell disease screening programme at GOSH). Figure 7.18 shows the turbo spin echo (TSE) image, DW image and ADC_{AV} map for the scans performed before symptom onset and at 2, 6 and 49 days after symptom onset. In all the MRI scans after symptom onset, focal areas of increased T_2 can be observed. Each of these regions of T_2 abnormality was matched by an area of increased diffusion on the ADC_{AV} map. By days 31 and 49, the majority of

the lesions had resolved on the T_2 and diffusion MRI, although certain areas of increased T_2 persist and remained as high-signal areas on the ADC maps.

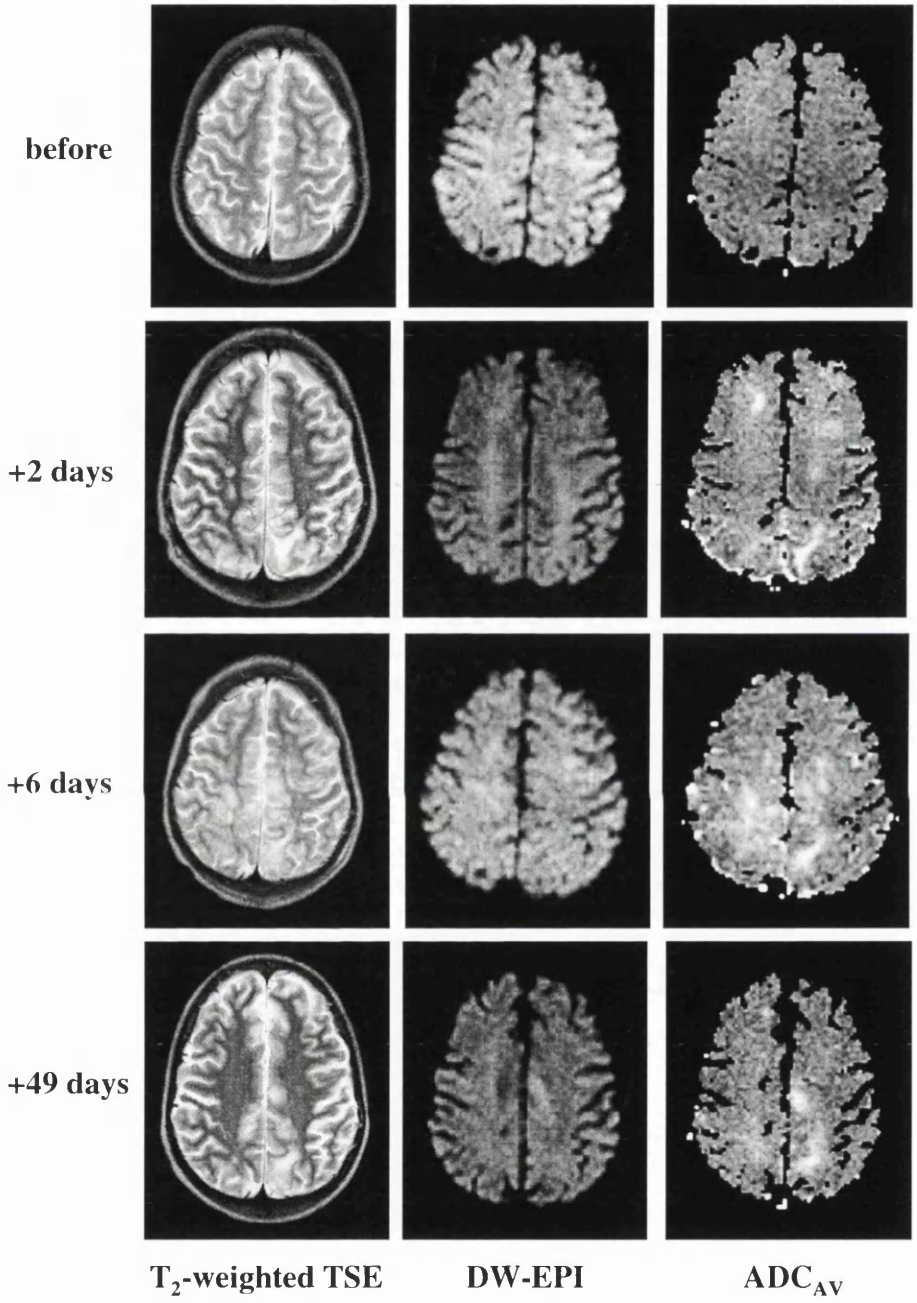

Figure 7.18.

Figure 7.18. Cyclosporin-induced neurotoxicity in a 9 year old child with sickle cell disease. MRI scans performed before initiation of cyclosporin treatment (top row), and 2 (second row), 6 (third row), and 49 (bottom row) days after initial neurological symptoms. Axial T_2-weighted TSE images (left), diffusion-weighted images (middle), and ADC_{AV} maps (right). Focal areas of T_2 hyperintensity and increased diffusion can be observed within both frontal and parietal lobes on all the scans performed after symptom

onset. By the time of the last scan, some of the lesions have resolved. None of the scans performed show any region with decreased diffusion associated with ischaemia.

Diffusion MRI provides a means by which cytotoxic oedema can be differentiated from vasogenic oedema. As mentioned in Section 7.1.4, it has been suggested that cyclosporin-induced neurotoxicity is caused either by ischaemia or by passive extravasation of fluid into the interstitium due to the disruption of the blood-brain-barrier. Since none of the T_2-weighted hyperintensities were associated *at any stage* with decreased diffusion (see *Diffusion MRI and cerebral ischaemia* (Section 2.2.5)), the neurotoxicity mechanism cannot be related to ischaemia. Furthermore, many of the lesions (which had increased diffusion) resolved. Therefore, the diffusion MRI data suggest that the cyclosporin-induced oedema is mediated by reversible fluid extravasation and not acute ischaemia.

Similar diffusion findings were observed in a 4 year old child who underwent bone marrow transplantation. Two days after commencing cyclosporin treatment the child suffered seizures. Figure 7.19 shows the images from an MRI scan performed within 24 hours of symptom onset. Bilateral regions of increased T_2 and diffusion can be observed at this early stage, consistent with the findings in the previous child.

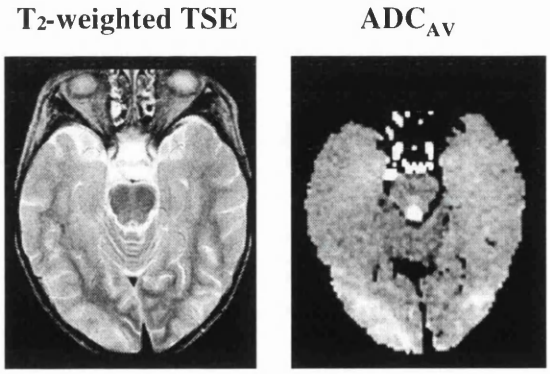

Figure 7.19.

Figure 7.19. Cyclosporin-induced neurotoxicity in a 4 year old child who underwent bone marrow transplantation. Axial T_2-weighted TSE image (left) and ADC_{AV} map (right) acquired approximately 2 days after commencing cyclosporin treatment. Bilateral areas of T_2 hyperintensity and increased diffusion can be observed in the occipital lobes.

The DWI findings were of particular value in the clinical management of the first child. Cerebral ischaemia secondary to sickle cell disease was considered as an alternative explanation for the T_2-weighted appearances, but because the diffusion data did not indicate the presence of ischaemia, exchange transfusions were not performed to lower the blood sickle concentration.

7.3.4.2 Sturge-Weber syndrome

Studies were performed on two patients with Sturge-Weber syndrome to investigate the diffusion properties of the abnormal tissue.

The first patient, a 4 month old girl with facial naevus since birth, was studied over a period of 10 months during which serial diffusion MRI measurements were performed. The child presented with status epilepticus 6 days before the first MRI examination, and intermittent seizures continued for 1 month. During this period, MRI was performed at 6, 12, and 25 days after initial presentation. The child was seizure-free for 3 months before a further MRI scan, which was performed 10 months after initial presentation.

Figure 7.20 (first column) shows MRI data from the first examination (6 days after initial presentation). An extensive region of T_2 hypointensity is clearly visible in the left hemisphere (right side of the image). This area shows reduced diffusion on the ADC_{AV} map. The post-contrast T_1-weighted image shows the angioma as a region of signal enhancement. A similar result was observed in the MRI scans performed at 12 (second column) and 25 days (third column) after the initial presentation, with a region of reduced T_2 and decreased diffusion. Although more extensive atrophy can be observed in the final scan (fourth row), interestingly, there is still an area of T_2 hypointensity and decreased diffusion 10 months after the initial presentation. The progressive atrophy can also be seen in the post-contrast T_1-weighted image. Figure 7.20 also shows the time course of the ratio of the ADC_{AV} of a ROI in the affected hemisphere to a similar region in the

contralateral side. There is a reduction of the ADC_{AV} (~20% decrease) which persisted for a period of 10 months. This time course contrasts with that observed in stroke (see Fig. 2.8 from Chapter 2) where a much larger reduction (~40%) is observed, and there is a 'pseudonormalisation' of the ADC_{AV} approximately 1 week after the onset.

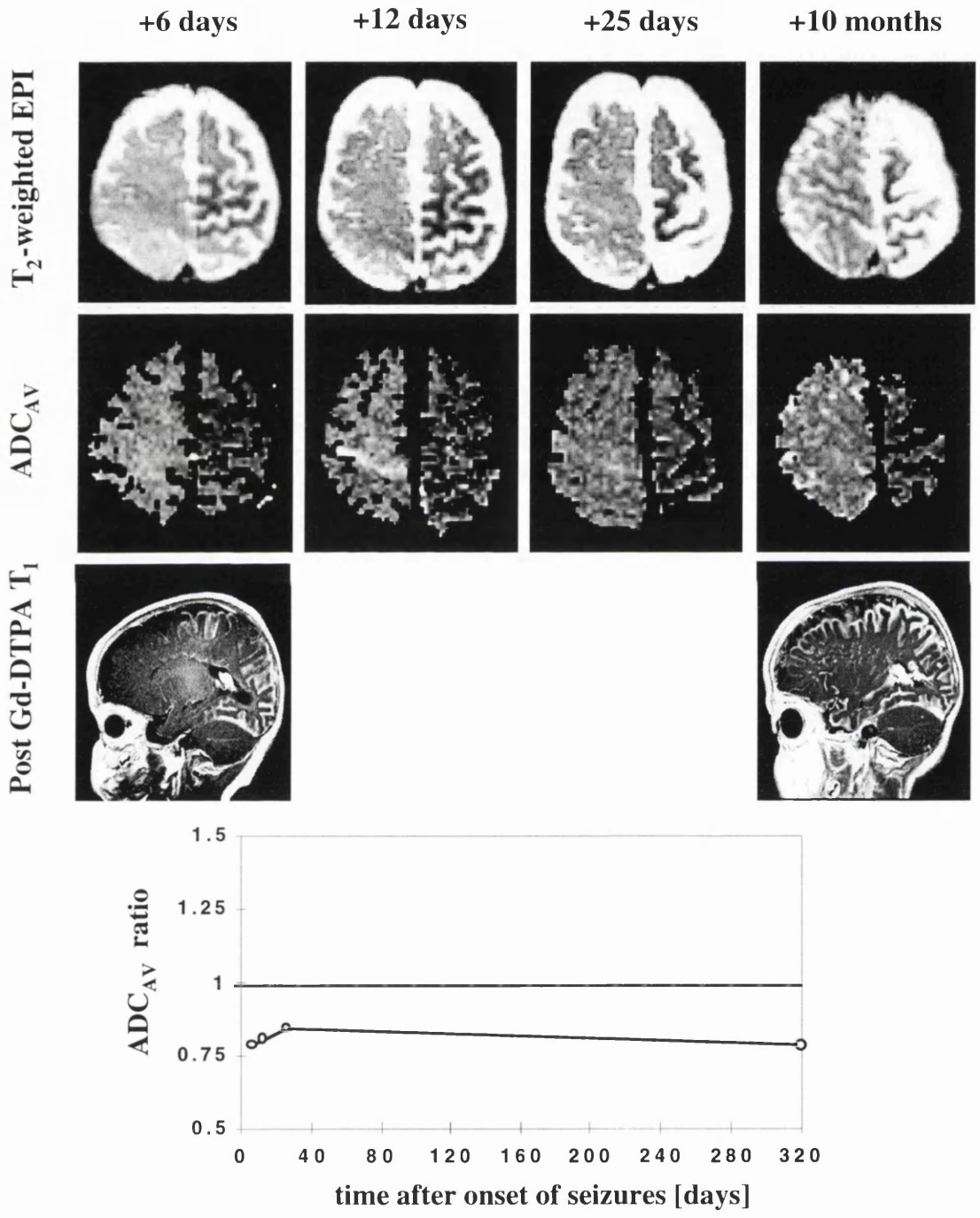

Figure 7.20.

Figure 7.20. Sturge-Weber syndrome in a 4 month old girl. MRI scans performed at 6 (first column), 12 (second column), 25 (third column) days, and 10 months (fourth

column) after initial presentation. Axial T_2-weighted EPI images (left), ADC_{AV} maps (middle), and sagittal post-contrast T_1-weighted images (right). A region of T_2 hypointensity and decreased diffusion can be seen in the left hemisphere (right side of the axial images) in all the scans performed. The angioma is shown as a region of signal enhancement in the post-contrast T_1-weighted images. A larger degree of atrophy is observed at the later scans, although there are still areas with reduced T_2 and decreased diffusion. The bottom graph shows the time course of the ratio of the ADC_{AV} of a ROI in the affected hemisphere to a similar region in the contralateral side.

More recently, a second child with Sturge-Weber syndrome was scanned. This was a 9 month old boy with facial naevus and emerging hemiparesis. He presented with facial twitching but no discharges on EEG. The MRI images (Fig. 7.21) show very similar results to the previous child: a region of T_2 hypointensity and reduced diffusion. In this case, the ADC_{AV} ratio was ~0.85.

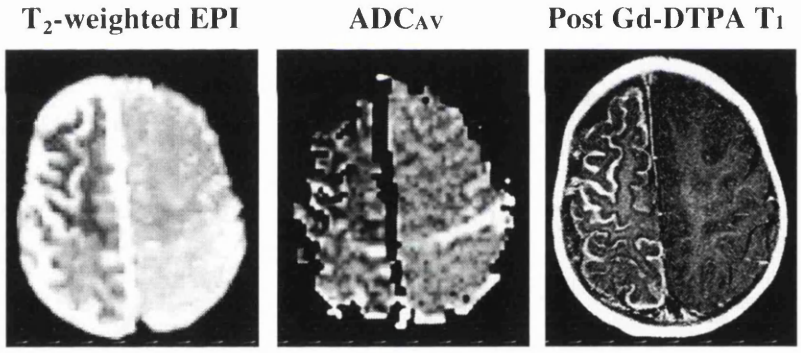

Figure 7.21.

Figure 7.21. Sturge-Weber syndrome in a 9 month old boy. Axial T_2-weighted EPI image (left), ADC_{AV} map (middle), and post-contrast T_1-weighted image (right). The scans show similar findings to these shown in Fig. 7.20. A region of reduced T_2 and decreased diffusion can be seen in the right hemisphere (left side of the images).

There has been evidence for reduced haemodynamic response to vasodilatory stimulus in Sturge-Weber syndrome. This was observed using CO_2 (Riela et al., 1985), acetazolamide (Okudaira et al., 1997), and during seizures (Aylett et al., 1999). Furthermore, the angioma is believed to be associated with decreased venous return and venous hypertension, which in turn produces ischaemia. The T_2 hypointensity is

consistent with increased levels of local deoxyhaemoglobin. The angioma, with its dilated veins, causes a large amount of deoxyhaemoglobin to be present within the region, which shortens the T_2 through a blood-oxygenation level dependent (BOLD) effect (Ogawa et al., 1990b). The diffusion data suggest that, not only is tissue compromised following prolonged seizure activity, but also that such a state can persist over a period of weeks. The combined diffusion/T_2 data are suggestive of tissue that is compromised, with an increased oxygen extraction fraction, but which has not proceeded into infarction.

However, in comparison to stroke, there is a reduction in the ADC_{AV}, but to a much smaller degree (only ~20%). Furthermore, there is a very different lesion evolution, with the ADC reduction persisting over a period of months. Therefore, it is possible that the reduced ADC values found ipsilateral to the haemangioma in both cases are not due to cell swelling (as in ischaemic stroke), but to background gradients from deoxygenated blood (Does et al., 1999). The comparatively large magnitude of the effect (i.e. 20% decreased in ADC vs. 6% at 2T in (Does et al., 1999)) may be related to the unusually high density of blood vessels associated with the haemangioma.

Abnormal perfusion and metabolism has been reported using PET and SPECT without any structural damage (Maria et al., 1998; Reid et al., 1997). This suggests a possible role for diffusion/perfusion MRI, which may help in the selection of suitable candidates for early neurosurgical intervention. Perfusion MRI was performed in both patients with Sturge-Weber syndrome, although the presence of the angioma introduces some technical difficulties in the interpretation of the DSC data: the slow venous outflow produces a significant contribution to the peak from recirculation of the contrast agent. Furthermore, due to the large amount of contrast agent in the angioma (with its dilated veins), the DSC-MRI data shows the angioma more than the tissue perfusion. However, this could be used to study the dynamic properties of the angioma, which is difficult to carry out using other techniques (Vogl et al., 1993).

7.4 CONCLUSION

As shown in this chapter, diffusion and perfusion MRI can add very useful information to that obtained using conventional MRI. They help in the understanding of the presenting aetiology, and in the identification of tissue 'at risk' of infarction. Furthermore, diffusion and perfusion can aid patient management and the evaluation of treatment outcome.

Combined diffusion/perfusion studies allow the identification of regions that are vulnerable to ischaemia, such as the watershed areas. These are regions in the interface between the territories supplied by different arteries, which are very susceptible to infarction. The mismatch area between the regions of diffusion abnormality and perfusion disturbance was found to identify these areas as tissue 'at risk' in many of the examples described in this chapter. This suggests that the combined diffusion/perfusion analysis can be sensitive enough to provide a characterisation of these areas. This can have important implications in patient management and outcome, as discussed in Section 9.1 in Chapter 9.

8. Early Changes in Water Diffusion, Perfusion, T_1 and T_2 During Focal Cerebral Ischaemia in the Rat Studied at 8.5 T

8.1 INTRODUCTION

Diffusion-weighted imaging (DWI) and measurements of the apparent diffusion coefficient (ADC) now provide a means of investigating early events in cerebral ischaemia (Moseley et al., 1990; van Bruggen et al., 1994; Hoehn-Berlage, 1995). As discussed in Chapter 2 (Section 2.2.5), the observed decrease in ADC coincides with the initial phase of cerebral oedema (cytotoxic oedema), characterized by a shift of water from the extracellular to the intracellular space. There is evidence that this process of cell swelling may be associated with energy failure and the resulting breakdown of ionic homeostasis within regions of severely reduced blood flow (Busza et al., 1992). Cell swelling may also occur as a result of osmotic changes associated with the accumulation of lactate (Kohno et al., 1995). In order to characterise the flow thresholds for these phenomena, and to investigate areas of more moderately reduced perfusion which are not visualised on DWI but which may nevertheless be at risk, there is considerable interest in combining ADC measurements with the measurement of tissue perfusion. T_2* measurements provide an additional approach to the early assessment of damaged or compromised tissue, because of their sensitivity to changes in the oxygenation state of haemoglobin (Ogawa et al., 1990a; Roussel et al., 1995).

All of these MRI techniques could prove valuable in the early diagnosis of cerebral damage and in guiding therapeutic interventions. In contrast, more conventional T_1- and T_2-weighted MRI investigations are generally regarded as being less useful in this early stage, because of their poor sensitivity to ischaemic events during the first few hours after stroke. Later on in the evolution of the disease process, however, there are increases in T_1 and T_2 that are believed to reflect changes in total water content associated with vasogenic oedema. However, animal experiments have shown that there is no direct relationship between the temporal evolution of total water content and changes in relaxation times (Knight et al., 1992; 1994; Helpern et at., 1993). This presumably reflects the fact that there are other factors apart from vasogenic oedema that can influence the observed relaxation properties of tissue, such as flow effects (Detre et al., 1992), alteration in the amounts of oxyhaemoglobin and deoxyhaemoglobin (Ogawa et al., 1990a; Thulborn et al., 1982; Gomori et al., 1987; Bryant et al., 1990), tissue oxygenation (Tadamura et al., 1997), and the exchange of nuclear spin magnetisation between the "free" and "bound" proton pools (Lynch, 1983; Ordidge et al., 1991). All of these effects could also influence T_1 and T_2 in the acute phase of stroke, and so the question arises as to whether early measurements of the relaxation times could provide additional information about the evolving pathophysiology of stroke.

In the studies described in this chapter, therefore, investigations of water diffusion, perfusion, T_1 and T_2 were carried out during the first 4-6 hours following permanent middle cerebral artery (MCA) occlusion in the rat. A high magnetic field strength (8.5 T) was used, which has well-recognised benefits for perfusion measurements (Detre et al., 1992), and which might also be expected to accentuate some of the effects that can influence relaxation times.

8.2.1 Animal preparation

Ten male Wistar rats, weighing 130-150g, were prepared for MCA occlusion, which was subsequently carried out remotely with the animal in the magnet. The surgical procedure was based on a modified Zea Longa approach (Zea Longa et al., 1989) adapted for a vertical magnet. Anaesthesia was induced with 3% halothane/O_2 and continued via a nose cone at 1.25% halothane for the duration of the surgery. Rectal temperature was recorded and maintained at 37.5±0.5°C. The remote occluding device was a blunted 0.24 mm nylon thread occluder, which was inserted into the internal carotid artery (ICA) and advanced to the origin of the carotid canal. By advancing a further 9 mm, the origin of the MCA could be occluded.

To minimise motion artefacts during imaging, the skin was reflected from the dorsal aspect of the skull and connective subcutaneous tissue removed between the lambda and bregma. A strip of clear plastic, securely fixed to the animal probe, was glued to the area of cleaned skull using an epoxy resin. No discernible image artefacts were produced from the epoxy glue. Once the animal was inside the magnet, the halothane concentration was reduced to 0.8% in a gas mixture of 70% N_2O and 30% O_2.

8.2.2 Imaging protocol

All experiments were carried out in an 8.5 T vertical magnet (Oxford Instruments, Oxford, UK) operating at 360 MHz, interfaced to a SMIS (Surrey Medical Imaging Systems, UK) console. The system has gradient coils with an internal diameter of 54 mm and a maximum gradient strength of 160 mT/m, with a minimum switching time of 200 μs. A 38 mm diameter birdcage coil was used as a radiofrequency (RF)

transmitter/receiver. The studies were performed in a single coronal slice (2 mm thick), approximately 7 mm from the interaural line.

The experimental protocol involved surgery, and approximately 2 h for positioning, shimming and the acquisition of control data (pre-occlusion), followed by remote occlusion of the MCA, and subsequent continuous imaging for 4-6 h (Fig. 8.1).

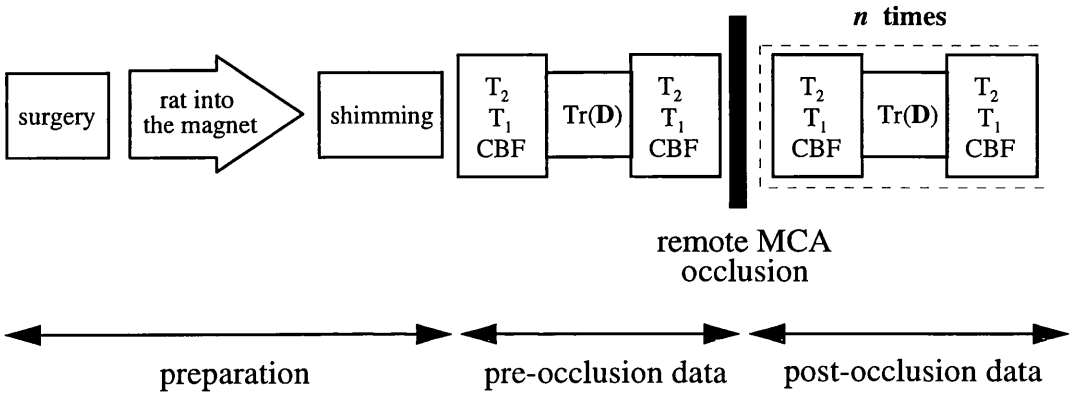

Figure 8.1.

Figure 8.1. Schematic description of the experimental protocol used for the experiments described in this chapter. It consisted of three parts: experiment preparation, acquisition of pre-occlusion data, and acquisition of post-occlusion data.

The following imaging sequences were used to study the time-course of each parameter:

- T_1 *measurement:* series of 20 TurboFLASH inversion recovery images (Deichmann and Haase, 1992). Imaging parameters were: TE= 2 ms; TR = 3.6 ms (231 ms per image); inter-FLASH delay = 2 ms and flip angle = 5°. To improve the signal-to-noise ratio (SNR), 20 averages were performed with a repetition time of 6 s. This inversion recovery sequence allows the measurement of T_1 in an efficient way by using a *single* RF inversion pulse, and sampling the recovery of the magnetisation by successive acquisitions of TurboFLASH images. However, the continuous application of low flip angles accelerates the recovery of the magnetisation:

$$M(t) = A - Be^{-t/T_1^*} \tag{8.1}$$

and a correction must be applied to convert the measured relaxation time (T_1^*) to the tissue T_1 (Deichmann and Haase, 1992):

$$T_1 = T_1^* \left(\frac{B}{A} - 1 \right) \tag{8.2}$$

For efficient spin inversion, a slice-selective adiabatic frequency offset corrected inversion (FOCI) pulse (Ordidge et al., 1996) was used. Figure 8.2 shows data from a typical inversion recovery data set (a), with the corresponding T_1 map (c). Figure 8.2b shows the dependency of the signal intensity on the inversion time for two regions of interest.

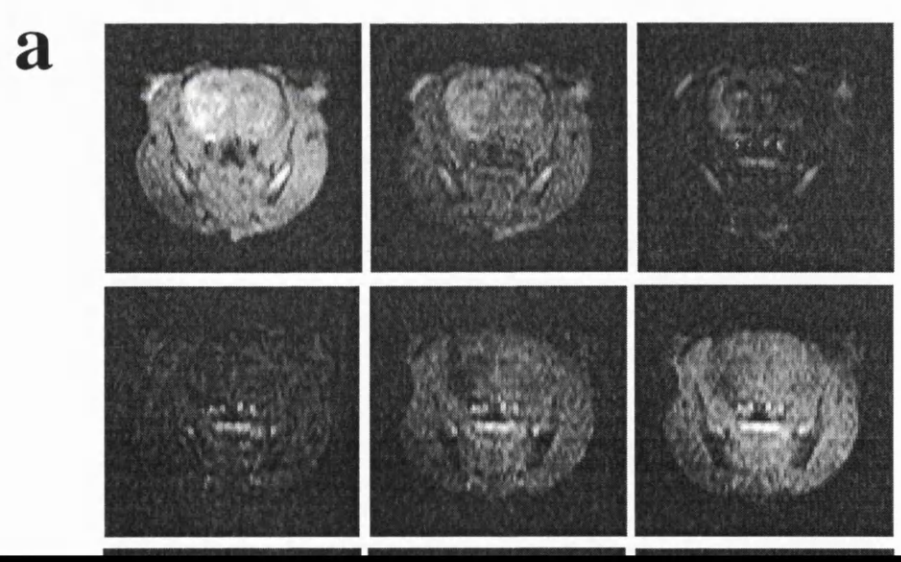

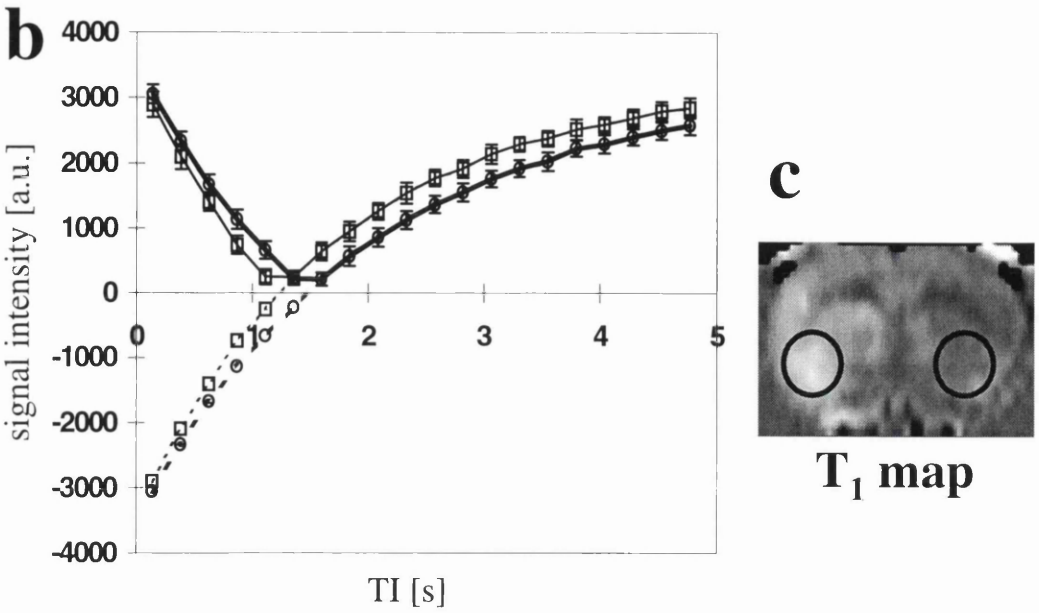

Figure 8.2.

Figure 8.2. Typical inversion recovery data in a rat ~4 h after MCA occlusion. Figure (a) shows 9 of the 20 inversion recovery TurboFLASH images (top left image: TI=380 ms, bottom right image: TI=2500 ms). The signal intensity (magnitude data) as a function of TI is displayed in (b) for two ROIs: an ipsilateral ROI (open circles and bold line), and a contralateral ROI (open squares and thin line). The dotted lines display the negative values for TI less than the 'null point', showing the typical inversion recovery single exponential decay. The error bars correspond to the SD in each ROI. Figure (c) shows the corresponding T_1 map and the two ROIs.

- *T_2 measurement:* four echo multi-spin-echo sequence. Imaging parameters: $TE_{\{n=1,4\}}$=35, 70, 105, 140 ms; TR=1000 ms. Four averages were performed to improve SNR. A multi-spin-echo sequence was chosen instead of a single spin-echo to minimise the acquisition time and, therefore, improve the time resolution. Furthermore, the effect of diffusion on the T_2 measurement using a multi-spin-echo sequence is minimised. Figure 8.3 shows a typical example of a T_2-weighted image, the corresponding T_2 map, and the dependency of the signal intensity on TE.

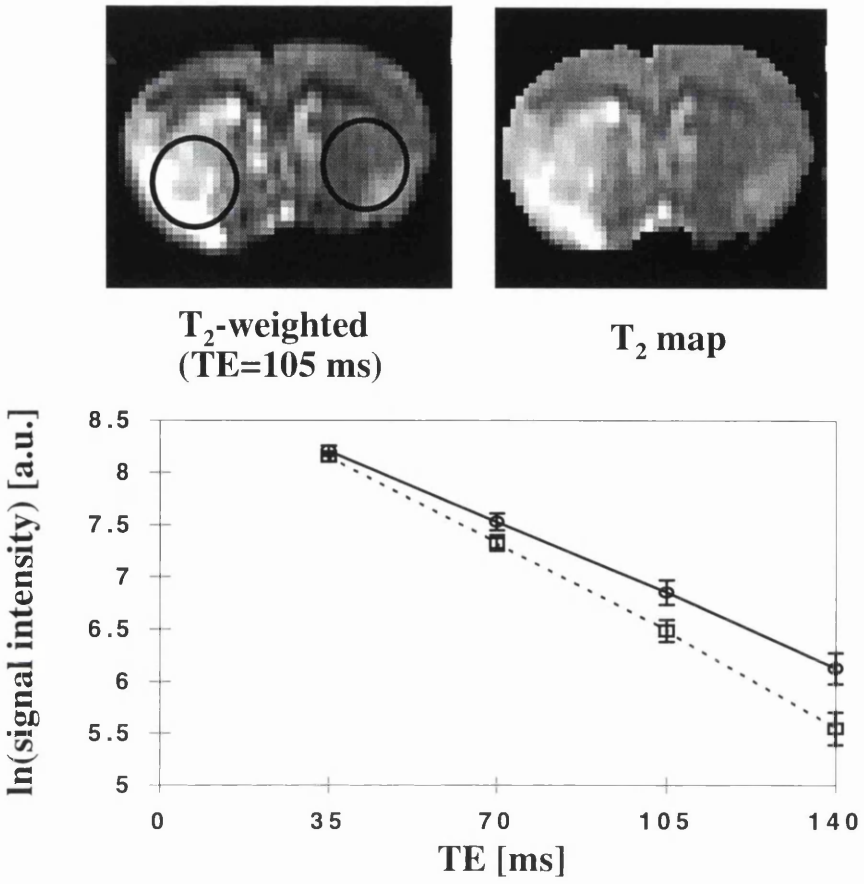

Figure 8.3.

Figure 8.3. Typical T_2-weighted image (3rd echo of the multi-SE data, TE=105 ms) and corresponding T_2 map for a rat ~4 h after MCA occlusion. The graph at the bottom shows the 'log' signal intensity as a function of TE for two ROIs (shown in the T_2-weighted image): ipsilateral (open circles and solid line), and contralateral (open squares and dotted line).

- *Trace of the diffusion tensor (Tr(***D***))*: single scan trace-weighted imaging sequence (Pattern III, Mori and van Zijl, 1995). Imaging parameters: TE= 80 ms; TR= 1000 ms. Diffusion parameters: δ=5 ms; Δ=5.4 ms (diffusion time = 3.7 ms); 3 *b*-values (30, 800 and 1700 s/mm^2), and 4 acquisitions were averaged for each *b*-value. This sequence has an intrinsically short diffusion time and long TE. This is in order to accommodate the various bipolar gradients needed to cancel the contribution from the off-diagonal terms of the diffusion tensor, thereby producing an image proportional to the trace (Mori and van Zijl, 1995). In this way, trace maps can be calculated directly from trace-weighted images without having to acquire separate

DW images in three orthogonal directions. Figure 8.4 shows typical trace-weighted images, together with the Tr(**D**) map.

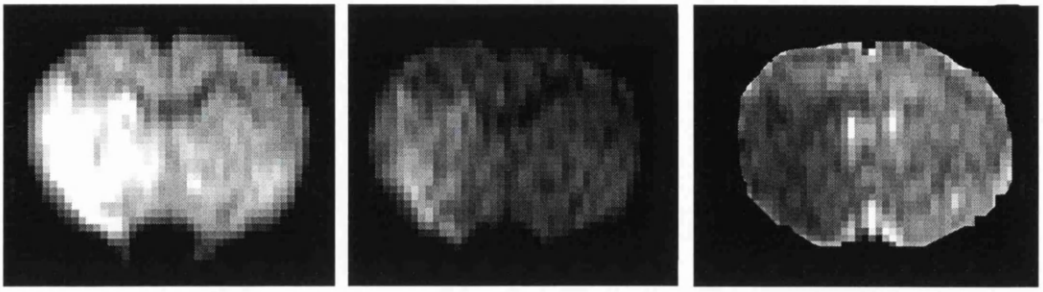

Figure 8.4.

Figure 8.4. Typical DW images (b-value=800 and 1700 s/mm^2), and corresponding Tr(**D**) map for a rat ~4 h after MCA occlusion. The graph at the bottom shows the 'log' signal intensity as a function of b-value for two ROIs: ipsilateral (open circles and solid line), and contralateral (open squares and dotted line).

- *Perfusion measurement*: two different sequences were used:

  Sequence I: continuous arterial spin labelling (CASL) (Williams et al., 1992) was performed inverting the arterial spins using adiabatic fast passage (Dixon et al., 1986). A 5 s continuous RF pulse was applied at a 9 kHz offset, in the presence of a field gradient (1.6 G/cm). This combination of parameters inverts a slice in the neck approximately 15 mm proximal to the imaging slice (Fig. 8.5). The 5 s 'tagging' is necessary to allow for a steady state to be reached. In this way, perfusion (f) can be calculated using Eq. (2.13) from Chapter 2.

  The labelling period was immediately followed by a TurboFLASH acquisition ('centre-out' phase encoding), with imaging parameters: TE= 2ms; TR=5ms (320ms per image); flip angle =14°. The 'centre-out' modality was chosen instead of the sequential phase-encoding for two reasons. Firstly, since the bulk of the image intensity is determined by the central portions of k-space, the

sequential approach will not represent the magnetisation at the end of the labelling period, but it will be further T_1-weighted due to the approach to a steady state with application of successive low flip angle RF pulses. Since the 'centre-out' approach acquires the centre portion of *k*-space at the beginning, this will be immediately after the end of the labelling period, therefore better representing the desired magnetisation. Secondly, the 'centre-out' approach allows for a larger RF flip angle to be used, increasing the SNR. Since the perfusion signal difference to be measured is very small (~6% at 8.5T), 25 acquisitions were averaged to further improve the SNR.

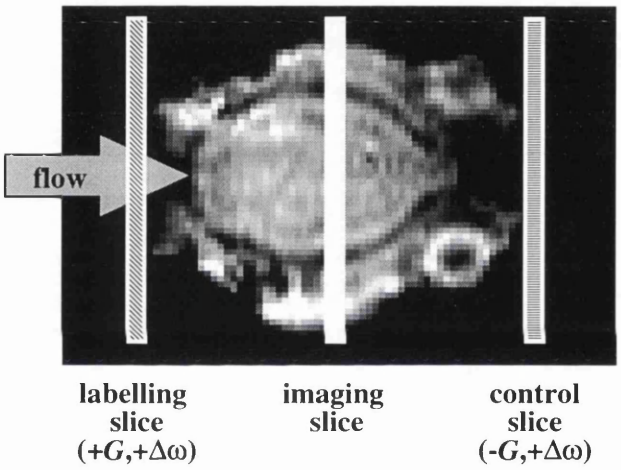

Figure 8.5.

Figure 8.5. Axial scout image of the rat brain, showing the schematic position of the imaging slice and control and inversion planes. The offset of the inversion pulse was chosen for each animal by altering the slice select gradient (*G*) until the plane of inversion was ~2 mm proximal to the rear of the brain in this image; this corresponded on average to a ~15 mm offset from the imaging slice. The control plane was then chosen by default to be symmetrically opposite by reversing the polarity of the slice-select gradient (and using the same frequency offset $+\Delta\omega$ for the off-resonance irradiation).

Since quantification using CASL is based on a steady state approach, it is not necessary to wait for full relaxation between averages; i.e., regardless of the initial state of the magnetisation, each steady state (M_b^{inv} for the labelling, and

M_b^{cont} for the control) will be the same (see Eqs. (2.14) and (2.15) from Chapter 2). Therefore, a delay of only 10 ms was introduced between successive perfusion measurements.

To account for the magnetisation transfer effects (see Section 2.3.2.1.1.1), control measurements were made by reversing the field gradient (Pekar et al., 1996). This effectively moves the 'tagging' plane to a position symmetrically opposite the imaging plane (see Fig. 8.5), and therefore the arterial blood magnetisation does not become tagged. The degree of arterial spin water inversion, α, was estimated in normal rats using Zhang's technique (Zhang et al., 1993). In this method, images are acquired at the level of the carotid arteries and the amplitude of the off-resonance RF is increased until a maximum (negative) signal is observed in the arteries. From these data a value of 0.71 was obtained for the degree of inversion [$\alpha=(M_{(RF=0)}-M_{(RF)})/2M_{(RF=0)}$]. Figure 8.6 shows an example of a spin labelled image, as well as a perfusion-weighted image (ΔM), and T_{1app} and perfusion maps.

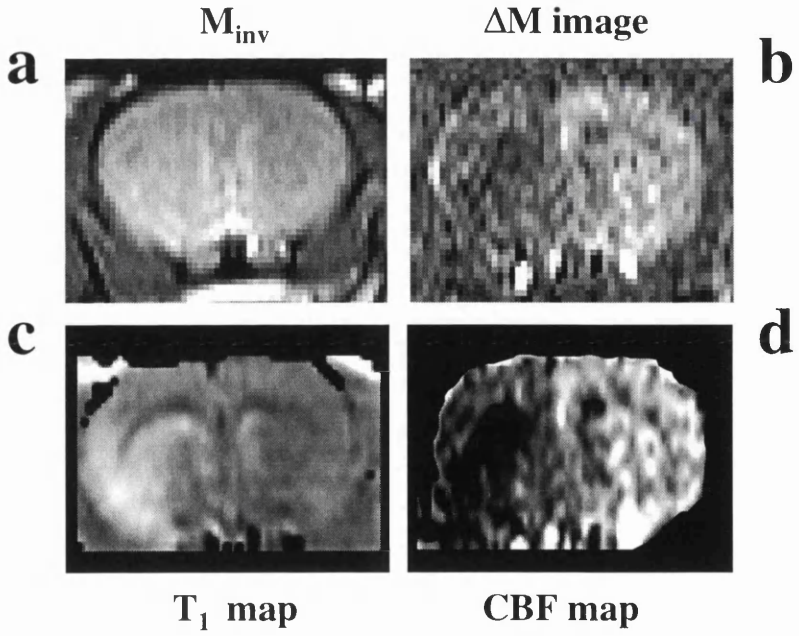

Figure 8.6.

Figure 8.6. An example of the images which are used to create a perfusion map. (a) shows the spin labelled image (M_{inv}) and (b) shows the result of subtracting this image

from the control image. A T_{1app} map (c) is then combined with these images according to Eq. (2.13) to produce a quantitative perfusion map (d).

Sequence II: after most of these experiments were completed, an improved protocol for obtaining quantitative perfusion maps was implemented (Alsop and Detre, 1996), in which a delay was introduced between the end of the tagging and image acquisition. As discussed in Chapter 2 (Section 2.3.2.1.1.2), this results in more accurate quantification because the contribution of vascular blood to the perfusion signal is suppressed. A further two normal animals were studied in order to assess the effect of a significant vascular signal contribution. A 500 ms delay was found to be necessary in order to produce an acceptable level of vascular signal (Fig. 8.7).

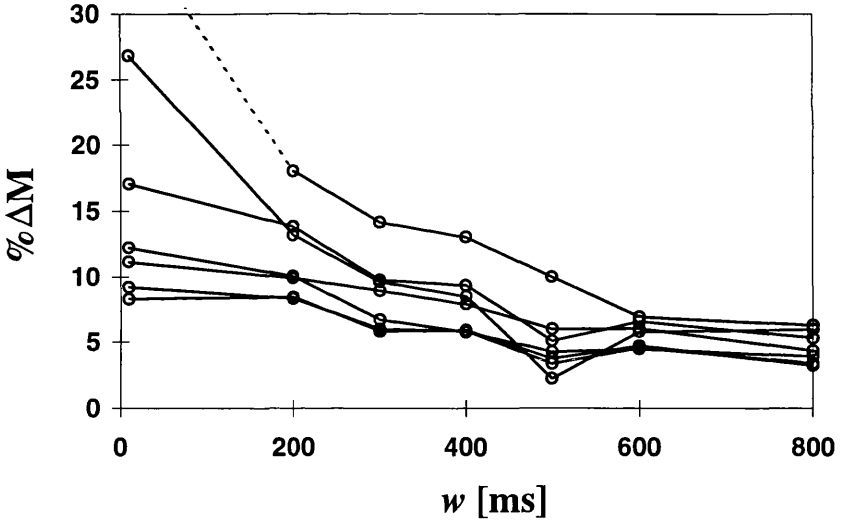

Figure 8.7.

Figure 8.7. Variation of measured perfusion weighted signal with length of post-labelling delay (*w*) in a control rat. Seven different grey matter ROIs including some contribution from bright vessels were selected. With very short delays (10 ms), perfusion is significantly overestimated due to the intraluminal signal contamination effects. With increasing delay, the intensity in regions with very high signal intensity rapidly decays, while the intensity in the regions selected for the absence of bright vascular structures remains almost constant with delay. All the regions have similar signal at delay of approximately 500 ms or greater.

For the quantification of perfusion using *sequence II* (see Eqs. (2.18) and (2.19) from Chapter 2), the T_1 of arterial blood (T_{1a}) was assumed to be 2000 ms, the transit time from the tagging plane to the capillary exchange sites of the vasculature (δ) was assumed to be 900 ms, and the 500ms post-tagging delay (w) was assumed to be larger than the time required for blood to flow from the tagging plane to the arteries within the vascular compartment (δ_a). The apparent T_1 in the absence of off-resonance radiation (T_{1ns}) was measured with an inversion recovery sequence (see Eq.(8.2)), and the apparent T_1 in the presence of off-resonance radiation (T_{1s}) was measured from the signal intensity dependency of the control images as the length of the off-resonance RF pulse (τ) was increased (Alsop and Detre, 1996):

$$M(\tau) = \left(M_b^0 - M_b^{cont}\right)\exp\left(-\tau / T_{1s}\right) + M_b^{cont} \tag{8.3}$$

Figure 8.8 shows perfusion-weighted images acquired with different post-tagging delays. It can be seen that for longer w, the contribution from vascular signal is reduced.

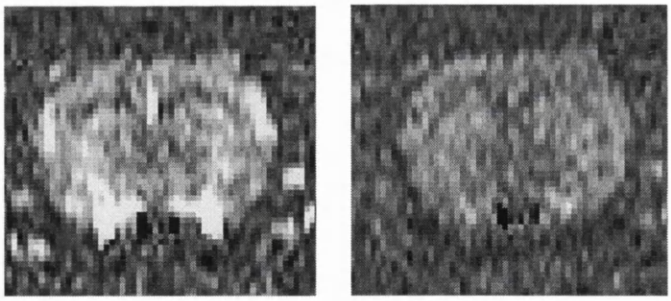

Figure 8.8.

Figure 8.8. Perfusion weighted images (ΔM) with two different post-labelling delays: 10 ms (left image), and 500 ms (right image). Although the longer delay reduces the signal difference between the control and labelled images, the image is not dominated by the very bright signal intensity from the vascular structures.

All the sequences used a 40 mm FOV and a 128x64 acquisition matrix size, which was then zero filled to 128x128 before Fourier transformation.

8.2.3 Data processing and analysis

Maps of T_1, T_{1s}, T_2 and Tr(**D**) were generated by non-linear curve fitting on a pixel by pixel basis using routines written with IDL software (RSI, Boulder, Colorado). Two-parameter fits (single exponential) were used with the T_2 and Tr(**D**) data, while a three-parameter fit was used with the T_1 (according to Eq.(8.1)) and the T_{1s} data (according to Eq.(8.3)). The T_1 maps were then used in the calculation of perfusion, using the corresponding equations (Eq.(2.13) for *sequence I* and Eq.(2.18) for *sequence II*). A constant uniform value of 0.9 ml/g was assumed for the brain-blood partition coefficient (Herscovitch and Raichle, 1985).

A study of the time dependence of the various MR parameters was performed in three regions of the brain (see Fig. 8.9). One region was positioned in the contralateral normal hemisphere, while the other two were in the affected hemisphere: one in the core, and the other in a border area of moderate ischaemia. The ROI in the core of the lesion was defined as the area with the largest change in diffusion, as seen on the Tr(**D**) maps at a late stage (4-6 h post-occlusion). It always lay within the thalamic and hypothalamic region, but its exact location was slightly different in each animal. A border region (in the frontal parietal cortex, between the areas supplied by the middle and anterior cerebral arteries) was defined in 8 of the 10 animals as a region of moderately reduced blood flow with no change in Tr(**D**).

In order to analyse the time evolution of the different parameters and to examine regional differences, separate multiple linear regression calculations were used to fit polynomials to the data obtained from each animal. This was done independently for the pre- and post-occluded phases, and the regression coefficients, or parameters

derived from them, were used as summary parameters in univariate analyses (Matthews et al., 1990). When a paired *t* test was used, the two animals that did not have a border region were excluded from the analysis. In order to document the absolute values of the various parameters, these are quoted as the 'mean ± standard error' over the total number of animals for each ROI (n=10 for the core and contralateral regions, and n=8 for the border region). It is important to note, however, that these standard errors were not used in any subsequent analysis of the within-subjects effects, which was performed using the paired *t* test and a selected summary parameter.

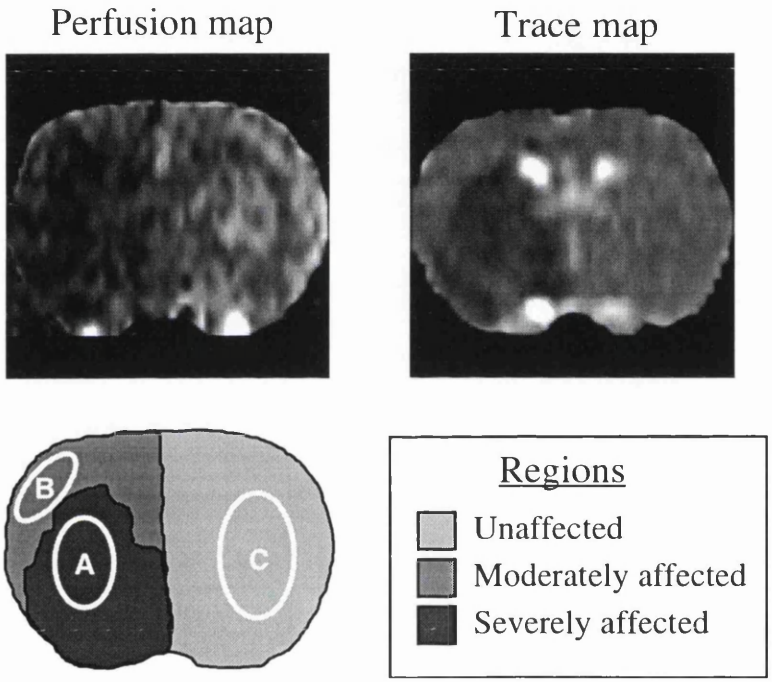

Figure 8.9.

Figure 8.9. Typical maps of perfusion and trace obtained from a rat ~4 h after MCA occlusion (top row). Schematic representation of the three main areas: "unaffected area", where a relatively small and transient reduction in flow was detected; "moderately affected area", with reduced CBF but normal Tr(**D**); and "severely affected area", in which both the CBF and Tr(**D**) were significantly reduced. The white ROIs represent typical regions used for the time-course analysis: core region (**A**), border region (**B**), and contralateral region (**C**).

Figure 8.9 shows calculated perfusion and Tr(**D**) maps ~4 h after MCA occlusion, together with a schematic representation of the three main areas that were used for all the subsequent analyses. Region (A) is a "severely affected area" in the core of the lesion, with reduced diffusion; region (B) is a "moderately affected area", with reduced cerebral blood flow (CBF) but no reduction in diffusion; and region (C) is an "unaffected area", where a relatively small and transient reduction in flow was detected. Figure 8.10 shows perfusion, Tr(**D**), T_1 and T_2 maps from a typical animal, and demonstrates regions of decreased CBF (~4 h post-occlusion), reduced diffusion (~4 h post-occlusion), increased T_1 (~5 min post-occlusion) and decreased T_2 (~1 min post-occlusion). In the following sections, the time-course data for perfusion, diffusion, and the two relaxation times in the three selected ROIs are discussed.

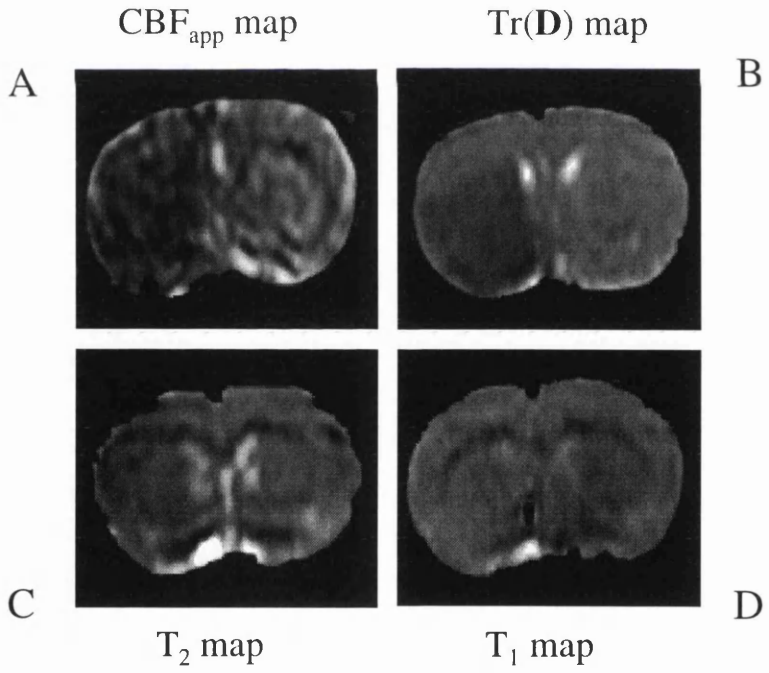

Figure 8.10.

Figure 8.10. Typical maps obtained from an occluded rat. Figure **(A)** shows a perfusion map, with reduced flow in the occluded side (time ≈ 4 h). Figure **(B)** shows a trace map (time ≈ 4 h), with a region of reduced diffusion. Figure **(C)** shows a T_2 map (time ≈ 1 min), with a region of reduced T_2. Figure **(D)** shows a T_1 map (time ≈ 5 min), with a region of increased T_1. The dark spot in the T_1 map is due to a DC artefact.

8.3.1 Perfusion (CBF)

Figures 8.9 (top left image) and 8.10a show typical perfusion maps obtained 4 h after occlusion, and Figure 8.11 shows the time-course data for the three ROIs. The mean CBF before occlusion was 186 ± 11 ml/100g/min (range 144-244 ml/100g/min) in the core region (Fig. 8.11a), 146 ± 8 ml/100g/min (range 111-175 ml/100g/min) in the border region (Fig. 8.11b), and 205 ± 14 ml/100g/min (range 128-248 ml/100g/min) in the contralateral region (Fig. 8.11c). The high CBF values and the large variability in the measurements is attributed, at least in part, to effects not accounted for in the quantification of perfusion, such as the contribution of vascular blood to the signal intensity (Alsop and Detre, 1996; Ye et al., 1997a), and the effect of magnetisation transfer (McLaughlin et al., 1997; Zhang et al., 1993). Both of these effects contribute to an overestimation of perfusion. The presence of a heterogeneous high vascular signal makes the measurement very dependent on the position of the ROI, and this could explain the large variability and the difference between regions prior to occlusion. Alsop et al (1996) and Ye et al (1997a) have recently shown that the flow rates are substantially overestimated when the vascular signal is not eliminated. Therefore, the values obtained in the present experiment with CASL (*sequence I*) are referred to as *apparent* cerebral blood flows (CBF_{app}).

It may be seen from Figure 8.11a that, after the initial drop induced by occlusion, the CBF_{app} in the core remained approximately constant. When CBF_{app} was less than ~20 ml/100g/min, the measured perfusion was within the noise level, which explains the negative data points. A decrease in CBF_{app} was also observed in the other two ROIs, with some of the rats showing a more variable flow in these two regions than in the core. This variability may be a reflection of autoregulation, which was lacking in the core of the lesion (Diarnagl and Pulsinelli, 1990). Due to this variability, and the intrinsically low SNR in the measurement of perfusion using MRI, the difference ΔCBF_{app} between the mean pre-occluded measurement and the average of the first two post-occluded values was used as a summary variable to study the drop in CBF_{app}.

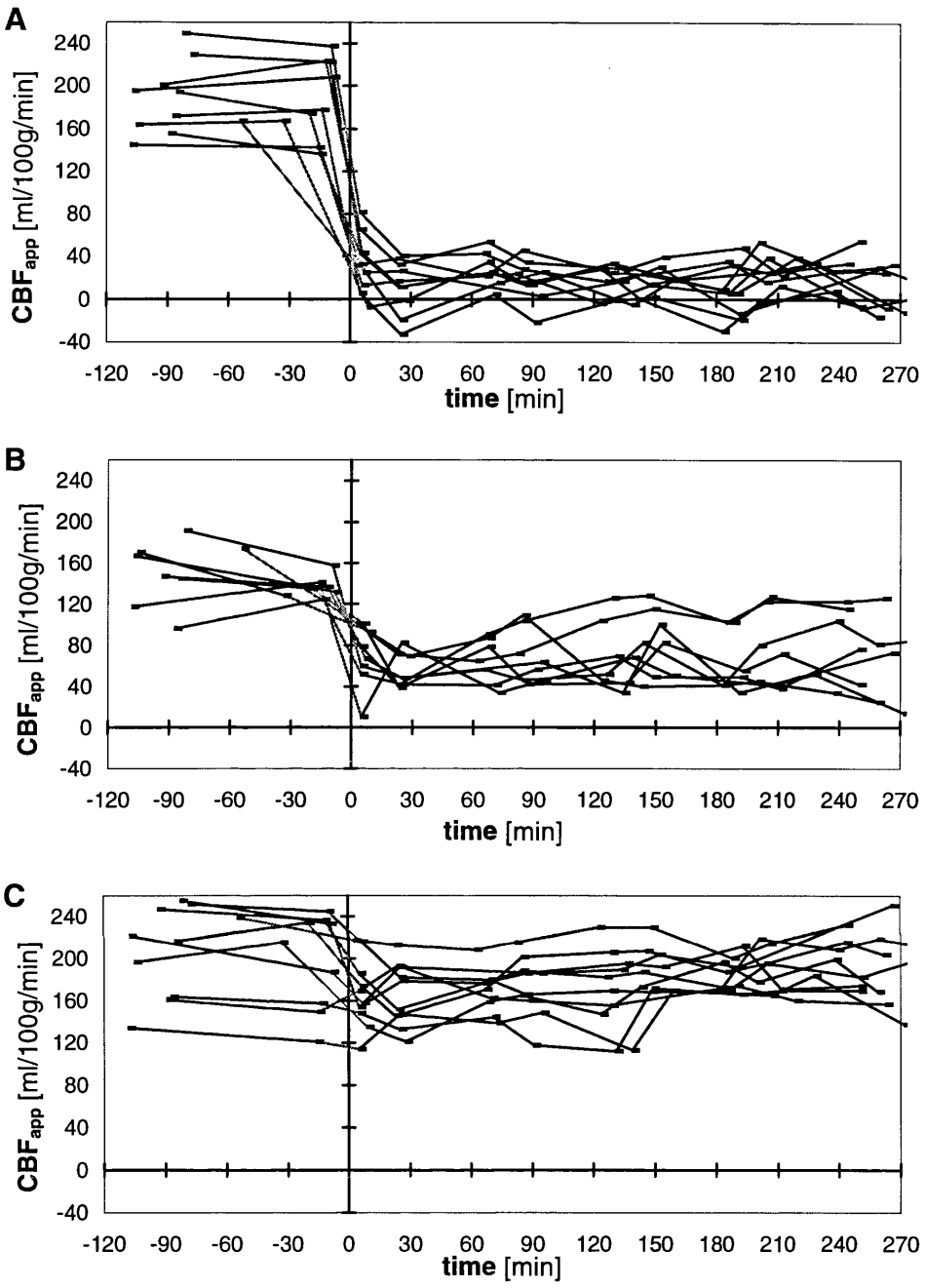

Figure 8.11.

Figure 8.11. CBF_{app} time-course for the core (**A**), border (**B**) and contralateral (**C**) regions. Each line represents the time-course for a different animal, and joins successive measurements. The origin on the time axis indicates the time of occlusion. The grey lines join the last pre-occluded measurement to the corresponding first post-occluded measurement for each animal.

Although both ischaemic regions showed a highly significant reduction in CBF_{app} ($p<0.0001$ for both regions), ΔCBF_{app} was significantly larger (paired *t* test, $p<0.0001$)

in the core (mean reduction = 163±8 ml/100g/min) than in the border region (mean reduction = 83±6 ml/100g/min). The relatively small initial flow change in the contralateral side (mean ΔCBF_{app}=39±11 ml/100g/min) was also statistically significant (p=0.01). After this initial drop, the perfusion in the contralateral hemisphere gradually returned to pre-occluded values.

As mentioned above, the absolute value of CBF was overestimated. A better estimation of the true perfusion values was obtained using *sequence II*, in which a delay is introduced between the end of tagging and image acquisition. Measurements were made using ROIs similar to those used for the present time-course analyses. The mean CBF values from two normal rats were compared to the values obtained when no delay was introduced (as was the case for the rats that underwent MCA occlusion). When no delay was used (*sequence I*), the mean CBF values (CBF_{app}) were 185, 187, and 208 ml/100g/min, in the areas that correspond to core, border, and contralateral region, respectively. These values are similar to the pre-occlusion values obtained from the MCA occlusion group. In contrast, when the delay was added (*sequence II*), the calculated CBF were reduced to 85, 93, and 90 ml/100g/min in these three regions.

Table 8.1 summaries the results from the analysis of the CBF data.

Table 8.1.

	MCA occlusion rats		normal rats
ROI	**CBF_{app} (pre-occlusion)**	**ΔCBF_{app} (initial change)**	**CBF (sequence II)**
contralateral	205 ± 14	39±11 (19%)	90
core	186 ± 11	163±8 (88%)	85
border	146 ± 8	83±6 (57%)	93

Table 8.1. Summary of analysis of CBF data. The CBF is expressed in units of ml/100g/min. The values in brackets correspond to the percentage CBF change from the pre-occluded values.

8.3.2 Water diffusion (Tr(D))

Figures 8.9 (top right image) and 8.10b show typical trace maps obtained ~4 h after occlusion, and Fig. 8.12 shows the time-courses of Tr(**D**). The normal pre-occluded Tr(**D**) values were 0.83±0.02, 0.81±0.01 and 0.83±0.01 x10^{-3}mm^2/s, in the core, border, and contralateral regions, respectively. In the core region (Fig. 8.12a), Tr(**D**) was reduced by ~23% relative to pre-occlusion at the first time point (t≈50 min). Thereafter, it showed a gradual decrease for ~2-3h after occlusion, towards an asymptotic value of 0.51±0.02 x10^{-3} mm^2/s. The time-course was very different in the border region (Fig. 8.12b), where no reduction in the Tr(**D**) was observed (p=0.9). Furthermore, a paired *t* test showed that there was no significant difference (p=0.1) between the asymptotic values in the border and contralateral regions, which remained unchanged throughout the experiment. The mean asymptotic values in these regions were: 0.80±0.01 x10^{-3} mm^2/s in the border and 0.82±0.01 x10^{-3}mm^2/s in the contralateral region.

Table 8.2 summaries the results from the analysis of the diffusion data.

Table 8. 2.

ROI	Tr(D) (pre-occlusion)	%ΔTr(D) (initial change)	Tr(D) (asymptote)
contralateral	0.83±0.01	-	0.82±0.01
core	0.83±0.02	23%	0.51±0.02
border	0.81±0.01	-	0.80±0.01

Table 8.2. Summary of analysis of diffusion data. The Tr(**D**) is in units of 10^{-3}mm^2/s. Only the values of %ΔTr(**D**) which achieved significance are displayed.

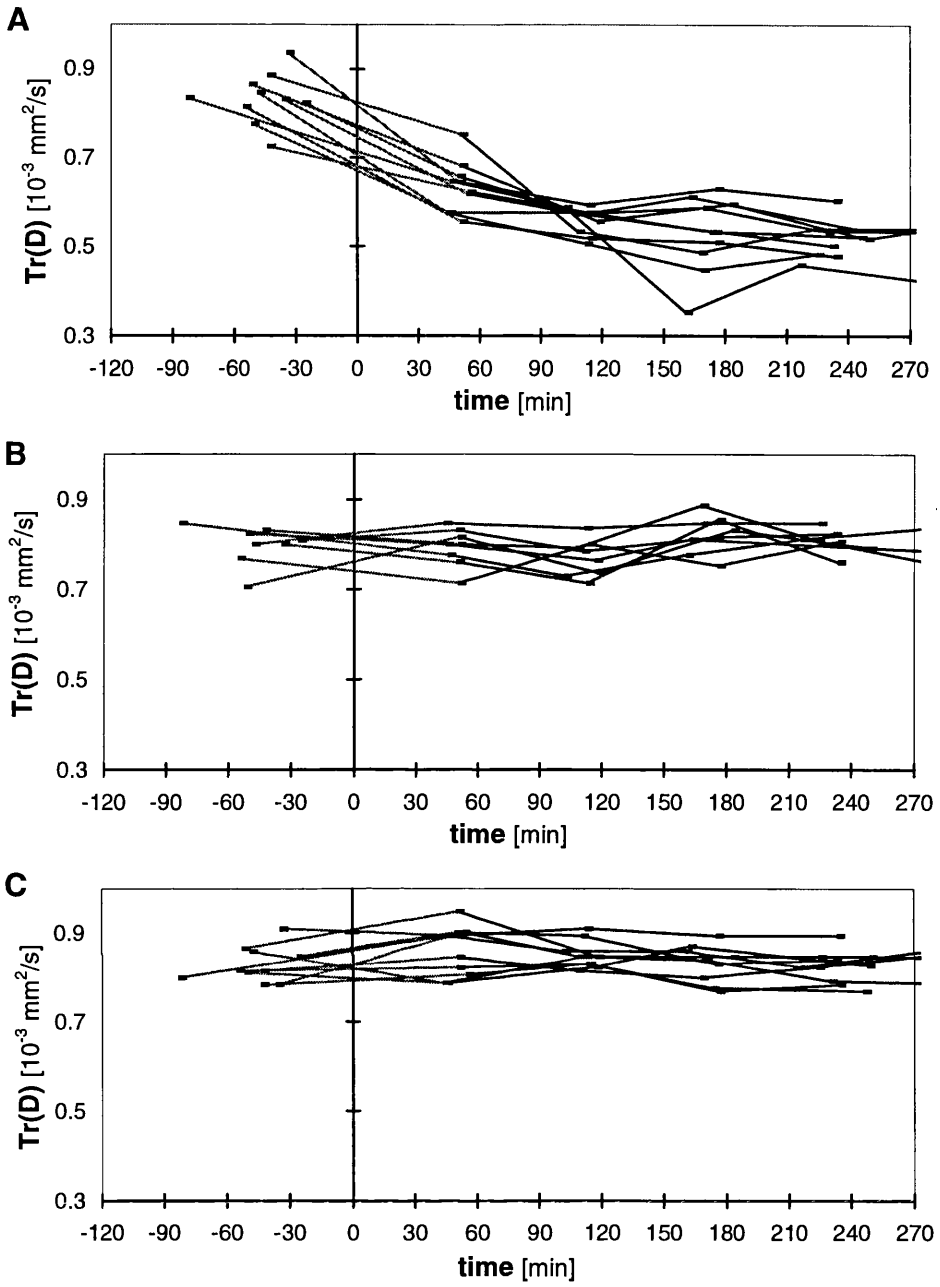

Figure 8.12.

Figure 8.12. Time-course of the trace of the diffusion tensor for the core **(A)**, border **(B)** and contralateral **(C)** regions. See legend to Fig. 8.11 for details.

8.3.3 Spin-spin relaxation time (T_2)

Figure 8.10c shows a T_2 map obtained ~1 min following occlusion, and Figure 8.13 shows the time-course data for the core (Fig. 8.13a), border (Fig. 8.13b) and the

contralateral (Fig. 8.13c) regions. The mean pre-occluded T_2 values were 42.5±0.9 ms in the core, 40.7±0.5 ms in the border region, and 41.8±0.7 ms in the contralateral region. A very rapid decrease in T_2 from its pre-occluded value was seen in all rats in both the border and core regions at ~1 min post-occlusion. After this early drop, the behaviour was different for each ROI. In the border region, T_2 returned to normal values (by 30-60 min after occlusion), thereafter increasing more slowly, while in the core region the T_2 values rose linearly for the duration of the measurements. An analysis of the T_2 changes for times >1 h was performed using the slopes obtained from linear regression analysis of the individual time-course data. The statistical procedure outlined by Dobson (1990) for comparing a reduced model against a full model showed that a first order polynomial provided an adequate description of the data for times >1 h. Both the core and the border region exhibited a statistically significant slope ($p<0.0001$ and $p<0.002$, respectively), with a mean value of 1.77±0.24 ms/h in the core, and 0.39±0.07 ms/h in the border region. A paired *t* test showed that these slopes were significantly different ($p=0.003$). In contrast, the slope in the contralateral region was not significantly different from zero ($p=0.7$), with a mean value of 0.08±0.17 ms/h.

The time resolution in the present study was insufficient to provide a detailed description of the time dependence of the rapid initial drop in T_2. Therefore, the difference between the average of the pre-occluded values and the first post-occluded measurement (time≈1 min) was used to characterise this initial decrease. Both the core (mean value = -2.19 ±0.29 ms) and the border region (-3.18±0.50 ms) yielded a statistically significant initial decrease ($p<0.0001$ and $p<0.001$, respectively), while the change in the contralateral region (0.19±0.32 ms) was not significant ($p=0.6$).

Table 8.3 summaries the results from the analysis of the T_2 data.

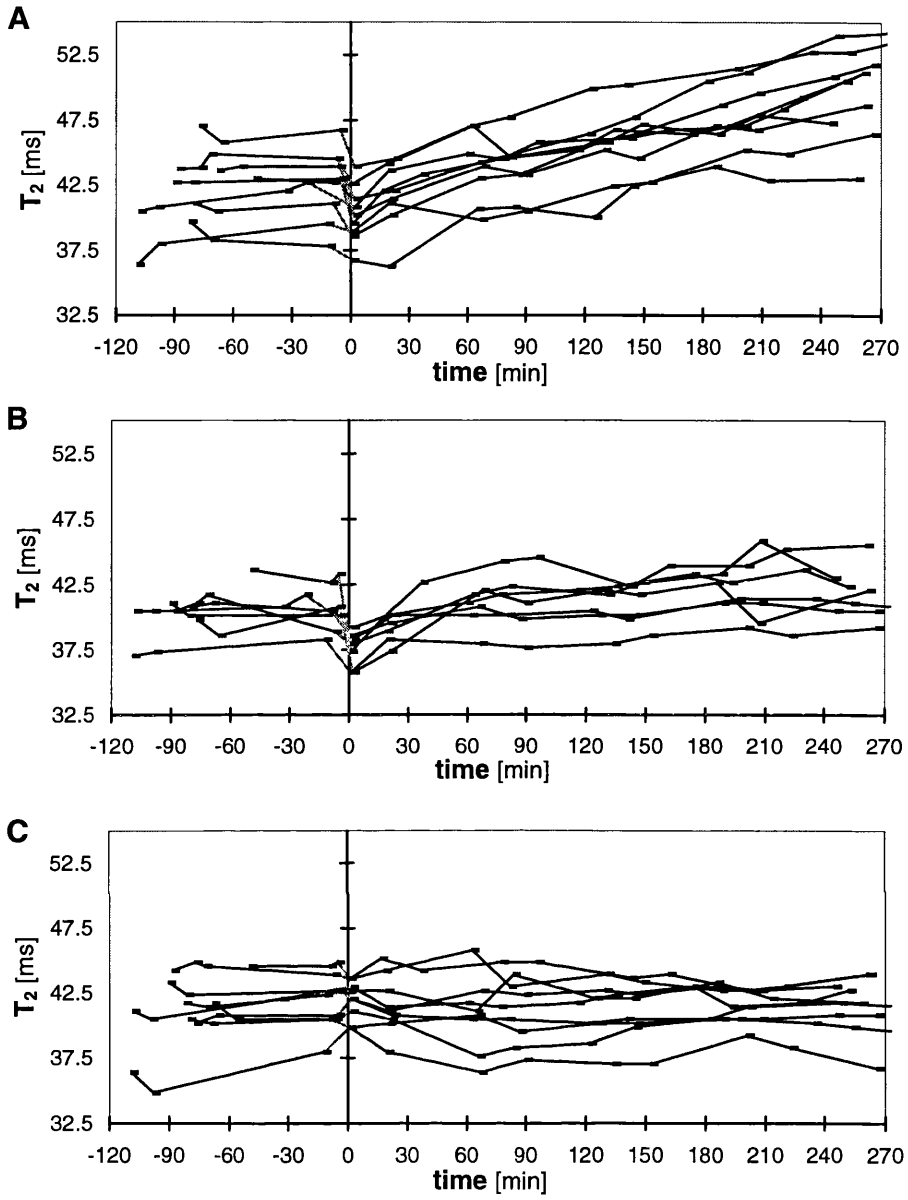

Figure 8.13.

Figure 8.13. T_2 time-course for the core **(A)**, border **(B)** and contralateral **(C)** regions. See legend to Fig. 8.11 for details.

Table 8.3.

ROI	T_2 (pre-occlusion)	ΔT_2 (initial change)	ΔT_2 (slope >1h)
contralateral	41.8±0.7	0.19±0.32 -	0.08±0.17 -
core	42.5±0.9	-2.19±0.29 (5%)	1.77±0.24 (4%)
border	40.7±0.5	-3.18±0.50 (8%)	0.39±0.07 (1%)

Table 8.3. Summary of analysis of T_2 data. T_2 is expressed in units of ms, and the slope (third column) is in ms/h. The values in brackets correspond to the percentage T_2 change from the pre-occluded values (only the values of $\%\Delta T_2$ which achieved significance are displayed).

8.3.4 Spin-lattice relaxation time (T_1)

Figure 8.10d shows a typical T_1 map obtained ~5 min following occlusion, and Fig. 8.14 shows the time-course data for the core (Fig. 8.14a), border (Fig. 8.14b) and the contralateral (Fig. 8.14c) regions. The mean pre-occluded T_1 values were 1718±25 ms in the core, 1756±18 ms in the border region, and 1676±30 ms in the contralateral region. A rapid increase in T_1 occurred in the two ischaemic regions within 5 min of occlusion (first post-occluded measurement). The time evolution after this early increase was different in these two regions, progressively increasing at a slow rate in the core, while it remained approximately constant in the border region.

The initial change in T_1 was too rapid, relative to the time resolution of this study, for its time dependence to be analysed. Consequently, the rapid and slow-response phases of the time-course data were examined separately. An analysis of the slow-response phase (t>25min) was performed by fitting separate polynomials to the T_1 data obtained from each animal. The individual values predicted by the regression model at 45 and 240 min were then used to calculate the rate of change in T_1 during this interval. The 45 and 240 min time points were selected in preference to the 25 min and last

measurement data because the confidence interval of the estimates increases at the extremities of the time interval. The mean rate of change of T_1 in the core was 46.1±5.5 ms/h, which is significantly different from zero ($p<0.0001$) while the mean value in the border region was -2.3±1.6 ms/h, which does not achieve significance ($p=0.2$). The value in the contralateral region was -5.6±1.9 ms/h, which is statistically significant compared with zero ($p=0.02$). This decrease in T_1 towards the pre-occluded values occurs simultaneously with the recovery in CBF in the contralateral ROI.

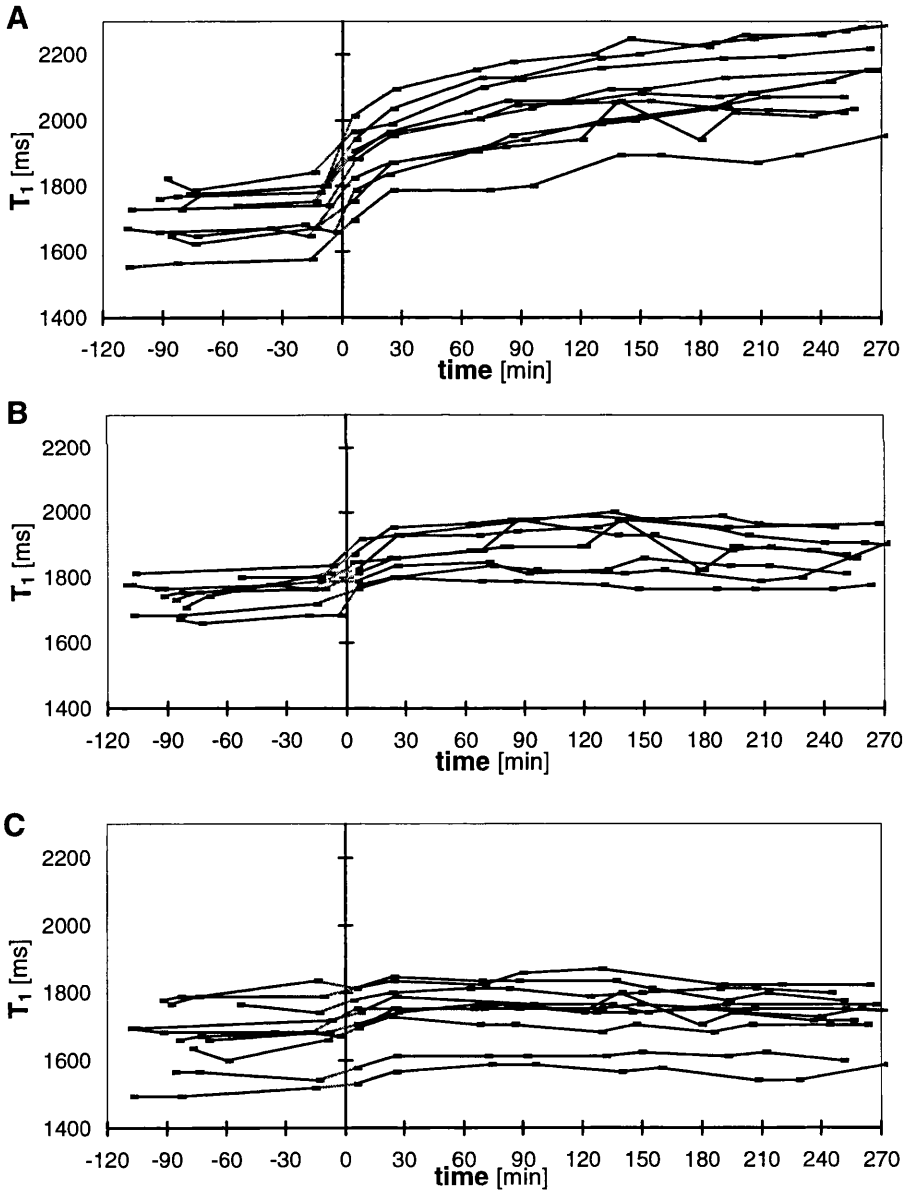

Figure 8.14.

Figure 8.14. T_1 time-course for the core (**A**), border (**B**) and contralateral (**C**) regions. See legend to Fig. 8.11 for details.

An additional characterisation of the differing T_1 behaviour in the three regions was obtained by examining the difference between the 45 min value predicted by the regression model and the average pre-occluded T_1 values. All three ROIs yielded differences that were significantly different from zero (mean values of 249±12 ms in the core, 126±10 ms in the border, and 68±7 ms in the contralateral region). The three pair-wise tests on the differences were also highly significant (paired *t* tests: core vs. border region, $p<0.0001$; core vs. contralateral region, $p<0.0001$; and border vs. contralateral region, $p=0.0005$), showing that the change was significantly different in each region.

Although it was not possible to analyse the time dependence of the rapid, initial T_1 change, the difference between the average of the pre-occluded T_1 values and the first post-occluded measurement ($t\approx5$ min) was used as a summary variable. The values obtained for the core (mean value =148±11 ms) and the border region (69±10 ms) were significantly different from the values obtained in the contralateral region (35±6 ms) (paired *t* test on the difference: $p<0.0001$ and $p<0.01$ respectively). The results demonstrate that high field MRI detects an immediate T_1 response to an ischaemic insult.

Table 8.4 summarises the results from the analysis of the T_1 data.

Table 8. 4.

ROI	T_1 (pre-occlusion)	ΔT_1 (initial change)	ΔT_1 (0-45min)	ΔT_1 (45-240min)
contralateral	1676±30	35±6 (2%)	68±7 (4%)	-5.6±1.9 (0.3%)
core	1718±25	148±11 (9%)	249±12 (14%)	46.1±5.5 (2.7%)
border	1756±18	69±10 (4%)	126±10 (7%)	-2.3±1.6 -

Table 8.4. Summary of analysis of T_1 data. T_1 is expressed in units of ms, and the 'slope' (fourth column) is in ms/h. The values in brackets correspond to the percentage

T_1 change from the pre-occluded values (only the values of $\%\Delta T_1$ which achieved significance are displayed).

8.4 DISCUSSION

Longitudinal measurements of CBF, Tr(**D**), T_1 and T_2 were performed in the acute (first 4-6 h post-occlusion) period after MCA occlusion in the rat. In this rat model of MCA occlusion, it was shown that T_1 and T_2 changes are observed at 8.5 T in regions of reduced blood flow within a few minutes following occlusion. These changes occur not only in the core of the lesion but, more importantly, in a border region where there is a much less severe reduction in blood flow and no reduction in the apparent diffusion of water. This region represents tissue 'at risk', and may represent the target for possible therapies.

Regional cerebral blood flow was measured using the non-invasive MR perfusion imaging technique known as CASL (Detre et al., 1992; Williams et al., 1992). In addition to the expected decrease in CBF in the occluded hemisphere there was also a small but significant decrease in the contralateral region. This phenomenon has been reported previously (Allegrini et al., 1996). It was shown that an autoregulatory response to the ischaemic insult in one hemisphere was the cause of the CBF changes in the contralateral side.

The measurement of perfusion using CASL offers many advantages, including its non-invasive character, the possibility of continuous monitoring, and direct spatial registration to other MR images. However, great stability is demanded from the MR system, and reliable quantification of perfusion remains a major challenge. Recent improvements in methodology have led to more accurate quantification (Alsop and Detre, 1996; Ye et al., 1997a; McLaughlin et al., 1997; Zhang et al., 1993). However, the very low CBF in the occluded regions introduces two main problems. Firstly, quantification of the resulting very small signal difference requires an extremely large

SNR in the two images used to obtain the difference. Secondly, there is an increased transit time from the magnetically tagged region to the imaging slice, and a more heterogeneous distribution of transit times throughout the slice, resulting in an underestimation of perfusion. The spins relax during the transit time to the tissue, and the true degree of spin labelling is decreased compared to the assumed value (in normal rats). This overestimation of α produces an underestimation of the calculated perfusion (see Eq.(2.13) from Chapter 2).

In the present study, a substantial reduction in the measured flow values was obtained in normal animals by using a technique in which a delay is introduced between the end of tagging and image acquisition (Alsop and Detre, 1996). Our preliminary findings in two animals, using a 500 ms delay (*sequence II*), gave mean normal perfusion rates that were ~50% of the values obtained without delay (*sequence I*). This result is not necessarily readily extrapolated to human studies, as measurements depend on several factors such as the vascular fractions, blood velocity, sequence time delay, and T_1 of tissue and blood. However, it is interesting that this reduction is similar to that obtained in human studies (Alsop and Detre, 1996; Ye et al., 1997a). The quantification using *sequence II* should in principle be more accurate, because it reduces the signal contribution from vascular water spins. However, validation studies are needed to substantiate the increased accuracy. Furthermore, the improved accuracy of this technique for measurements in the occluded region remains to be established. Although the sensitivity to different transit times is reduced with this technique (Alsop and Detre, 1996), the very long transit times present in the occluded regions may still be problematic. Any quantitative analysis of low CBF values must take these factors into account. It is for this reason that no attempts were made to estimate the flow thresholds for energy failure in this model of MCA occlusion. While the vascular contribution and the magnetisation transfer introduce an overestimation, the presence of long transit times underestimates the CBF. Therefore, the overall effect will depend on the relative contribution of these factors.

The high Tr(**D**) values reported in this study are to be expected due to the short diffusion time (t_d) used in the diffusion-weighted sequence (see Fig. 2.4 from Chapter 2). This pulse sequence was recently compared to a sequence with the same TE but a much longer t_d (25 ms). Although the measured Tr(**D**) values were different, the areas of reduced diffusion were not significantly different (Lythgoe et al., 1997), and the sequence was found to be accurate in the characterisation of the ischaemic region. Consistent with previous studies (van Bruggen et al., 1994; Hoehn-Berlage, 1995; Lythgoe et al., 1997), the diffusion measurements reported here show a decrease in ADC, with a reduction of ~40% in the trace of the diffusion tensor in the ischaemic core region after ~4 h of ischaemia. Moreover, the combined analysis of CBF and Tr(**D**) maps have allowed the definition of a region of moderate ischaemia (border region), where no reduction in diffusion was detected over a sustained period of 4-6 hours, despite the reduction in perfusion. Presumably the flow in this region remained above the threshold required to maintain the cellular energy status, so that the ionic and osmotic balance of the cells remained normal. Further studies may reveal whether the low ADC region does eventually expand into the border region, and whether this displays the same or higher flow thresholds when compared with the core region.

It is interesting to note that the border region in the present work is similar to one of the border regions defined by Jones et al (1989) in a study of CO_2 reactivity. This region showed a much lower reactivity of CBF to changes in arterial pCO_2, and they suggested that the tissue was haemodynamically compromised, and may become infarcted, representing therefore tissue 'at risk'.

The most striking finding in the present study is the observation of very early changes (within a few minutes following MCA occlusion) in the relaxation times T_1 and T_2, both in the border region as well as in the core region. A decrease in T_2 was observed immediately after a reduction in blood flow. Although a similar effect has been observed previously in spectroscopic measurements of water relaxation (Busza et al., 1994; van der Toorn et al., 1994) and a corresponding T_2* effect has been seen using

gradient-echo (GE) imaging (Roussel et al., 1995), there has been less emphasis on early T_2 changes in spin-echo images. A hypointense region using spin-echo imaging has been reported previously (Quast et al., 1993; Mancuso et al., 1995), but although a relatively long TR was used, complete separation of the T_2 from the T_1 contribution was not possible. The results shown in the present work clearly demonstrate a decrease in T_2 after ischaemia, which contrasts to the later increase in T_2 that is usually attributed to vasogenic oedema. Since this work was completed, a similar study of the acute T_2 changes in focal cerebral ischaemia in rats at 9.4 T was published (Gröhn et al., 1998). They detected similar decreases in T_2 following onset of ischaemia, as well as regions with T_2 decrease (4-15%) but without diffusion changes.

The similarity of the findings obtained with GE and SE imaging suggests a common underlying mechanism for the early decrease in T_2* and T_2 relaxation. One possibility is an increase in the amount of deoxyhaemoglobin (deoxyHb) in the ischaemic area. It has been proposed previously (Busza et al., 1994) that the initial T_2 change was due to the dephasing of water spins as they diffuse through the local field gradients caused by the accumulation of deoxyHb. This effect would be greater at 8.5 T than at the lower field strengths typically used for MRI, which may be the reason for the effect not being observed in investigations of cerebral ischaemia at lower field strengths.

More recently van Zijl et al (1998), based on the work of Bryant et al (1990), have suggested a vascular mechanism for the reduction in T_2, with the vascular water relaxation enhanced through fast exchange across the red blood cell membrane, and the tissue relaxation enhanced via a slow exchange with the more rapidly relaxing blood pool. Based on a mild hypoxic hypoxia model, they were able to account for the observed changes in T_2 using only this vascular mechanism. However, the extension of this model to cerebral ischaemia remains to be shown. Whatever the mechanism (diffusion or exchange), the reduction in T_2 is larger for single echo than for multi-echo acquisition. It should be noted that the dependency on the inter-echo spacing (τ_{CPMG}) is different for the two mechanisms (Bryant et al., 1990):

$$\frac{1}{T_{2app}} = \frac{1}{T_2} + \frac{1}{12} DG^2\gamma^2\tau_{CPMG}^2 \qquad \text{for diffusion} \qquad (8.4)$$

$$\frac{1}{T_{2app}} = \frac{1}{T_2} + p_i B^2 T_{ex}\left[1 - \frac{2T_{ex}}{\tau_{CPMG}} \tanh\left(\frac{\tau_{CPMG}}{2T_{ex}}\right)\right] \qquad \text{for exchange} \qquad (8.5)$$

where n is the number of echoes (or 180° pulses), D is the diffusion coefficient in an effective magnetic field gradient G, p_i is the probability of sampling the i-th environment, B is the change in resonance frequency associated with the exchange, and T_{ex} is the mean lifetime in the i-th environment. Further experiments characterising this dependency may differentiate between the two mechanisms.

It is notable that, although the reduction of CBF in the border region was less than in the core, there was no significance difference between these two regions with respect to the T_2 change (paired t test, p=0.09). Similar findings for T_2* were obtained using GE imaging (Roussel et al., 1995). However, interpretation of this regional similarity is difficult, for the levels of deoxyHb depend not only on CBF, but also on the cerebral blood volume (CBV), the oxygen extraction fraction (OEF) and the haematocrit levels. Moreover, the effect of the deoxyHb on T_2 may depend in turn on the diffusional properties of the water, which also differ between the core and border regions. The subsequent T_2 increase in the core region may be related to the partial recovery of the OEF (Pappata et al., 1993), or the compression of capillaries due to cytotoxic oedema leading to CBV reduction (Roussel et al., 1995). It may also reflect the development of vasogenic oedema over the time-course followed.

It should be noted, however, that due to the minimum TE used in the present study (35ms ~0.8 T_2), the T_2 measurements were weighted towards the long components (extracellular and, possibly, vascular fraction and CSF). Although the CSF contribution is negligible (particularly in the core), the small contribution from the vascular fraction

might be important and further studies are needed to characterise the different contributions to the observed T_2 effect.

The increase in T_1 occurred prior to the onset of vasogenic oedema, which is thought to be responsible for the elevated T_1 values at later times (and which may, at least in part, account for the slow component of the T_1 increase seen in the core region). These early T_1 changes have not been reported at low field strengths and the phenomenon may therefore be field dependent.

Although the early T_2 decreases in the core and border regions were indistinguishable in magnitude, the initial increase in T_1 was smaller in the border region. Furthermore, the mean rate of change after ~1h was significantly different from zero for T_2 but not for T_1. Therefore, in the present experiment, T_2 seems to be more sensitive than T_1 to the time dependent changes that occur in the border region. However, these observations may be sequence dependent, since it was shown that the T_2 measurements using a multi-spin-echo sequence are dependent on the inter-echo interval (Thulborn et al., 1982).

One possible explanation for the observed initial increase in T_1 is its dependence on flow. Since a selective inversion was used for the measurements of T_1, there is a flow contribution to the observed T_1 (see Eq.(2.16) from Chapter 2). Thus, before MCA occlusion

$$\frac{1}{T_{1app}^{(before)}} = \frac{1}{T_{1b}^{(before)}} + \frac{f_{before}}{\lambda} + k_f^{(before)} \tag{8.6}$$

while after occlusion

$$\frac{1}{T_{1app}^{(after)}} = \frac{1}{T_{1b}^{(after)}} + \frac{f_{after}}{\lambda} + k_f^{(after)}. \tag{8.7}$$

If the only change in T_1 is due to flow (i.e., $T_{1b}^{(after)}=T_{1b}^{(before)}$ and $k_f^{(after)}=k_f^{(before)}$), the percentage change in the observed T_1 can be expressed as:

$$\frac{\Delta T_{1app}}{T_{1app}^{(before)}} = \left(\frac{\lambda}{(f_{before} - f_{after})T_{1app}^{(before)}} - 1 \right)^{-1} \tag{8.8}$$

Using the more accurate technique described by Alsop et al (1996), the mean CBF value in normal rats (f_{before}) was measured to be approximately 90 ml/100g/min. Even in the extreme case of zero flow post-occlusion (f_{after}=0 ml/100g/min), a 90 ml/100g/min pre-occluded CBF would account for a change in T_1 of at most ~3%. However, a larger initial (t≈5 min) increase in T_1 was observed in the core (~9%). In order to explain the increase in T_1 as being solely a result of reduced tissue perfusion, a change of ~260 ml/100g/min in blood flow would be required:

$$\Delta f = f_{before} - f_{after} = \frac{\lambda}{T_{1app}^{(before)}} \left(1 + \frac{T_{1app}^{(before)}}{\Delta T_{1app}} \right)^{-1} \tag{8.9}$$

Even in this situation, the subsequent progressive increase in T_1 could not be accounted by flow alone, since T_1 continues to increase, without a further decrease in CBF. Therefore, although changes in flow can account for part of the observed T_1 increase, it cannot be the only effect responsible for this change, and there must also be a change in T_{1b} and/or k_f.

An effect associated with the paramagnetic properties of deoxyHb, as proposed for the early T_2 drop, is unlikely to play an important role since it has been shown that T_1 is much less affected by the levels of deoxyHb than T_2 (Thulborn et al., 1982; Gomori et al., 1987; Bryant et al., 1990). Another possibility is the loss of O_2, which acts as a relaxation agent in tissue due to the paramagnetic properties of molecular oxygen itself. It has been shown previously (Tadamura et al., 1997) that T_1 is modified by alterations

in the dissolved O_2 concentration, although the response was dependent on the tissue type. After ischaemia, the amount of dissolved O_2 would be reduced, leading to an increase in T_1. The effects of deoxyHb on T_2 and dissolved O_2 on T_1 changes are similar to the situation observed using paramagnetic MR contrast agents, such as Gd-DTPA (see Fig. 2.9 in Chapter 2). In the case of an intact blood-brain barrier (BBB), the contrast agent remains intravascular and the main effect is a T_2 decrease. On the other hand, when there is BBB breakdown, the contrast agent is dissolved in the tissue producing a significant effect on T_1. Therefore, the deoxyHb (in a similar way to the situation of an intact BBB with contrast agents) would mainly affect T_2, while the dissolved O_2 (similar to the situation of BBB breakdown with contrast agents) would mainly affect T_1.

Another possible cause of the increase in T_1 is a change in water environment during ischaemia. It is known that changes in the "bound" pool as well as changes in the exchange rate of magnetisation between the different water pools have an influence on the observed relaxation times (Lynch, 1983; Wolff and Balaban, 1989). This effect has been previously suggested (Ordidge et al., 1991) as one of the possible explanations for the increases in T_1 and T_2 observed after 2 hours of ischaemia, i.e. before the development of vasogenic oedema. It is possible that the same effect may be responsible for part of the early changes observed at high field. Ewing et al have recently reported a decrease in the exchange rate of magnetisation between "bound" and "free" pools (k_f) as early as 45 min after infarction (Ewing et al., 1999). However, further studies are needed in order to show that these changes are also present in the first few minutes of ischaemia.

It is interesting to note that at high field strength, the acute changes in T_1 (an increase) and T_2 (a decrease) contribute to the same type of signal intensity change (a decrease) when using a SE sequence. Therefore, by choosing the parameters to produce a very heavily T_1- and T_2-weighted sequence (such as in one of the long TE images in the multi-echo sequence used here), the weighting effects add, and the lesion can be readily

observed without the need for subtracting the pre-ischaemic image (Fig. 8.15). This is of great relevance for future clinical studies performed at high field strength, where there is the practical problem of no pre-ischaemic data since the patient arrives at the hospital typically a few hours after the ischaemic onset.

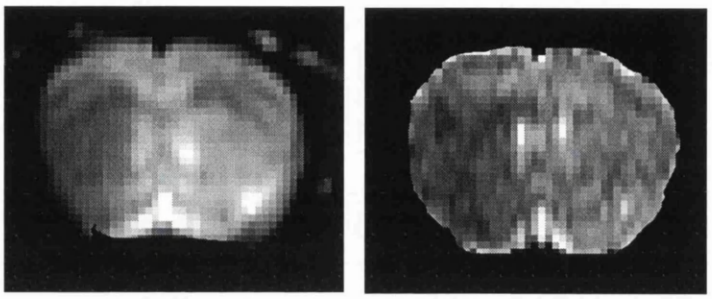

Figure 8.15.

Figure 8.15. Spin-echo image, very heavily T_2- and T_1-weighted (TE=70 ms, TR=1000ms), acquired ~1 min after MCA occlusion in a rat. There is a clear region of hypointensity due to the acute T_2 decrease and T_1 increase following occlusion. This region is similar to that with decrease diffusion in the trace map acquired several hours after onset of ischaemia.

In summary, high field MRI studies in a rat model have provided the novel observation of T_1 and T_2 imaging changes in the first few minutes after ischaemia was reported. The T_1 and T_2 changes occurred not only in the core of the lesion, where there was a severe reduction in blood flow and a decrease in water diffusion, but also in a border region where the flow was only moderately reduced with no change in water diffusion. The combined analysis of the T_1 and T_2 changes, together with perfusion and diffusion measurements, provides a means of distinguishing between "core" and "border" regions at high field strength, and may help to characterise tissue 'at risk' that is compromised but potentially salvageable.

9. General Discussion

The work described in this thesis is centred on the use of MRI techniques for the study of cerebral ischaemia. As described in Chapter 1, the main objectives were the implementation of quantitative diffusion MRI on a whole body 1.5 T clinical scanner (described in Chapter 4 and Chapter 5), the evaluation of the limitations of quantification of perfusion using dynamic susceptibility contrast MRI (DSC-MRI) in stroke (described in Chapter 6), the application of diffusion and perfusion MRI to the study of brain abnormalities in childhood (described in Chapter 7), and the study of the acute changes in MR parameters following middle cerebral artery (MCA) occlusion in the rat at 8.5 T (described in Chapter 8).

There are some related issues that require further discussion. These will be addressed in this chapter, as well as future work to be done.

9.1 Can diffusion/perfusion studies make a difference to patient outcome in stroke?

This is a very important issue, and was the main point of debate in the recent first meeting of the "Diffusion and perfusion study group" of the International Society for Magnetic Resonance in Medicine (ISMRM, Philadelphia, USA, 1999).

The answer to this question depends on the patient population. For a general elderly adult population, it seems that diffusion and perfusion MRI have not made a large difference to functional outcome. One possible reason is the lack of definite treatment, since treatments using neuroprotective agents or anticoagulants are still under development. However, diffusion and perfusion MRI are playing an important role in this context, in helping to select appropriate subgroups of patients for evaluation of the response to particular treatments. A further problem with a general patient population is the difficulty of carrying out preventative treatment. In most cases, a stroke has occurred before any intervention can be attempted, and the aim is to avoid the enlargement of the lesion.

The findings discussed in the Chapter 7 suggest that the situation can be very different in certain group of children with high risk of stroke, such as those with sickle cell disease and moyamoya disease. For both groups, there are commonly used interventions: transfusion in sickle cell disease, and revascularisation in moyamoya disease. Although these treatments are far from ideal, studies using diffusion and perfusion MRI may help to evaluate their usefulness. More importantly, they may play a very important role in identifying the patients who might benefit with these treatments, even before any stroke has occurred (i.e. preventative treatment). This requires the identification and evaluation of tissue 'at risk', which raises an important question: *'can MRI identify tissue 'at risk'?'*. The main problem is what 'at risk' tissue means. Although any abnormal tissue is in principle 'at risk', ultimately it is defined by the tissue which will become infarcted if no intervention is performed. The areas of mismatch between diffusion and perfusion suggest tissue which has a compromised supply of oxygen and nutrients but with enough energy to maintain ionic homeostasis. It remains to be proven to what extent this (or part of this) tissue is 'at risk' of further deterioration. Some recent studies have been performed to address this issue (Schlaug et al., 1999; Beaulieu et al., 1999; Neumann-Haefelin et al., 1999; Karonen et al., 1999), although the results are not conclusive. The use of further MR information (such as the T_1 and T_2 changes observed at high field (Chapter 8)) may prove very useful in the characterisation of this tissue 'at risk' (see *Future work*).

9.2 What is the best perfusion MRI technique?

Two different perfusion techniques were described in this thesis: arterial spin labelling (ASL; Chapter 8) and DSC-MRI (Chapters 6 and 7). However, neither of these techniques is *ideal*, and each approach has its advantages and disadvantages.

9.2.1 Exogenous vs. endogenous contrast agent - multiple measurements

Although both methods can be considered as non-invasive (neither requiring ionising radiation), ASL has the extra benefit of using an endogenous contrast agent (magnetically labelled blood). Therefore, multiple measurements can be performed, in principle, without any restriction. Although multiple bolus injections of contrast agent can be performed, the acceptable maximum dose is limited. A lower dose would therefore have to be administered in multiple measurements, thus reducing the sensitivity of the technique. Furthermore, there may be some influence of each bolus on subsequent boluses when multiple measurements are performed with short time resolution.

9.2.2 Behaviour under extreme flow conditions

Although both techniques behave reasonably well in the range of normal CBF values, they have difficulties when dealing with very high or very low flow. Very high flows are problematic for the ASL technique, because the assumption of complete exchange is no longer valid (Silva et al., 1997a, 1997b). If this is not taken into account, the perfusion will be underestimated (since only a fraction of the arterial magnetisation is exchanged). In principle, very high flow can also be problematic for the DSC-MRI technique, since it will cause narrowing of the peak, making it more difficult to characterise the peak accurately for a given time resolution. However, due to the large dispersion through the lungs and heart, this is not likely to be a significant factor in practice.

The main limitation of both techniques is in the case of very low flow, which will be discussed later (see *Can MRI measure perfusion in stroke?* (Section 9.3)).

9.2.3 Regional coverage

Both techniques can be used in a multi-slice protocol, although the maximum number of slices is limited in each case. In DSC-MRI, the coverage is a compromise between the number of slices and the time resolution. For a full characterisation of the bolus passage, high time resolution is required (the sharper the bolus, the higher the time resolution required). For typical TR values (1.5-2.0 s), a coverage of up to 10-15 slices can be achieved using EPI. For the case of ASL, transit time limits the maximum number of slices (typically between 5-10 slices can be obtained, depending on the spatial resolution). For whole brain coverage, 3D acquisitions can be used (Petrella et al., 1997; Yang et al., 1998), although this tends to reduce the spatial resolution.

The 'best' MRI perfusion technique depends on the particular application. For example, the completely non-invasive character of ASL is ideal for functional MRI imaging studies (fMRI), as well as in any other application where serial measurements with short time resolution are required. An example of this is the study of early changes in MR parameters after MCA occlusion, as described in Chapter 8. On the other hand, in clinical studies of stroke, the larger coverage and extra available information (MTT and CBV) make the DSC-MRI technique more appropriate. Its shorter acquisition time (~1 min) is another very relevant factor, due to the already long MR protocols used in the investigation of stroke (typically, axial and coronal T_2-weighted images, sagittal T_1-weighted images, axial FLAIR, axial diffusion and perfusion, and MR angiography (MRA)).

9.3 Can MRI measure perfusion in stroke?

As mentioned in the previous section, the main limitation of the MRI perfusion technique is in the measurement of very low flows.

9.3.1 Signal-to-noise ratio (SNR) considerations

The first obvious limitation is the *low SNR* of the measurement. This can be improved in the ASL technique by increasing the number of averages (at the expense of increasing the measurement time). On the other hand, in the typical single bolus DSC studies, due to its dynamic character, averaging is not an option. One possible solution is the use of a larger dose of contrast agent, although the maximum dose is limited.

9.3.2 Arrival delays

SNR is not the only problem when measuring low flows. A second problem is related to the presence of *long arrival delays* for the arterial blood to the volume of interest (VOI), which may result from collateral circulation. Extra delays of up to several seconds can be observed in ischaemic tissue (see Chapter 7). To address this problem, there are two options: *minimise* the effect or *account for* its contribution.

9.3.2.1 Arrival delays and ASL

If the presence of long transit times from the tagging plane to the tissue is not accounted for, the quantification of perfusion using ASL can be underestimated (see the *Discussion* section in the chapter describing the rat MCA occlusion studies (Section 8.4)). Some modifications have been suggested to minimise this effect (Alsop and Detre, 1996, Wong et al., 1998a), and in pulsed ASL (PASL), the transit time insensitivity can be further

improved by slice profile optimisation (Pell et al., 1998). However, although the latest ASL sequences that have been proposed are less sensitive to differences in transit time (provided appropriate sequence parameters are chosen), very long transit times may nevertheless render the required parameters impractical.

The other possibility is to take account of the different transit times. This would require a knowledge of the transit time on a pixel by pixel basis. Some attempts have been made to measure the transit time using ASL techniques (Zhang et al., 1992, Ye et al., 1997a, Wong et al., 1997, Barbier et al., 1999), although the low SNR is a limiting factor, especially in white matter and regions of low flow. Another option would be to measure the regional transit time by using the bolus arrival time (BAT) information from a DSC experiment. This alternative has not yet been explored, and a combined ASL/DSC study may prove to be a powerful approach in cases with long transit delays (see *Future work* section).

However, the presence of very long transit delays is one of the fundamental limitations of the ASL technique for measuring CBF. Regardless of a full characterisation of the transit times to the different pixels, in the case of a very long delay it may be that the signal loses its tag by the time it arrives at the tissue (due to T_1 relaxation). Therefore, no effect would be observed. There is no simple solution to this, although the use of a higher magnetic field strength, with the associated longer T_1, would ameliorate the problem.

9.3.2.2 Arrival delays and DSC-MRI

Very long bolus arrival times are also a problem in DSC studies. As discussed in Chapter 6, the transit of the bolus from the site of injection to the VOI can introduce a delay, as well as dispersion (spread of the bolus shape). This dispersion effectively reduces the labelling (bolus sharpness), and therefore one can think of the dispersion as a 'relaxation' process (the more the spread of the bolus, the smaller the observed effect). In practice,

this 'relaxation' process seems not to be the main limitation. Although long delays of up to ~4 s that have been observed in some patients (see Fig. 7.3) would have been too long for ASL measurements (resulting in almost complete relaxation of the labelling), the bolus peak was still large enough to allow interpretation. In practice, it is not the spread of the peak *per se*, but the unknown contribution to its spread which limits the accuracy of DSC-MRI at very low flow. While one can account for the dispersion from the site of injection (typically a vein) to the artery where the arterial input function (AIF) is estimated, the extra dispersion from the artery to the input of the VOI (where the true AIF should be obtained) is not accounted for (Fig. 9.1). The simulations performed in Chapter 6 showed that if the delay and dispersion are not accounted for, there is a significant underestimation of CBF and overestimation of MTT, which may lead to erroneous interpretations.

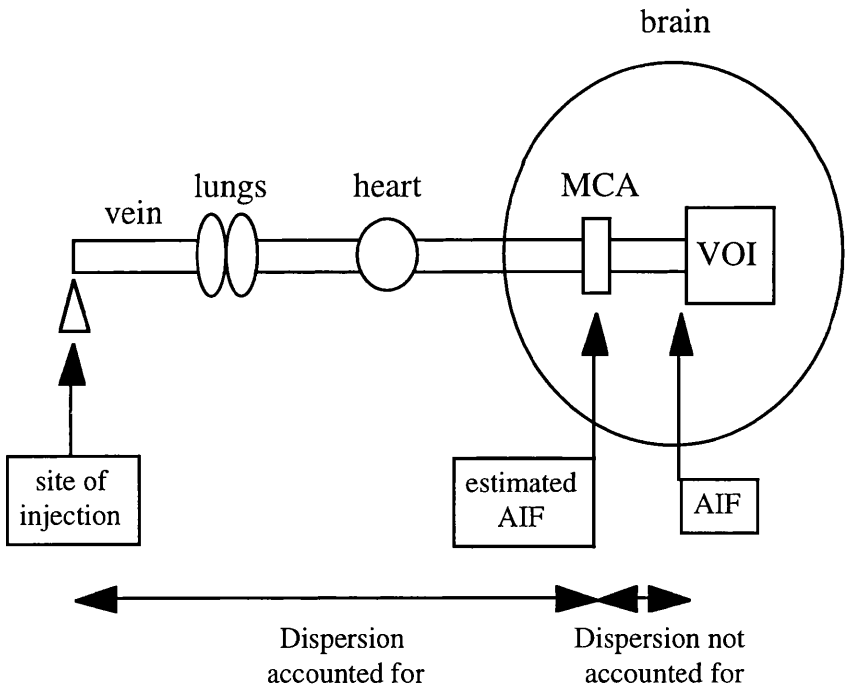

Figure 9.1.

Figure 9.1. Dispersion of the bolus. Schematic representation of the path taken by the bolus of contrast agent from the injection place (vein), through the lungs and heart, to the brain. The bolus is dispersed along this path. The AIF is estimated in a large artery (e.g., MCA), but the true AIF can be further dispersed between the large artery and the VOI. This extra dispersion is not accounted for, and it introduces errors in the measurement.

As mentioned in Chapter 6, Østergaard et al. (1999) have attempted to accounted for this effect by modelling the dispersion and incorporating it into the DSC analysis. Their preliminary results looks promising, but further studies are needed (see *Future work*).

Another possibility is to minimise the effect of delay and dispersion. The AIF is an *ideal* concept, which describes the input of contrast agent to *each* pixel. No method has been suggested to measure the true AIF, and the quantification of DSC data relies on the *estimation* of the AIF from a major artery. Therefore, in order to minimise the effect of delay and dispersion, the AIF should be measured as close as possible to the VOI. In normal situations, most of the dispersion occurs between the site of injection and the site where the AIF is estimated (major artery), and therefore a single AIF for the whole brain is a reasonably good approximation. However, in cases where the vascular supply is abnormal (and unfortunately therefore, when the perfusion measurement is particularly relevant), the extra delay and dispersion from the major artery to the affected tissue may become very important. Apart from this limitation, there are further problems when measuring the AIF from a major artery. Firstly, since a high time resolution is required, images with low spatial resolution are commonly used. Therefore, partial volume with tissue can introduce an underestimation of the AIF. Secondly, there can be artefacts resulting from the susceptibility changes induced during the passage of the bolus (Hou et al., 1999). Susceptibility-related signal changes during data acquisition can result in shifting of signal intensity across the image.

9.4 Future work

- *Combined ASL/DSC studies.* As mentioned above (Section 9.3.2.1), the combined used of both MRI perfusion techniques might prove to be a very powerful approach. Although the information of BAT from the DSC-MRI experiment provides 'relative' transit time information, it is possible in principle to select one of the imaging slices

through the plane where the tagging will be performed in the ASL experiment. In this way, the BAT to the arteries in this slice can be used as a 'reference' to obtain absolute transit time measurements on a pixel by pixel basis. Provided the delay is not long enough to cause complete relaxation of the tagging, the necessary number of averages could be performed to yield enough SNR for accurate quantification of perfusion using ASL and the transit time information. It should be noted that the DSC experiment must be performed *after* the ASL measurement to avoid the reduction in blood T_1 due to the presence of the contrast agent.

- *Is the diffusion/perfusion mismatch area tissue 'at risk'?*. As mentioned above, preventative treatment may rely on the identification of 'at risk' tissue. Further studies are required in order to properly characterise the tissue which has a perfusion abnormality with normal diffusion. This is likely to require a further understanding of the processes involved in the acute stage of infarction. A combined analysis of diffusion, perfusion, T_1, and T_2, should provide new insights into these mechanisms. Furthermore, a comparison with other techniques such as MRA and transcranial Doppler (TCD) might provide the possible link between the vascular abnormality and the tissue status.
- *Quantitative diffusion analysis*. One of the difficulties of working with children is that many of the MR properties are age dependent. It is well known that changes in water content and myelination take place in the first few years of life. Therefore, the diffusion properties of tissue water are expected to be age dependent. Preliminary studies not included in this thesis suggest that this age dependence seems to extend beyond that observed in other MR parameters, such as T_2. Further studies are needed to verify this preliminary finding. Another factor that needs further characterisation is the regional variability of the ADC. The preliminary data suggest that the average ADC (ADC_{AV}) of white matter is higher than that of grey matter and cerebellum. This has important implications for the detection of subtle abnormalities. Planned studies include:

    a) Sickle cell disease subgroup analysis. Although a simple visual analysis did not identify any subgroup of sickle cell disease patients with different diffusion

properties, a more rigorous quantitative study should be performed. This would increase the sensitivity to abnormalities as has been observed using quantitative T_1 imaging in sickle cell disease (Steen et al., 1998, 1999). Comparison between different groups of patients with sickle cell disease (e.g., 'symptomatic and asymptomatic', or 'with and without cerebrovascular disease', or 'with and without previous infarctions', etc.) may help to identify appropriate patients to include in the transfusion programme. A preliminary analysis has shown that there seems to be no significant difference in diffusion in the non-infarcted regions between sickle cell disease patients with and without previous infarctions. However, no age dependence was included in the analysis. Further studies to verify this result and to compare the different patient groups are required.

b) Quantitative diffusion measurements in patients with Sturge-Weber syndrome. Further studies are needed to understand the small (as compared to stroke) but persistent diffusion reductions observed in Sturge-Weber syndrome. Furthermore, there have been suggestions that the contralateral side to the angioma is sometimes abnormal, and that this was related to the progression of the neurological impairment (Okudaira et al., 1997). However since most of the Sturge-Weber syndrome patients are very young, the age dependence contribution of the diffusion is very important. Absolute quantitative studies of diffusion could help to identify those patients who will have progressive neurological symptoms.

c) Evolution of the stroke lesion. All the published studies on evolution of the ADC in stroke have been performed in adults. Although the qualitative behaviour seems to be also valid in childhood stroke (see Chapter 7), the time scale is not necessarily the same. A characterisation of the time dependence of the ADC following stroke would be of great help. This study requires the separate analysis of the different tissue types, because our preliminary data suggests that white matter may evolve differently from grey matter (see Chapter 7).

- *Dispersion in DSC-MRI data.* The approach recently proposed by Østergaard et al. (1999) seems very promising, although it has only been applied to normal volunteers. The patients with moyamoya disease are an ideal group of patients to test the model, since most of them have delayed perfusion to watershed areas of the brain. The main problem with this analysis would be the need for a 'gold standard' to compare the results using the new model. Correlation with ASL/DSC studies (see above), PET or SPECT measurements may prove helpful in this context.
- *Injection protocol.* There is a practical issue when a power injector is used to inject the bolus of contrast agent. If the injection is done manually, this is usually performed 'as fast as possible' in order to produce a sharp bolus. However, the use of very fast injection rates with the power injector can induce patient movements, particularly in young children. Since the total amount of volume contrast (proportional to body weight) is very small in children, it is possible there is no need to use very high injection rates. This is also especially important in patients with sickle cell disease who sometimes have very fragile veins, with the associated possibility of extravasation of the contrast. Since most of the dispersion is introduced during the passage of the bolus through the lungs and heart, it is possible that for the small volumes used for children the injection time could be increased without reducing significantly the sensitivity of detection of the peak. This could help to minimise the number of failures (those due to patient movement, or contrast extravasation). A study of the relationship between the injection time and peak width of the AIF may help to address this issue, although effects such as cardiac rate and blood pressure may need to be taken into consideration.
- *Diffusion MRI using segmented EPI.* Although single shot diffusion-weighted EPI produce high quality diffusion maps, it still has some limitations. The main two drawbacks of the technique for the work at Great Ormond Street Hospital for Children are the low spatial resolution and the susceptibility distortions in the temporal lobes. The first is particular relevant to the study of sickle cell disease, where many patients are found to have small lesions in the white matter. The second drawback is relevant to the large patient population at Great Ormond Street Hospital for Children with

temporal lobe epilepsy. At present the quality of the ADC maps obtained with single shot EPI is not adequate for a robust analysis of diffusion abnormalities in the temporal lobes. We have done some preliminary work using diffusion-weighted segmented EPI with navigated-echo correction (Butts et al., 1997). However, further work is required to optimise the acquisition and processing of the data, and to validate the sequence on phantoms and volunteers. Similarly, a fast sequence with less sensitivity to image distortions would improve the quality of the perfusion DSC-MRI in the temporal lobes. However, with perfusion there is an extra limitation. Since those fast imaging techniques are much slower than single shot EPI, the maximum number of slices for a given time resolution is reduced. This implies that they would be better used to target certain regions, such as the temporal lobes in epilepsy.

10. References

Adams R, McKie V, Nichols F, Carl E, Zhang DL, McKie K, Figueroa R, Litaker M, Thompson W, Hess D (1992). The use of transcranial ultrasonography to predict stroke in sickle cell disease. *N. Engl. J. Med.* **326**:605-610.

Adams R, McKie VC, Hsu L, Files B, Vichinsky E, Pegelow C, Abboud M, Gallagher D, Kutlar A, Nichols FT, Bonds DR, Brambilla D (1998). Prevention of a first stroke by transfusions in children with sickle cell anemia and abnormal results on transcranial Doppler ultrasonography. *N. Engl. J. Med.* **339**:5-11.

Ahn CB, Kim JH, Cho ZH (1986). High-speed spiral scan echo-planar NMR imaging. *IEEE Trans. Med. Imaging* **5**:2-7.

Aicardi J (1998). Diseases of the nervous system in childhood (2nd edition). Cambridge, Cambride University Press. pp. 542-547.

Alexander AL, Tsuruda JS, Parker DL (1997). Elimination of Eddy Current Artifacts in Diffusion-Weighted Echo-Planar Images: The Use of Bipolar Gradients. *Magn. Reson. Med.* **38**:1016-1021.

Allegrini PR, Hoehn-Berlage M, Busch E, Krüger K, Kerskens CM (1996). NMR imaging observations of rat brain perfusion changes during stroke: Interpretation based on combination with physiological parameters, in "Proc. ISMRM, 4th Annual Meeting, New York", p.319.

Alsop DC, Detre JA (1996). Reduced transit-time sensitivity in noninvasive magnetic resonance imaging of human cerebral blood-flow. *J. Cereb. Blood Flow Metab.* **16**:1236-1249.

Alsop DC (1997). Phase insensitive preparation of single-shot RARE: application to diffusion imaging in humans. *Magn. Reson Med.* **38**:527-533.

Alsop DC, Detre JA (1998). Multisection cerebral blood flow MR imaging with continuous arterial spin labeling. *Radiology* **208**:410-416.

Anderson A, Gore J (1994). Analysis and correction of motion artifacts in diffusion-weighted imaging. *Magn. Reson. Med.* **32**:379-387.

Armitage P, Berry G (1987). Statistical methods in medical research. Oxford: Blackwell Scientific Publications (2nd. edition); p. 91

Armstrong FD, Thompson RJ, Wang W, Zimmerman R, Pegelow CH, Miller S, Moser F, Bello J, Hurtig A, Vass K. (1996). Cognitive functioning and brain magnetic resonance imaging in children with sickle cell disease. *Pediatrics* **97**:864-870.

Axel L (1980). Cerebral blood flow determination by rapid-sequence computed tomography *Radiology* **137**:676-686.

Axel L (1995). Methods using blood pool tracers. Part II. In: *Diffusion and perfusion magnetic resonance imaging* (Le Bihan D., ed), New York, Raven Press, pp 205-211.

Aylett SE, Neville BGR, Cross JH, Boyd S, Chong WK, Kirkham F (1999). Sturge-Weber syndrome: cerebral haemodynamics during seizure activity. *Dev. Med. Child Neurol.* **41**:480-485.

Baird AE, Benfield A, Schlaug G, Siewert B, Lovblad KO, Edelman RR, Warach S (1997). Enlargement of human cerebral ischemic lesion volumes measured by diffusion-weighted magnetic resonance imaging. *Ann. Neurol.* **41**:581-589.

Baird AE, Warach S (1998). Magnetic resonance imaging of acute stroke. *J. Cereb. Blood Flow Metab.* **18**:583-609.

Barber PA, Darby DG, Desmond PM, Yang Q, Gerraty RP, Jolley D, Donnan GA, Tress BM, Davis SM (1998). Prediction of stroke outcome with echoplanar perfusion- and diffusion-weighted MRI. *Neurology* **51**:418-426.

Barbier EL, Silva AC, Kim HJ, Williams DS, Koretsky AP (1999). Perfusion analysis using dynamic arterial spin labeling (DASL). *Magn. Reson. Med.* **41**:299-308.

Basser PJ, Mattiello J, Le Bihan D (1994). MR Diffusion Tensor Spectrosopy and Imaging. *Biophys. J.* **66**:259-267.

Basser PJ (1995). Inferring Microstructural features and the physiological state of tissues from diffusion-weighted images. *NMR Biomed.* **8**:333-344.

Basser PJ, Pierpaoli C (1996). Microstructural and physiological features of tissues elucidated by quantitative-diffusion-tensor MRI. *J. Magn. Reson.* **B111**:209-219.

Basser PJ, Pierpaoli C (1998). A simplified method to measure the diffusion tensor from seven MR images. *Magn. Reson. Med.* **39**:928-934.

Bassingthwaighte JB, Goresky GA (1984). The cardiovascular system. In: *Handbook of Physiology* (Renkin EM and Michel CG, eds), Bethesda, American Physiology Society, pp 549-626.

Beaulieu C, de Crespigny A, Tong DC, Moseley ME, Alberts GW, Marks MP (1999). Longitudinal magnetic resonance imaging study of perfusion and difusion in stroke: evolution of lesion volume and correlation with clinical outcome. *Ann. Neurol.* **46**:568-578.

Benveniste H, Hedkund LW, Johnson GA (1992). Mechanism of detection of acute cerebral ischemia in rats by diffusion-weighted imaging resonance microscopy. *Stroke* **23**:746-754.

Berninger WH, Axel L, Norman D, Napel S, Redington RW (1981). Functional imaging of the brain using computed-tomography. *Radiology* **138**:711-716.

Bloembergen N, Purcell EM, Pound RV (1948). Relaxation effects in nuclear magnetic resonance absorption. *Phys. Rev.* **73**: 679.

Boesch C, Gruetter R, Martin E (1991). Temporal and spatial analysis of fields generated by eddy currents in superconducting magnets: optimization of corrections and quantitative characterization of magnet/gradient systems. *Magn. Reson. Med.* **20**: 268-284.

Boxerman JL, Hamberg LM, Rosen BR, Weisskoff RM (1995). MR contrast due to intravascular magnetic-susceptibility perturbations. *Magn. Reson. Med.* **34**:555-566.

Bracewell RN (1978). The Fourier transform and its applications, 2nd. edn. McGraw-Hill, New York.

Branch CA, Hernandez L, Yongbi M, Helpern JA (1998). Estimation of arterial arrival time and cerebral response characteristics of perfusion measurements with arterial spin labeling. In: *"Proc. ISMRM 6th Annual Meeting*, Sydney, Australia, pp 375.

Bruder H, Fischer H, Reinfelder H-E, Schmitt F (1992). Image reconstruction for echo planar imaging with nonequidistant k-space sampling. *Magn. Reson. Med.* **23**:311-323.

Bryant RG, Marill K, Blackmore C (1990). Francis. Magnetic Relaxation in Blood and Blood Clots. *Magn. Reson. Med.* **13**:133-144.

Buonocore MH, Gao L (1997). Ghost artifact reduction for echo planar imaging using image phase correction. *Magn. Reson. Med.* **38**:89-100.

Busza AL, Allen KL, King MD, van Bruggen N, Williams SR, Gadian DG (1992). Diffusion-Weighted Imaging Studies of Cerebral Ischemia in Gerbils. Potential Relevance to Energy Failure. *Stroke* **23**:1602-1612.

Busza AL, Lythgoe MF, Allen KL, Williams SR (1994). T_2 Decrease in Acute Global Cerebral Ischaemia in the Gerbil - the Contribution of Magnetic susceptibility Gradients, in *"Proc. SMR, 2nd Annual Meeting*, San Francisco", p.1389.

Butts K, Pauly J, de Crespigny A, Moseley M (1997). Isotropic diffusion-weighted and spiral-navigated interleaved EPI for routine imaging of acute stroke. *Magn. Reson. Med.* **38**:741-749.

Buxton RB, Frank LR, Wong EC, Siewert B, Warach S, Edelman RR (1998). A general kinetic model for quantitative perfusion imaging with arterial spin labeling. *Magn. Reson. Med.* **40**:383-396.

Calamante F, Williams SR, van Bruggen N, Kwong, KK, Turner R (1996). A model for quantification of perfusion in pulsed labeling techniques. *NMR Biomed.* **9**:79-83.

Calamante F, Thomas DL, Pell GS, Wiersma J, Turner R (1999). Measuring cerebral blood flow using magnetic resonance techniques. *J. Cereb. Blood Flow Metab.* **19**:701-735.

Carr HY, Purcell EM (1954). Effects of diffusion on free precession in nuclear magnetic resonance experiments. *Phys. Rev.* **94**:630-638.

Chapman B, Turner R, Ordidge RJ, Doyle M, Cawley M, Coxon R, Glover P, Mansfield P (1987). Real-time movie imaging from a single cardiac cycle by NMR. *Magn. Reson. Med.* **5**:246-254.

Chen W, Zhu X-H (1997). Suppression of physiological eye movement artifacts in functional MRI using slab presaturation. *Magn. Reson. Med.* **38**:546-550.

Crockard HA, Gadian DG, Frackowiak RSJ, Proctor E, Allen K, Williams SR, Ros Russell RW (1987). Acute cerebral ischemia: concurrent changes in cerebral blood flow, energy metabolites, PH, and lactate measured with hydorgen cearance and ^{31}P and ^{1}H nuclear magnetic resonance spectroscopy. II Changes during ischaemia. *J. Cereb. Blood Flow Metab.* **7**:394-402.

Crozier S, Beckley FA, Eccles CD, Field J, Doddrell DM (1994). Correction for the effect of induced B_0 shifts in localized spectroscopy and imaging by direct frequency modulation. *J. Magn. Reson.* **B103**:115-119.

Crozier S, Eccles CD, Beckley FA, Field J, Doddrell DM (1992). Correction of eddy-current-induced B_0 shifts by receiver reference-phase modulation. *J. Magn. Reson.* **97**:661-665.

Davis D, Ulatowski J, Eleff S, Izuta M, Mori S, Shungu D, van Zijl PCM (1994). Rapid monitoring of changes in water diffusion coefficients during reversible ischemia in cat and rat brain. *Magn. Reson. Med.* **31**:454-460.

Deichmann R, Haase A (1992). Quantification of T_1 Values by Snapshot-FLASH NMR Imaging. *J. Magn. Reson.* **96**:608-612.

Detre JA, Leigh JS, Williams DS, Koretsky AP (1992). Perfusion imaging. *Magn. Reson. Med* . **23**:37-45.

Dirnagl U, Pulsinelli W (1990). Autoregulation of cerebral blood flow in experimental focal brain ischemia. *J. Cereb. Blood Flow Metab.* **10**:327-336.

Dixon WT, Du LN, Faul DD, Gado M, Rossnick S (1986). Projection angiograms of blood labeled by adiabatic fast passage. *Magn. Reson. Med.* **3**:454-462.

Dobson AJ (1990). "An Introduction to Generalized Linear Models", chapters 5 and 6. Chapman and Hall, London.

Does MD, Zhong J, Gore JC (1999). In vivo measurement of ADC change due to intravascular susceptibility variation. *Magn. Reson. Med.* **41**:236-240.

Doyle M, Chapman B, Turner R, Ordidge RJ, Cawley M, Coxon R, Glover P, Coupland RE, Morris GK, Worthington BS, et al., (1986). Real-time imaging of adults at video frame rates by magnetic resonance imaging. *Lancet* **2**:682.

Duong TQ, Ackerman JJH, Ying HS, Neil JJ (1998). Evaluation of extra- and intracellular apparent diffusion in normal and globally ischemic rat brain via ^{19}F NMR. *Magn. Reson. Med.* **40**:1-13.

Earley CJ, Kittner SJ, Feeser BR, Gardner J, Epstein A, Wozniak MA, Wityk R, Stern BJ, Price TR, Macko RF, Johnson C, Sloan MA, Buchholz D (1998). Stroke in children and sickle-cell disease: Baltimore-Washington Cooperative Young Stroke Study. *Neurology* **51**:169-176.

Edelman RR, Siewert B, Darby DG, Thangaraj V, Nobre AC, Mesulam MM, Warach S (1994). Qualitative mapping of cerebral blood-flow and functional localization with echo-planar MR-imaging and signal targeting with alternating radio-frequency. *Radiology* **192**:513-520.

Edelman RR, Chen Q (1998). EPISTAR MRI: Multi-slice Mapping of Cerebral Blood Flow. *Magn Reson Med* **40**:800-805.

Ehman RL, Felmlee JP (1989). Adaptive technique for high-definition MR imaging of moving structures. *Radiology* **173**:255-263.

Ellinger R, Kremser C, Schocke M, Auer A, Felber S, Aichner F (1998). The impact of the arterial input function on quantitative evaluation of susceptibility contrast enhanced MRI studies. *in "Proc., ISMRM, 6th Annual Meeting*, Sydney, Australia" p. 1207.

Ewing JR, Jiang Q, Boska M, Zhang ZG, Brown SL, Li GH, Divine GW, Chopp M (1999). T_1 and Magnetization Transfer at 7 Tesla in Acute Ischemia in the Rat. *Magn. Reson. Med.* **41**:696-705.

Falconer JC, Narayana PA (1997). Cerebrospinal fluid-suppressed high-resolution diffusion imaging of human brain. *Magn. Reson. Med.* **37**:119-123.

Farrar TC, Becker ED (1971). Pulse and Fourier transform NMR. Introduction to theory and methods. Academic Press, New York. pp46-65.

Farzaneh F, Riederer SJ, Pelc NJ (1990). Analysis of T2 limitations and off-resonance effects on spatial resolution and artifacts in echo-planar imaging. *Magn. Reson. Med.* **14**:123-139.

Fischer H, Ladebeck R (1998). Echo-planar imaging image artifacts. In "Echo planar imaging. Theory, techniques and application" (Schmitt F, Stehling MK, Turner R, eds.). Springer, Berlin. pp 179-200.

Fisel CR, Ackerman JL, Buxton RB, Garrido L, Belliveau JW, Rosen BR, Brady TJ (1991). MR contrast due to microscopically heterogeneous magnetic- susceptibility:

numerical simulations and applications to cerebral physiology. *Magn. Reson. Med.* **17**:336-347.

Franconi F, Symms MR, Lethimonnier F, Jones R, Schreiber W, Barker GJ (1997). Measurement of ghosting in echo planar imaging: a multi-center study, *in "Proc., ISMRM, 5th Annual Meeting*, Vancouver, Canada". p. 1807.

Frank LR, Wong EC, Buxton RB (1997). Slice profile effects in adiabatic inversion: application to multi-slice perfusion imaging. *Magn. Reson. Med.* **38**:558-564.

Friston KJ, Ashburner J, Poline JB, Frith CD, Frackowiack RSJ (1995). Spatial realignment and normalization of images. *Human Brain Mapping* **2**:165-189.

Fullerton GD (1992). Physiological Basis of Magnetic Relaxation. In: "Magnetic Resonance Imaging, Vol.1" (Stark DD, Bradley WG, eds). St. Louis, Mosby Year Book, pp 88-108.

Gillis P, Koenig SH (1987). Transverse relaxation of solvent protons induced by magnetized spheres: application to ferritin, erythrocytes, and magnetite. *Magn. Reson. Med.* **5**:323-345.

Gobbel GT, Cann CE, Fike JR (1991). Measurement of regional cerebral blood flow using ultrafast computed tomography: theoretical aspects. *Stroke* **22**:768-771.

Gobbel GT, Fike JR (1994). A deconvolution method for evaluating indicator-dilution curves. *Phys. Med. Biol.* **39**:1833-1854.

Gomori JM, Grossman RI, Yu-Ip C, Asakura T (1987). NMR Relaxation Times of Blood: Dependence on Field Strength, Oxidation State, and Cell Integrity. *J. Comput. Assist. Tomogr.* **11**:684-690.

Gröhn OHJ, Lukkarinen JA, Oja JME, van Zijl PCM, Ulatowski JA, Traystmon RJ, Kauppinen RA (1998). Detection of acute cerebral hypoperfusion and reversible ischemia in the rat from reductions in the magnetic resonance imaging relaxation time T_2. *J. Cereb. Blood Flow Metab.* **18**:911-920.

Gückel FJ, Brix G, Schmiedek P, Piepgras A, Becker G, Kopke J, Gross H, Georgi M (1996). Cerebrovascular reserve capacity in patients with occlusive cerebrovascular disease: Assessment with dynamic susceptibility contrast-enhanced MR imaging and the acetazolamide stimulation test. *Radiology* **201**:405-412.

Hajnal JV, Bryant DJ, Kasuboski L, Pattany PM, De Coene B, Lewis PD, Pennock JM, Oatridge A, Young IR, Bydder GM (1992). Use of fluid attenuated inversion recovery (FLAIR) pulse sequences in MRI of the brain. *J. Comput. Assist. Tomogr.* **16**:841-844.

Harris RK (1983). Nuclear magnetic resonance spectroscopy. A physicochemical view. Pitman, London. pp 85-91.

Haselgrove JC, Moore JR (1996). Correction for distortion of echo-planar images used to calculate the apparent diffusion coefficient. *Magn. Reson. Med.* **32**:960-964.

Hedehus M, Steensgaard A, Rostrup E, Larsson HBW (1997). Investigation of the linear relation between R_2* and gadolinium concentration in vivo. In: *"Proc. ISMRM 5th Annual Meeting*, Vancouver, Canada". pp 1792.

Helpern JA, Ordidge RJ, Knight RA (1992). The effect of cell membrane water permeability on the apparent diffusion coefficient of water. In: *"Proc. SMRM, 11th Annual Meeting*, Berlin, Germany". p 1201.

Helpern JA, Dereski MO, Knight RA, Ordidge RJ, Chopp M, Qing ZX (1993). Histopathological correlations of Nuclear Magnetic Resonance Imaging Parameters in Experimental Cerebral Ischemia. *Magn. Reson. Imaging.* **11**:241-246.

Helpern JA, Branch CA, Yongbi M, Huang N (1997). Perfusion imaging by un-inverted flow-sensitive inversion recovery (UNFAIR) *Magn. Reson. Imaging* **15**:135-139.

Henkelman RM (1990). Does IVIM measure classical perfusion? *Magn. Reson. Med.* **16**:470-475.

Henkelman RM, Neil JJ, Xiang QS (1994). A quantitative interpretation of IVIM measurements of vascular perfusion in the rat brain. *Magn. Reson. Med.* **32**:464-469.

Hennig J, Nauerth A, Friedburg H (1986). RARE imaging: a fast imaging method for clinical MR. *Magn. Reson. Med.* **3**:823-833.

Herscovitch P, Raichle ME (1985). What is the correct value for the brain-blood partition coefficient for water? *J. Cereb. Blood Flow Metab.* **5**:65-69.

Hoehn-Berlage M (1995). Diffusion-weighted NMR imaging: Application to Experimental Focal Cerebral Ischemia. *NMR Biomed.* **8**:345-358.

Hossmann K-A, Hoehn-Berlage M (1995). Diffusion and perfusion MR imaging of cerebral ischemia. *Cerev. Brain Metab. Reviews* **7**:187-217.

Hou L, Yang Y, Mattay VS, Frank JA, Duyn JH (1999). Optimization of fast acquisition methods for whole-brain relative cerebral blood volume (rCBV) mapping with susceptibility contrast agents. *J. Magn. Reson. Imaging* **9**:233-239.

Howseman AM, Stehling MK, Chapman B, Coxon R, Turner R, Ordidge RJ, Cawley M, Glover G, Masfield P, Couplans RE (1988). Improvements in snap-shot nuclear magnetic resonance imaging. *Br. J. Radiol.* **61**:822-828.

Jackson A, Zhu XP, Li KL, Thacker NA. (1998). Contrast arrival time mapping in dynamic susceptibility Gd-DTPA enhanced MR imaging, *in "Proc. ISMRM, 6th Annual Meeting*, Sydney, Australia". p. 1217.

Jacquez JA (1972). Kinetics of distribution of tracer-labeled materials. In: *Compartmental analysis in biology and medicine*, Amsterdam, Elsevier Publishing Company, pp 84-101.

Jehenson P, Syrota A (1989). Correction of distortions due to the pulsed magnetic field gradient-induced shift in B_0 field by postprocessing. *Magn. Reson. Med.* **12**:253-256.

Jezzard P, Barnett AS, Pierpaoli C (1998). Characterization of and Correction for Eddy Current Artifacts in Echo Planar Diffusion Imaging. *Magn. Reson. Med.* **39**: 801-812.

Johnson G, Hutchison JMS (1985). The limitations of NMR recalled-echo imaging techniques. *J. Magn. Reson.* **63**:14-30.

Jones SC, Bose B, Furlan AJ, Friel HT, Easley KA, Meredith MP, Little JR (1989). CO_2 reactivity and heterogeneity of cerebral blood flow in ischemic, border zone, and normal cortex. *Am. J. Physiol.* **257**:H473-H482.

Karonen JO, Vanninen RL, Liu Y, Østergaard L, Kuikka JT, Nuutinen J, Vanninen EJ, Partanen PLK, Vainio PA, Korhonen K, Perkiö J, Roivainen R, Sivenius J, Aronen HJ (1999). Combined diffusion and perfusion MRI with correlation to single-photon emission CT in acute ischemic stroke. Ischemic penumbra predicts infarct growth. *Stroke* **30**:1583-1590.

Kennan RP, Zhong JH, Gore JC (1994). Intravascular susceptibility contrast mechanisms in tissues. *Magn. Reson. Med.* **31**:9-21.

Kim SG (1995). Quantification of relative cerebral blood flow change by flow-sensitive alternating inversion recovery (FAIR) technique - application to functional mapping. *Magn. Reson. Med.* **34**:293-301.

Kim SG, Tsekos NV (1997a). Perfusion imaging by a flow-sensitive alternating inversion recovery (FAIR) technique: application to functional brain imaging. *Magn. Reson. Med.* **37**:425-435.

Kim SG, Tsekos NV, Ashe J (1997b). Multi-slice perfusion-based functional MRI using the FAIR technique: comparison of CBF and BOLD effects. *NMR Biomed.* **10**:191-196.

King MD, van Bruggen N, Busza AL, Houseman J, Williams SR, Gadian DG (1992). Perfusion and diffusion imaging. *Magn. Reson. Med.* **24**:288-301.

Klose U (1990). *In vivo* proton spectroscopy in presence of eddy currents. *Magn. Reson. Med.* **14**:26-30.

Knight RA, Ordidge RJ, Helpern JA, Chopp M, Rodolosi LC, Peck D (1991). Temporal Evolution of Ischemic Damage in Rat Brain Measured by Proton Nuclear Resonance Imaging. *Stroke* **22**:802-808.

Knight RA, Dereski MO, Helpern JA, Ordidge RJ, Chopp M (1994). Magnetic Resonance Imaging Assessment of Evolving Focal Cerebral Ischemia. Comparison with Histhopathology in Rats. *Stroke* **25**:1252-1262.

Kohno K, Hoehn-Berlage M, Mies G, Back T, Hossmann KA (1995). Relationship Between Diffusion-Weighted MR Images, Cerebral Blood Flow, and Energy State in Experimental Brain Infarction. *Magn. Reson. Imaging* **13**:73-80.

Koshimoto Y, Yamada H, Kimura H, Maeda M, Tsuchida C, Kawamura Y, Ishii Y (1999). Quantitative Analysis of Cerebral Microvascular Hemodynamics with T2-weighted Dynamic MR Imaging. *J. Magn. Reson. Imaging* **9**:462-467.

Kwong KK, McKinstry RC, Chien D, Crawley AP, Pearlman JD, Rosen BR (1991). CSF-Suppressed Quantitative Single-Shot Diffusion Imaging. *Magn. Reson. Med.* **21**:157-163.

Kwong KK, Chesler DA, Weisskoff RM, Donahue KM, Davis TL, Østergaard L, Campbell TA, Rosen BR (1995). MR perfusion studies with T_1-weighted echo-planar imaging. *Magn. Reson. Med.* **34**:878-887.

Lassen NA, Henriksen O, Sejrsen P (1984). The cardiovascular system. In: *Handbook of Physiology* (Shepherd JT, Abboud FM, eds), Bethesda, American Physiology Society, pp 21-64.

Latour LL, Svoboda K, Mitra PP, Sotak CH (1994). Time-dependent diffusion of water in a biological model system. *Proc. Natl. Acad. Sci.* **91**:1229-1233.

Le Bihan D, Breton E, Lallemand D, Grenier P, Cabanis E, Laval-Jeantet M (1986). MR imaging of intravoxel incoherent motions: applications to diffusion and perfusion in neurologic disorders. *Radiology* **161**:401-407.

Le Bihan D, Turner R (1992). The capillary network: a link between IVIM and classical perfusion. *Magn. Reson. Med.* **27**:171-178.

Le Bihan D (1995). Diffusion and Perfusion Magnetic Resonance Imaging (Raven Press, Ltd. New York), pp 19-56.

Liu G, van Gelderen P, Duyn J, Moonen CTW (1996). Single-shot diffusion MRI of human brain on a conventional clinical instrument. *Magn. Reson. Med.* **35**:671-677.

Ljunggren S (1983). A simple graphical representation of Fourier-based imaging methods. *J. Magn. Reson.* **54**:338-343.

Lutsep HL, Alberts GW, de Crespigny A, Kamat GN, Marks MP, Moseley ME (1997). Clinical utility of diffusion-weighted magnetic resonance imaging in the assessment of ischemic stroke. *Ann. Neurol.* **41**:574-580.

Lynch LJ (1983). Water relaxation in heterogeneous and biological systems. In: J.S. Cohen (Ed.). Magnetic Resonance in Biology, Vol. 2. New York: John Wiley & Sons, 280-286.

Lythgoe MF, Busza AL, Calamante F, Sotak CH, King MD, Bingham AC, Williams SR, Gadian DG (1997). Effects of Diffusion Anisotropy on Lesion Delineation in a Rat Model of Cerebral Ischemia. *Magn. Reson. Med.* **38**:662-668.

Mancuso A, Karibe H, Rooney WD, Zarow GJ, Graham SH, Weiner MW, Weinstein PR (1995). Correlation of early Reduction in the Apparent Diffusion Coefficient of Water with Blood Flow Reduction During Middle Cerebral Artery Occlusion in Rats. *Magn. Reson. Med.* **34**:368-377.

Mansfield P, Grannell PK (1973). NMR 'diffraction' in solids? *J. Phys. C: Solid State Phys.* **6**:L422.

Mansfield P (1977). Multiplanar image formation using NMR spin-echoes. *J. Phys. C: Solid State Phys.* **10**:L55-L58.

Maria BL, Neufeld JA, Rosainz LC, Ben-David K, Drane WE, Quisling RG, Hamed LM (1998). High prevalence of bihemispheric structural and functional defects in Sturge-Weber syndrome. *J. Child Neurol.* **13**:1-11.

Marks MP, de Crespigny A, Lentz D, Enzmann DR, Albers GW, Moseley ME (1996). Acute and chronic stroke: navigated spin-echo diffusion-weighted MR imaging. *Radiology* **199**:403-408.

Matthews JNS., D.G. Altman, M.J. Campbell, P. Royston, Analysis of serial measurements in medical research. *Brit. Med. J.* **300**:230-255 (1990).

Mattiello J, Basser PJ, Le Bihan D (1994). Analytical expressions for the b matrix in NMR diffusion imaging and spectroscopy. *J. Magn. Reson.* **A108**:131-141.

Mattiello J, Basser PJ, Le Bihan D (1997). The b matrix in diffusion tensor echo-planar imaging. *Magn. Reson. Med.* **37**:292-300.

McLaughlin AC, Ye FQ, Pekar JJ, Santha AKS, Frank JA (1997). Effect of magnetization transfer on the measurement of cerebral blood flow using steady-state arterial spin tagging approaches: A theoretical investigation. *Magn. Reson. Med.* **37**: 501-510.

Meier P, Zierler KL (1954). On the theory of the indicator-dilution method for measurement of blood flow and volume. *Appl. Physiol.* **6**:731-744.

Mintorovitch J, Yang GY, Shimizu H, Kucharczyk J, Chan PH, Weinstein PR (1994). Diffusion-weighted magnetic resonance imaging of acute focal cerebral ischemia: comparison of signal intensity with changes in brain water and Na+, K(+)-ATPase activity. *J. Cereb. Blood Flow Metab.* **14**:332-336.

Mori S, van Zijl PCM (1995). Diffusion weighting by the trace of the diffusion tensor within a single scan. *Magn. Reson. Med.* **33**:41-52.

Moseley ME, Cohen Y, Mintorovitch J, Chileuitt L, Shimizu H, Kucharczyk J, Wendland MF, Weinstein PR (1990). Early Detection of Cerebral Ischemia in Cats: Comparison of Diffusion- and T2-Weighted MRI and Spectroscopy. *Magn. Reson. Med.* **14**:330-346.

Moser FC, Miller ST, Bello JA, Pegelow CH, Zimmerman RA, Wang WC, Ohene-Frempong K, Schwartz A, Vichinsky EP, Gallagher D, Kinney TR (1996). The spectrum of brain MR abnormalities in sickle cell disease: a report from the cooperative study of sickle cell disease. *AJNR Am. J. Neuroradiol.* **17**:965-972.

Nagesh V, Welch KMA, Windham JP, Patel S, Levine SR, Hearshen D, Peck D, Robbins K, D'Olhaberruague L, Soltanian-Zadeh H, Boska MD (1998). *Srtoke* **29**:1778-1782.

Neumann-Haefelin T, Wittsack HJ, Wenserski F, Siebler M, Seitz RJ, Mödder U, Freund HJ (1999). Diffusion- and perfusion-weighted MRI. The DWI/PWI mismatch region in acute stroke. *Srtoke* **30**:1591-1597.

Ogawa S, Lee T-M, Nayak AS, Glynn P (1990a). Oxygenation-Sensitive Contrast in Magnetic Resonance Image of Rodent Brain at High Magnetic Fields. *Magn. Reson. Med.* **14**:68-78.

Ogawa S, Lee TM, Kay AR, Tank DW (1990b). Brain magnetic resonance imaging with contrast dependent on blood oxygenation. *Proc. Natl. Acad. Sci. USA* **87**:9868-9872.

Ohene-Frempong K (1991). Stroke in sickle cell disease: demographic, clinical, and therapeutic considerations. *Semin. Hematol.* **28**:213-219.

Ohene-Frempong K, Weiner SJ, Sleeper LA, Miller ST, Embury S, Moohr JW, Wethers DL, Pegelow CH, Gill FM (1998). Cerebrovascular accidents in sickle cell disease: rates and risk factors. *Blood* **91**:288-294.

Okudaira Y, Arai H, Sato K (1997). Hemodynamic compromise as a factor in clinical progression of Sturge-Weber syndrome. *Chid's Nerv. Syst.* **13**:214-219.

Ordidge RJ, Cresshull ID (1986). The correction of transient B_0 field shifts following the application of pulsed gradients by phase correction in the time domain. *J. Magn. Reson.* **69**:151-155.

Ordidge RJ, Helpern JA, Knight RA, Qing Z, Welch KMA (1991). Investigation of Cerebral Ischemia using Magnetization Transfer Contrast (MTC) MR Imaging. *Magn. Reson. Imaging* **9**:895-902.

Ordidge RJ, Helpern J, Qing Z, Knight R, Nagesh V (1994). Correction of motional artifacts in diffusion-weighted imaging. *Magn. Reson. Imaging* **12**:455-460.

Ordidge RJ, Wylezinska M, Hugg JW, Butterworth E, Franconi F (1996). Frequency Offset Corrected Inversion (FOCI) pulses for Use in Localized Spectroscopy. *Magn. Reson. Med.* **36**:562-566.

Oshio K, Feinburg DA (1991). GRASE (gradient- and spin-echo) imaging: a novel fast MRI technique. *Magn. Reson. Med.* **20**:344-349.

Østergaard L, Weisskoff RM, Chesler DA, Gyldensted C, Rosen BR (1996a). High resolution measurement of cerebral blood flow using intravascular tracer bolus passages. Part I. Mathematical approach and statistical analysis. *Magn. Reson. Med.* **36**:715-725.

Østergaard L, Sorensen AG, Kwong KK, Weisskoff RM, Gyldensted C, Rosen BR (1996b). High resolution measurement of cerebral blood flow using intravascular tracer bolus passages. PartII. Experimental comparison asn preliminary results. *Magn. Reson. Med.* **36**:726-736.

Østergaard L, Johannsen P, Poulsen PH, Vestergaard-Poulsen P, Asboe H, Gee AD, Hansen SB, Cold GE, Gjedde A, Gyldensted C (1998a). Cerebral blood flow measurements by magnetic resonance imaging bolus tracking: comparison with [O-15] H_2O positron emission tomography in humans. *J. Cereb. Blood Flow Metab.* **18**:935-940.

Østergaard L, Smith DF, Vestergaard-Poulsen P, Hansen SB, Gee AD, Gjedde A, Gyldensted C (1998b). Absolute cerebral blood flow and blood volume measured by magnetic resonance imaging bolus tracking: comparison with positron emission tomography values. *J. Cereb. Blood Flow Metab* **18**:425-432

Østergaard L, Chesler DA, Weisskoff RM, Sorensen AG, Rosen BR (1999). Modeling cerebral blood flow and flow heterogeneity from magnetic resonance residue data. *J. Cereb. Blood Flow Metab.* **19**:690-699.

Pappata S, Fiorelli M, Rommel T, Hartmann A, Dettmers C, Yamaguchi T, Chabriat H, Poline JB, Crouzel C, Di Giamberardino L, Baron JC (1993). PET study of changes in local brain hemodynamics and oxygen metabolism after unilateral middle cerebral artery occlusion in baboons. *J. Cereb. Blood Flow Metab.* **13**:416-424.

Pekar J, Jezzard P, Roberts DA, Leigh JS, Jr., Frank JA, McLaughlin AC (1996). Perfusion Imaging with Compensation for Asymmetric Magnetization Transfer Effects. *Magn. Reson. Med.* **35**:70-79.

Pell GS, Thomas DL, Lythgoe MF, Calamante F, Howseman AM, Williams SR, Gadian DG, Ordidge RJ (1998) Measurement of perfusion using arterial spin tagging with the FOCI Pulse. In: *"Proc. ISMRM 6th Annual Meeting,* Sydney, Australia". pp 1190.

Pell GS, Thomas DL, Lythgoe MF, Calamante F, Howseman AM, Gadian DG, Ordidge RJ (1999). Implementation of quantitative FAIR perfusion imaging with a short repetition time in time-course studies. *Magn. Reson. Med.* **41**:829-840.

Perman WH, Gado MH, Larson KB, Perlmutter JS (1992). Simultaneous MR acquisition of arterial and brain signal time curves. *Magn. Reson. Med.* **28**:74-83.

Petrella JR, DeCarli C, Dagli M, Duyn JH, Grandin CB, Frank JA, Hoffman EA, Theodore WH (1997) Assessment of whole brain vasodilatory capacity with acetazolamide challenge at 1.5 T using dynamic contrast imaging with frequency- shifted burst. *Am J Neuroradiol* **18**:1153-1161.

Pierpaoli C, Righini A, Linfante I, Tao-Cheng JH, Alger JR, Di Chiro G (1993). Histopathologic correlates of abnormal water diffusion in cerebral ischemia: diffusion-weighted MR imaging and light and electron microscopic study. *Radiology* **189**:439-448.

Pierpaoli C, Alger JR, Righini A, Mattiello J, Dickerson R, Des Pres D, Barnett A, Di Chiro G (1996a). High temporal resolution diffusion MRI of global cerebral ischemia and reperfusion. *J. Cereb. Blood Flow Metab.* **16**:892-905.

Pierpaoli C, Jezzard P, Basser PJ, Barnett A, Di Chiro G (1996b). Diffusion tensor MR imaging of the human brain. *Radiology* **201**:637-648.

Piomelli S (1991). Sickle cell disease in the 1990s: the need for active and preventive intervention. *Semin. Hematol.* **28**:227-232.

Porkka L, Neuder M, Hunter G, Weisskoff RM, Belliveau J, Rosen BR (1991). Arterial input function measurement with MRI. In: "*Proc. SMRM, 10th Annual Meeting*, San Francisco, USA". pp 120.

Press WH, Teukolsky SA, Vetterling WT, Flannery BT (1992). *Numerical recipes in C. The art of scientific computing*, Cambridge, Cambridge University Press.

Quast MJ, Huang NC, Hillman GR, Kent TA (1993). The evolution of acute stroke recorded by multimodal magnetic resonance imaging. *Magn. Reson. Imaging.* **11**:465-471.

Reeder SB, Atalar E, Bolster BD Jr., McVeigh ER (1997). Quantification and Reduction of Ghosting Artifacts in Interleaved Echo-Planar Imaging. *Magn. Reson. Med.* **38**:429-439.

Reese TG, Weisskoff RM, Wedeen VJ (1998). Diffusion NMR facilitated by a refocused eddy-current EPI pulse sequence, *in "Proc. ISMRM, 6th Annual Meeting*, Sydney, Australia". p. 663.

Reid DE, Maria BL, Drabe WE, Quisling RG, Hoang KB (1997). Central nervous system perfusion and metabolism abnormalities in Sturge-Weber syndrome. *J. Child Neurol.* **12**:218-222.

Rempp KA, Brix G, Wenz F, Becker CR, Guckel F, Lorenz WJ (1994). Quantification of regional cerebral blood flow and volume with dynamic susceptibility contrast-enhanced MR imaging. *Radiology* **193**:637-641.

Riela A, Stump D, Roach S (1985). Regional cerebral blood flow characteristics of the Sturge-Weber syndrome. *Pediatr. Neurol.* **1**:85-90.

Rordorf G, Koroshetz WJ, Copen WA, Cramer SC, Schaefer PW, Budzik RF, Schwamm LH, Buonanno F, Sorensen AG, Gonzalez G (1998). Regional ischemia and ischemic injury in patients with acute middle cerebral artery stroke as defined by early diffusion-weighted and perfusion-weighted MRI. *Stroke* **29**:939-943.

Rosen BR, Belliveau JW, Vevea JM, Brady TJ (1990). Perfusion imaging with NMR contrast agents. *Magn. Reson. Med.* **14**:249-265

Rosen BR, Belliveau JW, Buchbinder BR, Mckinstry RC, Porkka LM, Kennedy DN, Neuder MS, Fisel CR, Aronen HJ, Kwong KK, Weisskoff RM, Cohen MS, Brady TJ (1991). Contrast agents and cerebral hemodynamics. *Magn. Reson. Med.* **19**:285-292.

Roussel SA, van Bruggen N, King MD, Gadian DG (1995). Identification of Collaterally Perfused Areas Following Focal Cerebral Ischeamia in the Rat by Comparison of Gradient Echo and Diffusion-Weighted MRI.. *J. Cereb. Blood Flow Metab.* **15**:578-586.

Russell MO, Goldberg HI, Hodson A, Kim HC, Halus J, Reivich M, Schwartz E (1984). Effect of transfusion therapy on arteriographic abnormalities and on recurrence of stroke in sickle cell disease. *Blood* **63**:162-169.

Satoh S, Shibuya H, Matsushima Y, Susuki S (1988). Analysis of the angiographic findings in cases of childhood moyamoya disease. *Neuroradiology* **30**:111-119.

Schick F (1997). SPLICE: sub-second diffusion-sensitive MR imaging using a modified fast spin-echo acquisition. *Magn. Reson. Med.* **38**:638-644.

Schlaug G, Siewert B, Benfield A, Edelmann RR, Warach S (1997). Time course of the apparent diffusion coefficient (ADC) abnormality in human stroke. *Neurology* **49**:113-119.

Schlaug G, Benfield A, Baird AE, Siewert B, Lövblad KO, Parker RA, Edelman RR, Warach S (1999). The ischemic penumbra. operationally defined by diffusion and perfusion MRI. *Neurology* **53**:1528-1537.

Schmitt F, Stehling MK, Turner R, eds. (1998a). Echo planar imaging. Theory, techniques and application. Springer, Berlin.

Schmitt F, Wielopolski PA (1998b). Echo-planar image reconstruction. In "Echo planar imaging. Theory, techniques and application" (Schmitt F, Stehling MK, Turner R, eds.). Springer, Berlin. pp 141-178.

Schreiber WG, Gückel F, Stritzke P, Schmiedek P, Schwartz A, Brix G (1998). Cerebral blood flow and cerebrovascular reserve capacity: estimation by dynamic magnetic resonance imaging. *J. Cereb. Blood Flow Metab.* **18**:1143-1156.

Schwamm LH, Koroshetz WJ, Sorensen AG, Wang B, Copen WA, Budzik R, Rordorf G, Buonanno FS, Schaefer PW, Gonzalez G (1998). Time course of lesion development in patients with acute stroke - serial diffusion- and hemodynamic-weighted magnetic resonance imaging. *Stroke* **29**:2268-2276.

Schwartz RB, Bravo SM, Klufas RA, Hsu L, Barnes PD, Robson CD, Antin JH (1995). Cyclosporine neurotoxicity and its relationship to hypertensive encephalopathy. CT and MR findings in 16 cases. *AJR Am. J. Roentgenol.* **165**:627-631.

Sekihara K, Kohno H (1987). New reconstruciton technique for echo-planar imaging to allow combined use of odd and even numbered echoes. *Magn. Reson. Med.* **5**:485-491.

Silva AC, Zhang WG, Williams DS, Koretsky AP (1995). Multi-slice MRI of rat brain perfusion during amphetamine stimulation using arterial spin labeling. *Magn. Reson. Med.* **33**:209-214.

Silva AC, Zhang WG, Williams DS, Koretsky AP (1997a). Estimation of water extraction fractions in rat brain using magnetic resonance measurement of perfusion with arterial spin labeling. *Magn. Reson. Med.* **37**:58-68.

Silva AC, Williams DS, Koretsky AP (1997b). Evidence for the exchange of arterial spin labeled water with tissue water in rat brain from diffusion-sensitized measurements of perfusion. *Magn. Reson. Med.* **38**:232-237.

Sorensen AG, Weisskoff RM, Reese TR, Rosen BR (1996). Optimization of diffusion-weighted MR imaging for evaluation of acute stroke. In: *"Proc. SMR 3rd Annual Meeting*, Nice, France". p.1383.

Starmer CF, Clark DO (1970). Computer computations of cardiac output using the gamma function. *J. Appl. Physiol.* **28**:219-220.

Steen RG, Reddick WE, Mulhern RK, Langston JW, Ogg RJ, Bieberich AA, Kingsley PB, Wang WC (1998). Quantitative MRI of the brain in children with sickle cell disease reveals abnormalities unseen by conventional MRI. *J. Magn. Reson. Imaging* **8**:535-543.

Steen RG, Xiong X, Mulhern RK, Langston JW, Wang WC (1999). Subtle brain abnormalities in children with sickle cell disease: relationship to blood hematocrit. *Ann. Neurol.* **45**:279-286.

Stejskal EO, Tanner JE (1965). Spin diffusion measurements: spin echoes in the presence of a time-dependent field gradient. *J. Chem. Phys.* **42**:288-292.

Stewart GN (1894). Researches on the circulation time in organs and on the influences which affect it. Part I-III. *J. Physiol.* (London) **15**:1.

Sunshine JL, Tarr RW, Lanzieri CF, Landis DMD, Selman WR, Lewin JS (1999). Hyperacute stroke: ultrafast MR imaging to triage patients prior to therapy. *Radiology* **212**, 325-332.

Suzuki J, Kodama N (1983). Moyamoya disease-a review. *Srtoke* **14**:104-109.

Tadamura E, Hatabu H, Li W, Prasad PV, Edelman RR (1997). Effect of Oxygen Inhalation on Relaxation Times in Various Tissues. *J. Magn. Reson. Imaging.* **7**, 220-225.

Takeuchi K, Shimizu K (1957). Hypoplasia of the bilateral internal carotid arteries. *Brain nerve* **9**:37-43.

Thulborn KR, Waterton JC, Matthews PW, Radda GK (1982). Oxygenation dependence of the transverse relaxation time of water protons in whole blood at high field. *Biochim. Biophys. Acta* **714**:265-270.

Truwit CL, Denaro CP, Lake JR, DeMarco T (1991). MR imaging of reversible cyclosporin A-induced neurotoxicity. *AJNR Am. J. Neuroradiol.* **12**:651-659.

Turner R, Le Bihan D (1990). Single shot diffusion imaging at 2.0 Tesla. *J. Magn. Reson.* **86**:445-452.

Ukei K, Meyer F, Mellinger J (1994). Moyamoya disease: the disorder and surgical treatment. *Mayo Clin. Proc.* **69**:749-757.

Ulug AM, Beauchamp N, Bryan RN, van Zijl PCM (1997). Absolute quantitation of diffusion constants in human stroke. *Stroke* **28**:483-490.

van Bruggen N, Roberts TPL, Cremer JE (1994). The Application of Magnetic Resonance Imaging to the Study of Experimental Cerebral Ischaemia. *Cerebrovasc. Brain Metab. Rev.* **6**:180-210.

van der Toorn A, Verheul HB, van der Sprenkel J-WB, Tulleken CAF, Nicolay K (1994). Changes in Metabolites and Tissue Water Status after Focal Ischemia in Cat Brain Assessed with Localized Proton MR Spectroscopy. *Magn. Reson. Med.* **32**:685-691.

van der Toorn A, Syková E, Dijkhuizen RM, Vorísek I, Vargová L, Skobisová E, van Lookeren Campagne M, Reese T, Nicolay K (1996). Dynamic changes in water ADC, energy metabolism, extracellular space volume, and tortuosity in neonatal rat brain during global ischemia. *Magn. Reson. Med.* **36**:52-60.

van Gelderen P, de Vleeschouwer, Des Pres D, Pekar J, van Zijl PCM, Moonen CTW (1994). Water diffusion and acute stroke. *Magn. Reson. Med.* **31**:154-163.

van Zijl PCM, Eleff SM, Ulatowski JA, Oja JME, Ulug AM, Traystman RJ, Kauppinen RA (1998). Quantitative Assessment of Blood Flow, Blood Volume and Blood Oxygenation Effects in Functional Magnetic Resonance Imaging. *Nature Medicine* **4**:159-167.

Verheul HB, Balázs R, Berkelbach van der Sprenkel JW, Tulleken CAF, Nicolay K, Tamminga KS, van Lookeren Campagne M (1994). Comparison of diffusion-weighted MRI with changes in cell volume in a rat model of brain injury. *NMR Biomed.* **7**:96-100.

Villringer A, Rosen BR, Belliveau JW, Ackerman JL, Lauffer RB, Buxton RB, Chao YS, Wedeen VJ, Brady TJ (1988). Dynamic imaging with lanthanide chelates in normal brain: contrast due to magnetic-susceptibility effects. *Magn. Reson. Med.* **6**:164-174.

Vogl TJ, Stemmler J, Bergman C, Pfluger T, Egger E, Lissner J (1993). MR and MR angiography of Sturge-Weber syndrome. *AJNR Am. J. Neuroradiol.* **14**:417-425.

Walter MC, Patience M, Leisenring W, Eckman JR, Scott JP, Mentzer WC, Davies SC, Ohene-Frempong K, Bernaudin F, Matthews DC, Storb R, Sullivan KM (1996). Bone marrow transplantation for sickle cell disease. *N. Engl. J. Med.* **335**:369-376.

Warach S, Chien D, Li W, Ronthal M, Edelman RR (1992). Fast magnetic resonance diffusion-weighted imaging of acute human stroke. *Neurology* **42**:1717-1723.

Warach S, Gaa J, Siewert B, Wielopolski P, Edelman RR (1995). Acute human stroke studied by whole brain echo planar diffusion-weighted magnetic resonance imaging. *Ann. Neurol.* **37**:231-241.

Weisskoff RM, Chesler D, Boxerman JL, Rosen BR (1993). Pitfalls in MR measurement of tissue blood flow with intravascular tracers: Which mean transit-time? *Magn. Reson. Med.* **29**:553-559.

Weisskoff RM, Zuo CS, Boxerman JL, Rosen BR (1994). Microscopic susceptibility variation and transverse relaxation. Theory and experiment. *Magn. Reson. Med.* **31**:601-610.

Welch KMA, Windham J, Knight RA, Nagesh V, Hugg JW, Jacobs M, Peck D, Booker P, Dereski MO, Levine SR (1995). A model to predict the histopathology of human stroke using diffusion and T_2-weighted magnetic resonance imaging. *Stroke* **26**:1983-1989.

Wielopolski PA, Schmitt F, Stehling MK (1998). Echo planar imaging pulse sequences. In "Echo planar imaging. Theory, techniques and application" (Schmitt F, Stehling MK, Turner R, eds.). Springer, Berlin. pp 65-139.

Williams DS, Detre JA, Leigh JS, Koretsky AP (1992). Magnetic resonance imaging of perfusion using spin inversion of arterial water. *Proc. Natl. Acad. Sci. USA* **89**:212-216.

Wittlich F, Kohno K, Mies G, Norris DG, Hoehn-Berlage M (1995). Quantitative measurement of regional blood flow with gadolinium diethylenetriaminepentaacetate bolus track NMR imaging in cerebral infarcts in rats: validation with the iodo[C-14]antipyrine technique. *Proc. Natl. Acad. Sci. USA* **92**:1846-1850

Wolff S, Balaban R (1989). Magnetisation transfer contrast (MTC) and tissue water proton relaxation in vivo. *Magn. Reson. Med.* **10**:135-144.

Wong EC, Cox RW, Song AW (1995). Optimized isotropic diffusion weighting. *Magn. Reson. Med.* **34**:139-143.

Wong EC, Buxton RB, Frank LR (1997). Implementation of quantitative perfusion imaging techniques for functional brain mapping using pulsed arterial spin labeling. *NMR Biomed.* **10**:237-249.

Wong EC, Buxton RB, Frank LR (1998a). Quantitative imaging of perfusion using a single subtraction (QUIPSS and QUIPSS II). *Magn. Reson. Med.* **39**:702-708.

Wong EC, Buxton RB, Frank LR (1998b). A theoretical and experimental comparison of continuous and pulsed arterial spin labeling techniques for quantitative perfusion imaging. *Magn. Reson. Med.* **40**:348-355.

Yang Y, Frank JA, Hou L, Ye FQ, McLaughlin AC, Duyn JH (1998). Multi-slice imaging of quantitative cerebral perfusion with pulsed arterial spin labeling. *Magn Reson Med* **39**:825-32.

Ye FQ, Mattay VS, Jezzard P, Frank JA, Weinberger DR, McLaughlin AC (1997a). Correction for vascular artifacts in cerebral blood flow values measured by using arterial spin tagging techniques. *Magn. Reson. Med.* **37**:226-235.

Ye FQ, Mattay VS, Frank JA, Weinberger DR, McLaughlin AC (1997b). Calculation of cerebral blood flow using "delayed acquisition" arterial spin tagging approaches. In: *"Proc. SMR 5th Annual Meeting*, Vancouver, Canada". pp 1756.

Zaharchuk G, Ledden PJ, Kwong KK, Reese TG, Rosen BR, Wald LL (1999). Multislice perfusion and perfusion territory imaging in humans with separate label and image coils. *Magn. Reson. Med.* **41**:1093-1098.

Zea Longa E, Weinstein PR, Carlson S, Cummins R (1989). Reversible Middle Cerebral Artery Occlusion without Craniectomy in Rats. *Stroke* **20**:84-91.

Zhang WG, Williams DS, Detre JA, Koretsky AP (1992) Measurement of brain perfusion by volume-localized NMR spectroscopy using inversion of arterial water spins-accounting for transit-time and cross-relaxation. *Magn Reson Med* **25**:362-371.

Zhang WG, Williams DS, Koretsky AP (1993). Measurement of rat brain perfusion by NMR using spin labeling of arterial water - in vivo determination of the degree of spin labeling. *Magn. Reson. Med.* **29**:416-421.

Zhang WG, Silva AC, Williams DS, Koretsky AP (1995). NMR measurement of perfusion using arterial spin labeling without saturation of macromolecular spins. *Magn. Reson. Med.* **33**:370-376.

Zhu X, Li K-L, Thacker NT, Jackson A (1999). Noise reduction in dyanmic contrast enhanced MR imaging, *in "Proc. ISMRM, 7th Annual Meeting*, Philadelphia, USA". p. 1870.

Zierler KL (1962). Theoretical basis of indicator-dilation methods for measuring flow and volume. *Circ. Res.* **10**:393-407.

Zierler KL (1965). Equations for measuring blood flow by external monitoring of radioisotopes. *Circ. Res.* **16**:309-321.